The surfaces of the Moon and Mercury: an experimental and numerical approach to ion sputtering

Inaugural dissertation
of the Faculty of Science,
University of Bern

presented by

Noah Jäggi

from Biberist SO

Supervisor of the doctoral thesis:
PD. Dr. André Galli
Institute of Physics, University of Bern

The surfaces of the Moon and Mercury: an experimental and numerical approach to ion sputtering

Inaugural dissertation
of the Faculty of Science,
University of Bern

presented by

Noah Jäggi

from Biberist SO

Supervisor of the doctoral thesis:
PD. Dr. André Galli
Institute of Physics, University of Bern

Accepted by the Faculty of Science.

Bern, 31.03.2023

The Dean:
Prof. Dr. Marco Herwegh

Abstract

Energetic solar wind ions erode the surfaces of the Moon and Mercury through sputtering. The process of sputtering ejects material with suprathermal velocities into the collisionless exospheres of their respective rocky body. The suprathermal populations in the exosphere thus directly sample the surface. Given the solar wind precipitation rates and areas, exospheric compositions can be interpreted if the sputtering yield of solar wind ions is known. A better understanding of ion sputtering will allow to quantify its importance relative to competing suprathermal processes such as photon stimulated desorption and micrometeoroid impact vaporization.

In the context of this thesis, mineral analogues and regolith samples were prepared, irradiated, and analyzed. A new preparation method using a custom pellet die was developed to obtain exceptionally resilient mineral powder pellets, without the use of a binder or adhesives. The analysis included infrared measurements in the 7–14 μm range, covered by BepiColombo/MERTIS (2.5–15 μm). We conclude that the interaction volume of infrared radiation exceeds the depth amorphized by average-velocity solar wind ions and does not lead to reliably detectable shifts in the spectrum. The efficient and rapid amorphization of the upper layer was determined computationally, and supported experimentally in collaboration with Biber *et al.* [1]. Therein, a crystal lattice effect on the sputter yield could not be detected between mineral pellets with microscopically rough surfaces and the glassy thin films produced from the same mineral powder. The differences in sputter yields could be attributed to roughness effects, suggesting extensive amorphization of the powder pellet surface.

The laboratory sputter yield results for flat surfaces were used to evaluate the established sputter code SDTrimSP and motivate the addition of two new models. The first model differentiates between oxide-bound elements and unbound elements in the sample and assigns density according to either the element or the oxide. It is capable of reliably reproducing mineral densities with simulated amorphization, causing only minor density changes at the surface that do not negatively affect the model. The second model expands on the commonly used surface binding energies by assigning a binding energy within the bulk sample. This bulk binding energy is based on the enthalpy of formation required to break up the

oxides that make up the mineral. Both models rely solely on tabulated data and no parameter adjustment is necessary to fit laboratory data. The increased binding energies lead to a broadening of the energy distribution as observed in laboratory data of oxidized metal. At normal incidence, SRIM yields are up to a factor five above laboratory yields. SDTrimSP simulation results however are in unprecedented agreement with laboratory data when including the two newly implemented models.

In a sputter-unrelated part of this thesis, Mercury's earliest magma ocean and atmosphere were modeled. A special focus was put on the loss or accumulation of sodium over the magma ocean lifetime, in an attempt to explain the exceptionally high surface concentrations of moderately volatile elements such as sodium, potassium, sulfur, and chloride on Mercury. Under average 'young-Sun space weather conditions', the combined atmospheric loss from plasma heating, photoevaporation, Jeans escape, and photoionization only accounts for a $\leq$0.02% decrease of the total sodium present in the mantle. This low degree of loss supports formation models which are based on the accretion of primitive chondrites to explain contemporary Mercury observations.

In conclusion, this thesis has advanced the understanding of sputtering on rock-forming minerals relevant for the Moon and Mercury. It includes data of lower than previously assumed yields, the ruling out of a crystal lattice effect on the sputter process, and the implementation of two new sputter simulation models, which in combination show results with unprecedented agreement with laboratory data. The laboratory data-verified computed sputter yields and their angular and energy distributions will help to differentiate solar wind ion sputtering from competing space weathering processes that provide suprathermal species to the exospheres of the Moon and Mercury.

Contents

Overview

The surfaces of the Moon and Mercury are subject to impinging, highly energetic ions from the solar wind. The material that is ejected thereby supplies the exospheres surrounding the bodies. This process of particle emission by impinging ions is called sputtering. The goal of this thesis was to perform laboratory sputtering experiments in collaboration with the Technical University of Vienna and evaluate/improve computational sputter models.

The thesis contains an extensive introduction (Chapter 1) which covers additional information for the three publications included in Chapters 2, 3, and 4. The findings of the publications are then set in context to the introduction in the conclusions (Chapter 5).

Plain text summary

For the laboratory ion sputtering experiments, I sourced and prepared mineral samples which is covered in depth in Chapter 2. The challenge was the creation of mineral powder pellets that would survive extensive handling and transport between facilities. The outcome was a custom pellet die that allowed pressing of powder directly into custom stainless steel holders. Following this publication, the irradiated pellets are used in ongoing collaborations with Uppsala, Sweden, as well as to Berkley, USA. A second finding of Chapter 2 is tied to infrared analysis performed on the samples before and after irradiation. I discovered that the wavelength-shift of spectral features caused by solar wind ions is proportional to their kinetic energy. For average solar wind energies of 1 keV/amu, the changes are almost negligible. The shift of spectral features towards higher wavelengths are an order of magnitude below the ones observed by a group that used an order of magnitude larger energies. The consequence for this is that larger shifts in the mid infrared spectra of minerals present on the Moon and Mercury would require prolonged exposure to high energetic portions of the solar wind.

To address the validity of models to reproduce experimental sputter results, I used the new data from the irradiation experiments performed by our collaborators in Vienna and compared it to pre-existing sputter models (Chapter 3).

The lack of agreement between the results of established models and laboratory experiments led to me being involved in co-developing two modules in the well established binary collision approximation code SDTrimSP. The modules thereby improved how the code determines densities for mineral samples, and added a new way of setting binding energies based on known, tabulated data. An in-depth discussion of the different ways of modeling sputtering including the new modules in SDTrimSP is given in Chapter 3.

Whilst determining minerals relevant for the Moon and Mercury I was surprised by the particularly sodium-rich surface composition of Mercury. This fact combined with the large interest in sodium regarding exosphere observations on Mercury led to the question, if sodium on Mercury's surface could have been lost or accumulated during its early magma ocean state. I led a successful collaboration covering the whole system of magma ocean cooling times, magma to atmosphere source rates feeding into the atmospheric structure, speciation and, finally, loss rates. The resulting work is showcased in Chapter 4. During this collaboration, the requirement of sourcing vapor from a magma and the lack of open access codes led to me creating a minimal working product of an evaporation code based on the work of Lamoreaux *et al.* [2, 3]. Aaron S. Wolf incorporated the code as a plug-in called VapoRock[1] into the open-access ThermoEngine[2] code. The follow-up publication, where I was heavily involved in the validation and documentation of VapoRock, is not included in this thesis, but a pre-print which was accepted for publication on January 25 2023 can be found here [4].

Notable collaborations and future work

Mineral pellets are rough on a macroscopic level, unlike glassy thin-films (Appendix C in Chapter 2). The effect of roughness was experimentally investigated on pellets I supplied to my collaborators at TU Vienna [1]. As a result, Biber *et al.* successfully reproduced pellet yields by combining surface roughness maps with thin-film yields in the ray-tracing code SPRAY [5].

[1] https://gitlab.com/ENKI-portal/vaporock
[2] https://gitlab.com/ENKI-portal/ThermoEngine

For irradiation experiments on Lunar regolith, I wrote a successful proposal for obtaining 2.4 g of Apollo 16 sample 68501 (PI: André Galli) and consecutively created pressed regolith pellets. The results of the experiments will be published in peer-reviewed papers by the Group in TU Vienna after the publication of this thesis.

I created a database for sputter yields and the angular and energy distribution of yield for major rock-forming minerals. This allows to obtain a sputter estimate for any given surface composition without the requirement of running SDTrimSP. The database was too extensive to be included in the the sputter modeling publication. It will be published separately with applications to various exposed rocky bodies in space as well as comparisons to previous sputter yield assumptions of complex surfaces [e.g, 6, 7, 8].

Chapter 1

Introduction

The research questions that drive the publications included in Chapters 2–3 of this thesis are related to the origin, mineralogy, and exosphere of Mercury with applications to the Moon and other exposed rocky bodies. They read:

- What are representative mineral analogues for Mercury and the Moon?
- How well do pressed powder pellets reproduce the surface properties of a loose regolith?
- Does the crystal lattice of a mineral powder have an effect on its sputter yield or is a glassy thin film representative for a sputtered mineral?
- How well can laboratory data be reproduced using state-of-the-art ion sputter models and what are the consequences for the contribution of sputtering-derived species to the exospheres of Mercury and the Moon?
- Is the large sodium content observed on the surface of Mercury representative of its building blocks or accumulated during/after an early magma-ocean state?

Throughout the introduction I will give more weight to Mercury and use the Moon as a comparative, whereas the findings regarding solar wind ion sputtering will find applications for the Moon, Mercury, and other exposed rocky bodies. Similarly, the Mercury magma ocean publication (Chapter 4) aimed at quantifying surface alteration through atmospheric loss is not limited to Mercury, but could find applications on hot, rocky-exoplanets.

1.1 The surfaces of the Moon and Mercury

Both surfaces of the Moon and Mercury are beaten by harsh space weather, which requires deeper understanding when assessing analogue samples. For the Moon, the choice of analogue minerals or even regolith samples is rather straightforward. However, unlike the large quantities of Lunar rocks and soil samples that were acquired from Moon landings [e.g., 9], there has so far been no sample return mission from Mercury, and there are no imminent plans to change that [10]. The surface properties of Mercury are thus limited to conclusions drawn from observations of MESSENGER and a dash of Mariner 10. BepiColombo is scheduled to take up its measurement campaign orbiting Mercury in a two-orbiter setup by 2025 [11]. Nevertheless, the data from MESSENGER alone gave valuable insights into the surface properties of Mercury, which were then related to its formation history. I will briefly introduce the origins of both the Moon and Mercury and how they impact the choice of minerals (and regolith) that were used as samples in this thesis and ongoing work.

1.1.1 Moon: formation and composition

Although the process of Moon formation is still debated, a widely accepted and consistent hypothesis is the existence of a global magma ocean [e.g., 12, 13, 14, 15, 16] which followed a giant impact between a Mars-sized impactor 'Theia' and proto-Earth [e.g., 17]. The latter was already mostly differentiated into an sulfur-iron core and a silicate rich mantle, therefore the ejected material, which subsequently formed the Moon, has a different bulk Fe/Si ratio which is expressed in the small Lunar core (approx. 250 km or 20% of total radius). The mare basalt minerals are however comparably iron rich (reflected in bulk composition; Table 1.1), which is attributed to the incomplete differentiation into core and mantle. During magma ocean crystallization, initial Mg-rich olivine formation would drive up the iron contents within the remaining melt [18, and references therein]. At 75% crystallization of the magma ocean, the resulting high density of the magma ocean allowed for a lower density plagioclase (Na and Ca bearing aluminum silicate; $Na_{1-x}Ca_xAl_{1+x}Si_{3-x}O_8$) floatation crust which

is the origin for the anorthositic[1] Lunar highlands. At 90% crystallization, dense Ti-bearing species such as ilmenite ($FeTiO_3$) would form. The extensive fractional crystallization would evolve the remaining melt, which is retained in-between the floatation crust and the already crystallized mantle. This layer is labeled urKREEP and is abundant in potassium (K), rare earth elements (REE) and phosphorous (P), or KREEP elements for short [19]. The high abundance of heat-producing, incompatible elements in the KREEP layer could therefore remain molten over several hundreds of millions of years [19]. Samples returned from the Moon have included KREEP-rich specimens, however no urKREEP sample exists to date [20].

Major impacts during the partially molten stage led to the formation of large basins which were subsequently filled with basaltic melts, making up the Lunar maria. The mare basalts and highland plagioclase show complementary REEs, which supports a shared origin in the mantle [16, 20]. Interesting to note is the absence of maria on the far-side of the Moon, which, as a result, make up but 17% of the Moon's surface [21]. Furthermore, the KREEP accumulation and heat production is limited to the Lunar nearside, whereas the farside has a thicker anorthositic crust [22, 20]. For this reason, the majority of the Lunar surface is chemically represented by anorthosite rocks, or as a result, 89% of the Lunar surface contains more than 80% plagioclase. The remaining 20% is shared by mafic minerals such as clinopyroxene (diopside $CaMgSi_2O_6$ and enstatite $MgSiO_3$), olivine ($(Mg,Fe)_2SiO_4$) and the oxide ilmenite $FeTiO_3$ [e.g., 23].

Lunar regolith The Moon is covered by a regolith (Fig. 1.1); a loosely bound mixture of rock fragments, agglutinates (glass bonded aggregates), mineral grains, and glass [9, 24]. The regolith is sourced by mechanical disintegration of basaltic and anorthositic rocks (characteristic compositions are in Table 1.1), including a small ($<$2 %) meteoritic component. During the sample return missions, no landing site showed uniform regolith compositions [9]. This led to the conclusions, that regolith chemistry is controlled by the local bedrock

[1] anorthosite: a rock composed of $\geq$90% plagioclase and a small, $\leq$10% component of mafic (Mg and Fe-rich) minerals

types and their proportions in the soil, and that the regolith is about 4-5 m and 10-15 m thick in the mare and highland regions respectively [25].

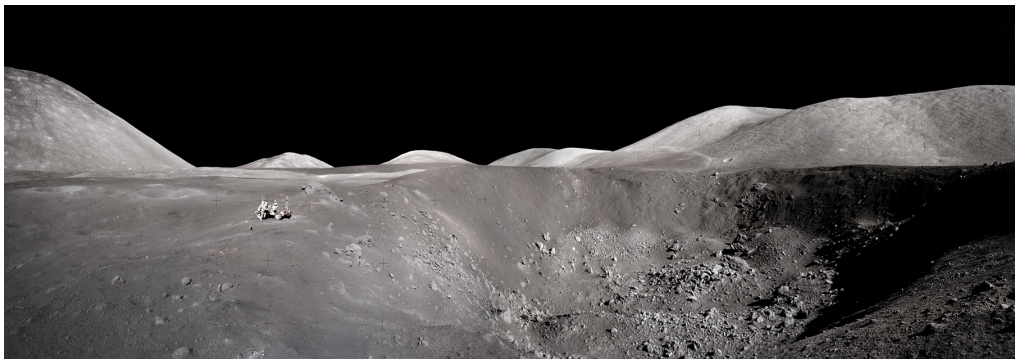

Figure 1.1: Apollo 17 Credit:NASA/JSC/ASU AndySaunders

Regolith exposure time When performing irradiation experiments, the ion fluence that is required to reach a constant rate of alteration is tied to an exposure age. For the Moon and Mercury, equilibrium in the laboratory experiments for solar wind speed He^+ impinging on a sample was reached within an equivalent of about 1000 and 300[2] years respectively (Ch. 2). The timescale at which the top centimeter of Lunar regolith is churned back, or 'gardened', into the deeper regolith is however still a matter of debate. Gault *et al.* [27] suggested ∼10 Ma for overturns caused by primary impactors. It was shown however, that secondary impactors exceed primary ones as a cause for mixing, and their inclusion in the same model reduces the time frame to 100-1000 years for a single turnover of the uppermost cm of regolith [28]. This would thus roughly coincide with the exposure time equivalents of the laboratory experiments. This would imply that regolith grains are not only recycled frequently, but also altered to a degree that is at least equal to the alteration that our laboratory experiments in the context of this thesis allows for. Lunar regolith grains express the alteration through space weathering in the form of an amorphous glass layer surrounding mineral grains [9, 24] and abundant agglutinates as well as pure glass components [29]. The grains that

[2]New, reduced solar wind ion precipitation rates for Mercury [Sec. 1.3.2; 26] increase the previous ∼100 year estimate from Chapter 2 by a factor of three.

have experienced several overturns are therefore strongly weathered and far from any ideal mineral.

Regolith properties and laboratory samples The continuous reprocessing of the Lunar regolith is expressed in the large range of grain sizes. Medians of grain sizes range from 42 to 800 μm and average between 60 and 80 μm [9]. When creating mineral powder pellets, this property could not be recreated. The cohesion of pure mineral powders is rather low and decreases with grain size (Ch. 2). No binder could be used as the surface needed to be free from contaminants. Furthermore, the laboratory experiment is run in an ultra-high vacuum chamber, prohibiting the usage of degassing adhesives. For this reason, the powder pellets were limited to the $\leq$30 μm grain size fraction, representative of only the smoothest regolith.

A goal of the thesis was to irradiate not only analogue minerals but also regolith. The scathing review of Taylor *et al.* in 2016 shifted our interest away from Lunar soil simulants[3] [30]. The conclusions of Taylor were, that the most recent simulants JSC-1 and its recreation JSC-1A both do not chemically represent the Lunar highlands or mare-soils. The only accurate property of the volcanic tuff mined for JSC-1A production is its $\sim$50% glass content [see section *"5. Example of a useless Lunar simulant"* in 30].

As an alternative, Taylor *et al.* suggested the use of the Lunar regolith sample 70050. This peculiar sample does not represent one single site, but instead samples the track of the Lunar Roving Vehicle (LRV) during the Apollo 17 mission [30]. The reason is, that the sample was collected from the regolith, that accumulated on the LRV during its employment. With this in mind, I applied for a rather large amount of this sample (2.4 grams) in order to create mineral pellets for ion irradiation experiments. The application was successful, but instead of sample 70050 we were offered the Lunar Highland sample 68501 sourced during the Apollo 16 mission [31, 32, 33, 34, 35], which we gladly accepted. This sample is currently being irradiated, and results are expected to

[3] A simulant tries to recreate the chemical and physical properties of a surface whereas an analogue, such as our mineral powders, do not.

be published after the end of this thesis together with my collaborators at TU Vienna.

Table 1.1: Elemental compositions in wt% for an average Apollo 11 Lunar Mare, Lunar highland represented by anorthosite [9], and Mercury's terranes after McCoy *et al.* [36] sorted by latitude

	Moon		Mercury terranes				
	Apollo 11 Mare Basalt	Highland Anorthosite	Southern hemi-sphere	High-Magnesium	Caloris Interior Basin	Low-Fast	Northern
O	43.31	45.55	39.65	37.21	41.31	41.13	42.27
Na	0.28	0.35	2.83	2.66	2.95	2.94	5.74
Mg	4.23	0.73	12.44	16.48	9.15	12.34	7.55
Al	5.34	17.68	7.79	5.32	9.44	7.05	6.04
Si	18.91	21.30	28.32	26.58	29.51	29.38	30.19
S	< 0.01	-	2.07	2.92	1.77	1.76	2.11
Cl	$\ll 0.01$	-	0.14	0.13	0.15	0.24	0.45
K	$\ll 0.01$	$\ll 0.01$	0.13	0.10	0.08	0.15	0.20
Ca	8.25	13.65	4.55	5.58	4.43	3.82	4.23
Ti	6.24	0.05	0.34	0.32	0.35	0.35	0.36
Cr	< 0.01	-	0.14	0.13	0.15	0.15	0.15
Mn	< 0.01	-	0.11	0.11	0.12	0.12	0.12
Fe	13.44	0.70	1.48	2.44	0.59	0.59	0.60
Total	100.01	100.00	99.99	99.98	100.00	100.02	100.01

1.1.2 Mercury: formation and composition

In stark contrast to the Moon, Mercury boasts a core which makes up the majority of its volume. The thickness of the silicate shell is estimated to be $\sim$400 km [38]. Compared to a Mercury radius of 2439.7 km the core thus makes up about 83% of its radius or 57% of its volume. The large core suggests high degrees of melting to the levels of a completely molten magma ocean state in order to have efficient metal segregation and core formation [39, 40]. The origin of the comparably thin mantle is still an open question. There are several pieces of evidence that suggest a volatile-rich crust and, possibly, mantle. One of which is the detection of surface Na, S, and Cl abundances that exceed the volatile-depleted Moon by an order of magnitude [Table 1.1; 9, 41, 42].

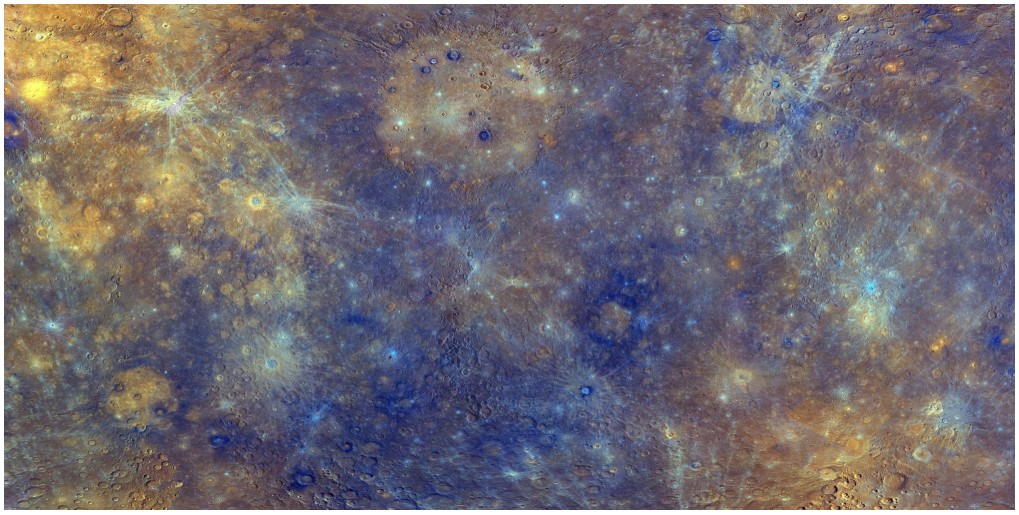

Figure 1.2: Enhanced color view of Mercury derived from MESSENGER's eight-color mosaic. The first and second component of the 11 wide angle camera narrow-band color filters of MESSENGER/MDIS [37] are colored green and red respectively. The blue represents the ratio of the reflected light wavelengths 433 nm (visible) to 996 nm (near infrared). As a result, younger features appear white (crater ejecta) or orange (Coriolis Interior Smooth Plains) and older terrains appear bluer (Intercrater Plains and Heavily Cratered Terrain). **Credit:** NASA/Johns Hopkins University Applied Physics Laboratory/Carnegie Institution of Washington. **Photojournal:** PIA17386

Formation A formation model for Mercury would have to explain not only the mantle-to-core ratio but also the planet's volatile-rich chemistry. A number of suggested formation models exist and include 1) accretion of primitive chondrites [43, 44]; 2) a giant impact in Mercury's past, analogous to the Moon [45, 46]; 3) mantle stripping through multiple hit-and-run collisions [47, 48, 46]; 4) erosion by small, high-energy impactors [49, 50]; or even 5) extensive evaporation [51]. So far, none of the proposed models can self-consistently explain all of the observational data of Mercury. For an excellent and detailed discussion on the different possible ways of formation, see Ebel *et al.* [44].

The most important implication for the Mercury magma ocean publication (Ch. 4) is the existence of a magma ocean at one stage of Mercury's evolution. Furthermore, Mercury could have been larger, according to the mantle stripping and impactor erosion theories. For this reason, we included a $\sim$35% larger initial size of Mercury in our models, inspired by accretion models [3290 km; 52] to explore the effect that size would have in the magma ocean cooling times and atmospheric loss rates. For representative magma ocean compositions

we chose an enstatite chondrite (EH4) and a Bencubbin class carbonaceous chondrite (CB). The EH4 composition thereby limits the partial melting process to a single-stage, which would result in a composition similar to Mercury's [53, 54, 55]. If the melting process was more elaborate, as modeled by Brown *et al.* [39], the CB chondrite composition is most accurately reproducing Mercury's contemporary surface composition [36].

Element mapping with MESSENGER

Gamma-Ray and Neutron Spectrometer (GRNS) – Detection of major elements including H, O, Na, Mg, Si, Ca, Ti, Fe, K, and Th by means of gamma-ray emissions spanning 0.1-10 MeV in energy and neutrons up to ∼7 MeV in energy [56]. Neutrons are thereby counted by a three-layer scintillation detector with a special sensitivity for H to detect polar deposits.

The gamma rays and neutrons are produced by Galactic Cosmic Rays (GCRs), which can travel through Mercury's thin exosphere. For each incident Galactic Cosmic Ray (GCR) particle, nine neutrons are produced on average [57], which can then react with nuclei and produce gamma-rays with element-characteristic, discrete energies that can be detected up to 1000 km from the surface. The gamma rays originate from the top ∼10 cm of the surface at generally low fluxes. For good statistics, many orbits are necessary [58, 56, 59]. The advantage of the GRS over XRS is its larger sampling depth compared to the µm-range of XRS.

X-Ray Spectrometer (XRS) – Detection of X-rays that are emitted through X-ray fluorescence (XRF) from excited planet surface atoms with characteristic energies in the range of 1-10 keV [60]. The Kα lines—produced by an electron transitioning to a vacancy in the innermost atom shell—for elements of interest within this range are Mg (1.254 keV), Al (1.487 keV), Si (1.740 keV), S (2.308 keV), Ca (3.691 keV), Ti (4.508 keV), and Fe (6.403 keV) [60]. The XRF is thereby stimulated through energetic X-rays emitted during solar flares that penetrate several tens of µm into the surface [60]. The solar X-ray spectrum is highly variable and therefore measured by an accompanying solar monitor [60, 61]. The advantage of XRS is the possibility to obtain elemental surface abundances from a single X-ray emission event, however the timing and rate of high-energy emission events is unforeseeable and the spectrum of exciting particles has to be well understood.

Surface composition Surface elemental-composition maps were first acquired by MESSENGER's suite of spectrometers, which included an X-Ray Spectrometer (XRS) [60], and a combined Gamma-Ray (GRS) and Neutron Spectrometer (NS) [56]. In general, Mercury's surface mainly consists of Al, Si, S, Ca, and minor Fe with a characteristic low O content [62, 63, 64, 61]. On average, compared to Earth and Moon, Mercury shows higher Mg/Si and lower Al/Si and Ca/Si ratios. Surface Fe is with 1-2 wt% comparably low to the 4-8 wt% on Earth [63, 65]. The coarse mapping of elements together with surface imaging then led to the distinction of characteristic terranes [Table 1.1; 66, 67, 68, 36].

Geochemical subdivision of Mercury:

- Early [>3.8 Ga; 69] volcanic products that were consecutively cratered by impacts. The interpretation is, that during the magma ocean solidification stage, high-temperature and high-Mg partial melts of the upper mantle created thin, laterally extensive surface units [36].

  Southern hemisphere - Corresponds to the Mercury average composition and is comprised of intercrater plains with minor occurrences of volcanic smooth planes [70]. It is not considered to be a geochemical unique terrane, and was not further subdivided due to the lack of available MESSENGER/GRNS data [66].

  High-Magnesium Terrane - Low elevation, highly cratered area with Mercury's highest Mg/Si ratios and relatively high S/Si, Ca/Si, and Fe/Si ratios [61, 71] situated around $\sim$30° North and -90° East adjacent to the Northern Terrane. Apart from the southern hemisphere, this terrane is the largest of all geochemical terranes distinguished by Peplowski *et al.* [66].

- Late volcanic period [$\sim$3.8-3.7 Ga; 70, 72, 73] with different chemical compositions likely due to different depths and extents of partial melting [74, 75].

  Northern Terrane - Makes up most of the Northern Smooth Plains (NSP) and boasts the largest Na/Si and Cl/Si ratios [factor $\sim$ 2 above Mercury mid-northern latitudes; 41, 76]

Low-Fast Terrane - Located in the mid-northern latitudes of the NSP. Named after the low amount of fast neutrons relating to locally reduced Mg, S, and Ca contents [67]. It further differentiates itself from the Northern Terrane through lower Na/Si and Ca/Si ratios and a higher Mg/Si ratios. Otherwise, the Low-Fast Terrane only exhibits minor differences (higher Cl, lower Ca) compared to the southern hemisphere.

Caloris Interior Plains (CIP) - Geochemical terrane that correlates with the Caloris Interior Smooth Plains. The Caloris impact feature is a $\sim$ 1500 km diameter crater[77, 78]. It exhibits the highest Al content of all terranes and its low Mg content is only undercut by the Northern Terrane [36].

Mercury's geological terranes Unlike the geochemical terranes, there are clearly distinguishable geological features into which Mercury can be subdivided roughly. They include:

- Northern Smooth Plains (NSP) - the largest area of volcanic origin. The NSP is crater-poor, occupying $\sim$7% of the planet surface and located around the Mercury's north pole [72, 70]
- Caloris Interior Smooth Plains - The smooth interior of the Caloris impact basin.
- Circum-Caloris Plains - The surrounding of the Caloris impact basin [61], also called Caloris exterior plains [36].
- Intercrater Plains and Heavily Cratered Terrain (IcP-HCT) - Collective term for the remaining surface which is not identified as smooth plains (NSP, Caloris impact basin). Hollows, 'swiss-cheese'-like features (Fig. 1.3) are featured prominently in proximity to craters [79] and the correlation between Mg and S within the IcP-HCT suggests the presence of sulfides [61].

Mercury's hollows A feature unique to Mercury are the rim-less depressions that exhibit a high reflectivity called hollows. Hollows were detected late

in the MESSENGER mission—when the spacecraft was at low altitudes over the northern hemisphere—-by targeted observations with MASCS/UVVS [79, 80, 81]. They occur predominantly in the low-reflectance material color unit of Mercury situated in basins and impact craters [82, 83, 84] and are rare in S-poor compositional terranes like the Caloris Basin [71, 85]. They are assumed to be geologically very young due to a lack of overlaying impact craters [86]. Their formation is still a mystery but the suggested mechanisms are no different to those acting on Mercury's surface. They include thermal desorption, photon stimulated desorption, micrometeoroid vaporization and solar wind ion sputtering [introduced in Sec. 1.2; 24, 86]. The limited variation in hollow depths suggests that deepening stops as soon as a thick enough lag layer forms that prevents further erosion [86].

MESSENGER/MASCS

The Mercury Atmospheric and Surface Composition Spectrometer [MASCS; 80] consisted of two experiments:

- The Ultraviolet and Visible Spectrometer (UVVS) covered wavelengths of the far-ultraviolet (115-180 nm), middle ultraviolet (160-320 nm), and visible (250-600 nm) light. MASCS/UVVS was designed to measure sunlight scattering intensities of known exospheric species (H, O, Na, K, Ca), and for the pre-MESSENGER era speculative ones (Mg, Fe, Al) [87, 88]. UVVS mapped the Mercury surface on a $\leq$10 km scale.
- The Visible-Infrared Spectrograph (VIRS) covered visible (300-1050 nm) to near infrared (850-1450 nm) wavelengths and mapped Mercury's surface reflectance on a 5-km spatial scale.

Although the composition of hollows is still debated, sulfides or carbon are likely candidates [62, 89]. The 'light blue' halos that surround the hollows (Fig. 1.3) have been speculated to be either carbon or sulfide dust grains [89]. The strong correlation with S, Ca and Mg-rich terranes motivates the use of sulfides like MgS and CaS as analogue material for Mercury [e.g., 90]. Similar to sodium, the sulfur on Mercury might not be bound in sulfides but instead be accumulated in the regolith. The abundance of hollows on Mercury was

determined to be ∼0.08% [85], making hollow-bound sulfides only a minor contributor the surface of Mercury. Nevertheless, understanding the behavior of sulfides exposed to space weathering is required to understand the formation of hollows and their composition.

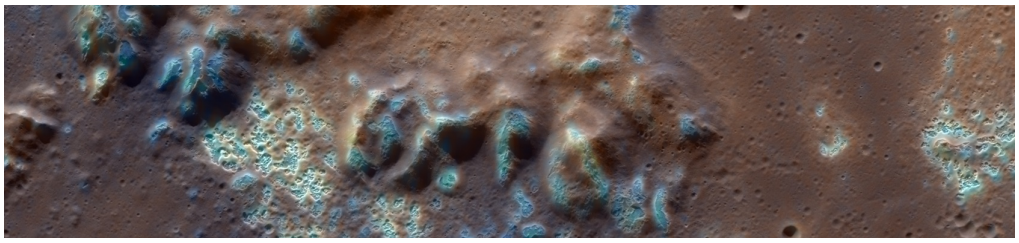

Figure 1.3: Hollows on the surface of Mercury. The thousands of similar depressions detected range between 20–1600 meters across with clusters spanning up to tens of kilometers [81]. The depths of hollows are in the order of a few tens of meters [81]. **Credit:** NASA/Johns Hopkins University Applied Physics Laboratory/Carnegie Institution of Washington

Mercury's volatiles There are two peculiar observations on Mercury that affect the selection of representative mineral analogues: Unlike the Moon, the abundance of sodium, sulfur, and volatiles in general are high and the oxygen fugacity is low.

The sodium enigma Mercury is characterized by large contents of sodium in its surface ranging 2.8 ± 0.4 wt% to 4.9 ± 0.7 wt% [41] and significantly exceeds the Lunar sodium of ≤ 1 wt% [Table 1.1; 9]. If this sodium were to be situated within a major rock-forming mineral that precipitated from a Na-rich melt, an equally Na-rich plagioclase would be expected. The range of sodium reported for Mercury thereby covers bytownite (20 at% Na; $Na_{0.2}Ca_{0.8}Al_{1.8}Si_{2.2}O_8$) to oligoclase (80 at% Na; $Na_{0.8}Ca_{0.2}Al_{1.2}Si_{2.8}O_8$). An observation that questions this assumption is the increase of volatile species (H, Cl, Na, and K) from the equator toward more northern latitudes [Compare southern hemisphere and Northern Terrane in Table 1.1; 41, 91, 92, 93]. The accumulation of H and Na seen in MESSENGER/GRNS measurements would thereby be attributed to thermal processes and re-deposition at cold, high latitudes [41, 92, 93]. Within the given uncertainty it is reasonable to assume that an intermediate (labradorite) to low sodium plagioclase (bytownite) is representative for Mercury's surface.

Iron, sulfur and fO_2 Mercury has an exceptionally low iron [mean of ∼1.5 wt%; 62, 63, 65] but high sulfur content [≤3.5 wt%; 94] (Table 1.1). From both quantities, an oxygen fugacity (fO_2) can be inferred which describes the amount of O_2 that is available to undergo a reaction and therefore represents the redox conditions of Mercury's crust [95]. If all of the surface iron were oxidized, the resulting fO_2 would lie 2.8–4.5 log units below the fO_2 of the iron-wustite (IW) equilibrium calculated at 0.1 MPa from thermodynamic data [94, 96, 97]. If sulfur is used as an oxybarometer [98], this would result in a mean fO_2 of IW-5.4 which makes Mercury more reduced than the Lunar surface [IW-2 to IW; 99, 100] or even its proposed building blocks (Sec. 5.3.3) and most reduced meteorites, the enstatite chondrites [IW-5; 101, 100]. The discrepancy between the fO_2 determined from iron and the one from sulfur is attributed to iron being present in sulfides instead of silicates, which was suggested by spectral data [96].

As a result of the low fO_2, sulfur was shown in experiments to become less siderophile and silicon to become more siderophile [98]. In the reducing environment, iron will form metallic iron instead of iron-oxide and is removed from the mantle which explains the low surface iron content [102, 96]. As a consequence, Mercury's magma ocean was likely depleted in iron whereas the increased siderophile behavior of silicon, caused by the extremely low fO_2, would allow for 15–20% Si to be present in Mercury's core [103, 94].

Mercury's earliest crust Another side-effect of iron removal is a low density of the magma ocean, which prevents silicate phases from becoming buoyant [96, 65, 104]. Vander Kaaden *et al.* [105] suggested that the only crust that would stay afloat in a low-FeO magma ocean would be graphite, ranging from 1 m to 20 km in thickness, depending on the present bulk carbon concentration. The strongly reducing conditions inferred from the high surface S/Fe would thereby allow for carbon to remain in the mantle without partitioning into the core [106]. The low density contrasts in such an environment would also prevent material overturn [105]. After its formation, the carbon layer would be covered by melt-derived volcanic rocks and dredged up to contribute to the observed Low Reflectance Material (LRM) [104] in quantities consistent

with upper carbon limits from MESSENGER/GRNS [0-4.1 wt% C on a three-standard-deviation level; 107, 104, 108]. The carbon flotation crust theory is to be taken with a grain of salt, however, as with an FeO enrichment in the melt as little as 0.2 wt%, a density contrast would exist, allowing for an early plagioclase crust to stay afloat [39].

The existence of a 1-20 km thick, stagnant carbon floatation crust on top of a magma ocean would actively prevent evaporation of the melt. In Chapter 4, an fO_2 of IW-1 is used instead of the proposed mean fO_2 of IW-5.4 [94], which would hinder the formation of a carbon crust due to the significantly increased solubility of carbon [109, 110]. The melting point of pure carbon at low pressure exceeds 3500 K [e.g. 111], which implies that a carbon crust would already be in place—or forming—at temperatures of 2400 K used as a starting point in the magma ocean model. To maximize the atmospheric loss caused by melt evaporation and degassing, it was thus necessary to assume that the initial fO_2 of the magma ocean was less reducing than inferred from today's crustal composition.

Mercury's regolith The properties such as grain size, and glass content in Mercury's regolith remain a mystery to this day. There are however several works that suggest Mercury's regolith to be intensely weathered, more so than on the Moon. Already in 1992, Cintala [112] proposed that the regolith of Mercury is more mature than the Lunar regolith based on assumed micrometeoroid fluxes and large surface temperatures. The author thereby predicted smaller grain sizes and a larger glass-component. Since these predictions, the Mercury Dual Imaging System (MDIS) onboard of MESSENGER provided a global eight-color mosaic [Figure 1.2; 37, 113, 114, 115]. This mosaic requires processing with a photometric model to correct effects due to phase angle and topography-affected effects such as incidence and emission angles [116]. Domingue *et al.* [116] compared two photometric models by Hapke [117, 118] and Kaasalainen and Shkuratov [119, 120] to evaluate their capabilities and, most relevant for this work, to make qualitative statements about Mercury's regolith. They concluded for Mercury that the regolith is smoother on the 100 μm scale and overall less blocky. Furthermore, the physical structure of

the regolith grains is different, likely due to a larger abundance of fine-grained opaques and/or nanophase products caused by space weathering. The intensity of the weathering on Mercury is also seen in the fast degradation rates of craters. Fassett *et al.* [121] deduced a factor two faster degradation rate on Mercury compared to the Moon from the low crater depth to diameter ratios of young features.

Representative laboratory samples The available qualitative properties of Mercury's regolith are difficult to reconcile with laboratory samples. Lower grain-sizes would be ideal, as pressed pellets are most robust when made of the more cohesive, fine-grained mineral powders. The larger intensity of space weathering on Mercury could continuously meld small grains together, which would lead to the predicted smoother [116], glass-rich [112, 24] surface, with a potentially smaller grain size [24]. The glass content of the regolith was neglected, as pure mineral powders were used for the samples. In hindsight, and as a consequence of this thesis, a pellet pressed from an amorphized mineral powder is expected to produce the same results as a crystalline one [1]. Amorphization of a sample exposed to ions with solar wind energy happens rapidly, therefore the results that are obtained after the sample surface reached equilibrium can be considered to be that of glass. Lastly, the admixing of opaques, such as carbon, would be feasible and definitely of interest, but was neglected in this thesis to keep the samples relevant for both the Moon and Mercury.

1.1.3 Infrared analysis

In order to determine the mineralogy of Mercury, infrared (IR) spectroscopy was used to complement the GRNS and XRS element maps [e.g., 122]. I will introduce IR spectroscopy in the visual and near infrared (VNIR, 0.6-2.5 μm) as well as mid infrared (MIR) and show how exposure to space weathering is known to cause spectral variations. The latter is given a stronger focus in the context of the MIR spectroscopy work presented in Chapter 2 as well as the inclusion of a MIR-spectrometer onboard of BepiColombo. Infrared spectra represent light intensity as they interact with a target. Commonly, IR spectra

are obtained in transmission, measuring the amount of light travelling through the sample when the light source is in contact with the sample. For remote sensing purposes, the effect of light scattering has to be taken into account, which led to the acquisition of reflectance spectra of minerals instead [123]. The main complication in interpreting IR spectra is their sensitivity to a list of sample and environment-related drivers:

- composition [123, 124]
- contaminants/darkening agents [125, 126, 127]
- grain size [128, 129, 130]
- temperature [90, 131, 132, 133]
- phase angle[4] [134, 135, 133]
- weathering [136, 137, 138, 139]

The space weathering effect in the near infrared The differences between weathered Apollo soils and freshly crushed regolith rocks in VNIR spectra was attributed to weathering by solar-wind ion sputtering and micrometeoroid impact vaporization [Sec. 1.2; 29, 139, 140, 141], the relative roles of which are still a matter of debate. The VNIR spectra of the exposed soils experience an overall loss in reflectivity (lower albedo), reddening—expressed in a shift towards higher wavelengths—and attenuating absorption features [142, 143, 140, 141]. These effects were attributed to the reduction of FeO into nanophase iron ($npFe_0$) within the amorphous rims which form during irradiation of Lunar grains [144, 145, 143, 146].

MESSENGER VNIR observations On Mercury, the VNIR spectrometer aboard of MESSENGER returned reflectance spectra which lack any strong absorption features [79, 147] attributed to the absence of transition elements [such as Fe and Ti; 122]. Nevertheless, the visible and near-IR spectra together with complementary observations allowed for several findings. To name a few: A decrease of the 1μm absorption band, as characteristic for Lunar weathering,

[4] angle between incident and reflected light

is not observed on Mercury, attributed to the absence of significant surface iron contents preventing formation of $npFe_0$ [104]; the low reflectance material (LRM) on Mercury contains 1-3 % more carbon than surrounding materials [108]; Mercury's hollows cannot be fully described by sulfides, but instead, the presence of Cr, Ti, and Ni bearing pyroxenes from the bedrock where the hollows were emplaced is suggested [148].

Space weathering effect in MIR The wavelength range of IR analysis related to Mercury was extended to the MIR (2.1-25 μm) with the MErcury Radiometer and Thermal infrared Imaging Spectrometer (BepiColombo/MERTIS), covering wavelengths of 2.5-15 μm on board of BepiColombo [149]. The features of note in MIR are the *Christiansen Feature* and the *Reststrahlen Bands*. The former is a transparency feature and reflectance minimum located around 8 μm, where the scattering of wavelengths is reduced due to matching refractive indices between the medium and the sample. As an example in SiO_2, the *Christiansen Feature* is located at 7.4 μm, where the refractive index $n_{7.4\mu m} = 1.0$, and thus equals the refractive index of air [150]. The *Reststrahlen Bands* are changes in the refractive index that inhibit electromagnetic radiation propagation in the medium, resulting in high reflection. They are caused by crystal lattice deformation, and stretching vibration motions of atoms [151, 152, 123]. The most relevant ones for BepiColombo/MERTIS include:

- At lower wavelengths, water adsorbed to a crystal lattice can be detected due to O-H stretching vibrations (2.9 μm) and H-O-H bending vibrations (6.1 μm), which cause the reflection of light.
- Between 8.5 and 12 μm, the most intense features occur in silicate spectra due to Si-O stretching caused by O-displacements.
- At wavelengths in the upper BepiColombo/MERTIS range, symmetric stretching of Si-O-Si, Si-O-Al, and (Si,Al)-O-(Si,Al) occurs between 12 and 16.7 μm due to Si and Al displacements instead of O displacements [153].

Capabilities and limitations of MIR The motivation to use MIR was the fact, that MIR features, especially the *Christiansen Feature*, were supposedly resistant to space weathering. This was shown for vitrification of minerals [154] and the

lack of correlation with exposure age in Lunar soils returned to Earth [155]. Ground-based MIR observations of Mercury were thereafter used to predict Mercury's surface composition [156] based on MIR spectra ranging 8-12.7 μm. Sprague et al. [156] proposed magnesium-rich orthopyroxene and olivine, Ca-, Mg-, Na-rich clinopyroxene, and K- and Na-bearing plagioclase feldspar based on this data. From LRO/Diviner data it became clear however, that the *Christiansen Feature* on the Lunar surface is indeed affected by weathering processes [136, 137, 138, 124]. This was shown for crater ejecta and ray deposits that show systematically shorter wavelengths than their more intensely weathered surroundings. In the same way, Lunar swirls, which are interpreted to inhibit space weathering show a *Christiansen Feature* at lower wavelengths compared to the adjacent terrains [124]. My contribution on the degree of spectra alteration caused by solar wind ion irradiation is included in Chapter 2.

LRO/Diviner

The Diviner Lunar Radiometer on board of the Lunar Reconnaissance Orbiter (LRO) is a 9 band multispectral infrared radiometer tasked to obtain detailed Lunar surface and subsurface temperatures. Among these bands, three narrow channels cover the typical *Christiansen Feature* wavelength (channels 3, 4, and 5 with 7.55–8.05, 8.10–8.40, and 8.38–8.68 μm respectively). With a ∼200 meter mapping resolution, a comprehensible and rather high resolution study of the *Christiansen Feature* on the Moon was conducted by Greenhagen *et al.* and Lucey *et al.* [136, 137, 138, 124].

1.2 The Exospheres of the Moon and Mercury

An exosphere of an exposed, rocky body is permanently supplied by space weathering processes and depleted by atmospheric loss. This section will first define the exosphere location within an atmosphere, which also finds its application in the magma ocean publication, where some processes act preferentially on the exosphere (Chap.4). I then introduce measurement techniques, their capabilities and limitations and summarize the observations of species in the exospheres surrounding the Moon and Mercury. This information is crucial when discussing the relevance of sputtering relative to other space weather-

ing processes and how each process competes to supply different exospheric populations.

Definition and bulk measurements On the Lunar surface, gaseous species exert $\sim 10^{-15}$ bar of atmospheric pressure [157, 158]. For Mercury, the Mariner 10 occultation experiment confined the maximum surface pressure to be $\leq 10^{-13}$ bar based on the upper limit density of 10^{12} atoms m^{-3} and an atmospheric temperature of 500 K [159, 160]. At such low pressures, the mean free path of a species i ($\lambda_i = 1/n_i\sigma_i$) exceeds its scale height ($H = k_B T/mg$) in the atmosphere and as a consequence, particle collisions are negligible. The number density for species i at the exobase, which defines the elevation at which the mean free path equals the scale height, is computed by [e.g., 161]:

$$n_{i,\mathrm{exo}} = \frac{1}{H_i \sigma_i} = \frac{m_i\, g(h)}{k_B\, T\, \sigma_i}, \tag{1.1}$$

with the gravitational acceleration as a function of height $g(h)$, the Boltzmann constant k_B, the temperature T, and the species specific cross section σ_i and mass m_i. On Mercury, for Sodium ($m_{Na} = 3.8175458 \times 10^{-26}$ kg, $\sigma_{Na} \approx 3.238 \times 10^{-19}$ m^2) on the surface of the subsolar point (T = 700 K [162], $g_{surf} = 3.7\ m\,s^{-2}$) this would equate to $n_{exo,Na} = 4.51 \times 10^{13}$ cm^{-3}. Comparing this to the Na surface density at the subsolar point of the Moon [57 ± 20 cm^{-3}; 163] and Mercury [$10^4 - 10^5$ cm^{-3}; 164], confirms that the exobase on both Mercury and the Moon coincides with their respective surface and that there is no collisional atmosphere. It also highlights the enigma that is the exceptionally high Na content in Mercury's exosphere. Interesting to note is also that the confirmed quantities and upper limits of species at Mercury only add up to 10^{-12} bar, which cannot account for the 10^{-13} bar of total pressure from the Mariner 10 occultation experiment [159, 160, 7]. It is speculated that the remainder of the exosphere is volatile material which so far was not detected [165].

1.2.1 Exospheric composition

Detection of species A typical observation of a species is done in two ways: direct measurements using a mass spectrometer, or indirectly by spectrographs that observe columns of gas. Ground-based observatories rely on spectrographs,

Mariner 10

Mariner 10 launched in November 1973 and performed three flybys at Mercury in March and September 1974 and March 1975. Due to the planet's 3:2 resonance with the Sun, Mariner 10 imaged the same hemisphere at each flyby (45% of the surface). It discovered the high degree of cratering and Mercury's global magnetic field. It also detected magnetospheric bursts of energetic charged particles and measured exospheric neutral hydrogen, helium and oxygen contents as well as Mercury's total atmospheric pressure [166, 167, 168].

where a sufficiently high density of particles within line of sight is needed to detect light intensity spectra as a function of characteristic wavelengths [e.g., MASCS/UVVS on MESSENGER had a detection limit of ∼100 Rayleighs; 80]. Even if no characteristic absorption line is observed with the spectrograph, given uncertainties, an upper limit of particles in the exosphere can be determined [e.g., 80]. For example, LRO/LAMP integrated Lunar exosphere observations over 7.7 million seconds from which upper limits for 27 species were calculated, without resulting in a new detection [169]. At the cost of global resolution of ground-based observations, spacecraft missions use a combination of light spectrographs and mass spectrometers to confirm the presence of a species around a planetary body at a high temporal and spatial resolution. A mass spectrometer is limited to sampling the species population which the satellite travels through, but can detect species with otherwise low abundances, along with their angular and energy distributions [e.g., MESSENGER/EPPS; 170]. A low abundance of a species and its properties can thus be detected in a particle detector by chance, whereas a large enough quantity of the species must be present to allow a detection using a spectrograph.

Observations When summarizing exospheric observations, I will focus on the rock-forming, refractory elements such as O, Na, Mg, Al, Si, K, Ca, and Fe, which make up the samples that were irradiated in the context of this thesis. Moreover, I will discuss Ti and S, since they bear special importance for the Moon (ilmenite) and Mercury (sulfides) respectively. According to the assumption of stoichiometry in ejected material relative to the surface

LRO/LAMP

The Lyman Alpha Mapping Project [LAMP; 171] is a far-ultraviolet imaging spectrograph aimed at detecting water ice, albedos and landforms in the Lunar permanently shadowed regions. It relies solely on the faint illumination by natural starlight and sky-glow illumination as light sources. LRO/LAMP also characterizes the Lunar exosphere and maps the reflectivity of the surface in the far-ultraviolet. Within its detection range, it is most sensitive between 125–193 nm to detect volatiles in the Lunar exosphere. It also was used to constrain upper limits of refractory elements including Mg, Al, Si, Ca, and Fe [169].

composition, all elements present at the surface should end up in the exosphere. Grava et al. [172] point out however, that there is already a strong discrepancy between Na and O in Mercury's exosphere. The stoichiometric assumption of the exosphere thus does not apply universally.

The ease at which an element is detected around a body in space is defined by the supply and lifetime of the species in the exosphere as well as its capability of light absorption. As an example, Na is relatively abundant—Apollo 12 mare basalts average to ∼20'000 ppm [Chap. 8 in 9]—and scatters sunlight efficiently (large g-value, see infobox), making it easy to detect [173]. Potassium (∼540 ppm) has a scattering efficiency which is twice as great as that of sodium, but its abundance in Lunar regolith is about two orders of magnitude lower [e.g, 9, 173], resulting in an exospheric abundance of about 1% of that of sodium [174, 165]. In comparison to Na and K, both Fe and Al are relatively abundant constituents of both the surface of Mercury and the Moon (Table 1.1). The LRO/LAMP upper limit for Al at the Moon is minute with 1.1 Al cm^{-3} [169], which explains why it remained elusive to ground-based and in-situ detections at both the Moon and Mercury.

Lunar exosphere So far, only Na and O have been detected in the exosphere of the Moon. Oxygen has recently been detected as energetic species on the Moon by the Chandrayaan-1 Energetic Neutral Analyzer [179]. Based on these observations, an upper limit for the exospheric surface density could be determined (11 cm^{-3} at the subsolar point) which is in line with LRO/LAMP

g-value: Connecting emission intensity and column density

A spectrograph looks at a column of gas of which the intensity of light that is scattered from the species contained is obtained as a function of wavelength. The conversion of the observed intensity I of a column of gas into a column density N is done with the relation $I = gN$, where the species-specific 'glow efficiency' g, called g-factor, that relates intensity to number of particles is required [175]. The g-factor is given by the number of photons scattered by each atom each second (photons s^{-1} $atom^{-1}$). The intensity I is given in Rayleighs which is defined as the column emission rate of 10^{10} photons per square metre per column per second ($1R = 10^6/4\pi$ photons cm^{-2} s^{-1} sr^{-1} [176]). This relation, as trivial as it may seem, suffers from the non-trivial determination of the species-specific g-values. The value for g depends not only on the radial velocity relative to the Sun, but also on the gravitational and radiation pressure accelerations after an atom is ejected from the surface [177, 178]. Recent revisions of the g-values relevant for Mercury (Na, K, Ca, and Mg) suggest, that the formerly published g-values are too low and result in overestimation of the column densities of high-velocity atoms [177, 178].

[169]. Other refractory elements such as Ti, Mg, Ca, Si, K, and Al eluded detection by spectrographs and therefore no confirmed density or column abundances are available. For Si and Ti upper limits exist [180], however the emission lines on which this observation is based were deemed unlikely to be populated [181]. Both Mg and Ca were so far not detected, except during the plume released by the LCROSS impact into the Cabeus crater [182]. For Ti, Mg and Al, preliminary detections from the LADEE Ultraviolet/Visible Spectrometer (UVS; [183]) were reported but no densities [184, 172].

Mercury's exosphere For Mercury's exosphere, the refractory elements Na, K, Ca and Mg were so far confirmed. Both Na and K were detected with relatively high surface abundances of $\sim 1.7 - 3.8 \times 10^4$ Na cm^{-3} and $\sim$500 K cm^{-3} respectively [185, 186]. The experiments pivotal in the in-situ detection of refractory elements were the Atmospheric and Surface Composition Spectrometer (MASCS) [80] and the Fast Imaging Plasma Spectrometer (FIPS) which is part of the Energetic Particle and Plasma Spectrometer (EPPS) [170] experiment. From MESSENGER/FIPS, solar wind protons and He^{2+} as well as species originating

from the planet surface were inferred from mass to charge ratio (m/q) data [187]. The overlap of different species with similar or identical m/q made the detections ambiguous. This includes the most abundant group of [Na^+, Mg^+], and the less abundant [Si^+, Fe^{2+}], [S^+, O_2^+, H_2S^+], and [C^+, Na^{2+}, Mg^{2+}].

The Mariner 10/UVS results give an estimated oxygen number density of 7×10^3 cm^{-3} at the subsolar point [166] which is comparable to sodium, but which could not be reproduced by the more sensitive MESSENGER/MASCS [188]. The ease at which MESSENGER/MASCS should have detected oxygen led to the possible explanations that either 1) the oxygen exosphere was more prominent in 1974; 2) the detections were instead upper limits or; 3) the observations were erroneous [188].

For species that are expected to exist but do not scatter light sufficiently (low g-value), only upper estimates for the density in the observed column are available. For example, the silicon upper limit in Mercury's exosphere is 5×10^{10} Si cm^{-2} [189]. The presence of relatively large quantities of sulfur on Mercury (Table 1.1) makes a detection of exospheric sulfur only a matter of time. Similar to silicon, sulfur was not observed most likely due to its small g-factor [172].

Mercury's spatial and temporal variations Mangano *et al.* [190] used observation data from the THEMIS telescope (located on the Canary Islands, Spain) to describe the sodium distribution on Mercury. The most common feature, making up 61% of the time of observation, is a double peak where two clearly differentiable enhancements are observed in the northern and southern hemisphere. These peaks can show varying degrees of asymmetry, have an offset to either North or South, or are connected by a narrow band. Similarly, MASCS/UVVS on MESSENGER detected seasonal variations of refractory elements [191, 192] such as the seasonal, but persistent dawn source of energetic calcium [193, 194] and the two differently energetic sources (thermal energies of $<$5000 K and $>$20000 K respectively) supplying the magnesium tail population [195] including a mid-morning source of magnesium [196]. More recently, aluminum and iron have been reported [197, 198] from ground-based Keck-1/HIRES observations.

Kinetic energy and temperature

Kinetic energies of exospheric particles are often given as thermal energies assuming the energy distribution function follows that of a Maxwell-Boltzmann (M-B) distribution. This is misleading, as the processes supplying the species can produce a non-thermal energy distribution. For the processes of electron and photon stimulated desorption it was shown, that the M-B distribution temperature obtained to fit the peak energy in experimental data is too wide and therefore does not fit experimental data [199]. The temperatures reported based on the M-B distribution are to be taken as a fit parameter equivalent to a velocity (km/s or in eV) and as a useful measure to compare thermal and non-thermal release processes.

1.2.2 Structure and supply of the exospheres

The dominant atomic species within an exosphere show variations in concentration and velocity as a function of the source region and supply processes. For example, the Lunar exosphere is observed to peak at the sub-solar point whereas Mercury's shows enhancements at high latitudes which change with time. The long-term changes from both ground-based and in-situ exospheric observations at Mercury thereby match the expected effect of solar wind variations and Mercury's position in its orbit affecting thermal, photon, and micrometeoroid exposure [200, 164].

On both the Moon and Mercury, two distinctive exospheric populations exist. The near-surface population includes species which have been interacting with the surface and are considered 'accommodated'. The suprathermal[5] population is made up of freshly ejected species of which some are capable of escaping the body's gravity [201]. The accommodated population expresses an approximate Maxwell-Boltzmann velocity distribution corresponding to the local surface temperature and is thus often labeled as the thermal population instead. Unlike the thermal species which are 'recycled' material that experienced extensive surface interaction, the suprathermal species in the exosphere can be used to directly sample the surfaces of Mercury and the Moon [201].

[5] exceeding Maxwell Boltzmann velocity distribution of 1000 K

In this section I will briefly introduce the processes which contribute thermal and suprathermal particles to the exosphere [202, 8, and references therein]. Neutrals produced by suprathermal processes can fall back to and interact with the surface and thus contribute to the accommodated population instead of escaping [201]. For this reason, the accommodated population is not only supplied by desorption processes such as thermal desorption (TD). Instead it also contains species from micrometeoroid impact vaporization (MMIV), photon and electron stimulated desorption (PSD/ESD), and ion sputtering (IS), that could not escape. The process of interest in this thesis, sputtering, will be extensively discussed in a separate section (Sec. 1.3) and compared to competing processes.

Thermal Desorption Thermal desorption (TD) considers the evaporation of surface bound atoms and include H, He, Ar, Ne, H_2, O_2, N_2, H_2O, OH, and CO_2 for the Moon and Mercury [157, 165]. For refractory elements, evaporation processes do not carry a large significance, although subsolar temperatures can reach fairly high temperatures on both the Moon (maximum: $\sim$390 K, minimum:$\sim$104 K [203, 204, 205]) and Mercury (700 K, $\leq$100 K) [162, 206]. For Mercury, both Na and K are also affected by thermal desorption due to the high dayside temperatures [202]. The large temperature differences between the day and nightside are the drivers for degassing at and around the subsolar point and recondensation on the nightside. This behavior is seen for Ar on the Moon, which follows a strong dependence with local time [157, 207]. The energy distribution of the ejected particles follows thermal ($<$ 1000 K) Maxwell-Boltzmann distributions [202] and thus only contributes to the accommodated population of the exosphere.

Photon Stimulated Desorption Photon-stimulated desorption (PSD) is a surface process where an atom or molecule is removed by absorbing a photon by the means of an electronic excitation process [208]. This process is only efficient for releasing volatiles and moderately volatile elements (Na and K) from mineral surfaces. Recent photon stimulated desorption experiments have shown that sulfur can be desorbed from MgS, which makes PSD an additional source of sulfur in Mercury's lower exosphere [209]. PSD results in

ion temperatures of 1000-1500 K that exceed TD, as observed in Na populations from MESSENGER/MASCS but temperatures are about a factor three to five below MMIV [210]. UV photon fluxes at the Moon and Mercury with sufficient energy to cause desorption ($>$ 5 eV) are 2×10^{14} [211, 212] and 2×10^{16} photons cm^{-2} s^{-1} [at aphelion; 209, 213] respectively.

Two years on Mercury in three Mercury days

Mercury is in a 3:2 spin resonance with the sun. This causes lower-than-average temperatures of the cold-pole longitudes due to them spending most of their time near Mercury's terminator [214].

Electron Stimulated Desorption Analogue to PSD, Electron Stimulated Desorption (ESD) is a process capable of releasing surface-bound neutrals and ions into the exosphere [192, 208, 211, 215, 216]. Like PSD, electron energies of $\geq$4 eV successfully desorb neutrals. For sodium, the resulting energies are thereby of 0.1 eV ($\approx$1160 K) for Na from a SiO_2 substrate [211] and 0.08 eV ($\approx$900 K) for Na from Lunar regolith [217]. Ionic species require electron energies of $\geq$ 25 eV however [211, 216], and result in larger ejecta energies [$\sim$ 2 eV $\approx$23000 K for Na^+; 211].

The process of ESD requires an impinging electron to eject an electron from the shell of a bound atom. For a detailed description of ESD, see McLain *et al.* [216] and references therein. As an example we assume a sample with Si^{4+}, K^+/Na^+ and O^- atoms. An electron can hit a non-bridging O^- and create a hole, ejecting an electron and neutralizing oxygen in the process. The system may then undergo intra-atomic Augur decay where an outer-shell electron falls into a lower shell with higher energy level. If a second electron is removed simultaneously, the oxygen becomes O^+. Coulomb repulsion between the newly formed O^+ and its surrounding Si^{4+} and K^+/Na^+ can now lead to ejection of either O^+ or K^+/Na^+. The resulting kinetic energy of an ejected alkali metal ion (K^+/Na^+) is thereby required to exceed 3-10 eV to prevent recapture by the surface [216]. Note that this energy exceeds the 2 eV seen in experimental results of Yakshinskiy *et al.* [211] and falls into the upper range of sodium

from solar wind ion sputtering [e.g., 218]. Furthermore, an ion exceeding 3 eV has enough kinetic energy to reach Mercury's escape velocity and thus ESD products should all be lost to space [216].

On the Moon, ESD is deemed a minor process, as the electron fluxes of up to $\sim 4 \times 10^8$ cm^{-2} s^{-1} with a mean temperature of $\sim 1.4 \times 10^5$ K ($\approx$12 eV) [219, 211] are exceeded by the photon flux with comparable velocities. This is also visualized in the proposed four order of magnitude larger contribution of PSD compared to ESD on the Moon [211]. On Mercury, the electron precipitation is modeled to be $10^9 - 10^{10}$ cm^{-2} s^{-1} with energies of several hundreds of eVs caused by acceleration in the planet's weak magnetosphere [220]. Schriver *et al.* [220] calculated yields of $10^{21} - 10^{23}$ ions s^{-1} for Mercury, which is reported to be on par with IS yields. The kinds of species emitted, based on experiments of Mercury regolith analogues, are however limited to H^+, H_2^+, O^+, H_3O^+, Na^+, K^+, and O_2^+ [216]. ESD is therefore a minor process on the Moon, but competing with IS and MMIV at Mercury due to the acceleration of electrons in the magnetosphere.

Micrometeoroid impact vaporization Observations of brightening occurring in the Lunar Na tail after the passage of the Leonid meteor stream highlighted the importance of impact vaporization [160]. Meteors that hit the surface of an airless body are called meteoroids and measure between 30 μm and 1 m in size [221]. The majority of the mass attributed to meteor populations is however within the range of 0.1 to 1000 μg, with a peak at 50 μg (or ∼400 μm diameter for $\rho = 2.2$ g cm^{-3} and $v_{impact} = 18$ km s^{-1}) measured at 1 AU in the space-borne Long Duration Exposure Facility [LDEF; 222]. At this sub-meteor size, the impactors are called micrometeoroids instead.

The distribution of micrometeoroids which impact the surfaces of the Moon and Mercury is not homogeneous however. Instead, there are four main meteor populations that show large variations in their energy distributions when compared at 1 AU [223, 224, 221]. The influx is thus reliant on models. At Mercury, the proposed fluxes of micrometeoroids 5–100 μm in size span two orders of magnitude ($\sim 10^{-14}$ to $\sim 10^{-16}$ g cm^{-2} s^{-1}) [112, 225, 226] whereas modeled Lunar fluxes are more consistent with $\sim 10^{-16}$ g cm^{-2} s^{-1} [112, 227,

228]. Further, the mean impact velocities of micrometeoroids on Mercury and the Moon are ∼20 km s^{-1}, and ∼14 km s^{-1} respectively [229]. It is important to note that the uncertainties in fluxes at Mercury can make MMIV either a dominating or unimportant release process, depending on the chosen flux model [202].

The way a meteoroid-impact provides species to the exosphere is through vaporization and subsequent photodissociation (or electron-impact dissociation, not covered here [172]). An impact generates ejecta which is a mixture of solids, liquids and vapor. The vapor easily reaches initial temperatures of up to 10'000 K for a 30 km/s impactor [230]. The vapor cloud subsequently cools down and the chemical composition of the vapor 'quenches' to form molecules at about 3500 K [231]. For this reason, MMIV is modeled with an average temperature of ∼3000-4000 K [232, 233, 234, 235]. The molecules within the vapor are consecutively broken up by photodissociation, resulting in atoms being delivered to the exospheres of the Moon and Mercury [231, 236, 237]. During photodissociation, excess energy from the reaction is passed to the reaction products. As an example, the energy increases experienced by Al-bearing species and their photodissociation probability at 3000 K on the Moon (located at 1 AU) are given in Table 1.2. Formation of Al from a two step photodissociation process from AlO_2 to AlO will impart the sum of E_{phot1} to the Al atom which will not exceed 2.6 eV. Obtaining the energy of the atoms depends on underlying models and in the case of Ca, results based on a three-step photodissociation (≤1.2 eV, [236]) underestimate energies from MESSENGER/MASCS observations around Mercury (≥2.6 eV or ≥30,000 K [238]).

Table 1.2: Probabilities of photodissociation P_{phot} at 3000 K and energies imparted on metal-containing products E_{phot1} at 1 AU [236]. The energy of a photon, hv, is the product of the Planck constant, h, and the frequency of the light, v.

Molecule	Reaction	P_{phot}	E_{phot1}
AlO	AlO + hv = Al + O	0.2	1.1 eV
AlO_2	AlO_2 + hv = AlO + O	10^{-4}	$<$ 1.5 eV
AlOH	AlOH + hv = Al + OH	0.1	$<$ 1.3 eV

Micrometeoroid impact vaporization is the main source of exospheric Mn,

Fe and Mg. Although MMIV can supply Na and K, desorption processes (PSD/ESD) are more relevant for the supply of volatile and moderately volatile elements [230]. Unlike desorption (TD, ESD, PSD) and solar wind IS, MMIV can act over the whole planetary surface and is not limited to areas exposed to the Sun or magnetosphere-surface interactions. The production of impact vapor derived Na, Ca and Mg however varies with Mercury's True Anomaly Angle that matches predictions based on heliocentric distance where Mercury moves in and out of the interplanetary dust disk [239, 194, 224]. Lunar exospheric Al was also shown to correlate with the passing Geminids meteoroid stream, but no densities or column abundances were so far detected by LADEE/UVS [172]. Furthermore, MMIV shows a pronounced dawn-dusk asymmetry with a maximum centered on the dawn hemisphere [193, 196, 191]. On the Moon, all species released by MMIV reach escape velocity due to the low gravity. On Mercury, species with masses up to oxygen are lost reliably whereas a large fraction of heavier species return to the surface which could actively change Mercury's regolith chemistry over geological timescales [202].

1.3 Solar Wind Ion Sputtering

The focus of this thesis lies in the quantification and characterization of sputter ejecta caused by solar wind ions irradiating the exposed surfaces of the Moon and Mercury. This is achieved in the laboratory in collaboration with TU Vienna [e.g., 1] and in computational models such as SDTrimSP [240]. I will briefly introduce the solar wind composition (Sec. 1.3.2), and to what degree the Moon and Mercury are exposed to it. This is followed by an evaluation of competing processes that supply the exospheres (Sec. 1.3.3), before giving an in-depth summary of sputter theory (Sec. 1.3.4), the laboratory experiments performed by our collaborators (Sec. 1.3.5), and the modeling which was done based on the laboratory results (Sec. 1.3.6).

1.3.1 Origins

Sputtering describes the process of removing surface atoms by the means of collisions caused by particles impinging a surface. First investigations into

sputtering looked into neutral particles hitting monoatomic samples. This was followed by alloys and compounds as well as irradiation with ions [241]. For the planetary science community, the irradiation of minerals with species and energies found in different solar system environments became the main focus for sputter experiments. This includes the irradiation-exposed ices on the moons around Jupiter as well as the solar wind exposed rocky bodies such as comets, asteroids, the Moon, and Mercury.

1.3.2 The solar wind

On Mercury and the Moon, highly energetic ions sourced from the ignition process of the Sun are responsible for the impact sputtering process. The ions that make up the solar wind are well defined thanks to measurements both in space and on the Moon [242, 243], far away from the influence of Earth's ionosphere. The solar wind is made up of mostly protons ($\sim$96%) and alpha particles ($\sim$4%) with heavier, multiply charged ions of O^{6-8+} and C^{5-6+} in the per mil range and more rare constituents like Ar^{6+} not exceeding the ppm range [244]. From implanted solar wind in regolith samples, Pepin [243] concluded that over the solar lifetime, the solar wind composition remained constant within a factor of two to three. Typical solar wind fluxes at the Moon are about 3×10^8 protons cm^{-2} with a medium speed of 440 km/s, resulting in kinetic energies of 1 keV/nucleus [245]. As a result of solar flares, an eruption of electromagnetic irradiation within the Sun's atmosphere, the high energy component of protons in the solar wind can temporarily exceed energies of 100 MeV/nucleus and reach fluxes of 10^2 protons cm^{-2}. At Mercury, the solar wind energies and their variations are comparable, however the fluxes are increased due to R^2 scaling with heliocentric distance [244].

Lunar solar wind environment As the Earth's vital companion, the Moon enters and leaves the magnetosphere of Earth during its orbit. About one fourth of the time it is thereby exposed to non-solar plasma with varying properties while travelling through the Earth's bow shock, the magnetosheath, and the magnetotail [246]. The Moon's nearside thus experiences more of the Earth's influence whilst the farside more frequently faces solar wind precipitation

[246]. For a detailed study of the Lunar farside-nearside asymmetry of proton precipitation, see Kallio, Dyadechkin, Wurz, *et al.* [246].

Mercury's solar wind environment

Solar wind exposure The upstream solar wind proton flux at Mercury is 1.1×10^9 cm^{-2} s^{-1} [e.g., 247], but the precipitation on Mercury is complicated by the presence of a weak magnetic field. The solar wind protons thus preferentially precipitate at the magnetospheric cusps, where open field lines caused by reconnection with the interplanetary magnetic field (IMF) are directly connected to the surface of Mercury [248, 249, 250, 251]. These open field lines then wander over the poles into the magnetotail. Furthermore, a narrow band of magnetospheric ions precipitate at the mid-latitudes in an 'auroral' precipitation, which is centered around the magnetospheric cusps [252, 253, 254]. Under extreme solar wind conditions, the auroral precipitation regions can expand all the way to the equator or, at even higher solar wind dynamic pressures, the magnetosphere can be compressed down to the surface, directly exposing the surface to 'nose' ion precipitation as it is mostly the case for the Moon [253, 255, 256].

Precipitation rates Under non-extreme solar wind conditions, model-based proton fluxes at the cusps are in the order of 10^8 cm^{-2} s^{-1} [254, 257] and $0.5 - 1.0 \times 10^9$ cm^{-2} s^{-1} [247, 258]. In comparison, non-solar wind ions sourced from the surface are calculated to precipitate at rates of $\sim 10^5$ cm^{-2} s^{-1} [233]. MESSENGER/FIPS data of cusp proton precipitation collected over the entire MESSENGER mission resulted in a mean proton flux of 1.0×10^7 cm^{-2} s^{-1}, whereas the peak precipitation fluxes vary over four orders of magnitude from 9.8×10^4 to 1.4×10^9 cm^{-2} s^{-1}, with a mean of 3.7×10^7 cm^{-2} s^{-1} [26]. The mean thereby lies one order of magnitude below the mean precipitation flux determined by Winslow *et al.* from MESSENGER/FIPS data of 3.7×10^8 cm^{-2} s^{-1} [259]. This discrepancy was however attributed to the precipitation variability not being observable by the method of Winslow *et al.* [26]. The auroral precipitation rates which surround the magnetospheric cusps are comparable to cusp precipitation rates with fluxes of up to $\sim 10^8$ cm^{-2} s^{-1} [253]. The nose

precipitation flux for a compressed magnetosphere during extreme solar wind pressure conditions however dwarfs both the cusp and auroral precipitation rates with $\sim 10^{10}$ cm^{-2} s^{-1} [253, 255].

1.3.3 Ion sputtering competitors

Refractory elements The main competitor to IS in regards to refractory elements is MMIV [221]. Both IS and MMIV supply atoms to the supra-thermal population of atoms in Mercury's exosphere [8, 202, and references therein]. The two ways to distinguish contributions by either process is the different temporal and spacial activity as well as the larger energy of IS-sourced particles:

- On the Moon, the line strengths of observed Ti and Mg decrease after each full Moon which links their production to solar wind exposure [172].
- The upper limit of the Lunar Al surface density agrees well with predicted IS contributions whilst MMIV would overestimate the density [181, 158].
- The calcium in Mercury's exosphere exhibits very high energies and scale heights corresponding to temperatures exceeding 20000 K [260, 261, 262]. Based on simulations, the thermal energies were constrained to reach up to 70000 K (or 6 eV in kinetic energy). This energy is so far not explicable by MMIV. Sputtered Ca easily exceeds 1.8 eV (≈20800 K; assuming a Thompson distribution with a peak at $\sim \Delta H_{\mathrm{sub}}/2$, see Chapter 3) and can thus produce Ca with the necessary thermal energies. At the Moon, however, the Ca in the exosphere is expected to be solely produced by MMIV [263, 8].
- The exospheric temperature of Mg coincides well with photodissociation of Mg-bearing molecules, however some observed Mg species exceed photodissociation energies [264]. The lack of short-time variations combined with annual recurring peaks in the Mg distribution that correlate with surface Mg-concentration was used to rule out sputtering as a major contributor [264].

These observations exemplify how sputtering by solar wind ions is an important competitor to MMIV for heavy refractory elements such as Ca, Al, Ti, and Fe

(with a questionable relevance for Mg).

Alkalis Ion sputtering was so far deemed unlikely to significantly contribute to the observed volatiles in Mercury's exosphere. As an example, the variable sodium peaks observed in the exosphere of Mercury (Sec. 1.2.1) express temperatures characteristic for PSD (1000-1500 K), but are confined to solar wind ion precipitation regions [201]. The interpretation of this observation is a diffusion enhanced by IS which causes a more efficient desorption [265, 266]. This highlights the necessity to not only understand sputtering by solar wind ions, but also the combined effects of space weathering processes.

1.3.4 Sputter theory

Sputtering is not limited to the removal of surface atoms but also includes other effects relevant for this thesis. These include backscattering [267, 268], trapping and re-emission of impinging particles [269], as well as changes in the surface structure [270]. The focus of the data that I worked with was primarily on sputter yield, which defines the focus of this theoretical background. The sputter yield Y describes the number of particles ejected per incident particle or simply

$$Y = \frac{\text{atoms removed}}{\text{incident particle}} \tag{1.2}$$

In detail, the yield depends on the impinging particle energy, mass and angle of incidence as well as the the target mass, crystallinity, crystal orientation and surface binding energy. The analytical sputter yield can be approximated following the work of Sigmund [271]. For explanations of the approximations included, see [6]. The approximation as given in [202] is:

$$Y_{\text{tot}} \approx \frac{3\alpha}{\pi\sigma_D E_b} \frac{\left(\frac{2m_{SW}}{m_{SW}+m_{\text{surf}}} Z_{SW} Z_{\text{surf}}\, e^2\right)^2}{\gamma E_{\text{in}}} 2\varepsilon s_n(\varepsilon) \tag{1.3}$$

where m_{SW} is the mass of the solar wind ion, m_{surf} the mass of the sputtered atom, Z_{SW} and Z_{surf} are the nuclear charges of the incident and sputtered particles respectively, E_i is the incident ion energy, E_b is the surface binding

energy, σ_D is the average diffusion cross-section, e is the elementary charge, α is a collision parameter, and $\gamma = (4\, m_{SW} m_{surf})/(m_{SW} + m_{surf})$. $s_n(\varepsilon)$ is the nuclear elastic stopping cross-section at the reduced energy ε of the incident ion which is given as

$$\varepsilon = \frac{\gamma E_{\text{in}}}{2e^2} \frac{1}{\frac{2m_{SW}}{m_{SW}+m_{\text{surf}}} Z_{SW} Z_{\text{surf}}} \frac{0.8853 a_0}{Z_{SW}^{0.23} + Z_{\text{surf}}^{0.23}} \tag{1.4}$$

where a_0 is the Bohr radius of the hydrogen atom. The nuclear elastic stopping cross-section is then computed depending on the reduced energy:

$$s_n(\varepsilon) = \begin{cases} \frac{1}{2\varepsilon} \frac{\ln(1+1.138\varepsilon)}{1+0.0132\varepsilon^{-0.787}+0.196\varepsilon^{0.5}} & \varepsilon < 30 \\ \frac{1}{2\varepsilon}\ln(\varepsilon) & \varepsilon > 30. \end{cases} \tag{1.5}$$

The parameters from the incident ion (E_{in}, m_{surf}, Z_{SW}) as well as the sample atoms (m_{surf}, ε, Z_{surf}) are well known. The parameters of the sample (E_b, σ_D, α, s_n) however, are unknown and need to be determined experimentally. Typical sputter yields for solar wind energy ions hitting silicates are small with < 1 atom per impinging ion, and therefore even with large ion fluxes the mass changes remain microscopic. For this reason, a high resolution measuring technique is necessary.

Kinetic and potential sputtering

An impinging ion is not only capable to deposit kinetic energy according to its velocity and mass, but also causes interactions based on its charge level (potential energy). The neutralization of the potential of an impinging, multiply charged ion has been shown to cause sputtering which exceeds the yield of particles attributed to kinetic processes only [272]. Progress in the field includes the irradiation of Lunar simulant material [273, 274, 275], plagioclase thin-films [276, 277], wollastonite thin-films [278], and augite thin-films [279]. The effect of potential sputtering which is most certain and most relevant for this thesis is an increase in total yield of ∼40% due to the potential energy in the solar wind [attributed to the abundant He^{2+}; 280].

1.3.5 Laboratory sputter experiments

The QCM technique A Quartz Crystal Micro-balance (QCM) uses the piezoelectric properties of a quartz crystal to *in situ* determine small mass changes. Commercial QCMs find their application in the deposition of material, however in the case of sputtering, the quantification of mass removed per incident angle is of interest instead. The QCM method was first introduced in 1959 by Sauerbrey [281] and was steadily improved at TU Wien e.g., Hayderer et al. in 1999, Golczewski et al. in 2009 and by Szabo et al. 2018 [282, 283, 278]. As a result, the technique was carried out by my collaborators at TU Wien at the high resolution and precision necessary to investigate solar wind ion sputtering. This section heavily leans on the latest QCM improvements presented in great detail in Brötzner [284], who represents the most recent improvements in the QCM setup at TU Wien. The theory relevant to this thesis is summarized hereafter.

The QCM is composed of a quartz resonator covered by two layers of Au which act as electrodes. By applying an alternating current, the resonator will enter a thickness-shear mode oscillation. The initial resonance frequency f_Q of the quartz thereby depends on the quartz mass m_Q and for small changes of mass (Δm) the relation to frequency changes (Δf) is linear with [281]:

$$\frac{\Delta m}{m_Q} = -\frac{\Delta f}{f_Q}. \tag{1.6}$$

To obtain a mass change per unit area A_Q, the quartz resonator density ρ_Q and thickness d_Q are introduced, resulting in

$$\Delta m_A := \frac{\Delta m}{A_Q} = -\frac{\Delta f}{f_Q}\rho_Q d_Q. \tag{1.7}$$

In order for equation 1.6 to hold, the radially decreasing sensitivity of the quartz resonator has to be taken into account. The free parameters of this sensitivity variation, which is in the shape of a Gauss curve, were previously determined using a focused ion beam instrument [285]. As a result, the whole area of non-vanishing sensitivity is irradiated to ensure equation 1.6 to hold.

When the quartz is covered by another substance, ρ_q and d_Q are substituted by ρ and d of the entire system instead. If the thickness of the thin film or the

amount of deposited material is small, the substance thickness and density can be neglected. In our case, the deposited material is of a negligible thickness in the orders of less than 100 nm, whereas the quartz crystal is about 300 µm in size.

A QCM only ever detects the integrated mass change for a certain applied fluence (ions deposited per area) and therefore cannot resolve the type of sputtered particles. This mass change per incident ion is computed given a constant ion beam density j, which is required to be evenly applied to the sensitive quartz resonator area. The total number of ions N_i hitting the surface during a time Δt is given by

$$N_i = \frac{j \Delta t A_Q}{q e_0}, \tag{1.8}$$

whereas q is the charge state of the ion and e_0 the elementary charge. The yield y is then computed as

$$y := -\frac{\Delta m}{N_i} = \frac{f_Q}{f} m \frac{q e_0}{j \Delta t A_Q} \tag{1.9}$$

and with equation 1.6,

$$y := \frac{\Delta f}{\Delta t} \frac{1}{j} \frac{\rho_Q d_Q q e_0}{f_Q} = \frac{\Delta f}{\Delta t} \frac{1}{j} \mathbb{C} \tag{1.10}$$

where the last term only consists of known parameters which can be summarized as a constant $\mathbb{C}$.

Deposition of material onto a QCM is performed by Pulsed Laser Deposition (PLD) [286]. In brief, in a vacuum a pulsed laser creates a plasma plume from a target material which is then deposited onto another target. An O_2 gas is used to ensure oxides forming in the deposit whilst the target heating supports re-crystallization of the deposited material. Early investigations have shown, that the re-deposited material does not re-crystallize but rather a glassy film is produced [277]. This is attributed to the high melting temperatures of oxide minerals compared to the cold or lightly heated QCM. In comparison to glass, a crystalline target experiences increased coherent forces of an intact mineral

lattice which is expected to negatively affect the sputter yield. In the case of using a fine-grained powder sample we would further expect the surface roughness to play an important role as it did in works related to mono-atomic targets such as Be [287].

In order to measure yields from a sample that cannot be deposited on a QCM, a QCM is employed as a catcher instead, a so called *Catcher*-QCM (C-QCM). The sputter ejecta travels with energies low enough (< 50 eV) for sticking to occur at the C-QCM. This method is essential for measuring mineral sputtering but suffers from a range of complications.

The benefit of the catcher setup is the capability of varying the catcher location and therefore obtaining angular distribution data of sputtered material. The difference to previous works on angular distributions, such as Berger et al. 2017 [288], the current setup allows the relative location of the C-QCM to be moved radially at a fixed distance. This results in more appropriate data due to the radial nature of the sputter process.

The complications of the catcher setup are 1) the sputtering of the C-QCM surface by reflected particles ($-\Delta m$), 2) implantation of reflected particles ($+\Delta m$), 3) degassing of implanted projectiles ($-\Delta m$), and, not mentioned in Brötzner [284] 4) the sticking probability of ejected material ($-\Delta m$, if < 1). To mitigate these uncertainties, calibration measurements are performed where a thin film produced from the mineral of interest is irradiated and the mass changes are determined simultaneously on the underlying QCM and the C-QCM.

For the yield determination, the mass change at the catcher is divided by the total number if ions hitting the sample. The total number of ions N_i^{total} is thereby determined by using the total area of the ion beam A_b instead of the sensitive quartz area A_Q in equation 1.8

$$N_i^{\text{total}} = \frac{j \Delta t A_b}{q e_0}, \tag{1.11}$$

The mass change at the C-QCM is in turn approximated as

$$\Delta m = -\frac{\Delta f}{f_Q} \rho_Q d_Q A_Q. \tag{1.12}$$

where A_Q now describes the mass-change sensitive area of the C-QCM. By combining these equations we get the yield of the C-QCM, which omits the leading negative sign, due to mass ejected at the target leading to a mass increase at the catcher.

$$y_C = \frac{\Delta m}{N_i^{\text{total}}} = \frac{\Delta f}{f_Q}\,\rho_Q d_Q A_Q\,\frac{q e_0}{j \Delta t A_b} = \frac{\Delta f}{\Delta t}\frac{1}{I}\,A_C\,\mathbb{C} \tag{1.13}$$

where the total current $I = \Delta t\ j\ A_b$ is used instead of the current density j and all constant parameters are summarized in constant $\mathbb{C}$.

The irradiated, sensitive area of the catcher quartz is however subject to the position of the C-QCM. This area scales linearly with the solid angle, and so equation 1.13 becomes

$$y_{C,\Omega} = \frac{\Delta f}{\Omega} = \frac{\Delta f}{\Delta t}\frac{1}{I}\,r^2\,\mathbb{C}, \tag{1.14}$$

whereas the radius r denotes the distance between the centers of the catcher and the irradiated sample. At TU Wien this distance is 17 mm with a maximum sensitive radius of the QCM of 7 mm ($A_Q \approx 44$ mm^2), resulting in a total covered solid angle of $\Omega = A_Q/r^2 \approx 0.13$ sr.

1.3.6 Modeling of laboratory sputter results

A significant part of this thesis was related to connecting experimental data with simulation results. I will give a small overview on the approach of recreating quantitative sputtering experiment data using the binary collision approximation (BCA). This section is based on the excellent description of sputter modeling from the book by Behrisch and Eckstein [289].

The most prolific suite to simulate sputtering in solids is the SRIM package [290], which uses the the BCA code TRIM (The Range of Ions in Matter[291]). The relatively short simulation times, ease of use, and the capability to produce good statistics for angular distributions of sputtered atoms makes BCA the preferred tool for comparisons with experimental data. The the high number of particles simulated also allows BCA codes to take structural information into

account for, e.g., roughness evaluations (2D and 3D [292, 293]). In this thesis I worked with SDTrimSP [240], which is an improved version of TRIM including the dynamic sputter model TRIDYN [294, 295] which allows for composition changes with fluence.

Binary Collision Approximation In the BCA, the sequence of collisions between a moving and a resting atom are simulated. Both the projectile and the recoil are consecutively traced in three dimensions. The tracked atom is considered implanted if its energy drops below a certain cutoff energy, and sputtered if it crosses the surface. The positions of the atoms in rest are either randomized (amorphous sample) or predetermined following a mineral crystal lattice structure. The most established lattice code is MARLOWE [296] whereas SDTrimSP assumes a random distribution of atoms and is therefore also called a Monte Carlo BCA code [240].

Independent on the atom positions, the elastic energy transfer between the moving atom and the recoil is determined through conservation of energy and momentum. The angle at which the moving atom is scattered, ϑ, is tied to the conservation of momentum and can be calculated in the center-of-mass system by an integral:

$$\vartheta = \pi - 2p \int_R^\infty \left(r^2 \sqrt{1 - \frac{V(r)}{E_\mathrm{r}} - \frac{p^2}{r^2}} \right)^{-1} \mathrm{d}r, \tag{1.15}$$

with the interaction potential, $V(r)$, the energy of the recoil E_r, and the impact parameter, p, between the two colliding atoms. The impact parameter is defined as

$$p \leq \frac{\mu}{\sqrt{2\pi}}, \tag{1.16}$$

with the mean free path μ as a function of the target density $\mu = \rho^{-1/3}$ ([ρ] = atoms Å^{-3}).

For the interaction potential $V(r)$, *screened Coulomb potentials*[6]. For the simulations performed for minerals in particular, the "krypton-carbon" (KrC) potential

[6]The attraction caused by the nucleus of an atom reduced by electron shielding as a function of proximity. The screening length is thereby proportional to the nuclear charge of the atoms.

is used [297] and adjusted to the screening lengths of the individual atoms. The integration of the potential ultimately makes up the major computational effort in BCA simulations. The limitation of using *screened Coulomb potentials* is that changes in shell structures or charge states are not taken into account.

The inelastic energy loss affecting a particle in a BCA simulation is caused by interactions with electrons. The inelastic electronic energy loss does not affect the trajectory of the atom, and becomes significant at high energies. The loss is thereby tied to the atom velocity and either occurs continuously, like friction [Lindhard-Scharff energy loss; 298, 299] or locally, related to a collision as a function of the impact parameter [300, 301, Oen-Robinson energy loss]. The latter is lower in the low energy range ($\leq$keV). At higher energies, the Lindhard-Scharff loss is used instead. The electronic loss reaches a maximum at high energy (low MeV range) before decreasing following the Bethe-Bloch formula [302, 303] (approximately with the root of the ion velocity v^{-2}). For H and He, data tables are available to correct for deviations from the inelastic energy loss described by Lindhard-Scharff and Oen-Robinson [304].

The final and most controversial parameter in BCA models is the surface binding energy. It describes the binding strength of an atom to the surface which has to be overcome in order to leave the sample. The common implementation is that of a planar surface potential which causes energy loss and refraction of the ejecta towards the surface. The SBE is not known, but instead approximated by the energy required to transform an atom from its solid state into its gaseous state, known as the enthalpy of sublimation (ΔH_s). This enthalpy is based on monoatomic solids and not known for compound samples. The ΔH_s of monoatomic atoms is still widely used for compound samples, which is a topic I address in detail in Chapter 3.

Molecular Dynamics An alternative, but powerful tool to simulate sputtering are molecular dynamics (MD) simulations [305, 306, 307]. In brief, MD takes into account interactions of each atom with its surrounding atoms, which is done by solving the Newton's equations of motion within the system. This makes apparent, why MD is highly demanding in terms of computation and not suited to do investigations requiring extensive statistics.

To simulate sputtering in MD, the interatomic forces between all the atoms in the sample and the projectile have to be known. Interatomic potentials are used to describe the interatomic forces together with a coupling to the electronic system which poses the fundamental issue with MD [308]. During irradiation, the atom states deviate from the initial equilibrium condition. The appropriate interatomic potentials far from equilibrium could technically be computed, however the complex nature of the problem prevents large-scale applications. The advantage of MD is however, that no binding energies or defect forming energies are required, as they are included in the potentials. For further shortcomings and imitations in MD, I refer to Behrisch and Eckstein [289]. An example for the application of MD is the determination of the surface binding energy required to remove a surface atom from a sample, which can then be used in a BCS code for obtaining data with good statistics [218].

Chapter 2

Mineral powder pellets and solar wind induced alteration

Icarus 365 (2021) 114492

Contents lists available at ScienceDirect

Icarus

journal homepage: www.elsevier.com/locate/icarus

Creation of Lunar and Hermean analogue mineral powder samples for solar wind irradiation experiments and mid-infrared spectra analysis

Noah Jäggi [a,*], André Galli [a], Peter Wurz [a], Herbert Biber [b], Paul Stefan Szabo [b], Johannes Brötzner [b], Friedrich Aumayr [b], Peter Michael Edward Tollan [c], Klaus Mezger [c]

[a] Physikalisches Institut, Universität Bern, Sidlerstrasse 5, CH-3012 Bern, Switzerland
[b] Institut für Angewandte Physik, TU Wien, Wiedner Hauptstraße 8-10/E134, A-1040 Vienna, Austria
[c] Institut für Geologie, Universität Bern, Baltzerstrasse 1 + 3, CH-3012 Bern, Switzerland

ARTICLE INFO

Keywords:
Moon, surface
Mercury, surface
Experimental techniques
Solar wind
Spectroscopy

ABSTRACT

The surfaces of airless planetary bodies are subject to a barrage of charged particles, photons, and meteoroids. This high-energy space environment alters the surfaces and creates a tenuous atmosphere of ejected particles surrounding the celestial bodies. Experiments with well characterized analogue materials under controlled laboratory conditions are needed to interpret the observations of these atmospheres and improve composition models of such bodies. This study presents methods to create and analyze mineral powder pellets for ion irradiation experiments relevant for rocky planetary bodies including the Moon and Mercury. These include the pyroxenes diopside and enstatite, the plagioclase labradorite and the non-analogue pyroxenoid wollastonite. First ion irradiation experiments with diopside, enstatite and wollastonite pellets were performed under UHV with 4 keV He^+ at fluences of several 10^{21} ions m^{-2} (~100 and ~1000 years for Mercury and the Moon, respectively). The pellet's thermal IR reflectance properties were compared before and after irradiation showing monotonously shifting IR spectral features between 7 – 14 μm towards higher wavelengths. For all irradiated pellets, Reststrahlen bands shifted by ~0.03 μm. Surface abrasion was found to remove the sputter effect, which is restricted to the top few tens of nm of the surface. Additionally, ion irradiation experiments were performed in a quartz crystal microbalance catcher setup, where the mass sputtered from pellets was monitored. This proves, that the presented sample preparation method allows the study of irradiation induced sputtering and surface alteration on the surfaces of rocky planets under laboratory conditions.

1. Introduction

Surfaces of atmosphere-free planetary bodies are constantly exposed to space weathering. Ongoing processes include micrometeorite impacts, thermal and photon-stimulated desorption, and solar wind induced sputtering (Plainaki et al., 2016; Bennett et al., 2013; Wurz and Lammer, 2003). These processes alter primarily the surface, but also create a collision-free exosphere, which is detectable with particle instruments onboard space probes such as LADEE, LRO, MESSENGER or the ongoing BepiColombo mission (Orsini et al., 2020; Milillo et al., 2020; Elphic et al., 2014; Paige et al., 2010; Solomon et al., 2001). The exosphere generated by space weathering is directly coupled to the planet surface and its chemical and mineralogical composition. Thus models of coupled systems are of interest to explain exosphere observations and interpret remote sensing data of the altered surface, particularly for planets without sample return such as Mercury (Rothery et al., 2020; Hiesinger et al., 2020; Alnussirat et al., 2018; Mura, 2012; Wurz et al., 2010). To bridge the gap between surface/exosphere models and space observations/sample return, planetary surface analogues are exposed to artificial space weathering and consecutively analysed.

The rocky surface of the Moon and Mercury are widely covered by an unconsolidated layer of solids, composed of fractured bedrock, referred to as regolith. The components range from single crystal and impact agglutinates to rock breccias and whole rock components (i.e., Heiken et al., 1991). To keep the sample parameters simple enough to understand the effects of irradiation experiments, these were performed on single minerals or derivatives thereof. The selection of analogue material for the Moon therefore includes minerals found in various mare and highland compositions known through sample return missions (e.g., Heiken et al., 1991, Table 1). For the surface of Mercury, the mineralogy

* Corresponding author.
E-mail address: noah.jaeggi@space.unibe.ch (N. Jäggi).

https://doi.org/10.1016/j.icarus.2021.114492
Received 16 October 2020; Received in revised form 22 March 2021; Accepted 18 April 2021
Available online 26 April 2021

Table 1
Lunar and Hermean surface mineral analogues based on literature data. The most prominent mineral groups are highlighted in bold.

For Mercury (McCoy et al., 2018)		For Moon (Heiken et al., 1991)
	Pyroxene group	
Enstatite ($Mg_2Si_2O_6$) Diopside ($CaMgSi_2O_6$)		Ferrosilite ($(Fe,Mg)_2Si_2O_6$) Augite† ($(Ca,Mg,Fe,Al,Ti)_2(Si,Al)_2O_6$)
	Plagioclase group	
	$Na_xCa_{1-x}Al_{2-x}Si_{2+x}O_8$	
Labradorite to bytownite ($x \sim 0.5 - 0.2$)		Bytownite to anorthite ($x \sim 0.2 - 0$)
	Olivine group	
	$Mg_xFe_{2-x}SiO_4$	
Forsterite ($x = 2$)		Forsterite to fayalite ($x = 1.6 - 1.0$)
	Oxide group	
		Ilmenite ($FeTiO_3$))
	Sulfide group	
Niningerite (MgS)		

†While augite is a chemically extensive term, it is used specifically for (Fe,Ca, Mg)-pyroxene. With Al_2O_3 and TiO contents below 1 wt%, augites are representative of lunar highland pyroxenes, whereas mare basalt augites contain 2–3 wt% Al_2O_3 and TiO_2 (Heiken et al., 1991).

is inferred from remote sensing.

The data synopsis from MESSENGER's X-ray, gamma-ray and neutron spectrometer revealed fairly robust element ratios for provinces in the northern hemisphere of Mercury (Nittler et al., 2011). Based on this the estimated mineralogy for Mercury is dominated by pyroxene and plagioclase with minor olivine, and is thus similar to the Moon (McCoy et al., 2018; E. Vander Kaaden et al., 2017; Heiken et al., 1991). The prominent difference is the very low Fe-content of Mercury's silicates with <0.8 wt% FeO (Zolotov et al., 2013). In Table 1, a compilation of possible analogue materials for the Moon and Mercury is presented. The major rock forming minerals of Earth contain varying concentrations of Fe, which poses a challenge for the selection of minerals relevant for the low-Fe surface of Mercury. An example of an ideally Fe-free mineral is diopside from Zermatt, Switzerland, with ~2 wt% FeO, which was used in this study. To cover a FeO free end member next to diopside and enstatite, wollastonite is included, even though it is not an analogue for neither Moon nor Mercury. Further variations in composition among adequate analogues is not the focus of this study, but add an often neglected complexity.

This study focuses on space weathering by solar wind irradiation with typical ion energies of keV/nuc energies. This process is also referred to as sputtering and is initiated by energetic ions impacting a surface. The ions then lose all their energy through collisions with atoms and electrons in the rock- and regolith surface. (Nastasi et al., 1996; Sigmund, 1969). For Mercury and the Moon, the impinging ions are mainly solar wind H^+ and He^{2+} with contributions from heavier elements such as O^{5+}, O^{6+} and O^{7+} (Russell et al., 2016; von Steiger et al., 2000; Bame et al., 1975). Solar wind ions are the major contributor to space weathering on the Moon and Mercury. Furthermore the solar wind ion fluxes are constrained by MESSENGER measurements, opposed to micrometeorite fluxes, that are solely based on model calculations (e.g., Borin et al., 2009; Cintala, 1992). The penetration depth is a function of the ion energy and species, the impact angle, and the surface composition of the target. Defect formation by collision and the accumulation thereof gradually leads to amorphization and is capable of creating nanophase iron ($npFe^0$), as observed in the rims of lunar mineral grains (Pieters and Noble, 2016; Pieters et al., 2000; Keller and McKay, 1997).

The state of the art of sputter experiments is the irradiation of mineral thin films (Szabo et al., 2020; Szabo et al., 2018; Hijazi et al., 2017). To produce films suitable as planetary analogs, whole natural minerals are used as resource. The required size of the mineral used in the production of a thin film by Pulsed Laser Deposition (PLD) often exceeds that of naturally grown crystals and is thereby an important limiting factor. Using mineral pellets gives more flexibility in choosing samples for ion irradiation.

Another issue with PLD thin films made from silicates is the high solidus temperature of the minerals. Evaporation and consecutive deposition causes quenching and leads to glassy films (i.e., Hijazi et al., 2017). For this reason, potentially relevant aspects of sputtering, such as the influence of crystallinity and porosity, can only be studied with mineral powders or pellets representative of the physical, morphological, and mineralogical properties of planetary surfaces. Known behaviours of impacting ions on single crystals include channeling, which is the alignment of ions to the mineral lattice (Onderdelinden, 1966; Lindhard, 1965). Furthermore it is expected, that the material ejected by sputtering is decreasing with increasing porosity (Rodriguez-Nieva et al., 2011). How polycrystalline surfaces such as the regolith of Moon and Mercury behave is still unclear. For polycrystalline nonamorphizing materials such as bulk elemental metals it was shown however, that they behave different to single crystal samples and yields can be almost one order of magnitude larger (Schlueter et al., 2020). Apart from the expected differences caused by crystallinity and porosity, the use of mineral pellets in this regard takes into account that (1) minerals are the major components of Lunar soil samples, with an average of ~80 vol% (McKay et al., 1991, 2) mineral powders conserve stoichiometry, unlike thin-films produced with PLD, (Hijazi et al., 2017, 3) minerals and their powders have a long-range order and might show reduced formation of self-trapped excitons as suggested by Shluger and Stefanovich (1990), which are thought to be essential for sputter behavior caused by multiply charged ions Aumayr and Winter, 2004; Sporn et al., 1997). The use of mineral pellets is therefore of utmost interest when investigating sputter yields of planetary surfaces.

Surface properties and composition define the visual and infrared signal emitted by a planetary surface (i.e., Brunetto et al., 2020; Morlok et al., 2019; Pieters and Noble, 2016, and references therein). This study uses mid-infrared (MIR, 2.5–15 μm) reflectance spectra to investigate the effect that solar wind irradiation has on a pressed mineral pellet. The IR remote sensing data obtained by missions such as MESSENGER and the upcoming data from BepiColombo's MERTIS is, however, in the form of thermal emission infrared (TIR) (Morlok et al., 2019; Martin, 2018; Solomon et al., 2001). The conversion of emission to reflectance is described by Kirchhoff's law: Emission = 1 - Reflectance. The MIR spectra acquisition mode used in this study does, however, not allow a direct implementation of the law - to do so a hemispherical reflectance measurement would be necessary (Hapke, 2012; Thomson and Salisbury, 1993; Salisbury et al., 1994). Quantitative comparisons to TIR spectra are therefore not possible, however, the qualitative implications for IR features altered by irradiation is discussed and compared to previous studies using reflectance spectra.

Both reflectance and emission IR signals in the mid infrared are affected by a range of surface properties. These include high porosity being linked to grain size, causing reduced spectral contrast (Young et al., 2019; Salisbury and Wald, 1992), thermal alteration lowering reflectivity (Maturilli et al., 2017), large phase angles causing variations in the spectral shape (Maturilli et al., 2016; Varatharajan et al., 2019), a simulated lunar environment strongly changing feature locations (Lucey et al., 2017; Donaldson Hanna et al., 2017), solar wind irradiation strongly shifting features of meteorite-based powders (Lantz et al., 2017), and simulated micrometeorite impacts decreasing reflectance and slightly shifting features (Weber et al., 2020).

This study extends this list of parameters that influence IR spectra by acquiring reflectance MIR spectra for pellets exposed to solar wind He^+.

The ions thereby have equivalent kinetic energy to their solar wind counterpart He^{2+}. The reasoning behind this is to omit the increased yield caused by potential sputtering, which is not well understood, and was shown to exceed simulated levels from purely kinetic SDTrimSP codes (Szabo et al., 2020; Szabo et al., 2018; Hijazi et al., 2017; Mutzke et al., 2019; von Toussaint et al., 2017; Mutzke et al., 2013). The effect of irradiation on MIR reflectance spectra are then compared to results of previous space weathering experiments as well as TIR spectra of Lunar soils (e.g., Brunetto et al., 2020; Weber et al., 2020; Lantz et al., 2017; Salisbury et al., 1997). The results contribute to the understanding of the combined effects of thermal alteration, grain size, phase angle, the measurement environment, micrometeorite impacts, and ion irradiation on the Lunar and Hermean surface TIR signal. The observations are furthermore discussed in the light of the interaction dept. of solar wind in mineral powders using SDTrimSP.

This study also presents methods for creating analogue samples for space weathering experiments with the use of minerals that can serve as reasonable analogues, representing the composition of planetary surfaces. The creation of very stable pressed mineral pellets is necessary because the exposure to simulated space weathering effects (such as irradiation, temperature cycles etc.) and the full characterization of the samples before and after these processes implies extensive handling and transport between different laboratory facilities. The alternative of using whole minerals is rejected, as pure end members are rare and generally too small to be used in a sputter setup similar to the one used for the thin film samples, and because a pellet has more in common with regolith than a single crystal. In the conclusions and outlook the future of mineral pellets, their use for determining representative MIR spectra and their potential to determine sputter yields through ion irradiation experiments is presented.

2. Methods

2.1. Samples and pre-irradiation characterization

To cover the better part of Lunar and Hermean mineralogy, the main focus of this study lies on the pyroxenes, i.e., enstatite and diopside, and the mid-Na and Ca plagioclase labradorite. Wollastonite, although not expected to be present on Mercury, serves as an ideal, Fe-free, Ca-silicate pyroxenoid for Mercury and was already studied by Szabo et al. (2020, 2018). In pellet form it is most resilient to handling and therefore poses the largest number of MIR spectra obtained in this study. The mineral samples are centimeter-sized, monocrystalline enstatite and labradorite, whereas diopside and wollastonite are decimeter sized and polycrystalline. Whole mineral element compositions were determined at the thin section scale and are listed in Table 2. For this purpose, electron backscatter imaging and X-ray mapping with energy dispersive spectrometry (EDS) was carried out using a ZEISS EVO 50 scanning electron microscope at the Institute of Geological Sciences of the University of Bern. An acceleration voltage of 20 kV and a beam current of 1.5–3 nA was used and the EDS data was corrected with the ZAF procedure using the software TEAMS version 2 from EDAX. EDS was only used prior to irradiation, as it is not suitable for determining non-isochemical surface alteration on the spatial scale of the ion irradiation penetration depth. The interaction volume of the electron beam is several μm deep, whereas alterations caused by irradiation only change the top few nm of the sample significantly.

Table 2
Pellet pressing method used to press mineral pellets and scanning electron microscopy chemical analysis of whole minerals.

	Wollastonite	Diopside	Enstatite	Labradorite[‡]
Method[†]	1,2	1,2	1,2	2
Oxides	wt%	wt%	wt%	wt%
SiO_2	52.22 ± 2.37	54.16 ± 0.18	55.47 ± 3.91	53.3
Al_2O_3	b.d.	b.d.	0.70 ± 0.50	30.0
FeO	b.d.	2.25 ± 0.52	5.22 ± 0.65	0.6
MgO	b.d.	20.55 ± 1.65	38.61 ± 3.25	b.d.
CaO	47.78 ± 1.37	23.04 ± 1.12	b.d.	12.6
Na_2O	b.d.	b.d.	b.d.	3.6
K_2O	b.d.	b.d.	b.d.	b.d.

[†] Pellet creation method necessary for a successful pellet. Either (1) pellet glued onto holder or (2) pellet pressed directly into holder.
[‡] Results from electron probe micro analysis from Wenk et al. (1965) with ≤1 % relative error.
Oxide contents below detection limits are labeled as such (b.d.). Labradorite from Surtsey with composition from Wenk et al. (1965).

2.2. Preparation of pellets

Because every sample was handled multiple times for measurements in Bern before and after the irradiation experiments were performed in Vienna, they had to be mechanically more robust than fluffy, planetary regolith. Pellets are not a perfect analogue to regolith, but they offer the best compromise between the required stability and planetary surfaces. The compressed property of the pellet is expected to influence solar wind irradiation results as the surface porosity of a pellet, analogous to regolith surface porosity, effectively reduces the sputter yield (Cassidy and Johnson, 2005).

Wollastonite, enstatite, diopside, and labradorite minerals were ground in a RETSCH agate disk mill to the point where the powder started to agglomerate. Extensive grinding of wollastonite was prohibited by needle formation and alignment in the disk-mill, due to well-developed cleavage. Similarly, minerals like labradorite with a hardness matching that of agate had to be crushed first. This was achieved using a tungsten carbide disk mill for a few seconds. In the case of wollastonite this was followed by manual milling in an agate mortar.

Grain size determination of powders was conducted in a particle size analyzer (Malvern Mastersizer 2000), with a small volume wet sample dispersion unit (Hydro 2000S). Small representative fractions of all mineral powders were dispersed in distilled water and irradiated by a laser. The dimensional information was derived from the resulting diffraction pattern. Size fractions of wollastonite, diopside, and enstatite were generated by wet sieving. The fractions for wollastonite were 150 − 60 μm, 60 − 30 μm, and <30 μm. For diopside and enstatite, the powder fractions were 60 − 30 μm and <30 μm. The large grain size fractions are representative of the coarse grained Lunar regolith whereas the finest grain size fraction are expected to represent Mercury's surface (Heiken et al., 1991).

Two methods for pressing pellets were employed. In the first method, pellets were pressed between two pistons and were extracted from the pellet press die (PD) mantle interior. For one pellet, ~0.3 g of material was used, and a pressure of 239 MPa was applied for ≥5 min. Using this method, wollastonite and diopside pellets could be pressed reliably. Enstatite and labradorite, however, remained delicate and broke easily when handled. In order to increase the stability of all successfully produced pellets, they were subsequently glued onto custom manufactured stainless steel back plates (Fig. 1(b)). An ultra-high vacuum (UHV) and high temperature secure carbon-based paste obtained from *Plano GmbH* was used. All pellets included in the post-irradiation MIR study are the products of this first method. (Method 1 in Table 2).

The first method turned out to be insufficient for the production of high stability pellets of enstatite and labradorite as well as large grain size fractions of Diopside due to their weak adhesion (Section 3.3). To achieve more stable pellets, a second method of pressing powder directly into holders was developed. For one pellet, ~0.03g of material was used instead, reducing the amount of required material by over an order of magnitude. The pellets were pressed into holders without the use of a binder or glue by taking advantage of the intrinsic adhesion of the mineral powders (Fig. 1c). To counteract the low cohesion of mineral powders such as large grain size fractions of diopside, ~0.02g of fine-grained wollastonite was pressed in the holder as a base, upon which ~0.01g of the desired material was pressed. The pressure applied was

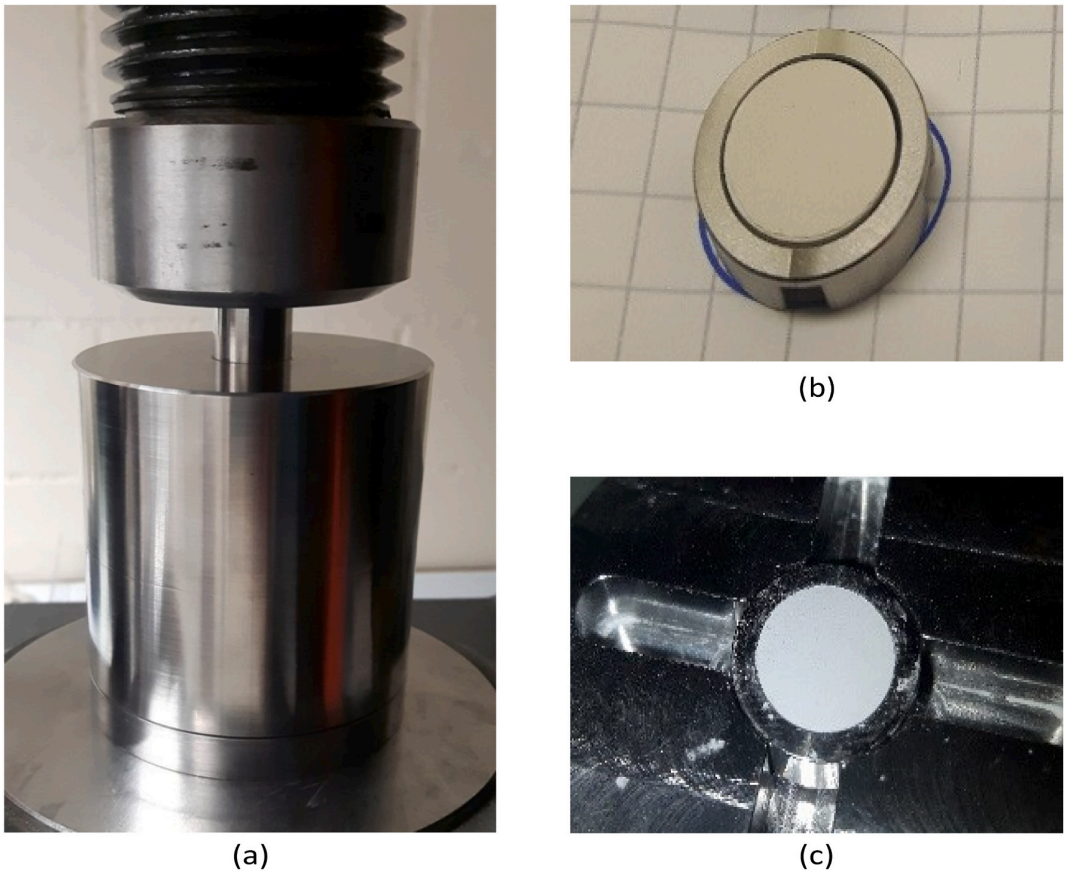

Fig. 1. (a) the custom pellet die in the press; (b) a pellet glued into its stainless steel holder by the means of vacuum secure glue and (c) a pellet pressed directly into a holder. Pellet diameters are 10 mm.

reduced to 80 MPa to avoid sample holder deformation. This procedure facilitates pellet extraction and minimizes pellet handling during creation. Powder fraction pellets of diopside used in the grain size reflectance MIR study are the products of this second method (Sections 3.4 & 3.5). In both methods, pellets were pressed in a custom made 10 mm diameter EXTRAMET EMT-210 alloy[1] PD and a 30 t hydraulic press (Fig. 1(a)).

2.3. Analysis methods before and after irradiation

Mid- to far-infrared micro reflectance measurements from 1.6 – 25 μm, covering the IR range of MERTIS, were done on pellets before and after irradiation using a Bruker Hyperion 2000 microscope attached to a Bruker Tensor FTIR spectrometer, at the Institute of Geological Sciences, University of Bern under ambient conditions. The FTIR is equipped with a Globar® infrared source, a liquid nitrogen-cooled mercury-cadmium-telluride detector, and a wire-grid polarizer. Backgrounds were regularly measured on a gold-coated slide, which has a reflectivity of about 100% for the selected wavelength range.

Reflectance spectra were collected with a total of 32 scans per measurement at a spectral resolution of 4 cm^{-1}. The locations of spectral features were reliably reproducible with an uncertainty of approximately 0.01 μm, therefore the position of spectral features are reported here to two decimal places. Background measurements through air were taken at 30 min intervals. Regular dry air purges of the chamber ensured low atmospheric contamination. MIR results were produced by taking spectra across the mineral pellet according to a predefined sampling map.

The predefined map covers the pellet in a cross from side to side with additional measuring points around the pellet center. The pellet holder was marked to maintain the same orientation and thus approximate location of the measurements following irradiation. The presented spectra are the average of the ten innermost data points located at and around the pellet center since this is the most homogeneously pressed and subsequently sputtered area. The spatial resolution of each point is ~25 μm; optical convolution effects are negligible (Ni and Zhang, 2008).

The extrema of each spectrum were determined using a python routine. The mean intensity of the ten measurements before and after irradiation is plotted and the variation in intensity is shown as a shaded area representing two standard deviations (2SD, Figs. 4 & 5). The difference of the extrema of each measured point before irradiation was compared to its equivalent after irradiation, averaged to a single shift. The mean and SD of an extrema location is reported together with the mean of all shifts at the given wavelength. The mean shift of a feature thereby often coincides in extent to one SD of the pre-irradiation feature position. A paired sample *t*-test was applied to compare the pre- and post-irradiation populations, finding *p*-values of <0.01 for all reported shifts, making them significant.

The choice of the MIR spectra range presented focuses on the location of the Christiansen feature (CF) around 8.5 μm, the Reststrahlen bands (RBs) between 8.5 – 12 μm and the transparency feature (TF) usually around 11 – 13 μm. The CF is an IR reflectance minimum,

[1] From Manufacturer: 89.0% W, 10.0% Co, 1.0% other carbides.

which is caused by the mineral refracting index matching the refracting index of the surrounding medium. RBs result from fundamental molecular vibrations caused by stretching of Si—O bonds (e.g., Salisbury, 1993). The TF is a wavelength range in which the mineral becomes optically thin as a result of a low absorption coefficient, with higher peaks in reflectance for samples with smaller grain-size (Donaldson Hanna et al., 2012; Salisbury and Wald, 1992). Mid-infrared spectroscopy of planetary analogs has shown that the TF is easily observed for powders with grain sizes < 25 μm therefore its observation is only expected for small grain size fractions of diopside and wollastonite (Morlok et al., 2019; Donaldson Hanna et al., 2012). Under a simulated lunar environment only the TF of olivine was detectable, being the most apparent of all mineral TF in the $11 - 13$ μm range (Donaldson Hanna et al., 2012). Variance in reflectance intensity and changes in MIR features are used for interpretation of pellet properties affecting spectra. This study focuses on RB shifts as a measure of alteration while trying to reproduce physical property-dependent changes in RB contrast, as shown in other studies. The MIR reflectance measurements are shown and discussed within the wavelength range of MERTIS $7 - 14$ μm although they cannot be directly compared with TIR spectra of future BepiColombo or of the lunar soils analysed by Salisbury et al. (1997). Direct comparisons are, however, possible with MIR data from Brunetto et al. (2020) who simulated solar wind irradiation using He^+, but with an order of magnitude higher energy.

2.4. Irradiation experiments

Ion irradiation under vacuum conditions was performed at the ion beam facility at TU Wien (TUW). In a first step, it was necessary to verify that the method of powder sample preparation is appropriate for irradiation in the ion beam facility. To this end, several pellet samples were transported to TUW and irradiated with a 4 keV He beam with a typical flux of $10^{16} - 10^{17}$ ions m^{-2} s^{-1} and fluences of several 10^{21} ions m^{-2}, representative for sputter experiments. The energy chosen reflects typical slow solar wind speeds of ~400 km s^{-1} and lies one order of magnitude below the extreme case scenario investigated by Lantz et al. (2017). For the fluxes of solar wind on the Moon and Mercury the fluence would correspond to an exposure of ~1000 and ~100 years (for fluxes see, e.g., Kallio et al., 2019; Winslow et al., 2017; McComas et al., 2009). This is applicable for the irradiation fluence used on the wollastonite and diopside pellets. During He irradiation of the enstatite pellet, the holder was partially sputtered as well, reducing the maximum fluence reached. Three wollastonite (WA1, WA2, WA3), one diopside and one enstatite pellet were irradiated. The samples were then sent back to University of Bern for MIR analysis.

The same facility was used for sputter experiments with PLD-produced films (Biber et al., 2020; Szabo et al., 2020; Szabo et al., 2018). In the case of the PLD method, the sample film was deposited on a quartz crystal microbalance (QCM), which directly measures the mass changes as the sample film is being irradiated. If a thick powder sample or pellet is used for sputter yield determination, the QCM must be mounted opposite of the sample to catch the ejecta from the irradiated sample (Fig. 2, Berger et al., 2017). The catcher QCM has a sensitive inner diameter of 7 mm, where a homogeneous deposition of material is assumed (Sauerbrey, 1959). The resulting area was used for calculating the total mass increase due to sputtered atoms sticking to the QCM. This technique demonstrably allows for measuring sputter yields as well as the angular distribution of sputtered particles (Stadlmayr et al., 2020). However, in order to avoid charging up of the insulating pellet samples, they have to be simultaneously irradiated with an electron flood source, which is installed in the setup at TUW.

To test the possibility of performing sputter yield measurements with mineral pellets in a catcher QCM-setup, a ≤ 30 μm fraction wollastonite pellet was irradiated by 2 keV Ar^+. Atomic force microscope images were taken to qualitatively compare the pellet surface roughness to glassy thin films. Mineral pellets thereby show an increased surface roughness (see appendix Fig. 8). To minimize stoichiometry changes on the catcher surface, a wollastonite coated QCM was used when irradiating the wollastonite pellet.

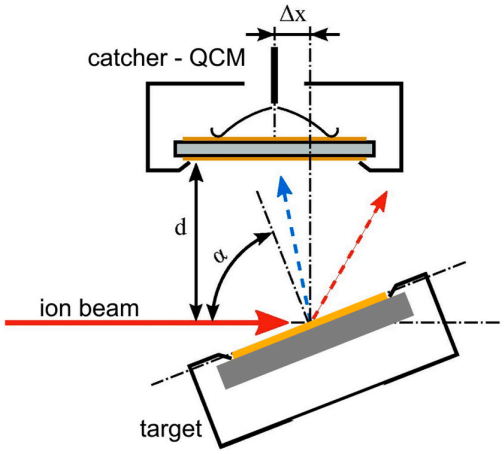

Fig. 2. Sputter setup with mineral pellet sample and quartz crystal microbalance (QCM) catcher. The mass change of the catcher QCM is a superposition of mass increase due to sticking of material ejected from the sample (blue arrow) and sputtering of the QCM itself due to reflected ions (red arrow). The distance d is measured from the target center and the catcher QCM. The angle of measured ejecta α is controlled by the offset Δx, describing the relative location of the catcher QCM to the sputtered target.For reference measurements, the target holder is replaced with a mineral coated QCM (Figure adapted from Berger et al., 2017). (For interpretation of the references to colour in this figure legend, the reader is referred to the web version of this article.)

3. Results

3.1. Chemical and physical properties

The weighted mean of the mineral powder grain diameters range from $23 - 28$ μm for diopside, enstatite and labradorite, and about 34 μm for wollastonite. The maxima in the grain size distributions lie below the weighted mean diameter, except for wollastonite, with a second, local maximum around 400 μm representing mineral needles still present after milling (Table 3).

3.2. First sputter yield results

Preliminary sputter experiments with 2 keV Ar^+ ions were performed in a catcher QCM setup (Sec. 2.4.). The sample was irradiated under an angle of incidence of 60° and at a distance d of 13 *mm*. The position Δx that coincides with a larger angle of the catching QCM relative to the target normal was varied to measure the material ejected in different directions (Fig. 2).

The mass increase of the catcher QCM per incident ion is shown in Fig. 3. A significant mass increase was resolved for all collection angles,

Table 3
Grain sizes of mineral powders used.

	Wo	Di	En	Lab
$\bar{d}$	34.20	25.85	23.32	28.27
$d(0.1)$	1.73	1.73	1.64	2.10
$d(0.5)$	12.65	16.47	15.68	19.06
$d(0.9)$	77.35	60.55	60.71	68.8

Alongside the weighted mean grain diameter $\bar{d}$, characteristic grain sizes for three sample fractions are given in the form of diameter d larger or equal to 10%, 50%, and 90% of sample as $d(0.1)$, $d(0.5)$, and $d(0.9)$, respectively.

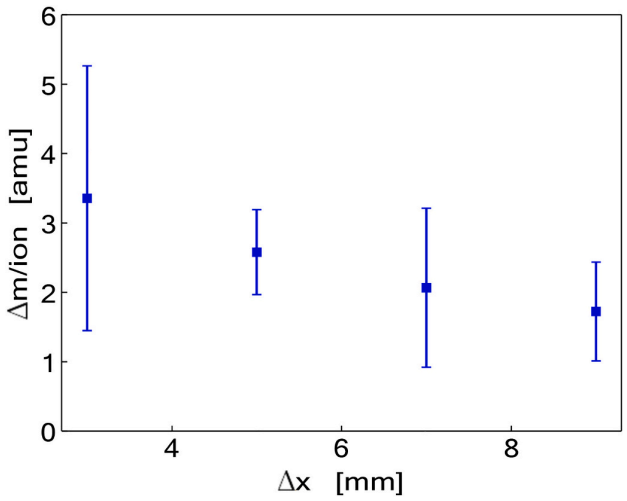

Fig. 3. Mass increase at the catcher QCM for various Δx positions when irradiating a wollastonite pellet with 2 *keV* Ar^+ ions under an angle of incidence of 60°. The distance was constant at $d = 13$ *mm*. The large uncertainties given originate from the small signal to background ratio.

which will allow the future determination of the total sputter yield. However, the mass increase per ion is highest at small Δx, when catcher angles are close to the center of the ejecta distribution. Furthermore, the signal intensity is small compared to the background, leading to large uncertainties on the reported mass changes.

3.3. Pellet mechanical stability

The pellet stability shows large variations between the materials used. The pellet stabilities are presented in order of increasing Mohs hardness for unsieved and sieved powder pellets. Wollastonite powder resulted in the most durable pellets at any grain size. Enstatite had the tendency of creating faults during depressurization whereas slightly harder diopside showed comparable cohesion to wollastonite. Labradorite, the hardest mineral used, showed slightly worse adhesion than diopside, which could be connected to its intermediate CaO content compared to diopside and enstatite (Table 2).

When using grain fractions, the $\leq$ 30 μm fractions showed the highest cohesion for all minerals, as expected. The 30 – 60 μm fractions of diopside, enstatite, and labradorite exhibit strongly reduced adhesion. The trend of reduced adhesion coincides with the increasing mineral hardness. Generally, the lowest fractions of mineral powders do not allow for stable pellets apart from wollastonite and diopside.

3.4. IR spectra of blank and grain size fraction pellets

The effect of transportation on the MIR results was controlled using an un-irradiated wollastonite pellet blank (see appendix Fig. 6). The MIR spectra after transportation showed no statistically relevant alteration in terms of the position of features or reflectance loss, but a slightly higher variance on the reflectance measurements. There is, however, no TF or change thereof identifiable. Notable deviations between pre- and post-irradiation pellets were observed for the wollastonite pellet WA1 and the enstatite pellet. The former did suffer transport damage in the form of abrasion, whereas the latter was contaminated by pellet holder rim sputtering and deposition onto the pellet. The results of handling-affected pellets are presented and serve as an insight into indirect alteration processes such as abrasion and deposition of sputter ejecta.

The wollastonite and diopside pellets from powder fractions show a strong dependence on grain size (Fig. 4). In general, large grain size fractions resulted in a reduced spectral contrast, and large variance in reflectance. Loss in reflectance occurs at the high grain size spectra for diopside and the low grain size spectra of wollastonite. The wollastonite RBs at 8.92, 9.72 and 10.86 μm nearly disappear for the lowest grain size fraction of <30 μm, as expected. The reflectance loss also results in RB broadening, as seen next to the 9.72 and 10.32 μm RB. On the contrary for diopside band broadening is observed at large wavelengths for the <30 μm grain size fraction. The TF cannot be identified, however, the intensity of the TF region is increasing slightly as expected for smaller grain sizes.

High contrast RBs of wollastonite show minor shifts as the grain size is reduced from 60 to 150 μm to the <30 μm fraction. The 9.38 ± 0.01 μm RB and the pre-irradiation global maximum at 10.32 ± 0.01 μm both shift by 0.01 μm to higher wavelengths. In both cases the shift is similar to the 2SD reported on the RB location. Major shifts of

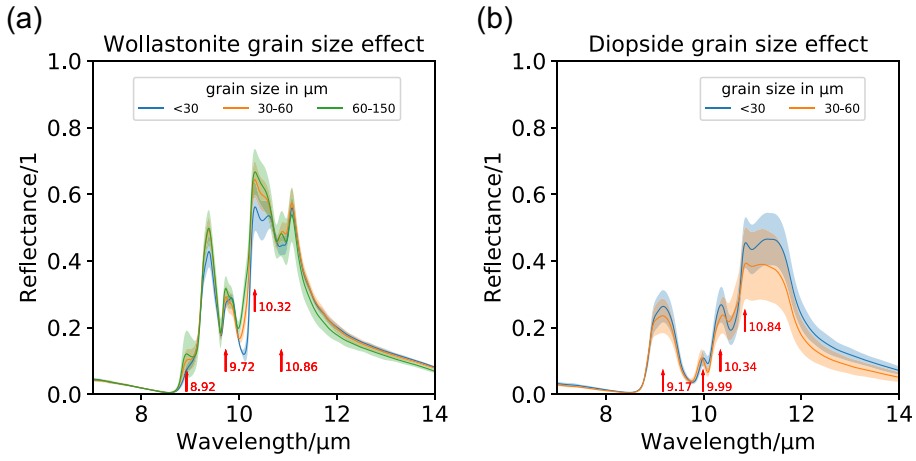

Fig. 4. Dependence of pellet reflectivity on grain size for pre-irradiation (a) wollastonite and (b) diopside. The largest grain size fraction resulted in the highest contrast between RBs, but also in the largest variations in TIR reflectivity (shaded area = 2SD). RB shifts are small or erratic towards lower and higher wavelengths for wollastonite and diopside.

~0.03 μm are found for minor RBs, strongly affected by the increase in spectral contrast such as the 9.73 ± 0.01, and 10.86 ± 0.01 μm RBs in Fig. 4. As those RBs are not persistent over all grain size spectra, they are not used to examine the effect of irradiation on the pellet spectra. The shift of the RBs at 8.93 ± 0.02 μm and 10.60 ± 0.01 μm, only visible in the 60 − 150 μm and <30 μm fraction spectra, respectively, are not reported due to the lack of distinguishable RBs in the spectra of other grain size fractions.

For diopside, the RBs have a low spectral contrast and show varying degrees of spectral shift when compared to the 30 − 60 μm grain size fraction spectra. The 9.18 ± 0.01 μm and the 9.99 ± 0.01 μm RB shift to higher wavelengths by 0.02 μm and 0.03 μm respectively. The 10.36 ± 0.01 μm RB, however, shifts to lower wavelengths by 0.03 μm, as does the global maxima at 10.86 ± 0.01 μm, which shows the smallest shift of 0.01 μm.

3.5. IR spectra of blank and irradiated pellets

Irradiated wollastonite, diopside and enstatite pellets show monotonous RB shifts towards higher wavelengths. An exception is the sputtered wollastonite pellet WA1, which had its top layers abraded during transport. Its MIR spectra strongly differ from the spectra of sputtered WA2 and WA3. The only RB shifts observed for WA1 are the 0.01 μm at the previous 9.234 ± 0.01 μm RB and the 0.02 μm at the global maximum 10.32 ± 0.01 μm, both towards higher wavelengths. The CF was located at 8.57 ± 0.01 μm and shifted 0.01 μm.

Both WA2 and WA3 show large shifts at all RBs after irradiation. The largest shifts of 0.05 μm and 0.03 μm were observed at the global maximum at 10.32 ± 0.01 μm and 10.32 ± 0.01 μm, respectively (Fig. 5(a)). Low contrast RBs with a high uncertainty on their position are not suited for comparison with pre-irradiation pellets but show similar or larger shifts than the high contrast RBs. The CF of WA2 does not shift within uncertainty 8.57 ± 0.01 μm, whereas for WA3 the shift is 8.57 ± 0.02 μm + 0.02 μm.

On the irradiated diopside pellet the high contrast RBs shift by 0.02 − 0.04 μm to higher wavelengths (Fig. 5(b)). The largest shift of 0.04 μm was observed at the 10.34 ± 0.01 μm RB. Similar in extent is the 0.03 μm shift of the pre-irradiation global maximum, situated at 10.84 μm. The CF shifted from 8.49 ± 0.02 μm by 0.02 μm towards higher wavelengths.

Irradiation of enstatite result in the smallest shifts of high contrast RBs by 0.01 − 0.03 μm towards higher wavelengths (Fig. 5(c)). The increase of reflectance variation among the measurements is attributed to the sample holder being sputtered, resulting in deposits on the outer rim of the pellet surface. In terms of shifts, the pellet behaves similarly to wollastonite and diopside in that the major shift is 0.03 μm at the 9.25 ± 0.02 μm RB. The pre-irradiation maxima experienced the largest shift of 0.03 μm, however being a wide RB resulted in a large uncertainty on its location at 10.49 ± 0.01 μm. The CF shift by 0.01 μm from 8.44 ± 0.01 μm, similar in magnitude to the CF shift of the WA3 pellet.

The TF is not identifiable for any of the irradiated pellets, however, the TF region just slightly increases for wollastonite and diopside pellets

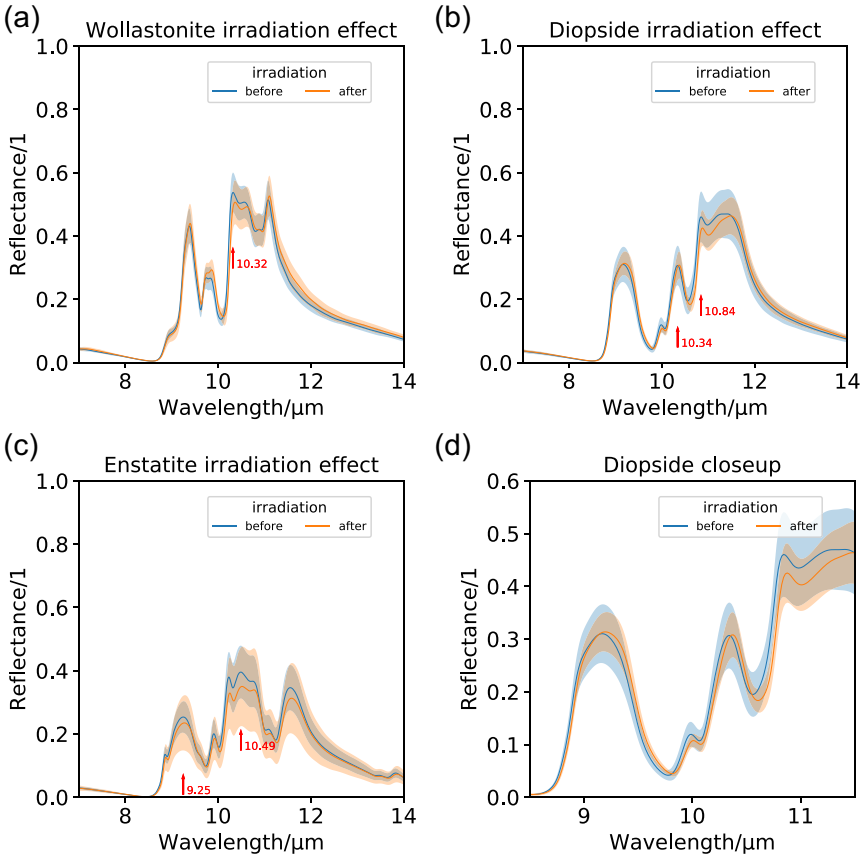

Fig. 5. Reststrahlen bands (RBs) of (a) wollastonite (WA2), (b) diopside, and (c) enstatite MIR reflectance data before and after irradiation. The wavelengths at which the largest and most notable shifts of RBs occur are highlighted by arrows and discussed in the text. All mineral pellets show a weak reflectance loss at the pre-irradiation global maximum. Enstatite further shows an increase in reflectance variance. All spectra show RB shifts towards higher wavelengths after irradiation. Filled areas show two standard deviations. A closeup of the diopside RBs is shown in (d), emphasizing the minor shifts caused by solar wind irradiation.

after irradiation (Fig. 5(a) & (b)), suggesting a minute increase in the amount of fine grain material at the pellet surface. A similar behavior would be expected for enstatite, however the large variations in reflectance measurements do not allow for such a statement (Fig. 5(c)). Unlike spectra from pellets that stayed intact, the WA1 spectra shows significant reflectance loss. The TF region behaves, however, similarly to the irradiated wollastonite pellets, as it decreases less strongly relative to the RBs (Appendix, Fig. 7).

4. Discussion

Pellet properties such as composition, overall stability and grain size as well as the effect of solar wind irradiation are discussed in the light of IR results. The combined effects and their implications are then compared to previous Lunar focused studies.

4.1. Effect of composition

The composition of the irradiated pellets did not affect the extent of feature shifts in MIR spectra. This is seen in FeO-free wollastonite pellets with RB shifts analogue to FeO-bearing enstatite (for composition see Table 2). This indicates that intensity loss and major RB displacements in MIR spectra of diopside and enstatite are not connected to formation of nanophase iron, as it would be the case in NIR (e.g. Yang et al., 2017; Pieters and Noble, 2016; Kuhlman et al., 2015; Loeffler et al., 2009; Salisbury et al., 1997). The effect on the MIR spectra by solar wind irradiation is therefore likely caused by comminution and vitrification, altering the physical properties of the sample (Pieters and Noble, 2016; Nakamura et al., 2012; Salisbury et al., 1997). Pellet darkening was not visually observed on the irradiated pellets, with an exception of the experiment with the enstatite pellet, where the pellet holder was partially irradiated, depositing holder material onto the pellet rims. The consequences were (1) local darkening on the pellet rims, as seen in the large standard deviation on reflectance of the spectra after irradiation, and (2) a lower flux reaching the surface, which might have resulted in comparably low RB shifts.

4.2. Effect of grain size and surface roughness

It was shown by Salisbury and Wald (1992) that particle size and porosity are critically linked, which leads to the question how grain size affects MIR spectra. Small particle size leads to lowered spectral contrast, while reaching a high packing density restores RB contrast. As expected, lower pellet grain sizes negatively affected reflectance and spectral contrast in MIR, but RB positions are intrinsic to the material and not shifted (Salisbury and Wald, 1992; Lyon, 1965). The compression of powders is likely responsible for the less drastic reflectance differences in the grain size MIR spectra comparisons as shown in Fig. 4. The loss in spectral contrast is however seen in the merging of the wollastonite RBs near 10.86 μm at smaller grain size (Fig. 5). This merging of exactly two RBs could be an effect of mineral orientation, which changes when compressing very fine-grained wollastonite due to its good cleavage and its elongated fibrous crystal habit. This was shown for singly crystal olivine and is likely to occur when powders are used (Stojic et al., 2021; Reynard, 1991). It would be expected however, that averaging measuring points counteracts such orientation effects. No such strong effect was observed for diopside, likely due to the less pronounced cleavage that leads to more granular powder during grinding.

An unexpected observation was made in the grain size fraction measurements of diopside pellets, which do not follow the expected increase in spectral contrast with larger grain size. This might be connected to the destruction of diopside grains during pellet creation. The TF region being lower at large grain sizes however would suggest that the grain size is indeed larger. For irradiated pellets, the TF cannot be identified. Nevertheless, the TF region suggests a decrease in grain size for irradiated pellets, even for the abraded WA1 pellet. This could be tied to the transport process loosening weakly bond grains on the surface. No conclusive statement can be drawn, as the differences of the TF are marginal and could be caused by the small shifts of RBs.

Mean Lunar regolith grain-size lying between 40 and 100μm are significantly larger compared to the pellets used in this study (Heiken et al., 1991). The surface roughness is, however, still larger than glassy thin films used in prior sputter yield determination experiments. This is visible in AFM images (see appendix Fig. 8).

4.3. Effect of irradiation

The reported shifts of RBs and CFs are an order of magnitude below the 0.4 μm shifts reported in Brunetto et al. (2020). This can likely be explained by the ion beam penetration dept. The penetration depths of the 40 keV He^+ ion beam from Brunetto et al. (2020) under an angle of 0° are 278, 286, 349, and 380 nm for enstatite, diopside, wollastonite and labradorite, respectively, as calculated by SDTrimSP. The 4 keV beam from this study penetrates only about 22 nm into a diopside or enstatite crystal under an angle of 45°. The penetration in wollastonite and labradorite are slightly higher with 27 and 30 nm, respectively. The penetration dept. of ions in the minerals is thereby inversely proportional to the mineral density given in atoms per $Å^3$. The penetration depth of IR, however, is similar to that of a microprobe, which means >1 μm for $7-14$ μm (Grzechnik et al., 1996).

Given this large interaction depth for IR, the shifts presented are interpreted to originate from a mixing of pristine material below an irradiated upper layer, as was proposed by Weber et al. (2020). The irradiation damage is reaching saturation in terms of damage per atom (dpa), which could add displacement of oxygen atoms to the proposed causes of irradiation-related CF shifts, together with vitrification and composition changes (e.g., Shluger and Stefanovich, 1990; Pieters and Noble, 2016). Furthermore, the irradiation damage of solar wind saturates under the given fluence. Therefore, the solar wind irradiation effect of He^+ on an IR spectrum will not exceed the shifts of 0.02 μm found in this study, which supports the proposition of Salisbury et al. (1997), that shifts ≤ 0.04 μm, as seen in the Apollo 16 soils samples, can be attributed to exposition to space weathering.

In relation to this, the extent of changes in CF position are expected to follow RB displacements as observed by Brunetto et al. (2020). In the present study, only some irradiated pellets show CF shifts of around 0.02 μm similar to the RB shifts. This is tentatively attributed to the lower interaction depth and a detection limit and not to an actual physical process.

Nash and Salisbury (1991) stated that vitrification does not cause shifts, or intensity loss, but loss of contrast. This latter coincides with the results of the present study, as in all pellets, the most intense RB lowered in intensity after irradiation, but the overall reflectance remained constant. Fitting the data of the CF positions in the Nash and Salisbury (1991) comparison plot of chemically identical crystalline powder and glass shows, however, that the CF does shift slightly. In Nash and Salisbury (1991), the Na-rich plagioclase end member albite shows a shift of ~0.04 μm towards lower wavelengths. This might be an indication of preferential sputtering of moderately volatile elements like Na, but it is unclear how this applies to minerals composed of refractory elements. This possibility of preferential sputtering will be further investigated once spectra of irradiated labradorite pellets become available.

An intense loss of MIR spectral contrast and strong shifts of features as shown in grain-size comparisons or shifts towards lower wavelengths were observed only to a minor extent on irradiated mineral pellets. This contradicts results from other studies where micrometeorite impacts were simulated using a pulsed laser, suggested to cause comminution and decompaction (Jiang et al., 2019; Weber et al., 2020). Note that the precision and representativeness of micrometeorite simulation by laser is limited by two major factors: (1) the fluxes of micrometeorites are not well known, nor is their chemical composition—the latter is generally disregarded when using a laser (i.e., Domingue et al., 2016, 2) realistic

simulations of micrometeorite impacts require large dust accelerators which are sophisticated and rare instruments (i.e, Thomas et al., 2017).

4.4. Speculative effect of porosity and compression

For irradiation experiments, the behavior of pellets compared to loose powder is difficult to foretell, as the grains are comparably large and the porosity low compared to data available from tungsten fuzz irradiation experiments (Stadlmayr et al., 2020). For the MIR results, a larger porosity connected to unconsolidated powder would decrease spectral contrast. For the understanding of irradiation effects on spectral features, mineral pellets are the most valuable samples. They provide clear MIR spectral features, enable easy handling, and can be used in the same irradiation setup as designed for thin-films. The use of pellets is thus necessary for a step towards representative analogues and for direct comparisons with thin-film irradiation experiments.

4.5. Speculative effect of mechanical abrasion and pellet creation

The solar wind irradiation effect is likely to be lost by removing the layers affected by irradiation, not only due to transport damage, but also by surface altering effects on the Moon and Mercury. The MIR spectra of the WA1 pellet demonstrates the former, whereas all but two RBs did not show any significant shifts (Appendix Fig. 7). The dataset is, however, not sufficient to prove this statement as the shifts in MIR might not be genuine.

Effects of pellet creation on MIR spectra are less evident, although the creation of pellets from grain fractions suggests that grains that are >30 μm are preferentially lost in a pellet as they exhibit poor adhesion. Any mineral with high rigidity seems to experience less grain deformation, or cold welding, causing pellet instability. The large variance in pre-irradiation MIR reflectance of measurements taken on high hardness mineral pellets could represent this lack of homogeneous compression, as a lower packing density causes intensity loss (Salisbury and Wald, 1992).

4.6. Comparison to previous Lunar focused studies

For the pellets irradiated in this study, shifts in RBs are monotonous towards higher wavelengths and lie around 0.03 μ**m** of displacement, similar to the CF shift reported in lunar soils (Salisbury et al., 1997). Furthermore, it was shown for LRO Diviner data, that the CF seems to have little sensitivity concerning physical and composition changes, but the RBs strongly alter between differently mature Lunar soils (Lucey et al., 2017). This is similar to the observed behavior of irradiated mineral pellets.

A difference is however the strong loss in reflectance, which is reminiscent of results from pulsed lasers used to simulate micrometeorite impacts (Weber et al., 2020). It is thus expected that the effect of micrometeorite impacts and contamination by other lithologies could override the effect of solar wind irradiation, however, more sophisticated experimental data would be necessary for alteration caused by micrometeorite impacts. Also, the timescales of the two studies are highly different. Weber et al. (2020) deposited a nominal energy of $\sim 15\ kJ/m^2$ which translates to 300 Ma of micrometeorite impacts, which is five and six orders of magnitude larger respectively compared to the irradiation exposure time for Mercury and the Moon in this study.

4.7. Sputter yield results

First indirect measurements of sputter yields for a pressed wollastonite pellet using a QCM as catcher showed a similar trend in the angular distribution as was observed for flat, polycrystalline tungsten by Stadlmayr et al. (2020). A more detailed investigation with a direct measurement of angular dependence is necessary to use such sputter data for exosphere models, also in respect to the sample surface roughness (Küstner et al., 1999). Stadlmayr et al. (2020) also compared their flat samples with so-called tungsten fuzz, a tungsten structure with micrometer-size porosity. Using combined sputter measurements and simulations, they observed a drastic decrease in sputtering in contrast to the reference sample. However, Rodriguez-Nieva et al. (2011) did not observe a significant effect of nano-size porosity on the sputter yield in a molecular dynamic study, indicating, that the scale where porosity exists is crucial for sputter results. It is unclear in regard to the MIR results how this would affect the observed shifts. Locally, within one grain the penetration depth is not affected by increased porosity, however it is unclear which effects could either increase or decrease penetration depth and therefore the extent of shifts caused by the mix of sampled material in MIR.

5. Conclusions and outlook

The method of high-stability pellet creation presented here is appropriate for the entire sequence of pre- and post-analysis, irradiation and sputter yield experiments, and sample transport. This study further demonstrates the ability to use the produced pellets in UHV irradiation experiment chambers to obtain sputter yields using a catcher setup, and to investigate the resulting surface alteration in the context of space weathering. Resilient wollastonite, enstatite and diopside pellets are successfully irradiated, whereas more fragile labradorite pellets can only be produced with the second pellet creation method. Labradorite irradiation results were therefore excluded from MIR analysis.

Overall, a change in grain sizes causes only minor shifts in MIR spectra RB positions, whereas irradiation experiments lead to RB shifts of up to 0.04 μm similar to increasingly mature lunar regolith (Salisbury et al., 1997). The intensity of the observed shifts can be linked to the sputter agent energy in comparison with Brunetto et al. (2020); Lantz et al. (2017). Slow, 4 keV solar wind He^+ irradiation saturates within 1000 and 100 a exposure for the Moon and Mercury, respectively, which limits the irradiation effect on regolith and motivates the applied fluence for future studies. How multiply charged impacting ions with slow and fast solar wind energy would affect IR spectra is still unknown and is of interest for a future study.

First QCM catcher measurements were obtained. The observed general trend of mass increase on the catcher QCM as a function of ejecta angle agrees well with previous data for flat, polycrystalline tungsten samples (Stadlmayr et al., 2020). For the evaluation of sputter yields in a future study, an analysis of various parameters, including quartz properties and geometry of the system is necessary (as in Stadlmayr et al., 2020). Especially, the significant roughness of the mineral pellet, which can be seen in seen in AFM images, although better representing unconsolidated regolith, must not be neglected (Küstner et al., 1999) (see appendix Fig. 8).

This study demonstrates that mineral powder samples are very suitable for irradiation experiments. From the irradiation of these samples, it was found that solar wind could be responsible for the shift of IR features up to 0.04 μm. The next goal is to obtain effective sputter yields, to determined yield angle dependency, and to evaluate implantation behavior of impinging ions for the mineral groups most representative for the surfaces of the Moon and Mercury.

Declaration of Competing Interest

None.

Acknowledgements

Financial support has been provided by the Swiss National Science Foundation Fund (200021L_182771/1) as well as the Austrian Science Fund FWF (Project No. I 4101-N36) and by KKKÖ (Commission for the Coordination of Fusion research in Austria at the Austrian Academy of Sciences ÖAW).

Special thanks go to, located at the University of Bern, Stefano Spadaccia, Clément Feller, and Antoine Pommerol from WP (pycnometer), Alfons Berger from GEO (SEM analysis), Julien Reyes, and Jörg Hermann from GEO (TIR analysis), Alice Vho from GEO (sieving), Urs Eggenberger, and Christine Lemp from GEO (milling); Daniela Fischer from GIUB (grainsize analysis). From Bruker we would like to thank Hans-Christian Koch for his expertise on FTIR related questions. A special thanks goes to Beda Hofmann from the Natural History Museum of Bern for providing high quality mineral samples of diopside (Sample number: B2699 / Location: Matterjoch, Zermatt VS, Switzerland) , bytownite (43528 / Dorado Mine, Casas Grandes, Chihuahua, Mexico.), and labradorite (38645 / Surtsey, Island).

Appendix A. Transport effect MIR spectra

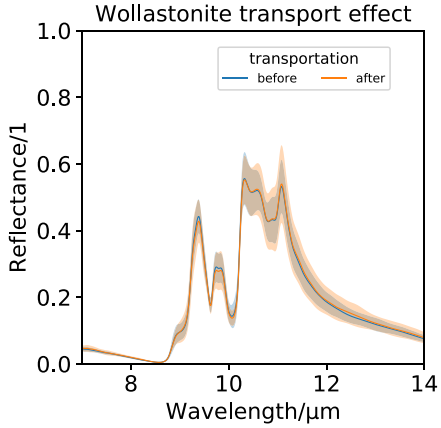

Fig. 6. TIR spectra of wollastonite blank showing a minor increase in reflectance variance after transportation.

Appendix B. Abrasion effect MIR spectra

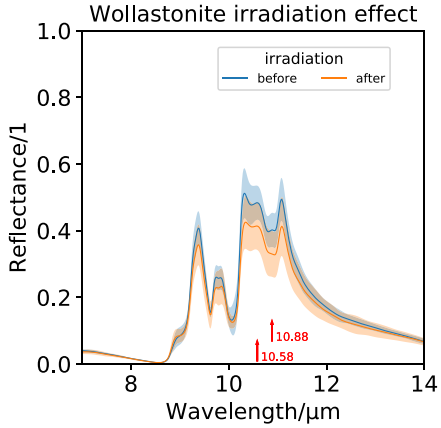

Fig. 7. MIR spectra of irradiated wollastonite showing a major decrease in reflectance variance after the top layer was abraded during transportation. Notable shifts of about 0.01 µm are only seen at the highlighted positions.

Appendix C. AFM images

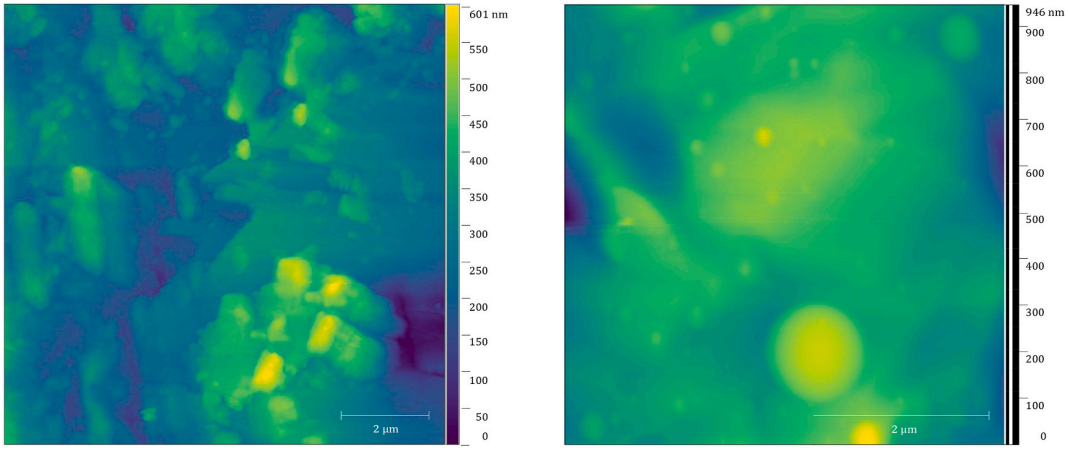

Fig. 8. AFM images of (a) irradiated wollastonite pellet with grain size <30 µm and of (b) a glassy wollastonite thin film as used in, e.g., Szabo et al. (2018).

References

Alnussirat, S.T., Barghouty, A.F., Edmunson, J.E., Sabra, M.S., Rickman, D.L., 2018. Contributions of solar-wind induced potential sputtering to the lunar surface erosion rate and it's exosphere. In: Nuclear Instruments and Methods in Physics Research Section B: Beam Interactions with Materials and Atoms, 420, pp. 33–39 https://www.sciencedirect.com/science/article/pii/S0168583X18300454?via{%}3Dihub{#}f0005. https://doi.org/10.1016/J.NIMB.2018.01.020.

Aumayr, F., Winter, H., 2004. Potential sputtering. In: Philosophical Transactions of the Royal Society of London. Series A: Mathematical, Physical and Engineering Sciences, 362, pp. 77–102. https://doi.org/10.1098/rsta.2003.1300.

Bame, S.J., Asbridge, J.R., Feldman, W.C., Montgomery, M.D., Kearney, P.D., 1975. Solar wind heavy ion abundances. Sol. Phys. 43, 463–473. https://doi.org/10.1007/BF00152368.

Bennett, C.J., Pirim, C., Orlando, T.M., 2013. Space-weathering of solar system bodies: a laboratory perspective. Chem. Rev. 113, 9086–9150.

Berger, B.M., Szabo, P.S., Stadlmayr, R., Aumayr, F., 2017. Sputtering measurements using a quartz crystal microbalance as a catcher. In: Nuclear Instruments and Methods in Physics Research Section B: Beam Interactions with Materials and Atoms, 406, pp. 533–537. https://www.sciencedirect.com/science/article/pii/S0168583X16305250. https://doi.org/10.1016/J.NIMB.2016.11.039.

Biber, H., Szabo, P.S., Jäggi, N., Wallner, M., Stadlmayr, R., Niggas, A., Moro, M.V., Primetzhofer, D., Nenning, A., Mutzke, A., 2020. A detailed look on the interaction of solar wind helium with Mercury's surface in the laboratory. In: EGU General Assembly Conference Abstracts, p. 9895.

Borin, P., Cremonese, G., Marzari, F., Bruno, M., Marchi, S., 2009. Statistical analysis of micrometeoroids flux on Mercury. Astron. Astrophys. 503, 259–264. https://www.aanda.org/articles/aa/abs/2009/31/aa12080-09/aa12080-09.html. https://doi.org/10.1051/0004-6361/200912080.

Brunetto, R., Lantz, C., Nakamura, T., Baklouti, D., Le Pivert-Jolivet, T., Kobayashi, S., Borondics, F., 2020. Characterizing irradiated surfaces using IR spectroscopy. Icarus 345, 113722. https://doi.org/10.1016/j.icarus.2020.113722.

Cassidy, T.A., Johnson, R.E., 2005. Monte Carlo model of sputtering and other ejection processes within a regolith. Icarus 176, 499–507 https://www.sciencedirect.com/science/article/pii/S0019103505000813?via{%}3Dihub{#}fig 001. https://doi.org/10.1016/J.ICARUS.2005.02.013.

Cintala, M.J., 1992. Impact-induced thermal effects in the lunar and Mercurian regoliths. J. Geophys. Res. 97, 947. https://doi.org/10.1029/91JE02207.

Domingue, D.L., Chapman, C.R., Killen, R.M., Zurbuchen, T.H., Gilbert, J.A., Sarantos, M., Benna, M., Slavin, J.A., Schriver, D., Trávníček, P.M., Orlando, T.M., Sprague, A.L., Blewett, D.T., Gillis-Davis, J.J., Feldman, W.C., Lawrence, D.J., Ho, G. C., Ebel, D.S., Nittler, L.R., Vilas, F., Pieters, C.M., Solomon, S.C., Johnson, C.L., Winslow, R.M., Helbert, J., Peplowski, P.N., Weider, S.Z., Mouawad, N., Izenberg, N. R., McClintock, W.E., 2014. Mercury's weather-beaten surface: understanding mercury in the context of lunar and asteroidal space weathering studies. Space Sci. Rev. 181, 121–214. https://doi.org/10.1007/s11214-014-0039-5.

Donaldson Hanna, K.L., Wyatt, M.B., Thomas, I.R., Bowles, N.E., Greenhagen, B.T., Maturilli, A., Helbert, J., Paige, D.A., 2012. Thermal infrared emissivity measurements under a simulated lunar environment: Application to the Diviner Lunar Radiometer Experiment. J. Geophys. Res. Planets 117.

Donaldson Hanna, K.L., Greenhagen, B.T., Patterson, W.R., Pieters, C.M., Mustard, J.F., Bowles, N.E., Paige, D.A., Glotch, T.D., Thompson, C., 2017. Effects of varying environmental conditions on emissivity spectra of bulk lunar soils: application to diviner thermal infrared observations of the moon. Icarus 283, 326–342. https://doi.org/10.1016/j.icarus.2016.05.034.

Elphic, R.C., Delory, G.T., Hine, B.P., Mahaffy, P.R., Horanyi, M., Colaprete, A., Benna, M., Noble, S.K., 2014. The Lunar Atmosphere and Dust Environment Explorer Mission. https://doi.org/10.1007/s11214-014-0113-z.

Grzechnik, A., Zimmermann, H.D., Hervig, R.L., King, P.L., McMillan, P.F., 1996. FTIR micro-reflectance measurements of the CO32- ion content in basanite and leucitite glasses. Contrib. Mineral. Petrol. 125, 311–318. https://doi.org/10.1007/s004100050224.

Hapke, B., 2012. Theory of reflectance and emittance spectroscopy. Cambridge university press.

Heiken, G.H., Vaniman, D.T., French, B.M. (Eds.), 1991. Lunar Sourcebook-a user's Guide to the Moon. Cambridge University Press, Cambridge, United Kingdom. http://adsabs.harvard.edu/abs/1991lsug.book.....H.

Hiesinger, H., Helbert, J., Alemanno, G., Bauch, K.E., D'Amore, M., Maturilli, A., Morlok, A., Reitze, M.P., Stangarone, C., Stojic, A.N., Varatharajan, I., Weber, I., Arnold, G., Banaszkiewicz, M., Bauch, K., Benkhoff, J., Bischoff, A., Blecka, M., Bowles, N., Calcutt, S., Colangeli, L., D'Amore, M., Erard, S., Fonti, S., Greenhagen, B.T., Groussain, O., Helbert, J., Hiesinger, H., Hirsch, H., Jahn, J., Killen, R., Knollenberg, J., Kührt, E., Lorenz, E., Mann, I., Mall, U., Maturilli, A., Morlok, A., Moroz, L., Peter, G., Rataj, M., Robinson, M., Skrbek, W., Spohn, T., Sprague, A., Stöffler, D., Stojic, A., Taylor, F., Varatharajan, I., Venus, H., Warrell, J., Walter, I., Weber, I., Witzke, A., Wöhler, C., 2020. Studying the composition and mineralogy of the Hermean surface with the mercury radiometer and thermal infrared spectrometer (MERTIS) for the BepiColombo Mission: an update. Space Sci. Rev. 216, 1–37. https://doi.org/10.1007/s11214-020-00732-4.

Hijazi, H., Bannister, M.E., Meyer, H.M., Rouleau, C.M., Meyer, F.W., 2017. Kinetic and potential sputtering of an anorthite-like glassy thin film. J. Geophys. Res. Planets 122, 1597–1609. https://doi.org/10.1002/2017JE005300.

Jiang, T., Zhang, H., Yang, Y., Hu, X., Ma, P., Sun, Y., Britt, D., Wang, W., Lu, X., Huang, J., Hsu, W., Mei, B., Wei, R., 2019. Bi-directional reflectance and polarization measurements of pulse-laser irradiated airless body analog materials. Icarus 331, 127–147. https://doi.org/10.1016/j.icarus.2019.05.022.

Kallio, E., Dyadechkin, S., Wurz, P., Khodachenko, M., 2019. Space weathering on the moon: Farside-nearside solar wind precipitation asymmetry. Planet. Space Sci. 166, 9–22 https://www.sciencedirect.com/science/article/pii/S0032063318301818?via{%}3Dihub{#}fig 1. https://doi.org/10.1016/J.PSS.2018.07.013.

Keller, L.P., McKay, D.S., 1997. The nature and origin of rims on lunar soil grains. Geochim. Cosmochim. Acta 61, 2331–2341. https://doi.org/10.1016/s0016-7037(97)00085-9.

Kuhlman, K.R., Sridharan, K., Kvit, A., 2015. Simulation of solar wind space weathering in orthopyroxene. Planet. Space Sci. 115, 110–114. https://www.sciencedirect.com/science/article/pii/S0032063315001075. https://doi.org/10.1016/J.PSS.2015.04.003.

Küstner, M., Eckstein, W., Hechtl, E., Roth, J., 1999. Angular dependence of the sputtering yield of rough beryllium surfaces. J. Nucl. Mater. 265, 22–27 https://www.sciencedirect.com/science/article/pii/S0022311598006485{#}FIG 1. https://doi.org/10.1016/S0022-3115(98)00648-5.

Lantz, C., Brunetto, R., Barucci, M.A., Fornasier, S., Baklouti, D., Bourçois, J., Godard, M., 2017. Ion irradiation of carbonaceous chondrites: a new view of space

weathering on primitive asteroids. Icarus 285, 43–57. https://doi.org/10.1016/j.icarus.2016.12.019.
Lindhard, J., 1965. Influence of crystal lattice on motion of energetic charged particles. In: Matematisk-fysiske meddelelser Kongelige Danske Videnskabernes Selskab, 34. https://www.osti.gov/biblio/4536390.
Loeffler, M.J., Dukes, C.A., Baragiola, R.A., 2009. Irradiation of olivine by 4 keV He ⁺ : simulation of space weathering by the solar wind. J. Geophys. Res. 114, E03003. https://doi.org/10.1029/2008JE003249.
Lucey, P.G., Greenhagen, B.T., Song, E., Arnold, J.A., Lemelin, M., Hanna, K.D., Bowles, N.E., Glotch, T.D., Paige, D.A., 2017. Space weathering effects in diviner lunar radiometer multispectral infrared measurements of the lunar Christiansen feature: characteristics and mitigation. Icarus 283, 343–351. https://doi.org/10.1016/j.icarus.2016.05.010.
Lyon, R.J., 1965. Analysis of rocks by spectral infrared emission (8 to 25 microns). Econ. Geol. 60, 715–736. https://doi.org/10.2113/gsecongeo.60.4.715.
Martin, D.J.P., 2018. IR Spectroscopy of Planetary Regolith Analogues, Lunar Meteorites, and Apollo Soils. The University of Manchester (United Kingdom).
Maturilli, A., Helbert, J., Ferrari, S., D'Amore, M., 2016. On the effect of emergence angle on emissivity spectra: application to small bodies science of solar system materials examined from Hayabusa and future missions (II) 7. In: Planetary science. Earth, Planets and Space, 68, p. 84. https://doi.org/10.1186/s40623-016-0464-7.
Maturilli, A., Helbert, J., Varatharajan, I., Hiesinger, H., 2017. Emissivity spectra of analogue materials at Mercury P-T conditions. In: 48th Lunar and Planetary Science Conference, held 20-24 March 2017, at The Woodlands, Texas. LPI Contribution No. 1964, id.1427 48. http://adsabs.harvard.edu/abs/2017LPI....48.1427M.
McComas, D.J., Allegrini, F., Bochsler, P., Bzowski, M., Christian, E.R., Crew, G.B., DeMajistre, R., Fahr, H., Fichtner, H., Frisch, P.C., Funsten, H.O., Fuselier, S.A., Gloeckler, G., Gruntman, M., Heerikhuisen, J., Izmodenov, V., Janzen, P., Knappenberger, P., Krimigis, S., Kucharek, H., Lee, M., Livadiotis, G., Livi, S., MacDowall, R.J., Mitchell, D., Möbius, E., Moore, T., Pogorelov, N.V., Reisenfeld, D., Roelof, E., Saul, L., Schwadron, N.A., Valek, P.W., Vanderspek, R., Wurz, P., Zank, G. P., 2009. Global observations of the interstellar interaction from the interstellar boundary explorer (IBEX). Science (New York, N.Y.) 326, 959–962.
McCoy, T.J., Peplowski, P.N., McCubbin, F.M., Weider, S.Z., 2018. The geochemical and mineralogical diversity of mercury. In: Solomon, S.C., Nittler, L.R., Anderson, B.J. (Eds.), Mercury: The View after MESSENGER, 21. Cambridge University Press, Cambridge, United Kingdom, pp. 176–190. https://doi.org/10.1017/9781316650684 chapter 7.
McKay, D.S., Heiken, G.H., Basu, A., Blanford, G., Simon, S.B., Reedy, R., French, B.M., Papike, J., 1991. The lunar regolith. In: Heiken, G.H., Vaniman, D.T., French, B.M. (Eds.), Lunar Sourcebook-a user's Guide to the Moon. Cambridge University Press, Cambridge, United Kingdom, pp. 285–356 chapter 7. http://adsabs.harvard.edu/abs/1991lsug.book.....H.
Milillo, A., Fujimoto, M., Murakami, G., Benkhoff, J., Zender, J., Aizawa, S., Dósa, M., Griton, L., Heyner, D., Ho, G., Imber, S.M., Jia, X., Karlsson, T., Killen, R.M., Laurenza, M., Lindsay, S.T., McKenna-Lawlor, S., Mura, A., Raines, J.M., Rothery, D. A., André, N., Baumjohann, W., Berezhnoy, A., Bourdin, P.A., Bunce, E.J., Califano, F., Deca, J., de la Fuente, S., Dong, C., Grava, C., Fatemi, S., Henri, P., Ivanovski, S.L., Jackson, B.V., James, M., Kallio, E., Kasaba, Y., Kilpua, E., Kobayashi, M., Langlais, B., Leblanc, F., Lhotka, C., Mangano, V., Martindale, A., Massetti, S., Masters, A., Morooka, M., Narita, Y., Oliveira, J.S., Odstrcil, D., Orsini, S., Pelizzo, M.G., Plainaki, C., Plaschke, F., Sahraoui, F., Seki, K., Slavin, J.A., Vainio, R., Wurz, P., Barabash, S., Carr, C.M., Delcourt, D., Glassmeier, K.H., Grande, M., Hirahara, M., Huovelin, J., Korablev, O., Kojima, H., Lichtenegger, H., Livi, S., Matsuoka, A., Moissl, R., Moncuquet, M., Muinonen, K., Quèmerais, E., Saito, Y., Yagitani, S., Yoshikawa, I., Wahlund, J.E., 2020. Investigating Mercury's environment with the two-spacecraft BepiColombo mission. Space Sci. Rev. 216, 1–78. https://doi.org/10.1007/s11214-020-00712-8.
Morlok, A., Klemme, S., Weber, I., Stojic, A., Sohn, M., Hiesinger, H., Helbert, J., 2019. Mid-infrared spectroscopy of planetary analogs: a database for planetary remote sensing. Icarus 324, 86–103. https://doi.org/10.1016/j.icarus.2019.02.010.
Mura, A., 2012. Loss rates and time scales for sodium at mercury. Planet. Space Sci. 63-64, 2–7 https://www.sciencedirect.com/science/article/pii/S0032063311002728{#}f0015. https://doi.org/10.1016/J.PSS.2011.08.012.
Mutzke, A., Schneider, R., Bandelow, G., 2013. SDTrimSP-2D: Simulation of Particles Bombarding on a Two Dimensional Target-Version 2.0. http://hdl.handle.net/11858/00-001M-0000-0026-E06F-E.
Mutzke, A., Schneider, R., Eckstein, W., Dohmen, R., Schmid, K., von Toussaint, U., Badelow, G., 2019. SDTrimSP Version 6.00.
Nakamura, E., Makishima, A., Moriguti, T., Kobayashi, K., Tanaka, R., Kunihiro, T., Tsujimori, T., Sakaguchi, C., Kitagawa, H., Ota, T., Yachi, Y., Yada, T., Abe, M., Fujimura, A., Ueno, M., Mukai, T., Yoshikawa, M., Kawaguchi, J., 2012. Space environment of an asteroid preserved on micrograins returned by the Hayabusa spacecraft. Proc. Natl. Acad. Sci. U. S. A. 109, E624–E629. https://doi.org/10.1073/pnas.1116236109.
Nash, D.B., Salisbury, J.W., 1991. Infrared reflectance spectra (2.2-15 μm) of plagioclase feldspars. Geophys. Res. Lett. 18, 1151–1154. https://doi.org/10.1029/91GL01008.
Nastasi, M., Michael, N., Mayer, J., Hirvonen, J.K., James, M., 1996. Ion-Solid Interactions: Fundamentals and Applications. Cambridge University Press.
Ni, H., Zhang, Y., 2008. H2O diffusion models in rhyolitic melt with new high pressure data. Chem. Geol. 250, 68–78. https://www.sciencedirect.com/science/article/pii/S0009254108000806. https://doi.org/10.1016/J.CHEMGEO.2008.02.011.
Nittler, L.R., Starr, R.D., Weider, S.Z., McCoy, T.J., Boynton, W.V., Ebel, D.S., Ernst, C.M., Evans, L.G., Goldsten, J.O., Hamara, D.K., Lawrence, D.J., McNutt, R.L., Schlemm, C. E., Solomon, S.C., Sprague, A.L., 2011. The major-element composition of Mercury's surface from MESSENGER X-ray spectrometry. Science 333, 1847–1850. https://doi.org/10.1126/science.1211567.
Onderdelinden, D., 1966. The influence of channeling on cu single-crystal sputtering. Appl. Phys. Lett. 8, 189–190. https://doi.org/10.1063/1.1754548.
Orsini, S., Livi, S., Lichtenegger, H., Barabash, S., Milillo, A., Angelis, E.D., Phillips, M., Laky, G., 2020. SERENA : particle instrument suite for Sun-mercury interaction insights on-board BepiColombo. Space Sci. Rev. 217, 49.
Paige, D.A., Foote, M.C., Greenhagen, B.T., Schofield, J.T., Calcutt, S., Vasavada, A.R., Preston, D.J., Taylor, F.W., Allen, C.C., Snook, K.J., 2010. The lunar reconnaissance orbiter diviner lunar radiometer experiment. Space Sci. Rev. 150, 125–160.
Pieters, C.M., Noble, S.K., 2016. Space weathering on airless bodies. J. Geophys. Res. Planets 121, 1865–1884. https://doi.org/10.1002/2016JE005128@10.1002/(ISSN)2169-9100.JGRE25.
Pieters, C.M., Taylor, L.A., Noble, S.K., Keller, L.P., Hapke, B., Morris, R.V., Allen, C.C., McKAY, D.S., Wentworth, S., 2000. Space weathering on airless bodies: Resolving a mystery with lunar samples. Meteorit. Planet. Sci. 35, 1101–1107. https://doi.org/10.1111/j.1945-5100.2000.tb01496.x.
Plainaki, C., Lilensten, J., Radioti, A., Andriopoulou, M., Milillo, A., Nordheim, T.A., Dandouras, I., Coustenis, A., Grassi, D., Mangano, V., Massetti, S., Orsini, S., Lucchetti, A., 2016. Planetary space weather: scientific aspects and future perspectives. J. Space Weather Space Clim. 6, A31. https://doi.org/10.1051/swsc/2016024.
Reynard, B., 1991. Single-crystal infrared reflectivity of pure Mg2SiO2 forsterite and (Mg0.86,Fe0.14)2SiO4 olivine - New data and a reappraisal. Phys. Chem. Miner. 18, 19–25. https://doi.org/10.1007/BF00199039.
Rodriguez-Nieva, J.F., Bringa, E.M., Cassidy, T.A., Johnson, R.E., Caro, A., Fama, M., Loeffler, M.J., Baragiola, R.A., Farkas, D., 2011. Sputtering from a porous material by penetrating ions. Astrophys. J. Lett. 743, 5. http://lammps.sandia.gov. https://doi.org/10.1088/2041-8205/743/1/L5.
Rothery, D.A., Massironi, M., Alemanno, G., Barraud, O., Besse, S., Bott, N., Brunetto, R., Bunce, E., Byrne, P., Capaccioni, F., Capria, M.T., Carli, C., Charlier, B., Cornet, T., Cremonese, G., D'Amore, M., De Sanctis, M.C., Doressoundiram, A., Ferranti, L., Filacchione, G., Galluzzi, V., Giacomini, L., Grande, M., Guzzetta, L.G., Helbert, J., Heyner, D., Hiesinger, H., Hussmann, H., Hyodo, R., Kohout, T., Kozyrev, A., Litvak, M., Lucchetti, A., Malakhov, A., Malliband, C., Mancinelli, P., Martikainen, J., Martindale, A., Maturilli, A., Milillo, A., Mitrofanov, I., Mokrousov, M., Morlok, A., Muinonen, K., Namur, O., Owens, A., Nittler, L.R., Oliveira, J.S., Palumbo, P., Pajola, M., Pegg, D.L., Penttilä, A., Politi, R., Quarati, F., Re, C., Sanin, A., Schulz, R., Stangarone, C., Stojic, A., Tretiyakov, V., Väisänen, T., Varatharajan, I., Weber, I., Wright, J., Wurz, P., Zambon, F., 2020. Rationale for BepiColombo studies of Mercury's surface and composition. Space Sci. Rev. 216, 66. https://doi.org/10.1007/s11214-020-00694-7.
Russell, C.T., Luhmann, J.G., Strangeway, R.J., 2016. Space Physics: An Introduction. Cambridge University Press.
Salisbury, J.W., 1993. Mid-infrared spectroscopy: Laboratory data. In: Remote Geochemical Analysis: Elemental and Mineralogical Composition, p. 618.
Salisbury, J.W., Wald, A., 1992. The role of volume scattering in reducing spectral contrast of reststrahlen bands in spectra of powdered minerals. Icarus 96, 121–128. https://doi.org/10.1016/0019-1035(92)90009-V.
Salisbury, John W., Wald, Andrew, D'Aria, Dana M., 1994. Thermal-infrared remote sensing and Kirchhoff's law: 1. Laboratory measurements. J. Geophys. Res. Solid Earth 99, 11897–11911. https://doi.org/10.1029/93JB03600.
Salisbury, J.W., Basu, A., Fischer, E.M., 1997. Thermal infrared spectra of lunar soils. Icarus 130, 125–139. https://doi.org/10.1006/icar.1997.5809.
Sauerbrey, G., 1959. Verwendung von Schwingquarzen zur Wägung dünner Schichten und zur Mikrowägung. Z. Phys. 155, 206–222. https://doi.org/10.1007/BF01337937.
Schlueter, K., Nordlund, K., Hobler, G., Balden, M., Granberg, F., Flinck, O., Da Silva, T. F., Neu, R., 2020. Absence of a crystal direction regime in which sputtering corresponds to amorphous material. Phys. Rev. Lett. 125, 225502. https://doi.org/10.1103/PhysRevLett.125.225502.
Shluger, A., Stefanovich, E., 1990. Models of the self-trapped exciton and nearest-neighbor defect pair in SiO 2. Phys. Rev. B 42, 9664–9673. https://doi.org/10.1103/PhysRevB.42.9664.
Sigmund, P., 1969. Theory of sputtering. I. Sputtering yield of amorphous and polycrystalline targets. Phys. Rev. 184, 383–416. https://doi.org/10.1103/PhysRev.184.383 (arXiv:PhysRev.184.383).
Solomon, S.C., McNutt, R.L., Gold, R.E., Acuña, M.H., Baker, D.N., Boynton, W.V., Chapman, C.R., Cheng, A.F., Gloeckler, G., Head, J.W., Krimigis, S.M., McClintock, W.E., Murchie, S.L., Peale, S.J., Phillips, R.J., Robinson, M.S., Slavin, J. A., Smith, D.E., Strom, R.G., Trombka, J.I., Zuber, M.T., 2001. The MESSENGER mission to mercury: scientific objectives and implementation. Planet. Space Sci. 49, 1445–1465. https://doi.org/10.1016/S0032-0633(01)00085-X.
Sporn, M., Libiseller, G., Neidhart, T., Schmid, M., Aumayr, F., Winter, H.P., Varga, P., Grether, M., Niemann, D., Stolterfoht, N., 1997. Potential sputtering of clean SiO2 by slow highly charged ions. Phys. Rev. Lett. 79, 945–948. https://doi.org/10.1103/PhysRevLett.79.945.
Stadlmayr, R., Szabo, P.S., Mayer, D., Cupak, C., Dittmar, T., Bischoff, L., Möller, S., Rasiński, M., Wilhelm, R.A., Möller, W., Aumayr, F., 2020. Sputtering of nanostructured tungsten and comparison to modelling with TRI3DYN. J. Nucl. Mater. 532, 152019. https://doi.org/10.1016/j.jnucmat.2020.152019.
Stojic, A.N., Morlok, A., Tollan, P., Kohout, T., Hermann, J., Weber, I., Moreau, J.G., Hiesinger, H., Sohn, M., Bauch, K.E., Reitze, M.P., Helbert, J., 2021. A shock recovery experiment and its implications for Mercury's surface: the effect of high pressure on porous olivine powder as a regolith analog. Icarus 357, 114162. https://doi.org/10.1016/j.icarus.2020.114162.

Szabo, P.S., Chiba, R., Biber, H., Stadlmayr, R., Berger, B.M., Mayer, D., Mutzke, A., Doppler, M., Sauer, M., Appenroth, J., Fleig, J., Foelske-Schmitz, A., Hutter, H., Mezger, K., Lammer, H., Galli, A., Wurz, P., Aumayr, F., 2018. Solar wind sputtering of wollastonite as a lunar analogue material – comparisons between experiments and simulations. Icarus 314, 98–105.

Szabo, P.S., Biber, H., Jäggi, N., Brenner, M., Weichselbaum, D., Niggas, A., Stadlmayr, R., Primetzhofer, D., Nenning, A., Mutzke, A., Sauer, M., Fleig, J., Foelske-Schmitz, A., Mezger, K., Lammer, H., Galli, A., Wurz, P., Aumayr, F., 2020. Dynamic potential sputtering of lunar analog material by solar wind ions. Astrophys. J. 891, 100. https://doi.org/10.3847/1538-4357/ab7008.

Thomas, E., Simolka, J., DeLuca, M., Horányi, M., Janches, D., Marshall, R.A., Munsat, T., Plane, J.M., Sternovsky, Z., 2017. Experimental setup for the laboratory investigation of micrometeoroid ablation using a dust accelerator. Rev. Sci. Instrum. 88, 034501. https://doi.org/10.1063/1.4977832.

Vander Kaaden, K.E., McCubbin, F.M., Nittler, L.R., Peplowski, P.N., Weider, S.Z., Frank, E.A., McCoy, T.J., 2017. Geochemistry, mineralogy, and petrology of boninitic and komatiitic rocks on the mercurian surface: Insights into the mercurian mantle. Icarus 285, 155–168 https://www.sciencedirect.com/science/article/pii/S0019103516303116{#}fig0001 https://linkinghub.elsevier.com/retrieve/pii/S0019103516303116. https://doi.org/10.1016/j.icarus.2016.11.041.

Varatharajan, I., Maturilli, A., Helbert, J., Alemanno, G., Hiesinger, H., 2019. Spectral behavior of sulfides in simulated daytime surface conditions of mercury: supporting past (MESSENGER) and future missions (BepiColombo). Earth Planet. Sci. Lett. 520, 127–140. https://doi.org/10.1016/j.epsl.2019.05.020.

von Steiger, R., Schwadron, N.A., Fisk, L.A., Geiss, J., Gloeckler, G., Hefti, S., Wilken, B., Wimmer-Schweingruber, R.R., Zurbuchen, T.H., 2000. Composition of quasi-stationary solar wind flows from Ulysses/solar wind ion composition spectrometer. J. Geophys. Res. Space Physics 105, 27217–27238. https://doi.org/10.1029/1999JA000358.

von Toussaint, U., Mutzke, A., Manhard, A., 2017. Sputtering of rough surfaces: a 3D simulation study. Phys. Scr. T170, 014056. http://stacks.iop.org/1402-4896/2017/i=T170/a=014056?key=crossref.54a755fcf210fc637a4c40aaeacbc2f3. https://doi.org/10.1088/1402-4896/aa90be.

Weber, I., Stojic, A.N., Morlok, A., Reitze, M.P., Markus, K., Hiesinger, H., Pavlov, S.G., Wirth, R., Schreiber, A., Sohn, M., Hübers, H.W., Helbert, J., 2020. Space weathering by simulated micrometeorite bombardment on natural olivine and pyroxene: a coordinated IR and TEM study. Earth Planet. Sci. Lett. 530, 115884. https://doi.org/10.1016/j.epsl.2019.115884.

Wenk, E., Schwander, H., Wenk, H.R., 1965. Labradorit von Surtsey (island). Acta Natur. Islandica II 5.

Winslow, R.M., Philpott, L., Paty, C.S., Lugaz, N., Schwadron, N.A., Johnson, C.L., Korth, H., 2017. Statistical study of ICME effects on Mercury's magnetospheric boundaries and northern cusp region from MESSENGER. J. Geophys. Res. Space Physics 122, 4960–4975. https://doi.org/10.1002/2016JA023548.

Wurz, P., Lammer, H., 2003. Monte-Carlo simulation of Mercury's exosphere. Icarus 164, 1–13 https://www.sciencedirect.com/science/article/pii/S0019103503001234{#}FIG 001. https://doi.org/10.1016/S0019-1035(03)00123-4.

Wurz, P., Whitby, J.A., Rohner, U., Martín-Fernández, J.A., Lammer, H., Kolb, C., 2010. Self-consistent modelling of Mercury's exosphere by sputtering, micro-meteorite impact and photon-stimulated desorption. Planet. Space Sci. 58, 1599–1616.

Yang, Y., Zhang, H., Wang, Z., Yuan, Y., Li, S., Hsu, W., Liu, C., 2017. Optical spectroscopic characterizations of laser irradiated olivine grains. Astron. Astrophys. 597, A50. https://doi.org/10.1051/0004-6361/201629327.

Young, C.L., Poston, M.J., Wray, J.J., Hand, K.P., Carlson, R.W., 2019. The mid-IR spectral effects of darkening agents and porosity on the silicate surface features of airless bodies. Icarus 321, 71–81. https://doi.org/10.1016/j.icarus.2018.10.032.

Zolotov, M.Y., Sprague, A.L., Hauck, S.A., Nittler, L.R., Solomon, S.C., Weider, S.Z., 2013. The redox state, FeO content, and origin of sulfur-rich magmas on Mercury. J. Geophys. Res. Planets 118, 138–146. https://doi.org/10.1029/2012JE004274.

Chapter 3

Evaluation of new and recent sputter models

The Planetary Science Journal, 4:86 (15pp), 2023 May https://doi.org/10.3847/PSJ/acd056

New Compound and Hybrid Binding Energy Sputter Model for Modeling Purposes in Agreement with Experimental Data

Noah Jäggi[1], Andreas Mutzke[2], Herbert Biber[3], Johannes Brötzner[3], Paul Stefan Szabo[4], Friedrich Aumayr[3], Peter Wurz[1], and André Galli[1]
[1] Physikalisches Institut, University of Bern, Sidlerstrasse 5, CH-3012 Bern, Switzerland; noah.jaeggi@unibe.ch
[2] Max Planck Institute for Plasma Physics (IPP), D-17491 Greifswald, Germany
[3] Institute of Applied Physics, TU Wien, Wiedner Hauptstraße 8-10/E134, A-1040 Vienna, Austria
[4] Space Sciences Laboratory, University of California, 7 Gauss Way, Berkeley, CA 94720, USA
Received 2023 January 24; revised 2023 April 13; accepted 2023 April 24; published 2023 May 12

Abstract

Rocky planets and moons experiencing solar wind sputtering are continuously supplying their enveloping exosphere with ejected neutral atoms. To understand the quantity and properties of the ejecta, well-established binary collision approximation Monte Carlo codes like TRIM with default settings are used predominantly. Improved models such as SDTrimSP have come forward, and together with new experimental data, the underlying assumptions have been challenged. We introduce a hybrid model, combining the previous surface binding approach with a new bulk binding model akin to Hofsäss & Stegmaier. In addition, we expand the model implementation by distinguishing between free and bound components sourced from mineral compounds such as oxides or sulfides. The use of oxides and sulfides also enables the correct setting of the mass densities of minerals, which was previously limited to the manual setting of individual atomic densities of elements. All of the energies and densities used are thereby based on tabulated data, so that only minimal user input and no fitting of parameters are required. We found unprecedented agreement between the newly implemented hybrid model and previously published sputter yields for incidence angles up to 45° from surface normal. Good agreement is found for the angular distribution of mass sputtered from enstatite $MgSiO_3$ compared to the latest experimental data. Energy distributions recreate trends of experimental data of oxidized metals. Similar trends are to be expected from future mineral experimental data. The model thus serves its purpose of widespread applicability and ease of use for modelers of rocky body exospheres.

Unified Astronomy Thesaurus concepts: Solar wind (1534); Exosphere (499); Mercury (planet) (1024); The Moon (1692)

1. Introduction

In recent years there were several efforts to better constrain the erosion of rocky planetary bodies exposed to highly energetic solar wind ions. This includes investigating the effect of surface roughness (Biber et al. 2022) and porosity (Szabo et al. 2022b), performing ion irradiation experiments with mass yield measurements (e.g., Hijazi et al. 2017; Szabo et al. 2018, 2020a; Biber et al. 2022), and introducing a new surface and bulk binding energy (BBE) model from theory (Hofsäss & Stegmaier 2022; Morrissey et al. 2022). In this work, we discuss the parameter of density and its inclusion in SDTrimSP (Mutzke et al. 2019), as well as a new hybrid binding energy model that reliably recreates experimental sputter yields completely without the requirement to adjust input parameters. The new approach will be a valuable tool for modeling the ion sputtering contribution to exospheres (i.e., Pfleger et al. 2015; Suzuki et al. 2020; Kazakov et al. 2022; Killen et al. 2022).

1.1. Space Weathering of Exposed Rocky Surfaces

Exposed bodies in space are subject to solar wind irradiation. The main constituents of solar wind, H^+ and He^{2+}, thereby bear kinetic energies of approximately 1 keV amu^{-1}—equivalent to about 440 km s^{-1} (Wurz 2005; Gershman et al. 2012; Baker et al. 2013; Winslow et al. 2013). When hitting a surface, most ions are neutralized and enter the sample, with some fraction being reflected as either neutrals or even ions (Lue et al. 2011; Vorburger et al. 2013). The ions entering the sample initiate a cascade of collisions with a chance to eject particles from the near surface at suprathermal energies. This process is responsible for altering the surface composition and creating lattice defects, which leads to amorphization (Betz & Wien 1994; Loeffler et al. 2009; Dukes et al. 2011; Domingue et al. 2014).

Ion sputtering releases atoms from the surface having typical velocities that are significantly lower than the impinging ions (e.g., Thompson 1968), but large enough to form an extended exosphere with a significant fraction of atoms exceeding the escape velocity of any small body, including the Moon (2.4 km s^{-1}) and Mercury (4.3 km s^{-1}) (e.g., Wurz et al. 2007, 2010). Such exospheres allow for ground-based observatories and space probe missions such as LADEE and LRO at the Moon (Paige et al. 2010; Elphic et al. 2014) and MESSENGER (Solomon et al. 2001; McNutt et al. 2018) or the future BepiColombo (Benkhoff et al. 2010; Milillo et al. 2020; Orsini et al. 2021) at Mercury to detect them. These observations were used early on to self-consistently model Mercury's surface composition based on the four expected major processes contributing to the exosphere: solar wind ion sputtering, micrometeroid impact vaporization, photon-stimulated desorption, and thermal desorption (Madey et al. 2002;

Mura et al. 2009; Wurz et al. 2010; Gamborino & Wurz 2018; Wurz et al. 2022).

An important piece of information that is necessary to distinguish the exospheric species sourced from the surface is the process-specific energy distribution of the ejected material. For example, solar wind ion sputtering and micrometeroid impact vaporization compete in supplying Mercury's exospheric high-energy particle population with refractory species (e.g., Ca and Mg), while photon-stimulated desorption dominates the supply of energetic volatile and moderately volatile species (i.e., Na, K, and S; Mangano et al. 2007; Cassidy et al. 2015; Schaible et al. 2020; Grava et al. 2021; Janches et al. 2021). In the same way that fluxes, or precipitation rates, of the particles causing these processes are still in the process of being better constrained (i.e., proton precipitation for solar wind sputtering at Mercury's cusps in Fatemi et al. 2020; Glass et al. 2022; Raines et al. 2022), the understanding of the underlying physics is still a work in progress. At the Moon, precipitation rates seem comparably trivial to compute, but the Moon traveling through Earth's magnetotail and localized crustal fields add complexity to the system (e.g., Lue et al. 2011; Poppe et al. 2018; Nénon & Poppe 2020).

1.2. Sputter Models

To efficiently model ion-induced sputtering, binary collision approximation (BCA) models are used. The BCA codes track particles as they travel through the sample and cause recoils, which are in turn tracked throughout the sample. There are many different models available; however, we will focus on the results of the Monte Carlo–based, most widely used TRIM code (Biersack & Haggmark 1980) in the SRIM package (Ziegler et al. 2010) as well as its successor SDTrimSP (Mutzke et al. 2019), a combined and improved version of the static TRIM.SP (Biersack & Eckstein 1984), and the dynamic TRYDIN (Möller & Eckstein 1984).

TRIM has been shown to overestimate the sputter yield compared to experimental yields for minerals (Szabo et al. 2018). Exosphere modelers need more accurate inputs that are in line with the latest understanding of sputtering. There have been several suggestions on how to best recreate experimental data. Here are the major contributions that set the expectations and limitations of the current state-of-the-art sputter modeling:

1. Schaible et al. (2017) varied O-binding energies to better fit early experimental data for sputtering of Al_2O_3 and SiO_2 (Ken Knight & Wehner 1967; Roth et al. 1979). Increasing the O-binding energy decreases the O yield, but not enough to significantly improve the agreement.
2. Szabo et al. (2020a) suggested that the best agreement between the mass yield of an irradiated sample and SDTrimSP is obtained by (a) adjusting atomic densities to obtain an appropriate sample density, (b) adjusting the surface binding energy (SBE) of O to 6.5 eV, and (c) setting the SBEs of each element to the averaged SBE of all elements in the sample, resulting in an SBE that is highly dependent on the O concentration in the sample (Appendix). Although we found these parameters to work reasonably well for all kinds of silicates, the universality of these modifications is questionable.
3. Morrissey et al. (2022) determined SBEs using molecular dynamics (MD) and suggest lower sputter yield across all surface species due to an increase in the single component's binding energies. However, the restricted availability of species-specific SBEs prevents the applicability of the results on a broad range of minerals. This is also caused by the limited availability of interatomic potentials for each mineral system of interest.
4. Hofsäss & Stegmaier (2022) proposed completely neglecting SBEs and instead using only BBEs from tabulated data. This way, particles leaving the sample do not have to overcome a surface potential and instead lose energy with each recoil. Although they solely use tabulated data to set the BBE and propose a sound physical constraint on the cutoff energy for the tracing of the particles, they are still required to make use of an undisclosed level of implantation to find good agreement with experimental data.
5. Biber et al. (2022) used the in-house-built ray-tracing code SPRAY (Cupak et al. 2021) with data from SDTrimSP and atomic force microscope images to discuss the effect of surface roughness on the sputter yield of a powder pellet and a flat, glassy thin film. They found that a rough pressed pellet surface reduces the yield, especially at shallow incident angles (above 45° relative to surface normal). The cause of this reduced yield was related to surface roughness leading to shallower local incident angles, shadowing, and redeposition of material. For a detailed overview of rough surface sputter models see Küstner et al. (1998) and Arredondo et al. (2019).

All these models require varying degrees of adjustments of parameters when it comes to density, binding energies, cutoff energies, or roughness. To adequately describe the sputtering process on realistic surfaces, roughness has to be taken into account. This effect is not considered in this work, as we focus on the fundamental sputter physics within the sample, which is agnostic to properties affecting trajectories of impinging ions and ejecta. For this reason, we compare our results to experimental thin-film data, which are considered to be flat surfaces (Biber et al. 2022). We propose a new compound model for obtaining a realistic initial mineral density, as well as a hybrid binding energy model to obtain increased binding energies based on tabulated data that can recreate experimental results.

2. Methods of Computation

2.1. Model Parameters

Angular-dependent sputter yields for various different models were calculated with SDTrimSP to compare with a wide range of experimental data. To obtain good statistics in SDTrimSP, we modeled between 7.7×10^6 and 31×10^6 impactors for each of 19 incident angles between 0° and 89° relative to the surface normal (Mutzke et al. 2019). The step size was set to gradually decrease from an initial 10° for incidence close to the surface normal to 2° for incidence angles 80°–88°. We collected the information of up to 10^6 recoils leaving the sample and performed statistics based on the last 10^5 recoils. The data contain the species name, end energy, azimuth angle, and zenith angle. The fits of the data shown in the figures throughout this manuscript are described in Section 2.5. The inelastic loss model seven (inel = 7) is used in all SDTrimSP calculations, which determines the inelastic

Table 1
Major Rock-forming Minerals Required to Represent an Unknown Planetary Surface, Consisting of Volcanic Minerals

Group	Mineral	Formula	ρ_{ref}		$\rho_{compounds}$		$\Delta\mu_{compounds}$	ρ_{atomic}		$\Delta\mu_{atomic}$
			(g cm^{-3})	(atoms Å^{-3})	(g cm^{-3})	(atoms Å^{-3})	(unit of unity)	(g cm^{-3})	(atoms Å^{-3})	(unit of unity)
Plagioclase	Orthoclase	$KAlSi_3O_8$	2.56	0.0723	2.67	0.0754	−1%	1.36	0.0384	23%
	Albite	$NaAlSi_3O_8$	2.62	0.0786	2.70	0.0808	−1%	1.43	0.0429	22%
	Anorthite	$CaAl_2Si_2O_8$	2.73	0.0768	2.99	0.0840	−3%	1.53	0.0429	21%
	Nepheline	$NaAlSiO_4$	2.59	0.0747	2.84	0.0820	−3%	1.44	0.0414	22%
Pyroxene	Wollastonite	$CaSiO_3$	2.93	0.0760	2.91	0.0755	0%	1.45	0.0375	26%
	Diopside	$CaMgSi_2O_6$	3.40	0.0946	2.97	0.0827	5%	1.46	0.0405	33%
	Enstatite	$Mg_2Si_2O_6$	3.20	0.0960	3.05	0.0913	2%	1.47	0.0441	30%
	Ferrosillite	$Fe_2Si_2O_6$	3.95	0.0902	3.82	0.0872	1%	2.15	0.0491	22%
Olivine	Forsterite	Mg_2SiO_4	3.27	0.0980	3.21	0.0960	1%	1.46	0.0438	31%
	Fayalite	Fe_2SiO_4	4.39	0.0908	4.64	0.0900	0%	2.48	0.0512	21%
Oxides	Ilmenite	$FeTiO_3$	4.72	0.0937	4.83	0.0959	−1%	2.54	0.0504	23%
	Quartz	SiO_2	2.65	0.0797	2.65	0.0797	0%	1.51	0.0454	21%
Sulfides	Troilite	FeS	4.61	0.0632	4.61	0.0632	0%	3.89	0.0533	6%
	Niningerite	MgS	2.68	0.0573	2.68	0.0573	0%	1.91	0.0408	12%
	MnS	MnS	3.99	0.0552	3.99	0.0552	0%	3.80	0.0526	2%
	CrS	CrS	4.89	0.0701	4.89	0.0701	0%	3.70	0.0530	10%
	TiS	TiS	3.85	0.0580	3.85	0.0580	0%	3.07	0.0462	8%
	CaS	CaS	2.59	0.0432	2.59	0.0432	0%	1.74	0.0290	14%
Accessories	Spinel	$MgAl_2O_4$	3.64	0.1078	3.77	0.1115	−1%	1.58	0.0468	32%
	Chromite	$FeCr_2O_4$	4.79	0.0902	5.29	0.0996	−3%	2.88	0.0543	18%

Note. Differences in mean free path lengths ($\mu = \rho^{-1/3}$) are calculated as $\Delta\mu = \mu/\mu_{ref} - 1$. The density short forms are as follows: ρ_{ref}—mass densities and atomic densities calculated based on typical mineral densities found on webmineral (see also, e.g., Deer et al. 1992); $\rho_{compounds}$—densities calculated based on tabulated oxide and sulfide data from pure compound properties; ρ_{atomic}—densities calculated based on atomic data included in tables of SDTrimSP that are based on monatomic solids.

loss in the sample based on the Lindhard–Scharff stopping power model (Lindhard & Scharff 1961) unless there are corrections available (e.g., tables for H and He in Ziegler & Biersack 1985). For a detailed description of SDTrimSP, we encourage the reader to look into the accompanying literature (e.g., Mutzke et al. 2019).

The surface composition of irradiated samples show a clear fluence dependence until an equilibrium is reached. This was shown by Baretzky et al. (1992) for the oxide Ta_2O_5 and by Szabo et al. (2020b) in the form of the fluence dependence of experimental sputter data of minerals. Furthermore, the experimental sputter yields were best recreated using the dynamic mode of SDTrimSP (Szabo et al. 2020b). For this reason, all computations in this manuscript were performed in dynamic mode of SDTrimSP, and the results are for ejecta from a surface in equilibrium with the impinging ions. For irradiation with He, the fluence was set to 750 atoms Å^{-3}, whereas H irradiation required fluences of up to 3000 atoms Å^{-3} (or 3×10^{19} atoms cm^{-3}) at normal incidence in some models. The dynamic mode allows the sample to change with the ion fluence and best simulates the sample composition reaching an equilibrium with the solar wind ions, reproducing the fluence dependence of the experimental sputter yields. In detail, samples in SDTrimSP have an infinite lateral extent with a finite number of layers vertically. In our case, all layers have the same composition set initially and a thickness of 10 Å. After each fluence step, composed of about 10^5 impactors, the layers within the sample are updated according to the components that were either lost or gained within the last step.

Direct comparisons between SRIM and SDTrimSP calculations were performed for mass yield (amu ion^{-1}). In SRIM (Ziegler et al. 2010) we modeled 10^5 impinging H and He ions for static sputter yield results to obtain good statistics. We used the "Monolayer Collision Steps/Surface Sputtering" damage model. The mineral density was set to its default density, as calculated by SRIM from the atomic density value of each element component (comparable to ρ_{atomic} from tabulated data in SDTrimSP given in Table 1).

We will now introduce a few select parameter settings that are required to model sputtering of minerals. These comprise the dynamic mode of SDTrimSP, the different ways of introducing binding energies, including our new addition, and a new way for correcting sample density.

2.2. Binding Energy

The efficiency at which particles can be removed from a surface, the sputter yield, is in one part a function of the total binding energy of the system. The two common binding energies provided to a BCA model are the SBE and the BBE. The former is in the shape of a surface potential that has to be overcome to leave the sample. The latter is an energy that is subtracted from each recoil and simulates the interaction between neighboring atoms in the otherwise mineral-lattice-agnostic model that is SDTrimSP. It is possible to obtain a constant yield while keeping the sum of the binding energies constant (Möller & Posselt 2001). We now quickly introduce three different binding energy models, two of which are already established (pure SBE or BBE models) and one model that combines the two (SBE + BBE). The models are summarized in Table 2.

Table 2
The Different Energy and Density Models and Their Parameters

	SDTrimSP Model Presets					Manually Set Models	
	SB	SB-C	BB	BB-C	HB-C	BB_0[a]	HB[a]
SBE	ΔH_{sub}	ΔH_{sub}	0	0	ΔH_{sub}	0	ΔH_{sub}
BBE_f[b]	0	0	ΔH_{sub}	0	0	ΔH_{sub} + CBE	CBE
BBE_b[b]	…	0	…	ΔH_{sub} + CBE	CBE	…	…
ρ_f	atomic	atomic	atomic	atomic	atomic	atomic	atomic
ρ_b	…	compound	…	compound	compound	…	…
E_{cutoff}	$<\Delta H_{sub}$	$<\Delta H_{sub}$	$\Delta H_{sub}/3$	$\Delta H_{sub}/3$	$<\Delta H_{sub}$	$\Delta H_{sub}/3$	$<\Delta H_{sub}$
isbv	1	1	8	8	4	1	1

Notes. Short forms: SBE—surface binding energy; BBE—bulk binding energy; f—"free," unbound atom; b—compound-bound atom; CBE—chemical binding energy: $\Delta H_f/(m+n)$, where m and n are the number of cations and anions in a compound, respectively; E_{cutoff}—cutoff energy; ΔH_{sub}—enthalpy of sublimation; ΔH_f—enthalpy of formation of binary compound; isbv—model number in SDTrimSP input files.
[a] Each component is considered unbound with regard to its density and bound with regard to the BBE (CBE assigned). The BB_0 model is the original Hofsäss & Stegmaier (2022) model. The HB model is only used to demonstrate the effect of density independent of the hybrid binding energy model.
[b] For O, ΔH_{sub} is neglected and only CBE is used as a BBE, if any.

2.2.1. SB: Surface Binding Model

The surface binding (SB) model is the default calculation model for TRIM and SDTrimSP. In this approach, a particle may leave the sample only if its kinetic energy exceeds the SBE. Energy loss within the sample occurs through elastic energy transfer during collisions and inelastic electronic losses.

Although the SBE is an energy determined by the attractive forces of neighboring atoms (Sigmund 1969; Gades & Urbassek 1992), it is common practice to approximate the SBE as the atomic enthalpy of sublimation (ΔH_S). The exception are gases where the SBEs are based on the enthalpy of dissociation. For example, pure O does not form a solid, and therefore the dissociation enthalpy of oxygen $\Delta H_{diss}(O_2)$ is used instead of the sublimation enthalpy. Hobler and Morrissey showed for Si and Na that the atomic enthalpy of sublimation can severely underestimate the energy necessary to remove an atom from their crystalline structure (Hobler 2013; Morrissey et al. 2022). This was determined by the means of MD calculations, which take into account the bonds between atoms. The results have so far only been tentatively confirmed for nepheline ($NaAlSiO_4$; Martinez et al. 2017) where the sputtered secondary Na^+ ions express a peak in their energy distribution around 2.4 eV, which was attributed to an SBE of Na of 4.8 eV (Morrissey et al. 2022). This exceeds the tabulated value of 1.1 eV by a factor of 4.3. Interestingly, the secondary K^+ ion results of Martinez et al. (2017) would suggest K SBEs of 4 eV, also exceeding the tabulated value of 0.93 eV by the same factor. Morrissey et al. (2022) also found that within plagioclase—the primary Na-bearing mineral on a planetary surface—the SBE is increased to 7.9 eV in the Na end member albite ($NaAlSi_3O_8$), which would result in a reduction of the Na sputter yield from albite by a factor of 15. The MD results therefore show a positive correlation between SBE and Na coordination number (amount of neighboring atoms).

How the SBE of a damaged surface or, as outlined by Hofsäss & Stegmaier (2022), a nonnormal orientation of a mineral unit cell would differ from the ideal conditions chosen in MD simulations is unclear. Furthermore, the energy distributions of secondary ions do not necessarily represent their neutral counterparts, as neutralization of ejected particles is energy dependent, which can cause a significant offset of the ion distribution toward lower energies (Benninghoven et al. 1987; Van der Heide 2014). Another example that adds to the uncertainty of the link between neutral and ion energy distributions is from Betz (1987), who showed that ground-state Ba sputtered from a continuously oxidized Ba surface coincides with metastable Ba (originating from the decay of short-lived, excited-state Ba) and Ba ions from a nonoxidized surface. Ground-state Ba from a nonoxidized surface expresses a significantly lower peak energy that can be related to the ΔH_S. The energy distributions of ions, metastable atoms, and ground-state atoms coincide with each other and exceed ΔH_S. The larger energy of ions and metastable atoms are interpreted to be caused by matrix-dependent ionization processes (e.g., Dukes & Baragiola 2015), whereas the increased energy of the sputtered ground-state atoms from an oxidized sample is so far not well understood and depends on the procedure including a single initial oxidation or, as in Betz (1987), a continuous oxidation. What is certain is that the displacement and removal of atoms that would lead to changes in bonds within the sample alters coordination numbers and therefore the binding energy that has to be overcome for their removal. The interatomic potentials between the atoms in the sample would end up far from equilibrium, which is commonly neglected in MD simulations owing to computational load (Behrisch & Eckstein 2007). Lastly, Hobler (2013) compared MD and BCA results and concluded that the enthalpy of sublimation approximation works well in BCA to reproduce experimental data, even when the crystalline structure of the mineral is not taken into account. The reasoning behind this is that in MD simulations an increase of yield is tied to an increase in defect creation, which ultimately negates the effect of the higher SBEs in the MD simulation. The increased SBEs suggested by MD models are to be taken with caution, but it is established that an overall increase in energy loss within the sample is necessary to best fit experimental data.

2.2.2. BB: Bulk Binding Model

The bulk binding (BB) model was recently suggested by Hofsäss & Stegmaier (2022). It sets the SBE to zero, while setting a BBE for each component that has to be overcome for a component to be freed from their sample and that is lost during each recoil. The authors used the enthalpy of sublimation (E_s) for single-species samples (i.e., the tabulated values used as SBEs in the SB model). For binary compounds, such as oxides and sulfides in minerals, the enthalpy of formation (ΔH_f) has to

be overcome before the enthalpy of sublimation of each component, thereby increasing the energy loss in the sample (as suggested earlier by Dullni 1984).

In SDTrimSP, the implementation of the BB model is similar but slightly different. The sublimation enthalpy of species that form gases under standard conditions is neglected when determining E_{bulk} (Table 2). This is based on the assumption that, e.g., O from breaking up SiO_2 will already be in its gaseous state and thus will not be required to be sublimated, unlike Si. As an example, E_{bulk} (or BBEs) for the elements in the binary compound SiO_2 are, as implemented in SDTrimSP,

$$\begin{aligned} E_{\mathrm{bulk}}(\mathrm{Si}) &= E_s(\mathrm{Si}) + \frac{\Delta H_f(\mathrm{SiO_2})}{m+n} \\ &= 4.664\ \mathrm{eV} + \frac{9.441\ \mathrm{eV}}{3} = 7.701\ \mathrm{eV} \\ E_{\mathrm{bulk}}(\mathrm{O}) &= \frac{\Delta H_f(\mathrm{SiO_2})}{m+n} \\ &= \frac{9.441\ \mathrm{eV}}{3} = 3.147\ \mathrm{eV}, \end{aligned} \tag{1}$$

with m and n being the number of components Si and O in the compound (Si_mO_n). In SDTrimSP, this model is implemented as the SB model eight (isbv = 8), which is only available when using the new density model introduced in Section 2.4.2.

A side effect of setting the SBE to zero and only using a BBE is a lack of a planar attraction potential, and therefore no refraction of sputtered particles toward larger emission angles occurs (Jackson 1975; Roth et al. 1983; Gades & Urbassek 1992; Hofsäss & Stegmaier 2022). When a surface potential has to be overcome, the extent of the refraction acting on a particle leaving the surface of a sample is proportional to the ratio of the energy of the particle in relation to the potential that has to be overcome (Thompson 1968; Sigmund 1969):

$$\sin(\theta_1) = \sqrt{\frac{E_0}{E_0 - E_{\mathrm{sbe}}}}\,\sin(\theta_0), \tag{2}$$

with the incident energy E_0, the SBE E_{sbe}, the angle of the atom crossing the surface barrier θ_1, and the initial incident angle of the atom θ_0. Instead, in the BB model, any released particle inside the compound can travel freely through the surface, independent of its energy.

In BCA computations, a cutoff energy (E_{cutoff}) for each species is set that determines when a recoil is considered to be "at rest" and no longer causes collisions. In the SB model, E_{cutoff} is chosen to be 0.1 eV below the lowest, nonzero E_s of all species within the sample. Choosing a lower E_{cutoff} would increase computation times owing to the impactor traveling deeper into the sample before it is considered at rest. In the context of this work, longer impactor paths are irrelevant because recoils that are below E_{cutoff} do not contribute to the sputter yield. Any recoil from within the sample needs to exceed the SBE to leave the compound with an energy E_{ejecta} of

$$E_{\mathrm{ejecta}} = E_{\mathrm{recoil}} - \mathrm{SBE}. \tag{3}$$

This explains why the E_{cutoff} should not be chosen to exceed the SBE of any given component. A recoil of a relatively heavy species that is too slow to overcome the SBE is still capable of causing recoils of lighter species with kinetic energies exceeding their SBE.

For the BB model, however, the BBE is subtracted at each collision, after which recoils can leave the sample without further change of their energy. This energy can therefore be arbitrarily small and has to be limited by the cutoff energy for convergence. With the cutoff, E_{ejecta} cannot be inferior to the cutoff energy E_{cutoff},

$$E_{\mathrm{ejecta}} \geqslant E_{\mathrm{cutoff}}. \tag{4}$$

The suggested approach by Hofsäss & Stegmaier (2022) to obtain the best results to reproduce experimental data is to set a cutoff energy (E_{cutoff}) in the BB model that lies between $1/2$ and $1/8.5$ of the atomic E_s (the authors thereby favor a factor of $1/3$, which is also the default set for BB models in SDTrimSP). The effect of the absence of an SBE and the use of a BBE and E_{cutoff} on the energy distribution of the sputtered particles is evident, as the lower energetic tail of sputtered atoms is cut off at the given E_{cutoff}, and no Thompson distribution (Thompson 1968) is seen (Figure 1). For the example of SiO_2, we obtain

$$\begin{aligned} E_{\mathrm{cutoff}}(\mathrm{O}) &= \frac{E_s(\mathrm{O})}{3} = 0.861\ \mathrm{eV} \\ E_{\mathrm{cutoff}}(\mathrm{Si}) &= \frac{E_s(\mathrm{Si})}{3} = 1.555\ \mathrm{eV}. \end{aligned} \tag{5}$$

2.3. HB: New Hybrid Binding Energy Model

The planar potential on the surface is an issue, as its strength needs to exceed atomic enthalpies of sublimation to properly reproduce experimental data. The presence of such a surface potential is, however, supported by previous energy distribution measurements (Betz & Wien 1994; Samartsev & Wucher 2006; Martinez et al. 2017). Furthermore, metals covered by a layer of O_2 express energy peak broadening and a slight shift to larger energies (Dullni 1984; Wucher & Oechsner 1986, 1988). The energy distribution of the BB model is thus only fitting to sputtering of binary metal compounds where monotonously decreasing energy distributions were observed with peak energies close to zero (Szymoński 1981). In oxide-bearing minerals we would thus expect a behavior where the energy distribution is affected proportionally with the amount of available O. Neither the SB nor the BB model is capable of taking this into account, which demands a new model.

We introduce a hybrid binding energy model (HB) that uses the element enthalpy of sublimation as SBE and the enthalpy of formation for compounds as BBE. The energies thus represent a surface potential that has to be overcome and the bonds within the sample, which have to first be broken up before an atom is mobilized. The model is based purely on tabulated data, just like the BB model of Hofsäss & Stegmaier (2022) but without the need of a specific E_{cutoff} to best reproduce sputter yields and energy distributions. It therefore poses a promising alternative to the previous approaches for obtaining increased binding energies.

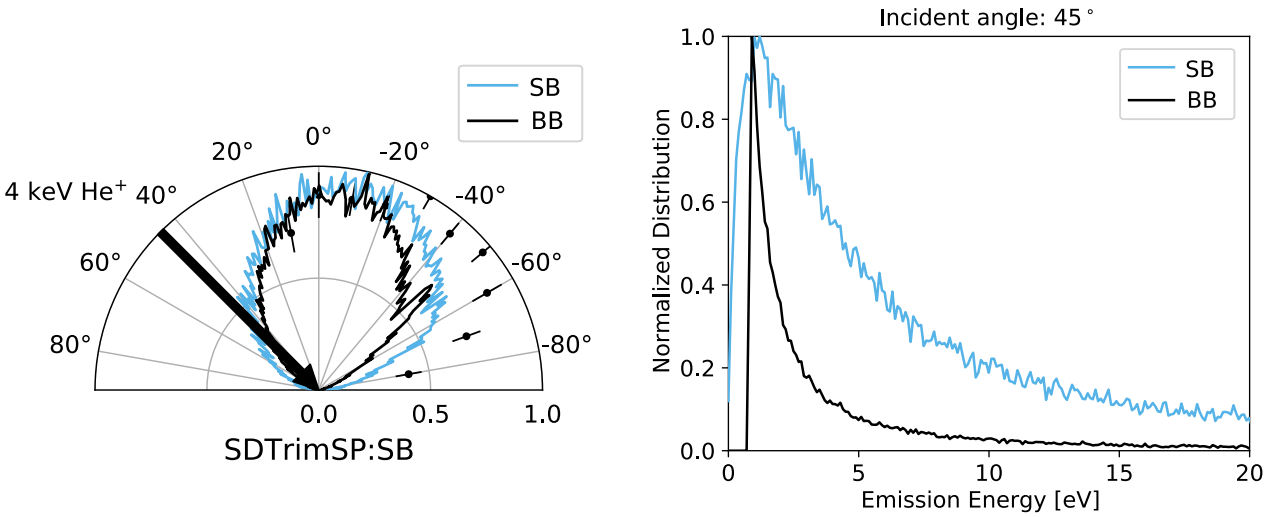

Figure 1. Model comparison for angular distributions of total sputtered mass yield (left) and energy distribution of sputtered O (right) from irradiated enstatite ($MgSiO_3$) for impinging He ions at an incident angle of 45° and energy of 4 keV. The BB model (black line) is based on the pure BBE assumption, where a lack of an SBE prevents scattering of the particles toward the surface, resulting in ejecta being preferentially emitted toward the surface normal. The energy distribution of the BB model does not express the characteristic Thompson distribution but instead shows a monotonously decreasing distribution, starting at the element-specific cutoff energy of $\Delta H_s/3$. The SB model (light-blue line) shown for comparison is calculated with an SBE instead of the BBE. The experimental data are from thin-film irradiation (Biber et al. 2022) and normalized to $y_{max} = 1$ with an error of one standard deviation.

As an example, the SBE and BBE for the binary compound SiO_2 result in

$$\begin{aligned} E_{\rm surf}({\rm Si}) &= E_s({\rm Si}) = 4.664\ {\rm eV} \\ E_{\rm bulk}({\rm Si}) &= \frac{\Delta H_f({\rm SiO_2})}{m+n} \\ &= \frac{9.441\ {\rm eV}}{3} = 3.147\ {\rm eV} \\ E_{\rm surf}({\rm O}) &= \frac{\Delta H_{\rm diss}({\rm O_2})}{2} = 2.582\ {\rm eV} \\ E_{\rm bulk}({\rm O}) &= \frac{\Delta H_f({\rm SiO_2})}{m+n} \\ &= \frac{9.441\ {\rm eV}}{3} = 3.147\ {\rm eV}. \end{aligned} \quad (6)$$

The BBEs that are determined from binary compounds only hold as long as we assume that each element remains bound over the course of irradiation. This is naturally not the case and led in consequence to the implementation of a more sophisticated compound model.

2.4. New Compound Model

We propose a simple model for sample compositions that serves two purposes. It allows discrimination between chemically bound atoms and "free" atoms (not chemically bound), and it allows us to use data of compounds (i.e., oxides and sulfides) to adequately approximate realistic mass densities of minerals. The simulation names using this compound model to differentiate between bound and unbound atoms, as well as density, are labeled by "-C" (HB-C, for the combination of compound and hybrid model; Table 2).

2.4.1. Discriminate between Bound and Free Atoms

Instead of using single atoms, the starting condition considers each atom to be bound to its respective compound —for example, Si and O are bound in SiO_2. If a recoil occurs with sufficient energy to overcome the BBE, the bound atom is unbound. The atomic species produced by breaking up compounds no longer have a chemical binding energy (BBE = 0; Table 2). If the remaining energy after the collision is large enough, the target atom can move through the sample. The atom then either comes to a halt and attempts to re-form a bond or is ejected. To prevent a major accumulation of atomic species, free atoms react to form the initially set compounds again whenever possible. In the current SDTrimSP implementation, the compound with the highest formation enthalpy is prioritized to re-form given the available O. This has the desired effect that oxygen is unlikely to ever exist as a free atom. In SDTrimSP, the compound hybrid model is implemented as the SB model four (isbv = 4). In the noncompound models BB and HB, each component within the sample has a fixed BBE owing to the atomic model not being capable of differentiating bound from free components (Table 2). They therefore do not behave identically to their compound counterparts (BB-C and HB-C), which causes major differences especially between the HB and HB-C energy and angular distributions (Section 3).

2.4.2. Set Atomic Density with Compounds

It was found that the best-fitting models to sputter yields for mineral require not only an increase in binding energy (as already hinted at in, e.g., Dullni 1984) but also an accurate model that reflects realistic material properties, including the atomic density (e.g., Szabo et al. 2020a). The default way of determining densities in SDTrimSP and TRIM is by using tabulated data of atomic species. In Szabo et al. (2020a), the authors follow Möller & Posselt (2001) and calculate a density for wollastonite ($CaSiO_3$) based on tabulated atomic densities, which results in 0.0376 atoms $Å^{-3}$. Increasing the density of oxygen ρ_O to 0.7 atoms $Å^{-3}$ (from an initial 0.04 $Å^{-3}$) leads to a bulk density more akin to the wollastonite density of

0.07412 atoms $Å^{-3}$, corresponding to 2.86 g cm^{-3}. This value for ρ_O exceeds the typical atomic density by over an order of magnitude. Therefore, in dynamical modeling removal of oxygen causes disproportionate changes to the surface density of the compound compared to removing any other element. To prevent this, we propose calculating mineral densities based on the tabulated atomic densities of compounds, which are simplified building blocks of minerals.

In SDTrimSP, the density of each layer of the sample is calculated based on the density of its components with

$$\rho = \left(\sum_{1}^{n} \frac{X_n}{\rho_n} \right)^{-1}, \tag{7}$$

where ρ is the density of the sample, X_n the atomic fraction, and ρ_n the density of the nth component.

The atomic densities and atomic fractions define the bulk density, and therefore the mean free path between two atoms in the sample. The mean free path μ is formulated in SDTrimSP as

$$\mu = \rho^{-1/3}. \tag{8}$$

In BCA simulations such as SDTrimSP, an ion traveling through the sample will gradually lose its energy through nuclear and electronic interactions, which influence its motion (e.g., Eckstein 1991). After the impinging ion has traveled the distance μ, a collision occurs (Eckstein 1991; Mutzke et al. 2019). High-density samples have small μ, and more energy is conserved between two collisions as the effect of electronic stopping is reduced.

Another effect of density is the distance between the atoms, and therefore it has an influence on the transferable energy during a collision. This energy is inversely proportional to the distance between the projectile and the center of the particle at rest. The farthest distance at which a collision occurs is the maximal impact parameter, where energy transfer is at its minimum

$$p_{\max} = \mu (2\pi)^{-1/2}. \tag{9}$$

With smaller μ, the minimum transferable energy becomes larger as the spacing between the atoms, and therefore the mean impact parameter, decreases. Higher densities therefore reduce the amount of low-energetic sputtered particles through recoils and lower the number of recoils as the energy is lost more quickly.

Mineral densities and calculated mean free paths of relevant rock-forming minerals are shown in Table 1. As an example, for enstatite ($\rho_{En} \sim 3.20$ g cm^{-3}), the default atomic model would result in

$$\begin{aligned} \rho_{En} &= \left(\frac{X_{Mg}}{\rho_{Mg}} + \frac{X_{Si}}{\rho_{Si}} + \frac{X_O}{\rho_O} \right)^{-1} \\ \rho_{En} &= \left(\frac{0.2}{0.0431} + \frac{0.2}{0.0499} + \frac{0.6}{0.0429} \right)^{-1} \text{ at } A^{-3} \\ &= 0.0442 \text{ at} A^{-3} \\ &= 1.47 \text{ g} cm^{-3}, \end{aligned} \tag{10}$$

whereas the compound model, using tabulated data for elements, results in

$$\begin{aligned} \rho_{En} &= \left(\frac{X_{MgO}}{\rho_{MgO}} + \frac{X_{SiO2}}{\rho_{SiO2}} \right)^{-1} \\ \rho_{En} &= \left(\frac{0.5}{0.1070} + \frac{0.5}{0.0797} \right)^{-1} \text{ at } A^{-3} \\ &= 0.0913 \text{ at} A^{-3} \\ &= 3.05 \text{ g} cm^{-3}. \end{aligned} \tag{11}$$

This example and the results in Table 1 demonstrate how using compound data recreates realistic mineral densities and, as a result, the mean free path within a sample well. Table 1 also shows that densities can be approximated without any manual adjustments compared to the default atomic model. Together with the hybrid binding energy model, it poses the first step in properly approximating oxides and oxide-derived minerals in Monte Carlo BCA codes such as SDTrimSP.

2.5. Fitting the Simulated Data

The modeled sputter yield by element and mass is fitted using an Eckstein fit based on the Yamamura et al. (1983) formula (Eckstein & Preuss 2003):

$$\begin{aligned} Y(\alpha) = Y(0) &\left\{ \cos\left[\left(\frac{\alpha}{\alpha_0} \frac{\pi}{2} \right)^c \right] \right\}^{-f} \\ &\times \exp\left\{ b \left(1 - 1 \Big/ \cos\left[\left(\frac{\alpha}{\alpha_0} \frac{\pi}{2} \right)^c \right] \right) \right\}, \end{aligned} \tag{12}$$

with the fitting parameters b, c, and f and the angle of incidence α. The value for α_0 is chosen as $\pi/2$ instead of being calculated by

$$\alpha_0 = \pi - \arccos \sqrt{\frac{1}{1 + E_0/E_{sp}}} \geqslant \frac{\pi}{2}, \tag{13}$$

because the projectile binding energy E_{sp} would be required or assumed, and for the typical solar wind energies E_0 in keV range with E_{sp} in the eV range, this would cause only minor deviations from $\alpha_0 = \pi/2$.

For the angular distribution of sputtered particles, the data are fitted using an adapted cosine fit function after Hofsäss & Stegmaier (2022) to take the nonsymmetrical nature of sputtered particles into account. The system of equations is as follows:

$$f(\phi) \begin{cases} A \cos^m \left(\frac{\pi}{2} \left(\frac{\pi + 2\phi}{\pi + 2\phi_{tilt}} - 1 \right) \right) & \phi \leqslant \phi_{tilt} \\ A \cos^n \left(\frac{\pi}{2} \left(1 - \frac{\pi - 2\phi}{\pi - 2\phi_{tilt}} \right) \right) & \phi \geqslant \phi_{tilt}, \end{cases} \tag{14}$$

with the scaling factor A, the tilt angle ϕ_{tilt}, the exponents m and n, and the angle ϕ.

The energy distribution data are fitted using a Thompson distribution (Thompson 1968),

$$f(E) = S \frac{E}{(E + E_0)^3}, \tag{15}$$

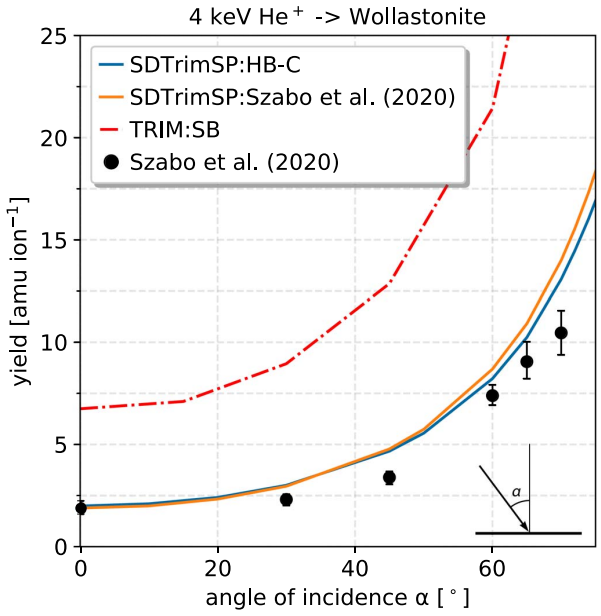

Figure 2. The agreement of the initial approach used to fit the experimental data (Szabo et al. 2020a) with the HB-C model is shown, including TRIM model results (Biersack & Eckstein 1984). The abbreviations are as follows: HB—surface binding energy (SBE) based on heat of sublimation and BBE on enthalpy of formation; C—densities calculated based on compound densities and differentiation between unbound and bound species. Szabo et al. (2020a) used an averaged SBE of all components after increasing the O_{SBE} to 6.5 eV. To reach the proper wollastonite density, they increased the O atomic density accordingly.

with a scaling factor S, the energy removed from the sputtered atom before it escapes the surface E_0 (approximately SBE, when considering a pure SB model) and the energy of the sputtered atom E. The energy peak is located at $E \approx E_0/2$.

3. Results

The validity of any new suggested model can ultimately only be verified through experimental data focusing on speciation of the sputtered material, as well as its angular and energy distribution. For now, we can only compare experimental sputter yield data in mass per impinging ion (amu/ion) and their angular distribution with model outputs. The composition of the modeled yield is stoichiometric. Lighter species are initially sputtered in an overstoichiometric way. With fluence and decreasing abundance of light species, the sputter yield composition approaches the initial sample stoichiometry, which evidently will not correspond to the sample surface composition in equilibrium. We know that the laboratory data correspond to fluences where this irradiation equilibrium is reached. For the scope of this work, we assume that the laboratory yield composition is indeed stoichiometric.

3.1. HB-C Model and Experimental Data

We first present the capabilities of the newly implemented hybrid binding energy model, which includes the compound model (HB-C). The results of the Szabo et al. (2020a) approach and the HB-C model are thereby largely identical when it comes to mass yields and recreate the experimental data reasonably well (Figure 2). The largest discrepancies lie in both the angular and energy distributions. A high SBE increases the refraction that occurs on the surface and therefore increases the spread of the angular distribution. We show this behavior in Figure 3, where the Szabo et al. (2020a) approach—with the highest SBEs of all model results shown in this work—leads to the largest tilt angle (27° at an angle of incidence of 45°) with the broadest angular distribution of all models (exponents $m = 4.9$ and $n = 1.4$ for He^+ on wollastonite). The homogeneous, atom-insensitive energy distribution of the Szabo et al. (2020a) approach is the consequence of using an identical SBE for each species (Figure 3).

3.2. All Model Comparison

In Figure 4 we compare the HB-C model with other models in relation to the experimental sputter yield data of wollastonite and enstatite. It is apparent that we find the experimental data lying between the HB-C model and the HB model. The latter thereby does not differentiate between bound and unbound species in the sample. Most relevant is that the experimental data are recreated using the HB-C model at normal incidence and close to normal incidence (<45°).

3.2.1. Angular Distributions

We compare to experimental angular distributions of Biber et al. (2022) with modeled data of enstatite in Figure 5. The largest agreement with experimental data is with the HB model, which expresses the strongest degree of forward sputtering (largest tilt angle) owing to the high binding energy of each species in the sample. The cases with lower or no BBE—this includes the unbound species within the HB-C model—clearly show a drastically reduced degree of forward sputtering compared to the HB model. Angular distribution data of TRIM are not shown, as it expresses distributions even narrower than the BB model (Figure 1 Hofsäss & Stegmaier 2022).

3.2.2. Energy Distributions

Although no experimental data exist for the irradiated enstatite, we present the modeled energy distributions of the sputter ejecta in Figure 6. The SB and SB-C models show a nearly identical energy distribution, while the HB and HB-C models express a smaller amount of low-energy particles and thus broader peaks. The more prominent, high-energy tail of sputtered particles in the HB model is due to the species experiencing large BBEs at any degree of applied fluence. In comparison, the compound model (HB-C) can build up free Mg that are consecutively sputtered without having to overcome a BBE. This in return increases the number of low-energy Mg in the energy distribution, which lies closer to the SB-C model. This is manifested in the Mg energy distribution peaking at 0.9 eV in the HB-C model compared to the 0.6 eV in the SB models and the 1.8 eV in the HB model.

4. Discussion

4.1. Sputter Yield

We were able to confirm that it is of utmost importance to properly set the density of the irradiated sample. It is evident in Figure 4 that under normal incidence the HB-C model that recreates the mineral density adequately fits the experimental data best for both H^+ and He^+ irradiation results.

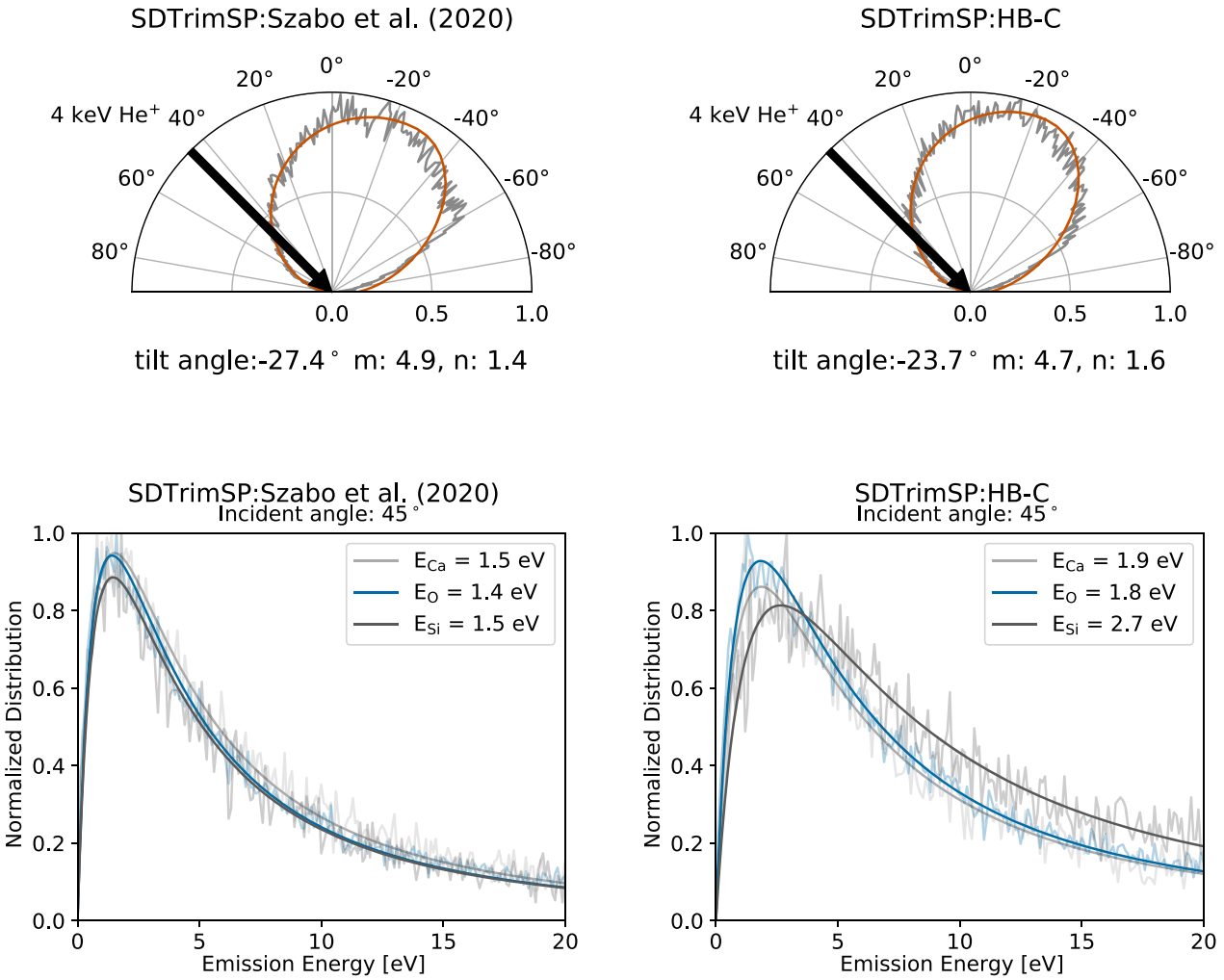

Figure 3. Modeled angular distribution of total sputter yield (data in gray, fit in orange) and energy distributions of sputter ejecta. The energy in the legend corresponds to the peak energy of the Thompson fit function, from wollastonite irradiated by 4 keV He^+. Szabo et al. (2020a) increased the O surface binding energy (SBE) to 6.5 eV, averaged SBEs for all elements, and increased O density to reach initial wollastonite density. The large surface binding energy causes a high degree of surface scattering of the ejected particles, whereas the averaging of the binding energies leads to an identical energy distribution for all species. The HB-C model uses both SBE and bulk binding energy to achieve an increase in binding energy while reliably reproducing mineral densities based on oxide compound data and differentiating between compound-bound and unbound atoms.

The experimental data of the H-irradiated wollastonite thin film express a significant deviation from SDTrimSP predictions for the flat surface sputter behavior. This could so far not be explained (Szabo et al. 2018). Nevertheless, all the experimental data in Figure 4 show good agreement with the HB-C model close to normal incidence and up to at least 45°. This is relevant for approximating irradiation of realistic, rough surfaces because yield enhancements between a flat and rough surface are generally small for incidence angles below 45° (Küstner et al. 1998; Biber et al. 2022). This is not due to impacts realistically occurring at normal incidence in nature, but due to surface roughness leading to locally reduced incidence angles for shallow impinging ions and therefore flattened mass yield distributions. This is discussed in Biber et al. (2022) for enstatite irradiation experiments and was previously shown for rough Bo and Be surfaces (Gauthier et al. 1990; Roth et al. 1991; Küstner et al. 1999).

4.2. Angular Distribution

We observed that no model can completely recreate the large polar tilt angle seen in experimental data (Figure 5). The model that comes closest is the HB model, which boasts large BBEs, subsequently leading to a rapid loss of energy with each recoil. The increased binding energy thus negatively affects the collision kinematics of long collision cascades and gives primary-knock-on collisions (i.e., Figure 2.6 in Behrisch & Wittmaack 1991) a higher significance in the angular distribution of sputtered material. More random ejecta from long collision cascades that would lead to ejecta distributions close to normal are reduced. As a consequence, the tilt of the angular distribution increases. This behavior has also been observed on binary alloys, both experimentally and through MD simulations. There, atoms sputtered from the second atomic layer form angular distributions toward the surface normal, whereas first-layer-emitted atoms have a broad

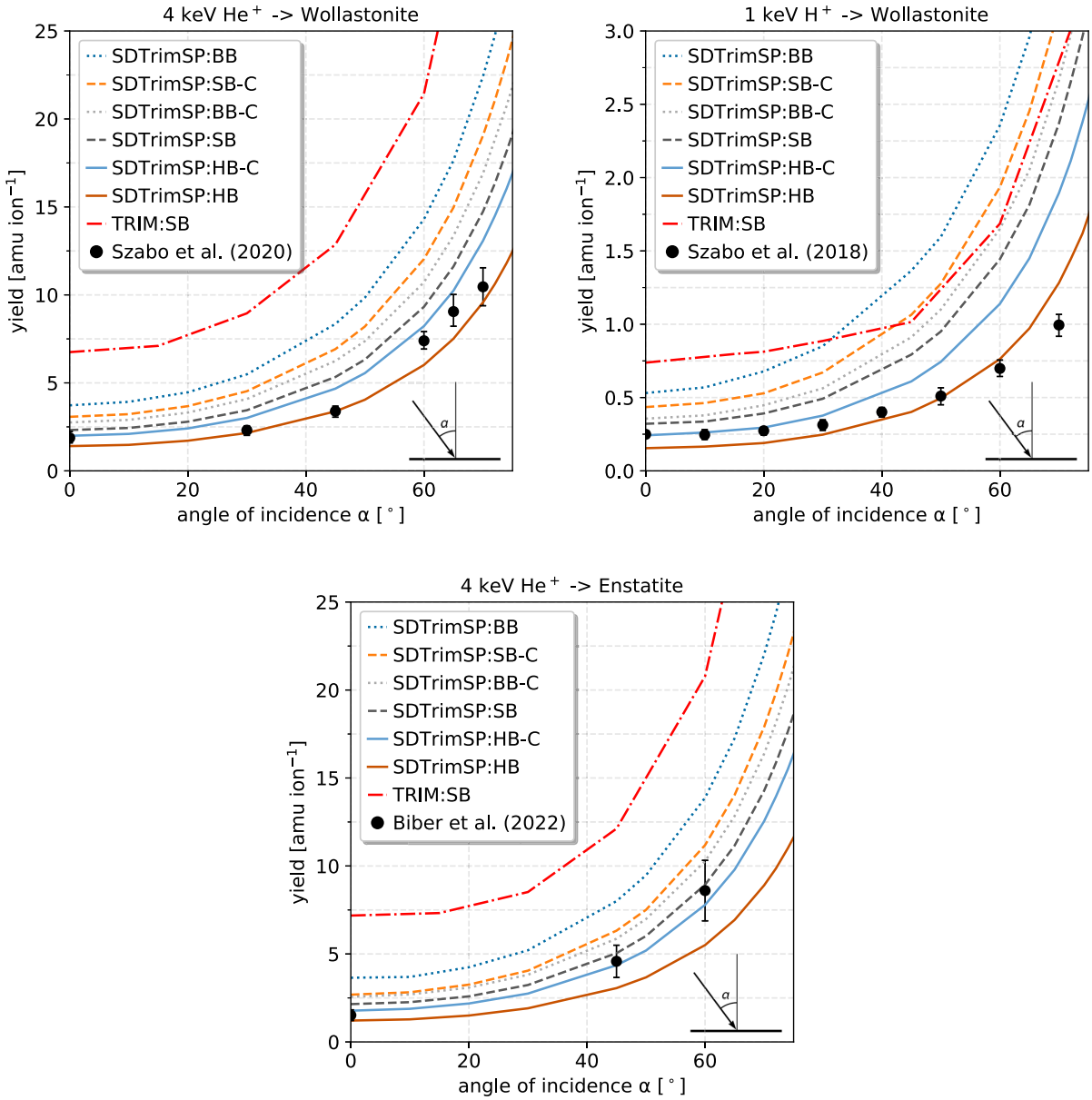

Figure 4. SDTrimSP model results compared to TRIM model results (red dashed–dotted line; Biersack & Eckstein 1984) and experimental data by Szabo et al. (2018; H^+ on wollastonite), Szabo et al. (2020a; He^+ on wollastonite) and Biber et al. (2022; He^+ on enstatite). Near-ideal mineral densities are obtained in models taking compounds (-C) into account, whereas the atomic cases represent lower densities, about a factor two below compound derived densities. Abbreviations and line styles are as follows: SB—dashed lines, tabulated enthalpy of sublimation as element surface binding energies; BB—dotted lines, tabulated enthalpy of sublimation as element bulk binding energies; HB—solid lines, tabulated enthalpy of formation as bulk binding energy and enthalpy of sublimation as surface binding energies; C—densities calculated based on compound densities and differentiation between compound-bound and unbound atoms.

distribution (Schwebel et al. 1987; Whitaker et al. 1993; Gnaser 1999). In all but the HB and HB-C models, components with low BBEs (if any) exist at the irradiation equilibrium. Energy loss within the sample is therefore less significant, which reduces the contribution of first-layer-emitted atoms and causes a near-circular plume of ejecta closer to the surface normal.

The width of the angular distribution, quantified in the cosine fit exponents (m and n; Figure 5), is also tied to the SBE. In all modeling approaches but the ones from Szabo et al. (2020a) and Hofsäss & Stegmaier (2022) the used SBEs are identical, and therefore the exponents are comparable. The BB model is narrowest (no surface potential, no refraction) and results in the lowest tilt angle with a visible forward-sputter contribution that is not able to significantly affect the tilt of the distribution. Both the HB-C model and especially the HB model lead to a larger tilt due to preventing randomly distributed, low-energy particles from leaving the surface and thus favoring forward-facing ejecta, which are observed as a peak around −60°. Toward increasing incident angles relative to the surface

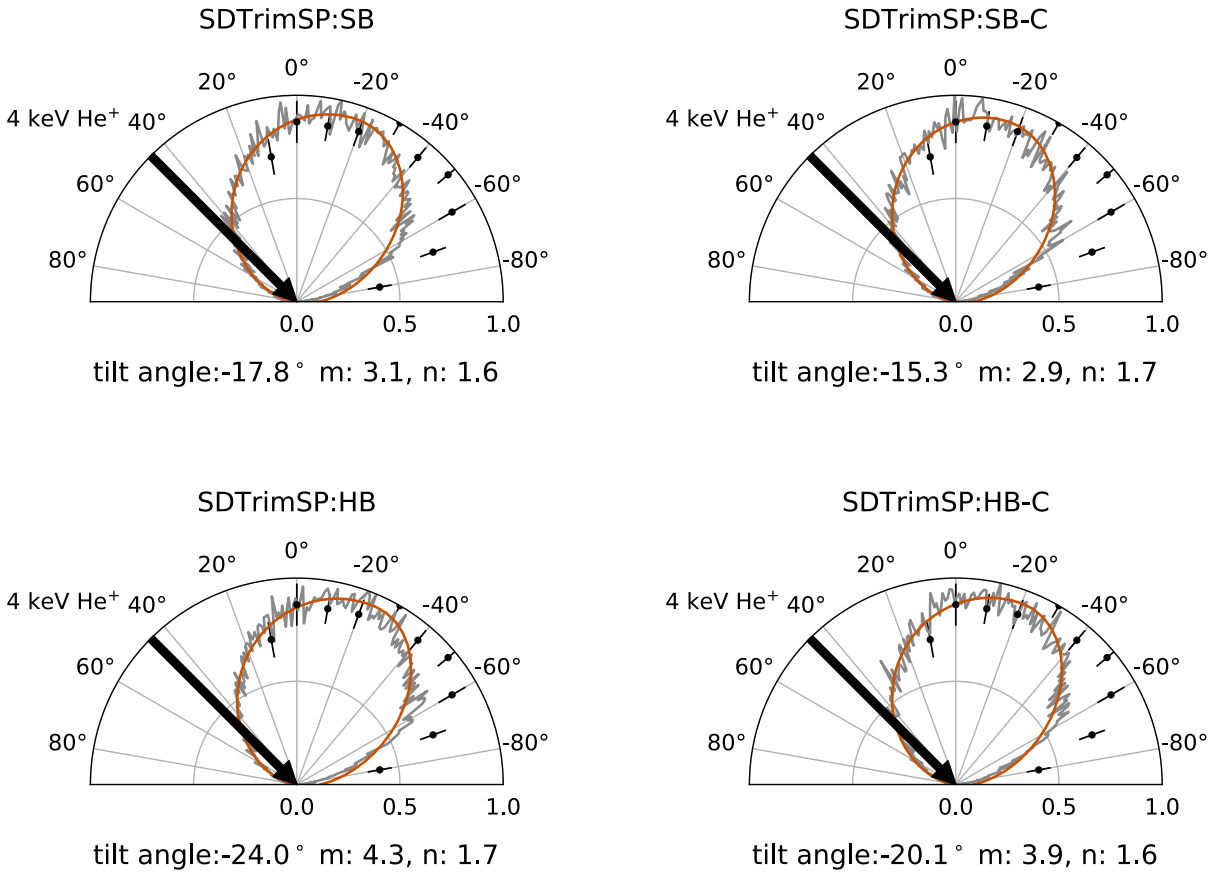

Figure 5. Polar angular distributions of total sputter yields from enstatite irradiated with 4 keV He^+ at an angle of 45° based on different model assumptions. The larger density prescribed by the compound model leads to a slightly more narrow angular distribution—seen in the smaller m fit exponents of 2.9 and 3.9 of the cosine fit—when compared to the atomic model m exponents of 3.1 and 4.3, respectively. If elements become unbound with irradiation (HB-C model), the effect of a BBE on the tilt angle is small compared to the SB model (+2.°3). If elements remain bound and experience a constant BBE and SBE (HB model), forward sputtering is more prominent (SB model tilt +6.°2). Abbreviations: SB–tabulated enthalpy of sublimation as element surface binding energies; HB—tabulated enthalpy of formation as BBE and enthalpy of sublimation as surface binding energies; C—densities calculated based on compound densities and differentiation between compound-bound and unbound atoms. Experimental data from thin-film irradiation (Biber et al. 2022) are normalized to y_{max}=1 with an error of one standard deviation.

normal (>45°, not shown), the number of single knock-on recoils increases independent of the chosen model, enhancing the peak size of the forward-aligned ejecta. Local shallow incident angles are unlikely to contribute to sputtering of a realistic, rough and/or porous sample. This is motivated by the strong sputter yield decrease observed at shallow incidence, which is related to processes of shadowing and redeposition (Küstner et al. 1999; Cupak et al. 2021; Szabo et al. 2022a; Biber et al. 2022). For this reason, the forward-facing peak at shallow incidence angles is not expected to be present for sputtering of regolith. Furthermore, the contribution to the total sputtered particles is negligible for nonshallow incident angles.

The sample roughness could in theory be another cause for the discrepancy between model and experimental data. The surface of the enstatite glassy thin film was analyzed using an atomic force microscope, and its roughness was deemed negligible (Biber et al. 2022). Furthermore, when compared to the angular distribution of a rougher surface, the thin-film angular distribution is nearly identical when normalized (Figures 2 and 3 in Biber et al. 2022). Roughness is therefore unlikely to account for the discrepancy seen in Figure 5.

4.3. Energy Distribution

Energy distributions of particles from SB models follow Thompson distributions with peak energies close to 1/2 of the SBEs used. The HB model, however, reaches peak energies that are approximately equal to the SBEs used (E_s(Mg) = 1.5, E_s(O) = 2.6, and E_s(Si) = 4.7), and the HB-C model shows elevated energies that are closer to SBE/2. At constant SBEs, the peaks of the energy distribution are widened with increasing BBEs (Figure 6). Models that include a BBE experience a shift toward larger energies with a broadening of the energy distribution, as low-energy particles are not reflected back into the sample. This behavior follows the O_2-covered metal irradiation experiments performed by Dullni (1984), Wucher & Oechsner (1986), and Wucher & Oechsner (1988). Therefore, the peak energies of the energy distributions, fitted by Thompson distributions, do not correspond to the enthalpy of sublimation ΔH_s of the atomic species, but rather the combination of enthalpy of formation ΔH_f of the oxide present with ΔH_s (Figure 3 in Dullni 1984). The expected energy distribution broadening in a system where O_2 is present is thus recreated by both the HB and HB-C models with the same

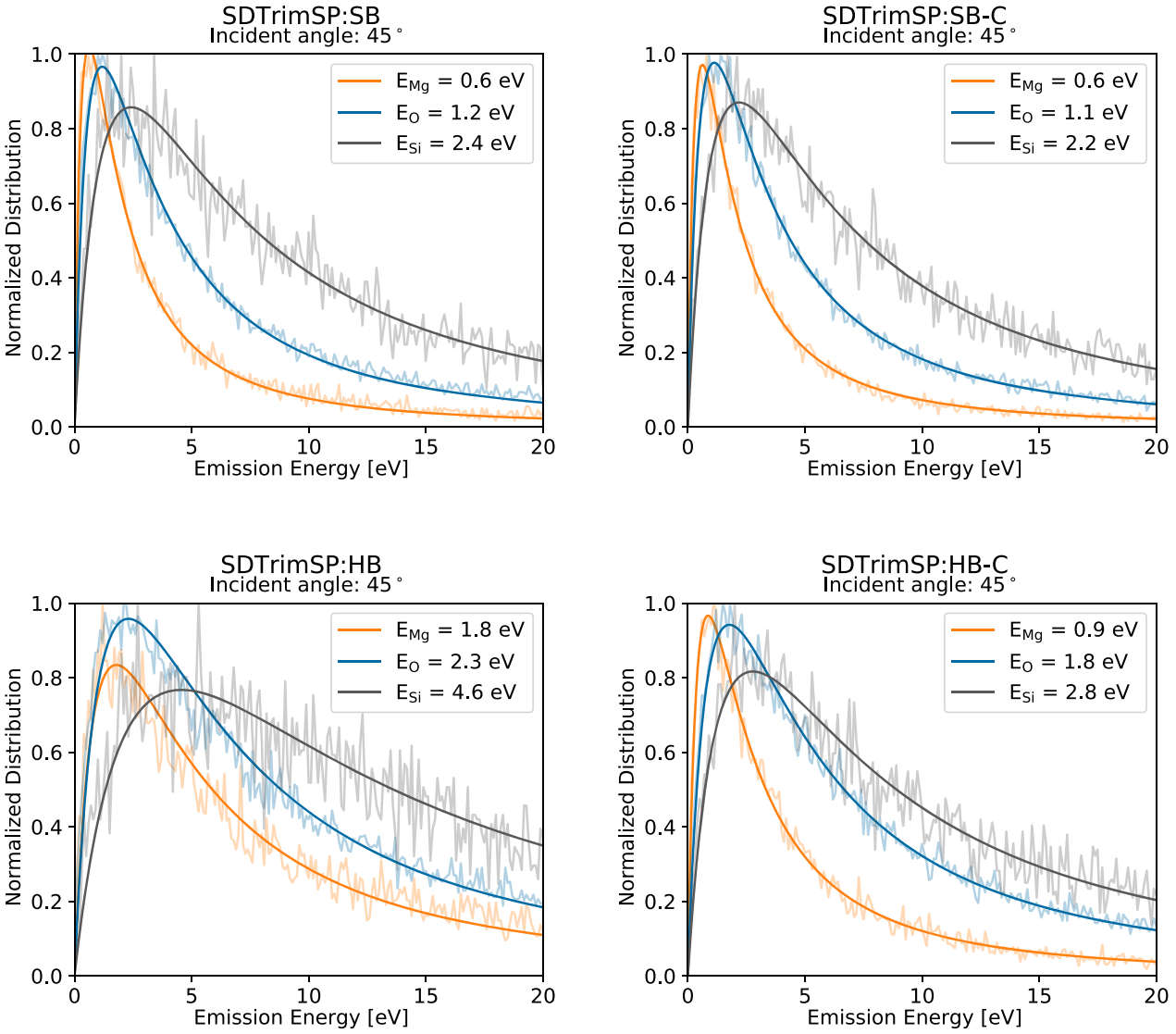

Figure 6. Energy distributions of sputtered elements from enstatite irradiated with 4 keV He^+ at an angle of 45° based on different model assumptions. The energy in the legend corresponds to the peak energy of the Thompson fit function. Abbreviations: SBE—tabulated enthalpy of sublimation as element SBEs; HB—tabulated enthalpy of formation as BBE and enthalpy of sublimation as SBEs; C—densities calculated based on compound densities and differentiation between compound-bound and unbound atoms.

underlying assumptions, making it a valuable addition to the SB and BB models, which, on the contrary, cannot recreate the broadening. The results are also reminiscent of the broadening observed by increasing SBEs as in Morrissey et al. (2022), and the conclusion is the same. Larger total binding energies lead to a larger high-energy fraction of the sputtered particles while reducing the number of ejected particles. In exospheres around solar-wind-exposed surfaces, less abundant but more energetic particles would then be detectable farther from the surface.

4.3.1. Inclusion of Intermediary Compounds

It becomes evident from Figure 6 that larger peak energies can be achieved if the atomic species remain in a bound condition. In the scope of this work we did not explore the formation of possible intermediates. The current implementation will always break up the compound, and one of the products will continue to travel through the sample. If there are enough free elements available, only the original oxide can form, and therefore the model—for the example of SiO_2—is limited to

$$SiO_2 \rightleftharpoons Si + O + O. \quad (16)$$

A more sophisticated model would need to include the following reactions:

$$SiO_2 \rightleftharpoons Si + O_2 \quad (17)$$

$$SiO_2 \rightleftharpoons SiO + O \quad (18)$$

$$SiO \rightleftharpoons Si + O \quad (19)$$

$$O_2 \rightleftharpoons O + O \quad (20)$$

$$Si_2 \rightleftharpoons Si + Si, \quad (21)$$

Table 3
Effect of an Increased Sodium Surface Binding Energy on Total Yield and Angular Distribution from Simulating 1 keV H^+ Irradiation on Albite ($NaAlSi_3O_8$)

	E_s(Na) (eV)	Y_{Na} ($10^{-3}\frac{at}{ion}$)	$\phi_{tilt}(45°)$ (deg)	m, n (unit of unity)
M22[a]	7.9	0.41	…	…
SB	7.9	0.79	34.4	5.1, 1.5
SB	1.1	1.08	16.1	3.0, 2.0
HB-C	1.1	1.10	18.9	3.9, 2.3

Notes.
[a] Computed in static mode; Y_{Na}—sodium sputter yield; E_s(Na)—SBE of sodium; $\phi_{tilt}(45°)$—angular distribution tilt angle at an ion incidence angle of 45° relative to surface normal; m, n—cosine fit exponents.
References. M22: Morrissey et al. (2022).

which would reduce the number of unbound atoms in the sample. The resulting energy distribution would thus lie closer to the hybrid model (HB), where atomic species are considered to remain bound in their compounds. To fully simulate the process of amorphization, we would need to know what drives the stability of the different products within a mineral in irradiation equilibrium.

4.4. Effect of Increased SBE

To demonstrate the effect of an increased SBE, we compared the standard SB model and the newly implemented HB-C model with the results of Morrissey et al. (2022). As of now, there are only SBEs available for Na in Na silicates with increasing coordination numbers (number of O atoms being a neighbor to Na). Therefore, we only compare the results for albite $NaAlSi_3O_8$ irradiated by 1 keV H^+ (Table 3). For a static computation in SDTRimSP of albite with increased Na binding energies of $E_s(Na) = 7.9$ eV Morrissey reported a yield of 4.12×10^{-4} Na/ion at normal incidence. If SDTrimSP is run in dynamic mode, the yield at the irradiation equilibrium is increased by a factor of two, to 7.90×10^{-4} Na/ion. If compared to the yields of the SB model (1.08×10^{-3} Na/ion) and the HB-C model (1.10×10^{-3}), the dynamic Na yields with $E_s(Na) = 7.9$ eV differ by 30%. This similarity in SB and HB-C equilibrium yield is due to free Na atoms in the HB-C model behaving identically to the Na in the BB model. Na_2O having the lowest enthalpy of formation and therefore bound Na in the HB-C model is not prioritized in forming bonds with free O, causing an accumulation of Na in the surface layer at irradiation equilibrium as a result. The increase in density and BBE that is imbued in the HB-C model therefore does not apply to Na at the irradiation equilibrium, as no surface Na_2O exists. The energy peak of the Morrissey approach ($E_s(Na) = 7.9$ eV) is, as expected, around 4 eV (approx. $SBE/2 = 7.8/2$) with the tilt angle exceeding the results of both the SB and HB-C models by a factor of two and expressing a wide distribution as given by the large fit exponents (m and n). In conclusion, the effect of increasing the SBE of Na is apparent not only in actual yields (−30%) but also in the angular and energy energy distributions.

4.5. Experiments Needed for Evaluation

Both the angular and energy distribution data of sputtered minerals depend on the chosen surface and BBEs. Extensive experiments to properly discriminate between different sputtered species, as well as obtaining the species' energy distribution, would be highly valuable for constraining surface and BBEs. Obtaining energy distributions would give a needed insight on the energy peak broadening effect occurring on minerals. If this was available, further restrictions on realistic binding energies could be enforced, whereas SBEs define the energy peak position and width and BBEs act as a "broadening agent" for further enhancing energy peak widths. As a side effect, the increasing and/or shifting of binding energies between SBE and BBE could achieve the desired forward tilt of the sputtered material while not degrading the agreement in total mass yields.

It would be pleasing, although unlikely, if experimental data of energy and angular distributions could be recreated based on solely tabulated thermodynamic data. Nevertheless, we expect SBEs to be larger than tabulated, as demonstrated for an ideal, intact crystal lattice in MD by Morrissey et al. (2022). Using one single SBE might not be appropriate to describe an altered sample, however. SBEs at various degrees of alteration would be necessary to understand the evolution of the SBE with increasing levels of amorphization. The correlation of SBE with coordination number shown by Morrissey is reminiscent of the SBE dependence on the degree of amorphization, and a similar behavior is expected for the surfaces of irradiated samples (Loeffler et al. 2009; Biber et al. 2022). One should, however, refrain from adjusting the SBE like a fit parameter to best reproduce experimental data. For now we propose the use of the HB-C model for recreating experimental mass changes, with the enthalpy of sublimation as SBE and the enthalpy of formation of the mineral-forming compounds as BBE.

5. Conclusions

We introduced a hybrid binding energy model in the BCA code SDTrimSP with an underlying compound model that combines tabulated data for SBEs, BBEs, and densities for mineral samples while differentiating between free and compound-bound components. With regard to previous modeling approaches, we offer an alternative that minimizes the number of free parameters further and well reproduces experimental data. The new compound hybrid model (HB-C) merges the pure SB and BB models while reproducing mineral properties. This includes proper mineral densities through tabulated compound data, but also combining surface and BBEs, which leads to increased energy loss within the collision cascade, causing energy peak broadening as expected in a O-dominated system (e.g., Dullni 1984).

Although the differences between the SB model and the HB-C model seem minor, the model infrastructure allows for further inclusions that are reasonable in terms of mineralogy and physics. Furthermore, comparisons with experimental sputter yields result in unprecedented agreement between 0° (normal incidence) and 45°, a range that is especially of interest for modelers that require sputter yields as inputs. The HB-C model thus convinces on the following points: (1) good agreement with existing experimental data in parameter spaces relevant to exosphere modelers; (2) corrects for underestimation of the default sample density computation based on atomic densities by using tabulated densities of compounds instead; (3) sets SBEs and BBEs based on tabulated enthalpy of sublimation and enthalpy of formation of compounds, respectively, which allows for a universal application to

minerals; (4) does not require setting parameters such as SBE, BBE, density, and cutoff energy (SB model four, isbv = 4, in SDTrimSP), therefore greatly increasing the ease of use. For the time being, the HB-C model does an exemplary job in recreating experimental sputter data while producing reasonable energy and angular distributions of ejecta.

Financial support has been provided by the Swiss National Science Foundation Fund (200021L_182771/1), the Austrian Science Fund FWF (project No. I 4101-N36), and KKKÖ (Commission for the Coordination of Fusion research in Austria at the Austrian Academy of Sciences ÖAW). The authors gratefully acknowledge support from NASA's solar system Exploration Research Virtual Institute (SSERVI) via the LEADER team, grant No. 80NSSC20M0060.

Software: SDTrimSP (Mutzke et al. 2019), TRIM (in SRIM package) (Biersack & Eckstein 1984; Ziegler et al. 2010).

Appendix
Averaging the Surface Binding Energies

If we assume, like in Szabo et al. (2020a), that the binding energy that has to be overcome is solely dependent on the number of bonds with O, called the coordination number, the SBE of any component would be a function of the O content in the sample. A way to simulate this effect of the coordination number of atoms is to assume an averaged binding energy, which is a mass balance over all species present in the compound. In SDTrimSP, this is implemented as the SB model two (isbv = 2, Mutzke et al. 2019):

$$\mathrm{SBE} = \sum q_i Es_i, \tag{A1}$$

where q_i is the concentration and Es_i is the SBE of component i. This results in a single SBE for all components and therefore the compound. This was applied in Szabo et al. (2020a) in addition to the density correction to best fit wollastonite ($CaSiO_3$) data. To illustrate this effect, let us assume an increased Es_O of 6.5 eV (Szabo et al. 2020a) and compare it to the default Es_O of 2.58247 eV. For nepheline, ($NaAlSiO_4$) this would result in an average Es of 5.03 eV for all species instead of 2.79 eV with

$$\begin{aligned} q_{\mathrm{Na}} = q_{\mathrm{Al}} = q_{\mathrm{Si}} &= 1/7 \\ q_{\mathrm{O}} &= 4/7 \\ Es_{\mathrm{Na}} &= 1.11\ \mathrm{eV} \\ Es_{\mathrm{Al}} &= 3.41\ \mathrm{eV} \\ Es_{\mathrm{Si}} &= 4.66\ \mathrm{eV} \\ Es_{\mathrm{O}} = 2.58\ \mathrm{eV} &\Rightarrow Es_{\mathrm{avg}} = 2.79\ \mathrm{eV} \\ Es_{\mathrm{O}} = 6.50\ \mathrm{eV} &\Rightarrow Es_{\mathrm{avg}} = 5.03\ \mathrm{eV}. \end{aligned} \tag{A2}$$

On first glance, this seems to work, as the suggested SBE for Na in a pristine, crystalline mineral is about 4.8 eV based on MD simulations (Morrissey et al. 2022). In the case of the major rock-forming mineral albite ($NaAlSi_2O_6$; $Es_{Na} = 8.4$ eV; Morrissey et al. 2022), the isbv = 2 approximation with $Es_O = 6.5$ eV nets an average SBE of 5.4 eV, which does not reproduce the high binding energies of Na suggested by MD. This suggests that adjusting SBEs based on a single component has its limits when it comes to simulating bond strengths of complex mineral structures.

ORCID iDs

Noah Jäggi https://orcid.org/0000-0002-2740-7965
Herbert Biber https://orcid.org/0000-0002-9854-2056
Johannes Brötzner https://orcid.org/0000-0001-9999-9528
Paul Stefan Szabo https://orcid.org/0000-0002-7478-7999
Friedrich Aumayr https://orcid.org/0000-0002-9788-0934
Peter Wurz https://orcid.org/0000-0002-2603-1169
André Galli https://orcid.org/0000-0003-2425-3793

References

Arredondo, R., Oberkofler, M., Schwarz-Selinger, T., et al. 2019, Nuclear Materials and Energy, 18, 72
Baker, D. N., Poh, G., Odstrcil, D., et al. 2013, JGRA, 118, 45
Baretzky, B., Möller, W., & Taglauer, E. 1992, Vacuu, 43, 1207
Behrisch, R., & Eckstein, W. 2007, Sputtering by Particle Bombardment: Experiments and Computer Calculations from Threshold to MeV Energies (Berlin: Springer), 507
Behrisch, R., & Wittmaack, K. 1991, Sputtering by Particle Bombardment III: Characteristics of Sputtered Particles (Berlin: Springer)
Benkhoff, J., van Casteren, J., Hayakawa, H., et al. 2010, P&SS, 58, 2
Benninghoven, A., Rudenauer, F. G., & Werner, H. W. 1987, Secondary Ion Mass Spectrometry: Basic Concepts, Instrumental Aspects, Applications and Trends (New York: Wiley)
Betz, G. 1987, NIMPB, 27, 104
Betz, G., & Wien, K. 1994, IJMSI, 140, 1
Biber, H., Brötzner, J., Jäggi, N., et al. 2022, PSJ, 3, 271
Biersack, J., & Haggmark, L. 1980, NucIM, 174, 257
Biersack, J. P., & Eckstein, W. 1984, ApPhy, 34, 73
Cassidy, T. A., Merkel, A. W., Burger, M. H., et al. 2015, Icar, 248, 547
Cupak, C., Szabo, P. S., Biber, H., et al. 2021, ApSS, 570, 151204
Deer, W. A., Howie, R. A., & Zussman, J. 1992, An Introduction to the Rock-forming Minerals (2nd ed.; Harlow: Longman Scientific & Technical)
Domingue, D. L., Chapman, C. R., Killen, R. M., et al. 2014, SSRv, 181, 121
Dukes, C., & Baragiola, R. 2015, Icar, 255, 51
Dukes, C. A., Chang, W. Y., Famá, M., & Baragiola, R. A. 2011, Icar, 212, 463
Dullni, E. 1984, NIMPB, 2, 610
Eckstein, W. 1991, Computer Simulation of Ion-solid Interactions, Vol. 10 (Berlin: Springer)
Eckstein, W., & Preuss, R. 2003, JNuM, 320, 209
Elphic, R. C., Delory, G. T., Hine, B. P., et al. 2014, SSRv, 185, 3
Fatemi, S., Poppe, A., & Barabash, S. 2020, JGRA, 125, e2019JA027706
Gades, H., & Urbassek, H. M. 1992, NIMPB, 69, 232
Gamborino, D., & Wurz, P. 2018, P&SS, 159, 97
Gauthier, E., Eckstein, W., László, J., & Roth, J. 1990, JNuM, 176, 438
Gershman, D. J., Zurbuchen, T. H., Fisk, L. A., et al. 2012, JGRA, 117, A00M02
Glass, A. N., Raines, J. M., Jia, X., et al. 2022, JGRA, 127, e2022JA030969
Gnaser, H. 1999, Low-energy Ion Irradiation of Solid Surfaces, Vol. 146 (Berlin: Springer), 41
Grava, C., Killen, R. M., Benna, M., et al. 2021, SSRv, 217, 1
Hijazi, H., Bannister, M. E., Meyer, H. M., Rouleau, C. M., & Meyer, F. W. 2017, JGRE, 122, 1597
Hobler, G. 2013, NIMPB, 303, 165
Hofsäss, H., & Stegmaier, A. 2022, NIMPB, 517, 49
Jackson, D. P. 1975, CaJPh, 53, 1513
Janches, D., Berezhnoy, A. A., Christou, A. A., et al. 2021, SSRv, 217, 50
Kazakov, A., Milillo, A., Lazzarotto, F., et al. 2022, EPSC, 16, EPSC2022–810
Ken Knight, C. E., & Wehner, G. K. 1967, Investigation of Sputtering Effects on the Moon's Surface, 3107 NASA, https://ntrs.nasa.gov/citations/19670028248
Killen, R. M., Morrissey, L. S., Burger, M. H., et al. 2022, PSJ, 3, 139
Küstner, M., Eckstein, W., Dose, V., & Roth, J. 1998, NIMPB, 145, 320
Küstner, M., Eckstein, W., Hechtl, E., & Roth, J. 1999, JNuM, 265, 22
Lindhard, J., & Scharff, M. 1961, PhRv, 124, 128
Loeffler, M. J., Dukes, C. A., & Baragiola, R. A. 2009, JGR, 114, E03003
Lue, C., Futaana, Y., Barabash, S., et al. 2011, GeoRL, 38, 3202
Madey, T. E., Johnson, R. E., & Orlando, T. M. 2002, SurSc, 500, 838
Mangano, V., Milillo, A., Mura, A., et al. 2007, P&SS, 55, 1541
Martinez, R., Langlinay, T., Ponciano, C. R., et al. 2017, NIMPB, 406, 523
McNutt, R. L., Jr., Benkhoff, J., Fujimoto, M., & Anderson, B. J. 2018, in Mercury: The View after MESSENGER, ed. S. C. Solomon, L. R. Nittler, & B. J. Anderson (Cambridge: Cambridge Univ. Press), 544

Milillo, A., Fujimoto, M., Murakami, G., et al. 2020, SSRv, 216, 93
Möller, W., & Eckstein, W. 1984, NIMPB, 2, 814
Möller, W., & Posselt, M. 2001, TRIDYN FZR User Manual, Technical Rep., FZR 317, Dresden: Forschungszentrum Rossendorf
Morrissey, L. S., Tucker, O. J., Killen, R. M., Nakhla, S., & Savin, D. W. 2022, ApJL, 925, L6
Mura, A., Wurz, P., Lichtenegger, H. I. M., et al. 2009, Icar, 200, 1
Mutzke, A., Schneider, R., Eckstein, W., et al. 2019, SDTrimSP v6.00, Max-Planck-Institut für Plasmaphysik
Nénon, Q., & Poppe, A. R. 2020, PSJ, 1, 69
Orsini, S., Livi, S., Lichtenegger, H., et al. 2021, SSRv, 217, 11
Paige, D. A., Foote, M. C., Greenhagen, B. T., et al. 2010, SSRv, 150, 125
Pfleger, M., Lichtenegger, H., Wurz, P., et al. 2015, P&SS, 115, 90
Poppe, A., Farrell, W., & Halekas, J. S. 2018, JGRE, 123, 37
Raines, J. M., Dewey, R. M., Staudacher, N. M., et al. 2022, JGRA, 127, e2022JA030397
Roth, J., Bohdansky, J., & Eckstein, W. 1983, NIMPR, 218, 751
Roth, J., Bohdansky, J., & Ottenberger, W. 1979, Data on low energy light ion sputteringIPP 9/26Max-Planck-Institut für Plasmaphysik, 98
Roth, J., Eckstein, W., Gauthier, E., & Laszlo, J. 1991, JNuM, 179, 34
Samartsev, A. V., & Wucher, A. 2006, ApSS, 252, 6470
Schaible, M. J., Dukes, C. A., Hutcherson, A. C., et al. 2017, JGRE, 122, 1968
Schaible, M. J., Sarantos, M., Anzures, B. A., Parman, S. W., & Orlando, T. M. 2020, JGRE, 125, e2020JE006479
Schwebel, C., Pellet, C., & Gautherin, G. 1987, NIMPB, 18, 525
Sigmund, P. 1969, PhRv, 184, 383
Solomon, S. C., McNutt, R. L., Gold, R. E., et al. 2001, P&SS, 49, 1445
Suzuki, Y., Yoshioka, K., Murakami, G., & Yoshikawa, I. 2020, JGRE, 125, e2020JE006472
Szabo, P. S., Biber, H., Jäggi, N., et al. 2020a, ApJ, 891, 100
Szabo, P. S., Biber, H., Jäggi, N., et al. 2020b, JGRE, 125, e2020JE006583
Szabo, P. S., Chiba, R., Biber, H., et al. 2018, Icar, 314, 98
Szabo, P. S., Cupak, C., Biber, H., et al. 2022a, Surfaces and Interfaces, 30, 101924
Szabo, P. S., Poppe, A. R., Biber, H., et al. 2022b, GeoRL, 49, e2022GL101232
Szymoński, M. 1981, PhLA, 82, 203
Thompson, M. W. 1968, PMag, 18, 377
Van der Heide, P. 2014, Secondary Ion Mass Spectrometry: An Introduction to Principles and Practices (New York: Wiley)
Vorburger, A., Wurz, P., Barabash, S., et al. 2013, JGRA, 118, 3937
Whitaker, T. J., Jones, P. L., Li, A., & Watts, R. O. 1993, RScI, 64, 452
Winslow, R. M., Anderson, B. J., Johnson, C. L., et al. 2013, JGRA, 118, 2213
Wucher, A., & Oechsner, H. 1986, NIMPB, 18, 458
Wucher, A., & Oechsner, H. 1988, SurSc, 199, 567
Wurz, P. 2005, in ESA TSP-600, The Dynamic Sun: Challenges for Theory and Observations, 11th European Solar Physics Meeting
Wurz, P., Fatemi, S., Galli, A., et al. 2022, SSRv, 218, 1
Wurz, P., Rohner, U., Whitby, J. A., et al. 2007, Icar, 191, 486
Wurz, P., Whitby, J. A., Rohner, U., et al. 2010, P&SS, 58, 1599
Yamamura, Y., Itikawa, Y., & Itoh, N. 1983, Angular Dependence of Sputtering Yields of Monatomic Solids (Nagoya: Nagoya Univ.)
Ziegler, J. F., & Biersack, J. P. 1985, in Treatise on Heavy-Ion Science, ed. D. A. Bromley (New York: Springer), 93
Ziegler, J. F., Ziegler, M. D., & Biersack, J. P. 2010, NIMPB, 268, 1818

Chapter 4

Mercury's magma ocean evolution and atmospheric loss

The Planetary Science Journal, 2:230 (18pp), 2021 December https://doi.org/10.3847/PSJ/ac2dfb

Evolution of Mercury's Earliest Atmosphere

Noah Jäggi[1], Diana Gamborino[1], Dan J. Bower[2], Paolo A. Sossi[3], Aaron S. Wolf[4], Apurva V. Oza[1,5], Audrey Vorburger[1], André Galli[1], and Peter Wurz[1]
[1] Physics Institute, University of Bern, Sidlerstrasse 5, 3012 Bern, Switzerland; noah.jaeggi@space.unibe.ch
[2] Center for Space and Habitability, University of Bern, Gesellschaftsstrasse 6, 3012 Bern, Switzerland
[3] Institute of Geochemistry and Petrology, Department of Earth Sciences, ETH Zurich, Clausiusstrasse 25, 8092 Zurich, Switzerland
[4] Earth and Environmental Sciences, University of Michigan, 1100 North University Avenue, Ann Arbor, MI 48109-1005, USA
[5] Jet Propulsion Laboratory, California Institute of Technology, Pasadena, CA 91109, USA
Received 2021 March 26; revised 2021 October 5; accepted 2021 October 7; published 2021 November 17

Abstract

MESSENGER observations suggest a magma ocean formed on proto-Mercury, during which evaporation of metals and outgassing of C- and H-bearing volatiles produced an early atmosphere. Atmospheric escape subsequently occurred by plasma heating, photoevaporation, Jeans escape, and photoionization. To quantify atmospheric loss, we combine constraints on the lifetime of surficial melt, melt composition, and atmospheric composition. Consideration of two initial Mercury sizes and four magma ocean compositions determines the atmospheric speciation at a given surface temperature. A coupled interior–atmosphere model determines the cooling rate and therefore the lifetime of surficial melt. Combining the melt lifetime and escape flux calculations provides estimates for the total mass loss from early Mercury. Loss rates by Jeans escape are negligible. Plasma heating and photoionization are limited by homopause diffusion rates of $\sim 10^{6}$ kg s^{-1}. Loss by photoevaporation depends on the timing of Mercury formation and assumed heating efficiency and ranges from $\sim 10^{6.6}$ to $\sim 10^{9.6}$ kg s^{-1}. The material for photoevaporation is sourced from below the homopause and is therefore energy limited rather than diffusion limited. The timescale for efficient interior–atmosphere chemical exchange is less than 10,000 yr. Therefore, escape processes only account for an equivalent loss of less than 2.3 km of crust (0.3% of Mercury's mass). Accordingly, $\leqslant$0.02% of the total mass of H_2O and Na is lost. Therefore, cumulative loss cannot significantly modify Mercury's bulk mantle composition during the magma ocean stage. Mercury's high core:mantle ratio and volatile-rich surface may instead reflect chemical variations in its building blocks resulting from its solar-proximal accretion environment.

Unified Astronomy Thesaurus concepts: Mercury (planet) (1024); Solar system terrestrial planets (797); Planetary atmospheres (1244); Planetary science (1255); Atmospheric composition (2120); Upper atmosphere (1748)

1. Introduction

MESSENGER data from X-ray, gamma-ray, and neutron spectrometers constrain the composition of Mercury's surface and motivate theories and models to understand Mercury's bulk composition, formation, and evolution. The surface composition and geology of Mercury are compatible with partial melting of cumulates that were originally formed by magma ocean crystallization (McCoy et al. 2018). Subsequent impact excavation exposed the cumulates at the surface (McCoy et al. 2018; Charlier et al. 2013). The low oxygen fugacity (fO_2) of the uppermost layer of Mercury's regolith, together with Mercury's large core size, suggests a reduced mantle where nominally lithophile elements such as Ca, Mn, Cr, and Ti are present in sulfides rather than silicates (Vander Kaaden & McCubbin 2016). Relative to basaltic rocks exposed at the surface of other terrestrial planets, a large amount of the moderately volatile element Na (3–5 wt%) is detected on Mercury's surface (Peplowski et al. 2014). Observations of Na variation in Mercury's exosphere may relate to nightside deposit formation and dawn reemission (e.g., Cassidy et al. 2016). Hence, it remains an open question how moderately volatile elements such as Na may have accumulated on the surface—whether from an extant or now-extinct process—and how their abundance compares to Mercury's bulk composition.

Magma oceans are pivotal in determining the initial conditions and subsequent evolution and chemical differentiation of terrestrial planets in the solar system (e.g., Elkins-Tanton 2012; Chao et al. 2021). Radiometric dating reveals that magmatic iron meteorites, which represent planetesimal cores, formed within 2 Myr of solar system formation (Kruijer et al. 2014). The rocky planet whose mass is most similar to that of Mercury, and for which samples are available, Mars, likely accreted, formed an iron core, and underwent complete solidification of its magma ocean within about 20 Myr of solar system formation (Bouvier et al. 2018). Crucially, rapid core formation in terrestrial planets requires a magma ocean to enable efficient metal segregation (Stevenson 1990). By analogy, and given its solar-proximal location, extensive melting is therefore expected to have occurred on proto-Mercury (Brown & Elkins-Tanton 2009; Vander Kaaden & McCubbin 2016). Following its crystallization, partial melting of magma ocean cumulates has been invoked to explain Mercury's contemporary surface composition (McCoy et al. 2018).

Energy from accretion and radiogenic heat (e.g., from ^{26}Al) may have driven the differentiation of Mercury if it formed sufficiently early in solar system history (Siegfried & Solomon 1974; Bhatia & Sahijpal 2017). Following a phase of rapid growth, the subsequent reduction of impactor flux would have enabled Mercury's magma ocean to cool and crystallize without additional large-scale remelting. During this

time, the mantle is expected to have stratified into a basal layer of olivine and a plagioclase- and clinopyroxene-dominated crust, which is now observed on Mercury's surface (Brown & Elkins-Tanton 2009). During the cooling of the magma ocean when the surface remains mostly molten, chemical species readily exchange between the interior, atmosphere, and exosphere—as occurred for other terrestrial planets in the solar system (e.g., Elkins-Tanton 2008).

Fegley & Cameron (1987) addressed the hypothesis that the anomalously high bulk density of Mercury (owing to a high core/mantle ratio) is the result of evaporation of silicate melt components from the surface of a Hermean magma ocean. They presumed that atmospheric loss was sufficiently slow that the atmosphere remained in equilibrium with the magma ocean. In their model, vapor was removed in a stepwise fashion and the composition of the magma ocean evolved accordingly. In reality, however, evaporated species are transported, mixed, and lost from the atmosphere and exosphere, with the flux at which loss occurs integrated over the magma ocean lifetime ultimately dictating the total mass loss. Therefore, consideration of interior, atmospheric, and exospheric processes is necessary to assess whether significant quantities of rock-derived atmospheres can be lost during the Hermean magma ocean stage.

Based on observations of solar-mass stars, the early solar extreme-ultraviolet (EUV) and X-ray fluxes were likely 400 times larger than they are today. This would have made photoionization a highly efficient nonthermal—and photoevaporation a highly efficient thermal—atmospheric escape mechanism (Johnstone et al. 2015; Tu et al. 2015). Other loss mechanisms of potential importance include atmospheric sputtering and kinetic escape (e.g., Jeans escape) that occur over the lifetime of the magma ocean. Nonthermal loss rates can be constrained by known plasma pressures at proto-Mercury owing to the incoming solar wind, as well as EUV luminosities of the early Sun estimated from population studies of nearby Sun-like stars (Ribas et al. 2014; Tu et al. 2015).

In this paper we establish the extent of element evaporation and loss from Mercury during its early magma ocean phase. Models are constructed of (1) the coupled evolution of the magma ocean and atmosphere, (2) the evaporation of metals and metal oxide species from the Hermean magma ocean, (3) the mixing ratios and abundances of molecular species throughout the atmosphere and at the exobase, and finally (4) loss rates of these species from the upper atmosphere. We discuss these results in the context of the chemical evolution of Mercury's surface environment, bulk composition, and present-day observations.

2. Method

2.1. Overview

Our combined modeling strategy provides insight into the initial composition and evolution of Mercury's exosphere by considering (1–2) energy and mass exchange between the interior and atmosphere, (3) speciation in the atmosphere, and (4–5) loss from the exosphere:

1. SPIDER (Bower et al. 2018, 2019, 2021) is a coupled interior–atmosphere model used to determine the surface temperature and lifetime of melt at the surface, as well as the pressure–temperature structure of the atmosphere. Magma ocean cooling is regulated by the atmospheric opacity, which depends on the pressure of atmospheric species and hence the solubility of species in melt.
2. VapoRock calculates the equilibrium partial pressures of metal-bearing gas species of the elements Si, Al, Mg, Ca, Na, Fe, and K above the magma ocean surface (Wolf et al. 2021). This determines the metal-bearing composition of the atmosphere as a function of temperature and the bulk composition of the magma ocean. It utilizes ENKI's ThermoEngine (http://enki-portal.org) and combines estimates for element activities in silicate melts with thermodynamic data for metal and metal oxide vapor species (Lamoreaux & Hildenbrand 1984; Lamoreaux et al. 1987).
3. VULCAN (Tsai et al. 2017, 2021) solves for the equilibrium chemistry of the atmosphere as a function of altitude by using element abundances for metals (output by VapoRock), volatile abundances (output by SPIDER), and the atmospheric pressure–temperature structure (also output from SPIDER). This provides the mixing ratios of atmospheric species, which are required to calculate escape at the exobase.
4. DISHOOM (Oza et al. 2019; Gebek & Oza 2020) is an atmospheric evolution model that computes the total mass loss of gaseous species to space due to ultraviolet (EUV) heating, surface heating, and plasma heating.
5. The Exospheric Monte Carlo (E-MC) model (Wurz & Lammer 2003; Vorburger et al. 2015; Gamborino et al. 2019) determines the rate of exospheric escape of particles due to Jeans escape and photoionization. It tracks particle trajectories using a thermal energy distribution that depends on the temperature at the exobase.

2.2. Cooling of the Magma Ocean

Previous thermal modeling of Mercury's interior has focused either on the accretion phase (Bhatia & Sahijpal 2017) or on its long-term evolution over billions of years (e.g., Stevenson et al. 1983; Spohn 1991; Grott et al. 2011; Tosi et al. 2013). Here, we model the thermal evolution of Mercury's magma ocean at the end of its accretion phase. At this time, the final magma ocean cools and crystallizes on a timescale short enough that there is negligible disruption so that our results remain independent of its accretion history. We model the thermal evolution of Mercury's magma ocean using SPIDER (Bower et al. 2018, 2019) to constrain the duration of melt at the surface as it cools from 2400 to 1500 K. This is necessary to compute the evaporation of metals and metal oxides at the planetary surface, prior to the formation of a surface lid around 1500 K. Heating by the decay of radiogenic isotopes ^{26}Al, ^{40}K, ^{232}Th, ^{235}U, and ^{238}U is included in our model, and the model starts from solar system time zero to obtain an upper estimate of the surface cooling time. The main parameters are provided in Table A1 (Appendix A) and are guided by the parameters and results from previous models of Mercury (Bhatia & Sahijpal 2017; Tosi et al. 2013).

Cases prefixed by "S" ("small Mercury"; Table 1) have a planetary radius of 2440 km, which is the present-day radius of Mercury. Cases prefixed by "L" have a radius of 3290 km, which assumes that Mercury was larger than at present day, perhaps due to mantle stripping driven by an impactor (Benz et al. 2008; Asphaug & Reufer 2014; Chau et al. 2018). Cases with "V" (volatile) consider the partitioning of carbon and

Table 1
Parameters for the Magma Ocean Cases

Case	R_P (km)	g (m s^{-2})	H_2O	H_2	CO_2	CO	SiO
			Pressure (bar) at 2000 K				
SN5	2440	3.7	⋯	⋯	⋯	⋯	$1.4E-4$
SN3	2440	3.7	⋯	⋯	⋯	⋯	$1.4E-4$
SV	2440	3.7	0.7	3.2	0.05	1.1	⋯
LN5	3290	4.0	⋯	⋯	⋯	⋯	$1.4E-4$
LN3	3290	4.0	⋯	⋯	⋯	⋯	$1.4E-4$
LV	3290	4.0	1.2	5.8	0.2	4.9	⋯

Note. Small (S) and large (L) Mercury models are inspired by models M1 and M4 from Bhatia & Sahijpal (2017), respectively. The second letter of the case name denotes with volatiles (V) and no volatiles (N). Nonvolatile cases have an additional number of either 5 or 3, to denote small (10^{-5} m^2 kg^{-1}) and large (10^{-3} m^2 kg^{-1}) SiO opacity, respectively (Semenov et al. 2003).

Table 2
Magma Ocean Surface Composition

Oxide (wt%)	EH4	CB	NSP Source	NSP Lava
SiO_2	62.73	50.70	53.67	58.70
Al_2O_3	2.58	4.60	4.75	13.80
MgO	30.24	36.90	36.89	13.90
CaO	1.99	3.30	2.26	5.81
FeO	0.00	3.50	0.02	0.04
Na_2O	1.71	0.19	1.97	7.00
K_2O	0.20	0.05	0.05	0.20
Total	99.45	99.24	99.61	99.45

Note. Compositions based on enstatite chondrites (EH4; Wiik 1956); CB chondrite chondrule data with bulk CB Na and K mass balanced for chondrules to fit bulk meteorite iron-silicate ratio (Weisberg et al. 2000, 1990; Lauretta et al. 2007); and northern smooth plains (NSP) composition for the lava and source (Namur et al. 2016; Nittler & Weider 2019).

hydrogen species, here termed volatiles, between the melt and atmosphere, as well as redox reactions (Bower et al. 2021). By contrast, cases with "N" (nonvolatile) do not consider volatiles but rather assume that SiO is the only IR absorbing species; a suffix of "5" denotes a low SiO opacity (10^{-5} m^2 kg^{-1}), and a suffix of "3" denotes a large SiO opacity (10^{-3} m^2 kg^{-1}), both at a reference pressure of 3×10^{-6} bar (Figure 2 in Semenov et al. 2003). For nonvolatile cases, the surface pressure of SiO is imposed in SPIDER as a function of surface temperature as determined by VapoRock calculations. Then, the atmospheric opacity and hence magma ocean cooling rate can be determined.

For cases SV and LV, carbon and hydrogen can exist as either reduced (CO, H_2) or oxidized (CO_2, H_2O) species, where the fO_2 is constrained to one log unit below the iron-wustite buffer ($\Delta IW = -1$, IW-1 hereafter). This is marginally higher than the most recent estimates for the fO_2 of Mercury's mantle (Cartier & Wood 2019). For cases SV and LV, we determine the total H and C abundances by calculating the ppmw necessary for an Earth-size planet to produce a 100 bar CO_2 (i.e., Venus-like atmosphere) and 270 bar H_2O (i.e., one Earth ocean mass) atmosphere. The abundances of H and C are equivalent to 330 ppmw of H_2O and 120 ppmw of CO_2, respectively. The mass of large Mercury's mantle is about a factor of 5 larger than small Mercury's mantle, resulting in a 5 times increase in the total volatile budget.

2.3. Evaporation from the Magma Ocean

At the high surface temperatures that characterize a magma ocean (>1500 K), the partial pressures of the vapor species of the major rock-forming oxides (e.g., SiO_2, $NaO_{0.5}$, $KO_{0.5}$) can become significant (Visscher & Fegley 2013; Sossi & Fegley 2018; Sossi et al. 2019). Gas-liquid equilibria for these elements are described by congruent evaporation, generalized as

$$M^{x+n}O_{(x+n)/2}(l) = M^xO_{x/2}(g) + \frac{n}{4}O_2(g), \quad (1)$$

where M is the metal, x is the oxidation state of the metal in its gaseous state, and n is the number of electrons exchanged in the reaction. Both x and n are integer values that may be $\geqslant 0$ or $\leqslant 0$. At equilibrium, the partial pressure of any given metal or metal oxide species in an ideal gas is given by

$$p(M^xO_{x/2}) = \frac{K_{(1)} X(M^{x+n}O_{(x+n)/2}) \gamma(M^{x+n}O_{(x+n)/2})^{(n/4)}}{(fO_2)}, \quad (2)$$

where $K_{(1)}$ is the equilibrium constant of the reaction (Equation 1), X is the mole fraction, and γ is the activity coefficient of the metal oxide melt species, $M^{x+n}O_{(x+n)/2}$. Equilibrium constants involving 31 gas species (Table B2, Appendix B) are calculated according to their thermodynamic properties given in Lamoreaux et al. (1987) and Lamoreaux & Hildenbrand (1984). Evident from Equation (2) is that estimates for the composition of the silicate melt in addition to the activity coefficients of its constituent components are required to correctly predict partial pressures. To this end, likely compositions representative of Mercury's crust, mantle, and possible precursors are shown in Table 2. The MELTS algorithm is used to estimate activity coefficients of melt oxide species (Ghiorso & Sack 1995). The fO_2 is constrained to lie one log unit below the IW buffer (IW-1), which is calculated according to O'Neill & Eggins (2002):

$$\log fO_2(IW) = 2\frac{-244118 + 115.559\,T - 8.474\,T\ln(T)}{\ln(10)RT}, \quad (3)$$

where T is temperature and R the gas constant. These ingredients together comprise the VapoRock code and permit calculation of equilibrium partial pressures over a range of temperatures, fO_2, and silicate melt compositions (Wolf et al. 2021).

2.4. Magma Ocean Composition

The composition of the early Hermean mantle is uncertain. To address how variability in the surface composition affects the evolved partial pressures of metal and metal oxide gas species, four compositions are investigated (Table 2): (1) enstatite chondrites (EH4), (2) Bencubbin chondrites (CB), (3) northern smooth plain (NSP) lava, and (4) NSP source. The first composition assumes that core–mantle differentiation was sluggish, with the composition of the magma ocean being approximated by enstatite chondrites (EH4), often cited as

Table 3
Surface Element Ratios at $T_{surf} = 2000$ K

Composition	Element Ratios						
	C/H	O/H	Mg/H	Si/H	Na/H	K/H	Fe/H
SV Case							
EH4	1.532E-01	2.472E-01	1.251E-06	1.469E-05	1.254E-04	1.121E-05	1.053E-08
CB			1.680E-06	1.039E-05	7.155E-05	5.785E-06	9.388E-06
NSP source			1.740E-06	1.020E-05	2.282E-04	5.254E-06	7.155E-07
NSP melt			9.642E-07	1.161E-05	3.480E-04	7.139E-06	1.351E-06
LV Case							
EH4	3.608E-01	4.641E-01	6.806E-07	7.997E-06	6.825E-05	6.104E-06	5.732E-09
CB			9.144E-07	5.653E-06	3.894E-05	3.148E-06	5.109E-06
NSP source			9.469E-07	5.551E-06	1.242E-04	2.859E-06	3.894E-07
NSP melt			5.248E-07	6.321E-06	1.894E-04	3.886E-06	7.354E-07

Note. Ratios are based on SPIDER and VapoRock results for magma ocean compositions given in Table 2. We neglect Al and Ca, as their vapor pressures do not exceed 10^{-9} bar at 2000 K for any composition.

appropriate starting compositions for Mercury owing to their high bulk iron content, strongly reduced nature, and the resemblance of partial melts thereof to Hermean surface compositions (Nittler et al. 2011). We assume that all FeO is extracted in the form of metallic iron to form Mercury's core, which results in high SiO_2 and MgO contents in the complementary silicate fraction.

The second composition is based on chondrules found in the Bencubbin class of carbonaceous chondrites (CB), which best reproduce Mercury's surface composition based on MESSENGER data (Brown & Elkins-Tanton 2009; McCoy et al. 2018). Spectrometric measurements of Mercury's surface show a crust rich in Na and S and poor in Fe relative to other basaltic rocks (Nittler & Weider 2019). Presuming that these abundances are representative of bulk Mercury, two other compositions are investigated: the NSP lava (NSP melt) that represents a volatile-rich composition observed on the surface, and its inferred mantle source (NSP source; Nittler & Weider 2019). These two compositions represent Mercury's crust and mantle, respectively. Although it is not anticipated that magma ocean crystallization produced the NSP melt composition directly, it is included to define an end-member opposing the CB composition that is Na and K poor and comparably Fe-rich (Table 2).

2.5. Atmospheric Structure

The atmospheric structure is constrained by the temperature at the magma ocean–atmosphere interface, the planetary equilibrium temperature, and the atmospheric composition and pressure (Appendix E). For nonvolatile cases, the calculated vapor pressures of Si, Na, K, Fe, Mg, Al, and Ca oxide species in equilibrium with the magma ocean (Figure 2) are used directly in the exospheric loss model (Section 2.6). SiO vapor pressures reported in Table 1 at $T_{surf} = 2000$ K are not strongly affected by the magma ocean composition and are in the range of $10^{-4\pm0.1}$ bar. For cases SV and LV in which Mercury's atmosphere contains outgassed H- and C-bearing gases, the partial pressures of H_2, H_2O, CO, and CO_2 are calculated by SPIDER according to volatile solubility and fO_2 buffered by the magma ocean at IW-1. A modified version of the VULCAN code is then used to compute the equilibrium chemical speciation in the atmosphere that contains both the metal-bearing gases and H and C volatiles (Tsai et al. 2017, 2021). VULCAN computes the atmospheric mixing ratios using the pressure–temperature (P–T) structure of the atmosphere.

VULCAN by default includes about 300 reactions for C, H, O, and N, to which we added reactions involving Si, Mg, Ca, Fe, Na, and K to obtain their equilibrium speciation (Table C3, Appendix C). Table 3 shows the initial element-to-hydrogen ratios used in the VULCAN calculations. Surface vapor pressures of Ca- and Al-bearing species did not exceed 10^{-6} bar in the magma ocean temperature range investigated and are thus excluded. For the remaining species we used a case-dependent P–T profile from SPIDER at a surface temperature of 2000 K to determine the mixing ratio of species in the atmosphere as a function of altitude. The P–T profile may imply condensation of certain elements initially present in the vapor, which may rain out of the atmosphere prior to escape. To assess this possibility, Gibbs free energy minimization of the atmospheric composition was performed throughout the atmospheric column using FactSage 7.3 (Bale 2016).

SPIDER and, for volatile cases, VULCAN provide descriptions of the atmospheric structure and composition needed to determine the altitude of the homopause and exobase. The homopause is the altitude at which molecular diffusion exceeds diffusion by eddies and thus separates the well-mixed lower atmosphere from the mass-separated upper atmosphere. The exobase is the altitude at which gas is loosely bound to the planet and is collisionless (Knudsen number = 1), resulting in efficient escape.

2.5.1. Homopause Level and Diffusion

To determine the homopause level z_{hom}, we require the particle density at the homopause n_{hom}. For a steady-state homopause height, the molecular coefficient D_{ik} is equal to the eddy diffusion coefficient K_{zz}, allowing us to solve for the particle density n_{hom}. The diffusion coefficient D_{ik} ($m^2\,s^{-1}$) within the homosphere is calculated for each major species using the Chapman−Enskog relation (Chapman & Cowling 1970). It determines the binary diffusion rate of a gaseous species i with mass m_i within a gas of average mass m_k:

$$D_{ik} = \frac{3\sqrt{k_B T_{skin}}}{8 n_{hom} \sigma_{ik}^2 \Omega_{ik}} \sqrt{\frac{1}{2\pi}\frac{m_i + m_k}{m_i m_k}}, \quad (4)$$

where k_B is the Boltzmann constant and $T_{\rm skin}$ the absolute temperature at the homopause (skin temperature). Homopause pressures ($P_{\rm hom} = n_{\rm hom} k_B T_{\rm skin}$) for each species are thereby about 10^{-6} bar for all cases. We approximate the intermolecular distance $\sigma_{ik} = \frac{\sigma_i + \sigma_k}{2}$ with the radius of the species relative to the mean species diameter weighted by the mixing ratio. The dimensionless collision integral Ω_{ik} is assumed to be unity.

The eddy velocity is often approximated by the atmospheric species thermal speed $v_{\rm th}$, and the characteristic eddy length scale $L_{\rm eddy}$ is approximated by the atmospheric scale height H (e.g., Atreya et al. 1986). Values for $K(z) = v_{\rm eddy} L_{\rm eddy}$ that are calculated based on this assumption exceed the suggested eddy diffusion coefficient upper limit of 320 $\rm m^2\ s^{-1}$ by several orders of magnitude (Vlasov & Kelley 2015). Hence, we use this upper limit in the volatile cases to determine $n_{\rm homo}$, which is based on the energy dissipation rate within Earth's atmosphere.

To compute the $z_{\rm hom}$ and $T_{\rm hom}$ for the volatile cases, we determine the altitude at which the P–T profile reaches a number density $n_{\rm homo}(K(z))$. As the number density at the homopause only depends on K_{zz} with the same order of magnitude for both volatile and nonvolatile cases, $n_{\rm homo}(K(z))$ is approximately 10^{18}–10^{19} at $\rm m^{-3}$. For the nonvolatile cases we do not obtain a $P(z)$–T profile from VULCAN for the nonvolatile cases owing to the absence of H-based species. We therefore use the barometric formula with gravity as a function of height to compute $z_{\rm hom}$.

2.5.2. Exobase Level

Due to the large difference in number density between the homopause and the exobase, the barometric formula is not applicable assuming an isothermal upper atmosphere with height-dependent gravity. We approximate the exobase height of early Mercury, which is subject to extensive loss, by finding an exobase height that results in a loss rate that is in equilibrium with the homopause diffusion rate. The loss from the exobase is proportional to the exobase height (increasing surface area), whereas diffusion from the homopause to the exobase is inversely proportional to the exobase height (decreasing density gradient). The exobase altitude $z_{\rm exo}$ of each species is determined for all cases by setting the homopause diffusion rate $\dot{M}_{{\rm diff},i}$ equal to the largest, diffusion-limited mass-loss rate of photoionization $\dot{M}_{\rm ion}$ (Equation (9), Section 2.6).

The homopause diffusion rate $\dot{M}_{\rm diff}$ in $\rm kg\ s^{-1}$ of a species i is obtained by multiplying the diffusion coefficient D_{ik} by the species number density gradient, the species mixing ratio at the homopause $n_i/n_{\rm hom}$, and the homopause surface area $A_{\rm hom}$:

$$\dot{M}_{{\rm diff},i} = -D_{ik} \frac{\Delta n_{\rm exo-hom}}{\Delta z_{\rm exo-hom}} m_i \frac{n_i}{n_{\rm hom}} A_{\rm hom}. \quad (5)$$

The number density of particles at the exobase $n_{\rm exo}$ is necessary to determine the number density gradient between the homopause and exobase and ultimately $z_{\rm exo}$. For a single species i, the exobase is defined at an altitude at which the particle free path ($\lambda_{\rm col} = 1/n_{\rm exo}\sigma_{\rm col}$) is equal to the exospheric scale height ($H = k_B T/mg$), and therefore (i.e., Gronoff et al. 2020)

$$n_{i,{\rm exo}} = \frac{1}{H_i \sigma_i} = \frac{m_i\, g(h)}{k_B\, T_{\rm skin}\, \sigma_i}, \quad (6)$$

with the collision cross section (CCS) σ_i, the skin temperature $T_{\rm skin}$, and the acceleration of gravity $g(h)$ at the exobase altitude $z_{\rm exo}$. In a multispecies atmosphere, each species has a specific mass and CCS, leading to a species-specific scale height and exobase density and altitude. The CCSs of each species are approximated as their respective atom or molecule size (Table D4, Appendix D). Typical values for $n_{\rm exo}$ are around 10^{12}–10^{13} atoms $\rm m^{-3}$, which coincides with $\sim 10^{-12}$ bar. The skin temperature used for determining $z_{\rm exo}$ and $z_{\rm hom}$ is derived from the atmosphere model (Appendix E):

$$T_{\rm skin} = \left[\frac{\epsilon\,(T_{\rm surf}^4 - T_\infty^4)}{2} + T_\infty^4 \right]^{1/4}, \quad (7)$$

with the magma ocean surface temperature $T_{\rm surf}$, emissivity ϵ (depends on optical depth and hence atmospheric composition and pressure), and equilibrium temperature T_∞.

2.6. Exospheric Loss

The E-MC escape model focuses on Jeans escape, photoionization, and photodissociation to investigate the loss of proto-Mercury's exosphere. These mechanisms compete for importance; Jeans escape acts at high exospheric temperatures, whereas photoionization and photodissociation act at large solar EUV and X-ray fluxes present during early times, respectively. The E-MC model simulates escape by tracking $\sim 10^5$ exospheric particles, with trajectories initiated at the exobase with a random angle and energy selected from a Maxwellian velocity distribution function (Vorburger et al. 2015). The initial energy of the exospheric particles depends on the exobase temperature, which decreases with time owing to magma ocean and atmospheric cooling.

The loss processes in the E-MC model are calculated on a particle-by-particle basis. As soon as a particle reaches Mercury's Hill radius (Table 4), it is assumed to have escaped Mercury's gravitational attraction and is subsequently removed from the simulation. Another loss process is through interaction with photons. At each altitude step starting from the exobase and moving away from the planet, the E-MC model calculates the probability of a particle being photodissociated or photoionized. If the particle is photodissociated, the code calculates the corresponding trajectories of the fragments and assesses the chance of escaping the gravitational well and the potential for subsequent photoionization. Ionized particles are considered lost from the exosphere, assuming they are picked up by the electromagnetic forces of the solar wind plasma or Mercury's magnetospheric plasma. Photoionization and photodissociation rates are scaled for each dominant species using the EUV flux of the early Sun. The EUV flux and mass loss are dependent on the rotational evolution of the Sun, with a fast rotator being much more active than a slow rotator (Johnstone et al. 2015; Tu et al. 2015). We consider a moderately fast rotating Sun, where the EUV luminosity $L_{\rm EUV}$ ($\rm J\ s^{-1}$) is

$$L_{\rm EUV} = (4.7 \times 10^{25})\, t^{-1.18}, \quad (8)$$

where t (Ma) is the time since the formation of the solar system. Typical values for the incident EUV fluxes at Mercury at 1 and 5 Ma are thereby $10^{3.0}$ and $10^{2.2}$ $\rm J\ s^{-1}\ m^{-2}$, respectively.

The loss is equal to the sum of the exospheric particles that have been either photoionized or lost through gravitational escape. The loss of a given species from the exosphere at a given time is then calculated using its mixing ratio at the exobase. For a given exobase temperature, the loss rate ($\dot{M} = dm/dt$) from the

Table 4
Escape Parameters λ_0 for Small Mercury and Large Mercury Cases at $T_{surf} = 2000$ K

Species	λ_0	μ_{atm} (amu)	T_{exo} (K)	z_{exo} (km)	Case
Small Mercury, $R_H = 72\ R_P$					
Na, K, Fe	7.8	24.1	1613	2670	SN5, SN3
H, C, O	7.6	14.3	1021	2370	SV
Large Mercury, $R_H = 90\ R_P$					
Na, K, Fe	15.7	24.1	1615	1890	LN5, LN3
H, C, O	15.3	14.3	893	2160	LV

Note. The escape parameter λ_0 with the respective mean molecular weight of the upper atmosphere μ_{atm}, as well as the exobase temperature T_{exo} and altitude z_{exo}. The Hill radius R_H in Mercury radii R_P describes the gravitational field of influence of Mercury in each case.

exosphere by photoionization $\dot{M}_{ion}$ is

$$\dot{M}_{ion} = \sum_{i=0} \psi_i^{source}\ \xi_i\ m_i A_{exo}, \tag{9}$$

where A_{exo} is the surface area of the exobase and $0 \leqslant \xi_i \leqslant 1$ is the fraction of lost particles of a species i with mass m_i, thermal speed of v_i^{therm}, and particle flux leaving the exobase of $\psi_i^{source} = n_i^{exo}\ v_i^{therm}$. The area of the exobase is equal to sum of the R_P and z_{exo} (Section 2.5). The total loss is determined by integrating the loss flux over the lifetime of surficial melt.

2.7. Atmospheric Loss and Surface Evaporation

Atmospheric loss by thermal processes (photoevaporation) and nonthermal processes (plasma heating) is determined using DISHOOM (Oza et al. 2019), using Equation (10) and Equation (11), respectively. Preliminary calculation of Jeans escape using DISHOOM demonstrated negligible loss due to surface heating compared to all other mechanisms. The escape parameters appropriate to proto-Mercury are summarized in Table 4.

Irradiation from the impinging solar wind plasma and high-energy photons may heat the atmosphere and drive escape at a level that is significantly larger than surface heating and photoionization. Upper atmospheric heating (photoevaporation) is caused by incoming X-ray and EUV photons that deposit heat into a neutral medium via molecular absorption (Watson et al. 1981) or photoelectric heating (Murray-Clay et al. 2009). This expands the atmospheric envelope beyond the gravitational influence of the body (R_H in Table 4). The heating can be estimated by energy-limited escape driven by EUV photons (Watson et al. 1981), which is a reasonable approximation to thermally driven hydrodynamic escape (Volkov & Johnson 2013; Krenn et al. 2021):

$$\dot{M}_U = \frac{\eta_{EUV}\ L_{EUV}\ 2\pi\ z_{abs}^2}{U_{env}}, \tag{10}$$

where z_{abs} is the absorption altitude, generally taken to be 1.25 planetary radii for an outgassing atmosphere (e.g., Johnson et al. 2015) where the X-ray and EUV photons can absorb and thereby deposit heat into the atmospheric molecules. We note that we use 1.25 Mercury radii R_P as a conservative lower limit in absorption altitude, as the homopause situated at $\sim$1.4 R_P represents an upper limit. The efficiency at which the atmosphere is heated, η_{EUV}, is uncertain, so we use 10^{-3} as a conservative lower estimate (Ito & Ikoma 2021) and 10^{-1} as an upper limit (Mordasini 2020). Both efficiencies that we used were previously applied to atmospheres that use vastly different planet parameters but similar enough, as they consider a metal oxide (nonvolatile) or an H/He (volatile) atmosphere, respectively. Hot Jupiter H/He envelopes, as well as volcanic atmospheres, suggest that η_{EUV} may be as large as 0.35 (Lellouch et al. 1992; Murray-Clay et al. 2009).

Mass loss due to plasma heating is observed at Jupiter's moon Io and is fundamentally driven by plasma ram pressure and magnetic pressure interacting with the atmosphere (e.g., Johnson 1990). Therefore, we estimate the atmospheric loss from an impinging plasma on Mercury by scaling to the plasma pressures measured at the Galilean satellites (Johnson 2004). Following Oza et al. (2019) and Gebek & Oza (2020), the mass loss of a species i by plasma heating at proto-Mercury is

$$\dot{M}_{P,i} = \frac{x_i}{\dot{M}_{i,Io}}\ \hat{P}\ \hat{U}\ \hat{v}_{ion}(\hat{h}_{exo})^2, \tag{11}$$

where x_i is the element fraction of the species i in the atmosphere and $\dot{M}_{i,Io}$ its atmospheric sputtering loss rate at Io. The total plasma pressure $\hat{P}$, gravitational binding energy $\hat{U}$, and ion velocity $\hat{v}_{ion}$ of Mercury are expressed as nondimensional values that are scaled to Io's corresponding values. The total plasma pressure is additive where $P_{tot} = P_{mag} + P_{ram}$. For the calculations we use a magnetic pressure $P_{mag} = 1.7$ nPa based on an estimation of Mercury's magnetic moment of 2.76×10^{12} T m^3 at the magnetopause standoff distance of 1.4 R_P. The ram pressure due to the solar wind varies from $\sim$10 to 30 nPa (Korth et al. 2012), yielding a total pressure of $\sim$12–32 nPa.

Evaporation from the magma ocean and atmospheric loss have to be equal to retain the atmospheric pressure and thus a steady state. The evaporation rate of a species is approximated by the Hertz–Knudsen–Langmuir equation. The evaporation rate of a species i with molar mass M_i over the surface of Mercury in mol s^{-1} is given by

$$\dot{M}_{evap,i} = M_i \frac{dn_i}{dt} = -4\pi R_P^2 M_i \frac{\gamma_{ev} P_{i,eq} - \gamma_{en} P_{i,s}}{\sqrt{2\pi M_i R T}}, \tag{12}$$

with the evaporation and condensation coefficients γ (set to unity for a liquid), surface pressure P_s, equilibrium pressure P_{eq}, and the Mercury radius R_P. By setting the homopause diffusion rate $\dot{M}_{diff,i}$ equal to the evaporation rate $\dot{M}_{evap,i}$, the equation is solved for the ratio of surface to equilibrium pressure, $p_{i,s}/p_{i,eq}$ for each species at each temperature step. For homopause diffusion rates, the ratio lies >0.99; therefore, the atmosphere up to the homopause is considered to be in equilibrium.

3. Results

3.1. Surficial Melt Lifetime and Atmospheric Structure

The surface temperature of the Hermean magma ocean cools from 2400 to 1500 K in around 400–9000 yr, depending on the planetary size (i.e., mantle mass) and efficiency of radiative

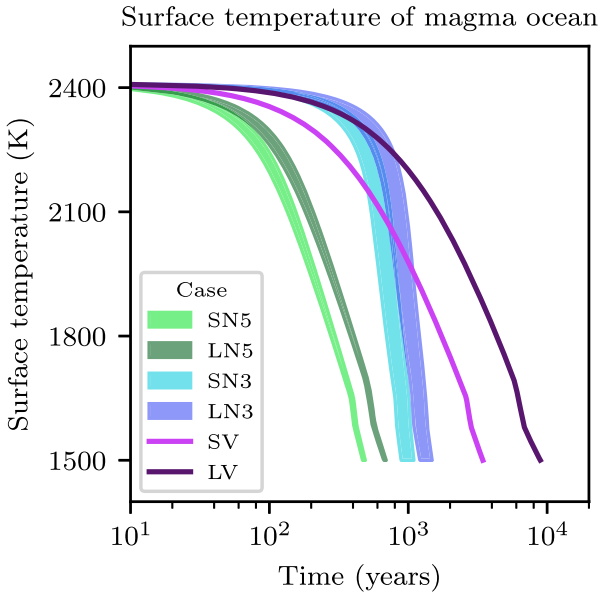

Figure 1. Evolution of the surface temperature of the Hermean magma ocean. For nonvolatile cases, the upper bound of cooling is provided by EH4 composition and the lower bound by Cb composition. See Table 1 for case parameters.

energy loss to space (Figure 1). The cooling rate is inversely proportional to R_P since it depends on the ratio of the planetary surface area to mantle mass. Hence, a large Mercury takes longer to cool than a small Mercury for otherwise-identical parameters.

3.1.1. Nonvolatile Cases

The cooling trajectory of nonvolatile cases is characterized by two episodes. First, when the surface temperature is high (early time), the pressure and hence opacity of SiO are large, and therefore cooling is slow. The second episode of cooling is rapid, since even a small decrease in surface temperature produces a drastic fall in both SiO pressure and opacity, driving the planet toward cooling like an ideal blackbody. Therefore, the cooling timescale for N5 cases is only marginally greater than for an ideal blackbody, which bounds the minimum cooling time to 470 yr. Increasing SiO opacity by 2 orders of magnitude increases the minimum cooling time to around 1000 yr (N3 cases), marginally affected by the chosen magma ocean composition.

Nonvolatile cases at 2400 K have thin atmospheres of <0.1 bar and comprise $>99.8\%$ gaseous Na, SiO, Fe, K, and Mg. The major constituents are Na and SiO at high temperatures, whereas the mixing ratio of SiO rapidly decreases below 2400 K (Figure 2). The partial pressure of Mg behaves similarly to SiO but does not exceed 1% of the atmospheric mixing ratio for any composition. The mixing ratios of Fe and K, however, are more variable because they depend on the assumed magma ocean composition and reach their highest mixing ratios of 9% and 2%, respectively, for CB and EH4 compositions with high FeO and K_2O (Table 2, Figure 2). Refractory components—AlO and Ca—have negligible partial pressures ($<10^{-6}$ bar at 2400 K) and are thus ignored in further calculations. The highest total surface pressure of metal-bearing species at low temperatures is obtained with the NSP melt composition. At 2400 K, the total surface pressure is 6.16×10^{-2} bar, which decreases to 8.52×10^{-6} bar at 1500 K.

Figure 3 shows the homopause levels of Na for the nonvolatile cases as a function of time for CB and NSP melt compositions. Exobase levels lie within a few hundreds of kilometers of the homopause and are omitted in the log–log plot as a result. During the magma ocean phase, the levels evolve within 470–660 yr for N5 cases and 1100–1480 yr for N3 cases. The homopause and exobase locations are only weakly sensitive to the planet size and gravity. The magma ocean composition, however, exerts a strong influence on the atmospheric structure. For the CB case, the homopause lies at 685 km, whereas for the NSP melt composition it lies at around 1258 km at a magma ocean surface temperature of 2400 K. The early inflation of an atmosphere above a cooling magma ocean is due to increasing $T_{\rm skin}$ caused by decreasing IR opacity as the partial pressure of SiO decreases (Equation (7)). Following this stage, the homopause altitude falls to 83 km (CB) and 439 km (NSP melt) at 1500 K. The exobase density and location are further dependent on the mean cross section of atmospheric species, which is tied to the composition-dependent vapor pressures (Equation (6)). The high vapor pressure of Na in the NSP melt relative to the CB composition lowers the mean molecular weight and the mean CCS of the atmosphere, which both increase its extent.

3.1.2. Volatile Cases

Volatile-bearing cases result in cooling times of 3400 yr (Case SV) and 8900 yr (Case LV). Both small proto-Mercury and large proto-Mercury have the same initial volatile abundances of C and H by ppmw, but this manifests in a larger total reservoir size of volatiles for a large proto-Mercury compared to a small one. The mass of volatiles in the atmosphere defines the surface atmospheric pressure, which in turn determines the optical thickness of the atmosphere and hence the efficiency of radiative cooling.

Atmospheres of volatile cases around a small and large proto-Mercury reach surface pressures of about 5 and 12 bar at a magma ocean surface temperature $T_{\rm surf}$ of 2000 K, respectively (Figure 4). This result is independent of the partial pressures of the metal-bearing species, as their contribution is $\leqslant 0.1$ bar at $T_{\rm surf} = 2000$ K. Thus, it is the outgassed hydrogen and carbon species (which depends on their solubilities) that dictates the surface pressure. VULCAN is then used to compute the equilibrium chemistry of the atmosphere accounting for the outgassed volatiles, as well as the metals and oxides. For both small and large Mercury, the atmosphere below the homopause is dominated by H_2 and CO with about 60 and 27 vol.%, respectively, at $T_{\rm surf} = 2000$ K. Between the homopause and the exobase the dominant H-, C-, and O-based species dissociate to monoatomic gases.

For all compositions, Na and K are the dominant metallic elements at $T_{\rm surf} = 2000$ K. At the surface their hydroxide forms NaOH and KOH are fairly abundant, but they dissociate toward the homopause (Table 4). Sodium hydride (NaH) is also present at the surface at pressures one order of magnitude lower than NaOH and remains about constant throughout the atmosphere, reaching similar mixing ratios to K. Potassium hydride (KH) is ignored, as no rate constant exists in the NIST kinetics database (kinetics.nist.gov).

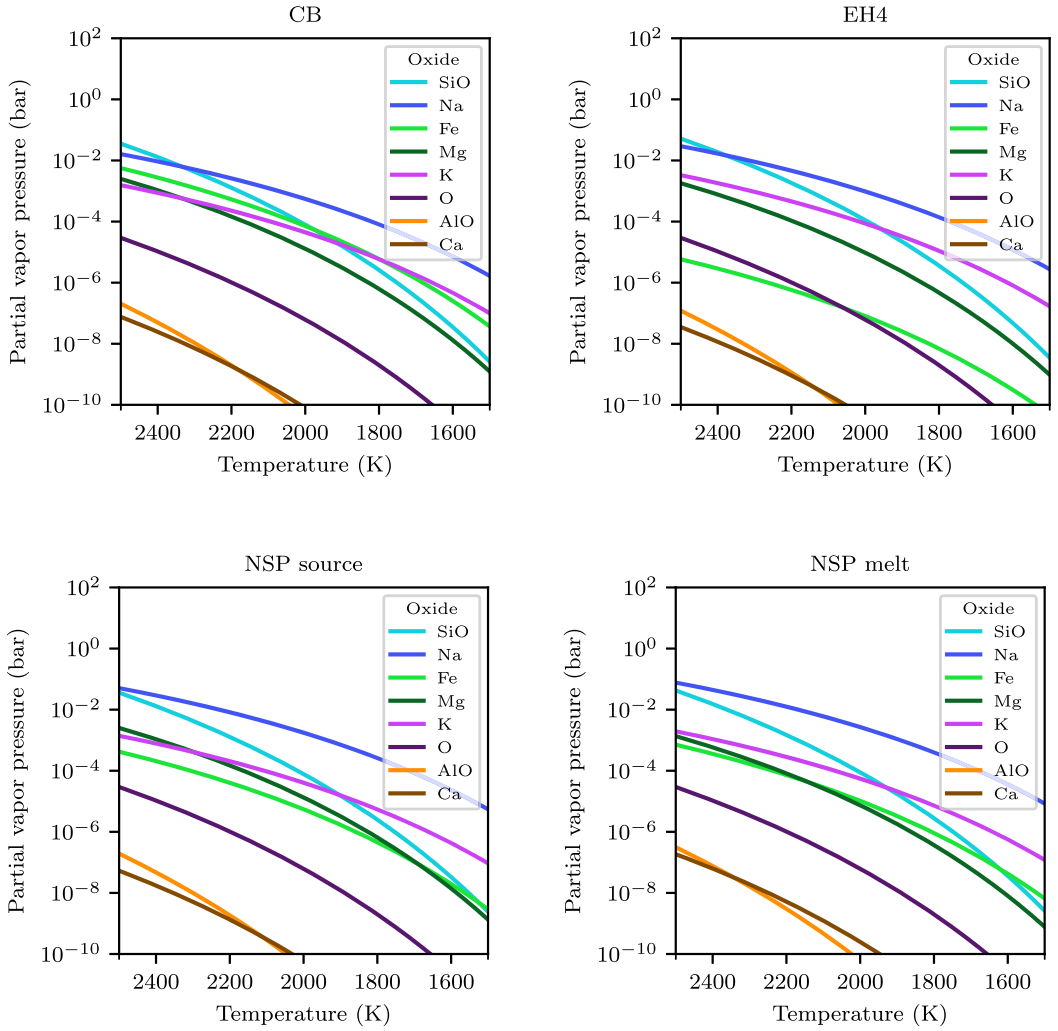

Figure 2. Oxide partial vapor pressures calculated using the CB, EH4, and NSP source and NSP melt composition. The mixing ratios are thereby reflected by the activities of the elements in the given melt composition. The high-Fe composition CB shows a large Fe partial pressure, comparable with K in the high-K compositions EH4 and NSP melt.

Exobase levels are situated up to 2910 and 2590 km for small and large Mercury with homopause levels down to 2360 and 2160 km, respectively. The *P*–*T* structure of the atmosphere gives $T_{\rm skin}$ values for the homopause and exobase of about 1021 and 893 K (Table 4), respectively, for small and large cases, which lies well below the $T_{\rm skin}$ calculated for the nonvolatile cases ($T_{\rm skin} = 1615$ K). The exobase levels of the volatile cases are thus comparable to the nonvolatile cases. Unlike the nonvolatile cases, the planet size has a large impact on the atmospheric structure, which is solely due to the difference in the total volatile reservoir (Section 3.1).

3.2. Atmospheric Loss

We find that the major atmospheric escape mechanism is photoevaporation (Equation (10)), with a lower limit of photoevaporation constrained to $10^{6.6}$ kg s^{-1} and an upper limit of $10^{9.6}$ kg^{-1} for both nonvolatile (Na) and volatile cases (H, C, and O). The upper limit is thereby roughly three orders of magnitude larger than the photoionization of the major atmospheric species. For the high heating efficiency ($\eta_{\rm EUV} = 10^{-1}$) case, loss rates become evaporation limited when reaching 1600 K as the surface-to-equilibrium pressure ratio approaches zero. For low heating efficiencies ($\eta_{\rm EUV} = 10^{-3}$), the ratio of surface to equilibrium pressure $p_{i,s}/p_{i,\rm eq}$ remains at >0.93 (Equation (12)). Photoevaporation as an approximation of thermally driven hydrodynamic escape (Equation (10)) therefore expresses the highest uncertainty on the stability of the atmosphere.

Figure 5 shows the integrated mass loss over the most extensive surficial melt lifetime of 8900 yr. The photoevaporative erosion *dR* of the surface can be estimated by assuming mass conservation where

$$\frac{dM}{dR} = 4\pi R_P^2 \rho_{\rm mantle}. \quad (13)$$

Using a mantle density of $\rho_{\rm mantle} = 3.5$ g cm^{-3} and assuming a high EUV heating efficiency of 10^{-1} at a large Mercury size allows for ~2.3 km loss of crust over the 8900 yr of the volatile case surficial melt lifetime. We have shown using Equation (12)

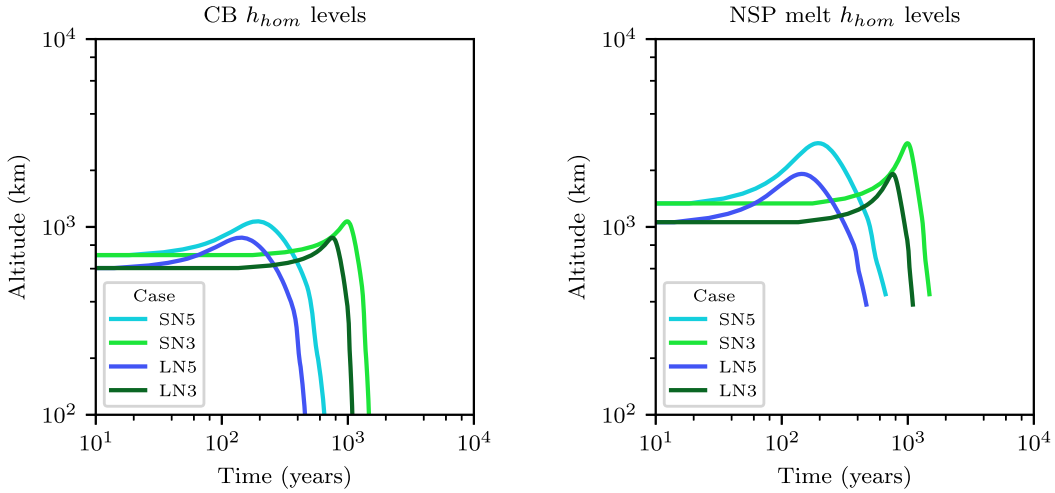

Figure 3. Homopause altitudes for sodium derived for the nonvolatile cooling scenarios for CB and NSP melt. Lines terminate when the surface temperature reaches 1500 K. The equilibrium exobase levels are not plotted, as they lie close to the homopause levels. Homopause levels for other species show the same trends and reach comparable elevations.

that this case becomes evaporation limited owing to the high photoevaporation rates. The total integrated loss when assuming an EUV heating efficiency of 10^{-1} is therefore lower than shown in Figure 5 but not significantly. This is due to most loss occurring during the early magma ocean stage, when the surface temperatures are high and evaporation is not limiting the potentially high photoevaporation rates.

Plasma-driven escape is diffusion limited, as a supply is required at the exobase (Equation (5)). The $\dot{M}_P$ calculated lie orders of magnitude below $\dot{M}_{\rm ion}$ as given in (Table 5) and therefore do not affect the atmospheric structure. Using an intermediate total pressure of 25 nPa, we find about $\dot{M}_P = 10^{3.4}$ kg s^{-1} for small and large, nonvolatile Mercury cases and about $\dot{M}_P = 10^{3.1}$ kg s^{-1} for volatile Mercury cases, respectively. The loss rates are thereby comparable to the plasma-driven escape observed on Jupiter's moon Io in SO_2 $\sim 10^3$ kg s^{-1} (Thomas et al. 2004).

Time-averaged mass-loss rates by photoionization are given in Table 5. Like nonthermal plasma-driven escape, nonthermal escape due to photoionization at the exobase (Equation (9)) is diffusion limited. As photoionization rates of nonvolatile cases follow the same trends independent of planet size, we report results focusing on a small proto-Mercury only, omitting the large Mercury photoionization rates, which are mostly within a factor of two for the dominant species (Table 5). The results of nonvolatile N5 cases are also not reported, as an almost isothermal atmosphere results in less than a factor of two larger loss rates at high temperatures.

Regarding the presence of metal-oxide-derived gaseous species, Gibbs free energy minimization of the vapor phase (using FactSage) along a case-dependent atmospheric *P–T* profile (Figure E1, Appendix E) indicates that Mg and SiO condense into clinopyroxene (1900 K) and then into olivine (≈1700 K) during cooling, by which temperature their fraction remaining in the gas is negligible. Iron persists in the vapor to lower temperatures, condensing partially into olivine before iron metal condenses at 1350 K. Therefore, while Mg and Si (and Ca and Al) all condense prior to reaching the exobase ($T \approx 1680$ K), Fe is likely to partially reside in the vapor phase. Sodium never fully condenses (nepheline, its major host mineral, condenses in very minor proportions below 1500 K), while K remains entirely in the vapor phase down to at least 950 K.

3.2.1. Loss from Nonvolatile Atmospheres

$\dot{M}_{\rm ion}$ in nonvolatile cases is sensitive to the chosen initial composition (Figure 6). The loss fluxes of the nonvolatile species of interest—SiO, Na, and K—are proportional to their mixing ratios in the atmosphere (Figure 2). In cases with high initial SiO partial pressures the mixing ratios and hence the diffusion-limited loss rates of Na and K increase during initial cooling as SiO becomes less abundant. This is most evident in the CB loss flux with an initially increasing loss rate despite decreasing temperatures (Figure 6).

In the low-Na and low-K composition CB, where SiO is the dominant metal oxide at high temperatures, loss fluxes of SiO reach up to 9.6×10^5 kg s^{-1} at $T_{\rm surface} = 2400$ K. The vapor pressure of SiO declines with respect to other dominant gas species (Na and K), thereby reducing its mixing ratio rapidly with decreasing temperature. The lower mixing ratio of SiO causes loss rates to drop to 9.4×10^2 kg s^{-1} at 1500 K. For the same composition, loss rates for Na and K are around 2.0×10^5 kg s^{-1} and 3.1×10^3 kg s^{-1} at $T_{\rm surf} = 2400$ K, increasing to 3.2×10^5 kg s^{-1} and 4.2×10^3 kg s^{-1} at $T_{\rm surf} = 1500$ K, respectively. For the high-Na end-member composition of NSP melt, the diffusion-limited loss rates for Na and K are 5.9×10^5 kg s^{-1} and 1.2×10^4 kg s^{-1}, respectively, when at $T_{\rm surf} = 2400$ K and decrease to 3.9×10^5 kg s^{-1} and 4.3×10^3 kg s^{-1}, respectively, when $T_{\rm surf} = 1500$ K. The ratio of Na to K diffusion rates is ∼100 and hence about one order of magnitude higher than their mixing ratios in the atmosphere. Integrated diffusion-limited losses over the surficial melt lifetimes are shown in Figure 7.

If we assume, based on FactSage results, that SiO and Mg are absent and only Na, K, and Fe remain in the atmosphere, the diffusion-limited loss rates for all cases peak in the small Mercury NSPm case with a fairly temperature-independent Na loss rate of about 10^6 kg s^{-1}. Loss rates for K and Fe are thereby about three orders of magnitude lower than that of Na and do not significantly contribute to the total loss. The difference in change

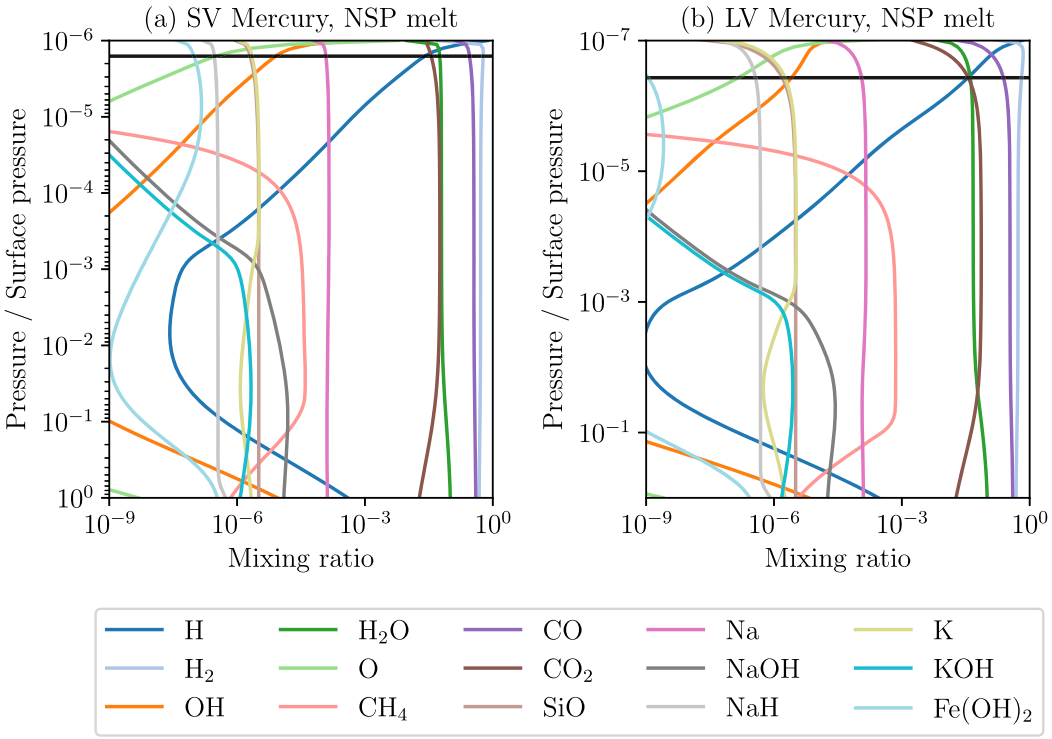

Figure 4. Major- and minor-element composition of the atmosphere for NSP melt composition with a surface temperature of 2000 K for (a) SV and (b) LV Mercury models. The surface pressure that normalizes the *y*-axis is 5.0 bar for SV and 12.1 bar for LV. The homopause level of H is plotted as a black horizontal line.

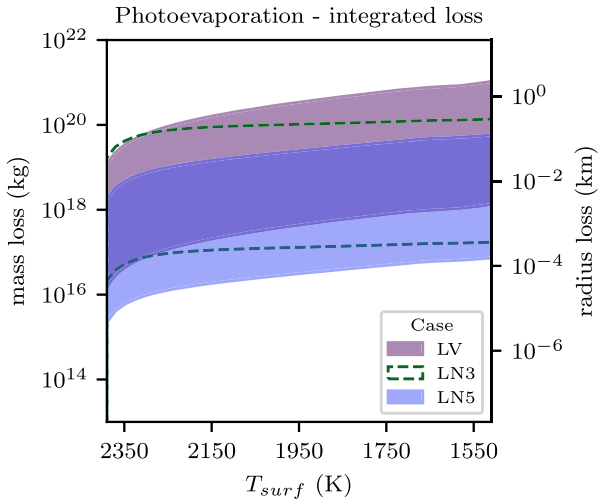

Figure 5. Integrated mass-loss rates of the bulk atmosphere through photoevaporation from 2400 to 1500 K for large Mercury cases. The shaded areas represent the uncertainty of loss rates based on initial conditions. For the N3 case only the upper and lower limits are shown as dashed lines, as it lies within both V and N5 areas. The highest loss rates assume upper limits for EUV luminosity only 1 Ma after Sun formation, $L_{\rm EUV}$(1 Ma), and heating efficiency of 10^{-1}, and the lowest assume $L_{\rm EUV}$(5 Ma) and heating efficiency of 10^{-3}. Using a mantle density of $\rho_{\rm mantle}$= 3.5 g cm^{-3} results in a maximum of crust material being lost to space ranging between 2.3 km and 16 cm, depending on the degree of XUV intensity and heating efficiency.

Table 5
Time-averaged Mass-loss Rates in kg s^{-1}

Mass Loss (log10)			
Process	Size	Emissivity	
		N5, N3	V
$\dot{M}_P$	S	3.4	3.1
	L	3.4	3.2
$\dot{M}_{\rm ion}$ ($\dot{M}_{{\rm diff},i}$)	S	5.6	5.6
	L	5.2	5.8
$\dot{M}_U$		$L_{\rm EUV}$	
		t = 1 Myr	t = 5 Myr
$\eta_{\rm EUV}(10^{-3})$	S	7.5	6.6
	L	7.6	6.7
$\eta_{\rm EUV}(10^{-1})$	S	9.5	8.6
	L	9.6	8.7

Note. Loss rates of plasma heating $\dot{M}_P$, photoionization $\dot{M}_{\rm ion}$, and photoevaporation $\dot{M}_U$. Photoevaporation is insensitive to the atmosphere's emissivity and composition but depends on the EUV flux and the EUV heating efficiency (end-members of 10^{-3} and 10^{-1}). The EUV flux is a function of the age of the solar system (Equation (8), after Johnstone et al. 2015; Tu et al. 2015).

of $\dot{M}_{\rm diff}$ and thus $\dot{M}_{\rm ion}$ between species with continued magma ocean cooling results from the constantly dropping total surface pressure simultaneously to shifting partial pressures. At low magma ocean surface temperatures, Na exerts most of the pressure, whereas at high temperatures condensing species, such as SiO, are the predominant contributors to the total pressure and mean molecular mass of the atmosphere (Figure 2). A lower surface pressure results in a lower homopause level and leads to

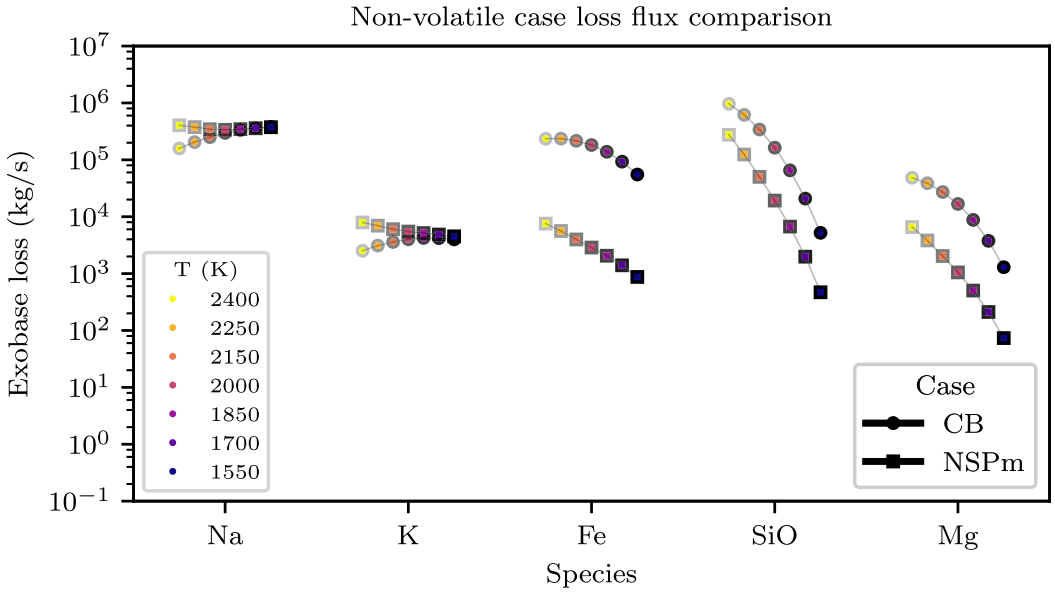

Figure 6. Mass-loss fluxes of exospheric species from 2400 to 1550 K plotted for the small Mercury N3 cases. The loss fluxes for large Mercury follow the same trends and are about a factor of two smaller. The N5 cases with isothermal atmospheres show a factor of two larger loss rates at high temperatures but the same species-related trends.

a smaller diffusion area and rate; however, the rapid decline of the SiO partial pressure in the atmosphere (n_{SiO}/n_{hom}) results in the sharp drop of SiO homopause diffusion rates (i.e., Equation 5) but increases the T_{skin} and therefore the extent of the atmosphere (Figure 3). Similarly, the loss rates through ionization at the exobase for a relatively low mean molecular weight ("light") Na-, K-, and Fe-based atmosphere are up to a factor of five higher than the 2×10^5 kg s^{-1} loss of Na from a "heavy" atmosphere, which includes Mg and notably SiO.

These limits are significant for atmospheric escape estimates by plasma heating, photoionization, or Jeans escape. All three of those processes are calculated from the exobase, which is for plasma heating and photoionization where ions and photons can access a rarefied neutral atmosphere. This is therefore diffusion limited, as a high flux is required to source the neutral species experiencing a momentum transfer from the plasma. Photoevaporation is not necessarily diffusion limited so long as a sufficiently large column exists at the altitude where EUV photons are able to absorb onto infrared-emitting molecules (z_{abs}, Figure 8). In N_2/CH_4 atmospheres (e.g., Kuiper Belt objects) the critical column density is estimated to be $\gtrsim 10^{18}$ cm^{-2} (Johnson et al. 2015), which is easily achieved at a fiducial absorption altitude of z_{abs} situated at $\sim$1.25 R_P, where the column density is equivalent to $\sim 10^{21}$ cm^{-2} for an isothermal scale height of $H \approx 150$ km at a $T_{surf} = 2000$ K. For a magma–silicate atmosphere, as studied here, SiO or a similar species would be able to reemit in the infrared, resulting in upper atmospheric expansion and Roche lobe overflow to space.

3.2.2. Loss from Volatile Atmospheres

In the volatile cases, assuming a speciation as encountered at the H homopause, the diffusion-limited loss fluxes of primary species lie between 10^4 and 10^5 kg s^{-1} for all major species (H_2, CO, H_2O, and CO_2) in the small and large proto-Mercury cases.

The loss fluxes of minor species Na and K are several orders of magnitude lower than those of the major species, at 10^1 and 10^0 kg s^{-1}, respectively. In the nonvolatile cases, loss fluxes of Na and K are directly proportional to their thermodynamic activities in the melt. Sodium activity increases by about a factor of 4.5 from the CB to NSP melt composition and K by a factor of two between NSP source and EH4, respectively. Relative to nonvolatile cases, loss fluxes for Na and K are several orders of magnitude lower in the high-pressure, volatile-rich atmosphere at $T_{surf} = 2000$ K.

If we assume the loss fluxes of the dominant H-, C-, and O-based species at $T_{surf} = 2000$ K to be constant over the lifetime of the molten surface (Section 3.1) and integrate them for small and large Mercury volatile cases, we obtain a total mass loss by photoionization of 4.1×10^{16} kg and 1.8×10^{17} kg, respectively. This exceeds the total photoionization mass loss from the low absorbing N5 nonvolatile case by only about one order of magnitude (Figure 7). The mass loss of Na in the volatile cases, however, only contributes about 10^{12} kg of the total, which is about four orders of magnitude below the total mass loss of the nonvolatile cases. Again, this assumes that the Na loss flux is constant in the volatile case. This is deemed appropriate because Na is only a minor component of such atmospheres, is lost at slow rates that represent an insignificant fraction of its total budget, and does not condense before reaching $T_{surf} = 1500$ K.

4. Discussion

4.1. Mass Loss of Proto-Mercury

Table 5 tabulates the total atmospheric loss rates due to the following escape mechanisms: ionization $\dot{M}_{ion}$, photoevaporation $\dot{M}_U$, and plasma heating $\dot{M}_P$. Figure 8 illustrates the atmospheric level from where the degassed magma ocean atmosphere is escaping.

We find that the loss fluxes from the exobase caused by photoionization and atmospheric sputtering are supply limited

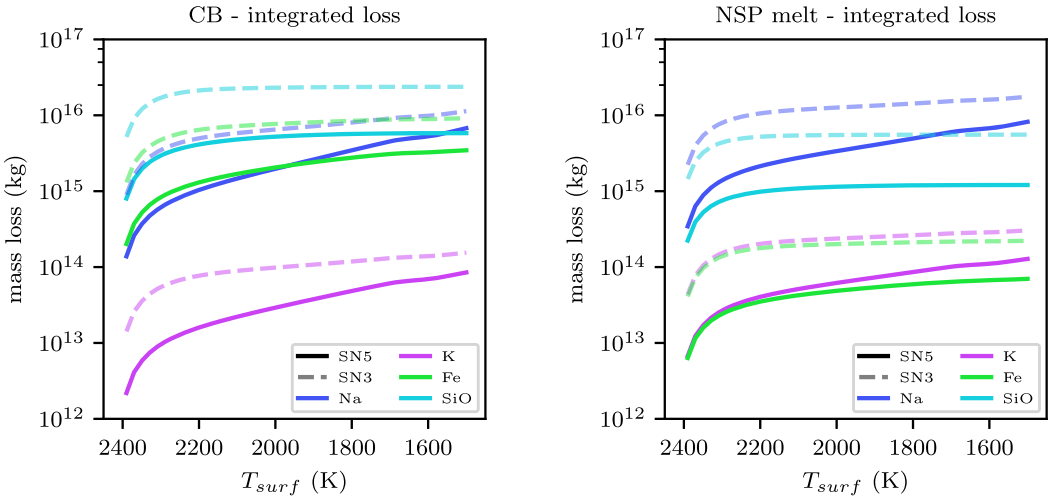

Figure 7. Integrated mass-loss rates of exospheric oxides and elements through photoionization as the magma ocean cools from a surface temperature of 2400 to 1500 K. SiO loss is shown, although it is unlikely to persist in the upper atmosphere, as it is consistently below its highest condensation temperature of $T = 1900$ K.

(in all volatile and nonvolatile cases) by homopause diffusion $\dot{M}_{\rm diff}$, which dictates the exobase elevation in order to remain in steady state. The maximum $\dot{M}_{\rm ion}$ of volatile and nonvolatile cases are comparable, even though their atmospheres are composed of different major species (nonvolatile case: Na and SiO; volatile case: H_2, H_2O, CO, and CO_2). This similarity is attributed to the higher $T_{\rm skin}$ of the nonvolatile cases at $T_{\rm surf} = 2000$ K, caused by IR opacity, which is tied to the mixing ratio of SiO. SiO pressure rapidly decreases with decreasing temperatures, which is contrary to CO_2 and H_2O in the volatile cases. A higher skin temperature in the nonvolatile cases hence compensates for the lower atmospheric pressures.

The photoevaporation rate is limited by the degree of upper atmospheric heating efficiency, $\eta_{\rm EUV}$, rather than by $\dot{M}_{\rm diff}$, as well as by the supply of gases from surface evaporation (Equation (12)). The assumption of a constant photoevaporation rate is thus only valid for evaporation at high temperatures above 1600 K, at which evaporation rates are fast enough for supply to be sustained, or for moderate mass-loss rates of about 10^7 kg s^{-1}. The majority of mass loss occurs at high temperatures (Figure 5) when surface evaporation rates are high compared to photoevaporative loss rates, the latter of which are independent of temperature and depend instead on the EUV flux.

The diffusion-limited loss rates by photoionization of the four major volatile species, H_2, H_2O, CO, and CO_2, from a volatile-rich atmosphere total $\sim 10^5$ kg s^{-1}. The loss of Na from a thick, volatile-rich atmosphere is inhibited by its low mixing ratios at the homopause and exobase. Therefore, diffusion-limited loss of Na is most efficient when the atmosphere is thin, reaching a few $\times 10^5$ kg s^{-1}, which coincides with the total mass-loss rates from volatile cases. The total integrated mass loss by photoionization from Mercury's exosphere is low for small volatile and nonvolatile cases with $\leqslant 4.1 \times 10^{16}$ kg and $\leqslant 3.0 \times 10^{16}$ kg, respectively.

The mass loss of single species is negligible compared to the total inventory of the magma ocean reservoir. For example, 0.033 wt% H_2O and a low estimate of 0.1 wt% Na in a total mass of $M_{\rm MO} \approx \times 10^{23}$ kg correspond to a reduction of the total H_2O reservoir mass (volatile cases) and Na (nonvolatile cases) by $\leqslant 0.02\%$. Assuming a well-mixed mantle reservoir, the bulk composition of Mercury would not significantly change even for species with low abundance in the reservoir and large loss rates such as H_2O, CO_2, and Na. Energy-limited escape via photoevaporation, however, can erode up to 2.3 km of Mercury's crust, which is equivalent in mass to 0.3% of small Mercury (Figure 5). Assuming small heating efficiencies, as well as a lower EUV flux, leads to integrated photoevaporation losses and eroded crust thicknesses that are reduced by four orders of magnitude.

Physical segregation between crystal and liquid during magma ocean cooling will induce chemical fractionation of element abundances with respect to those of the bulk mantle. Namely, the incompatible lithophile elements (Na, K, Al, and Ca) become enriched in late-stage liquids of a Hermean magma ocean. This effect is simulated by considering the composition of the NSP melt as a surface magma ocean analog relative to that of its inferred source. These differences notwithstanding, the partial pressures of metal-bearing gas species vary only marginally among EH4, CB, and NSP compositions. This is due to two factors: (1) vapor pressures of different elements vary by orders of magnitude among one another (e.g., compare Na with AlO), whereas abundances of these major elements vary only by a factor of 2–3 in most cases; and (2) higher mole fractions of Na and K in the NSP melt are partially compensated by their lower activity coefficients relative to the NSP source or EH4 composition. As we show in Section 3, all elements other than Na and K, and potentially Fe, condense before reaching the exobase. We can therefore conclude that the atmospheric pressure and speciation around proto-Mercury only depend on the abundance of volatile and moderately volatile elements.

4.1.1. Early Origin of Surface Na

In order to determine the potential impact of a magma-ocean-generated atmosphere on the surface composition of a small proto-Mercury, we calculate the total mass of Na in the atmosphere. We consider a hypothetical scenario in which the atmosphere collapses as soon as the first crust forms, coinciding with the termination of the magma ocean stage when a surface temperature of 1500 K is reached. To obtain a

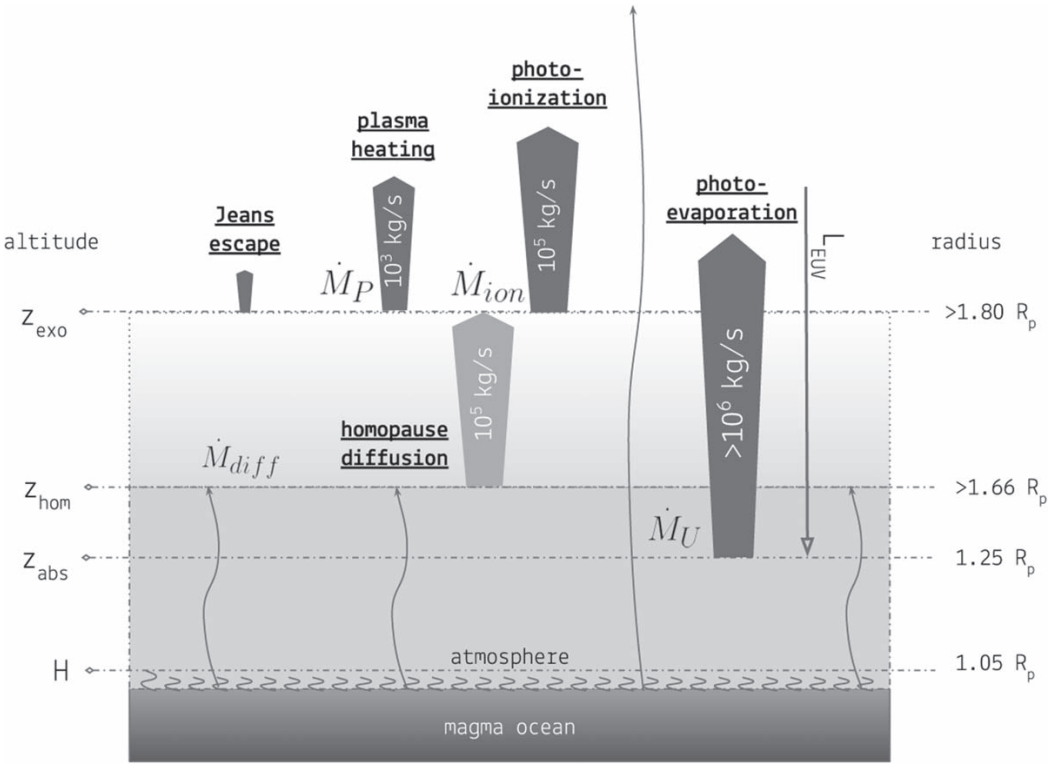

Figure 8. Mass-loss processes and their rates demonstrate the coupling between various atmospheric layers. R_P is the planet radius, z_{exo} is the exobase altitude, and z_{hom} is the homopause altitude that governs exospheric loss processes of Jeans escape, plasma heating $\dot{M}_P$, and photoionization $\dot{M}_{ion}$. z_{abs} is the absorption altitude where upper atmospheric heating (photoevaporation) $\dot{M}_U$ commences. The absorption altitude is assumed to lie below the homopause, and therefore photoevaporation is not limited by homopause diffusion.

result that is consistent with the notion of Na-poor building blocks (e.g., Humayun & Cassen 2000), we use the low-Na CB composition (Table 2) and its H- and C-absent pure Na atmosphere composition. The resulting total amount of Na integrated over the whole atmosphere yields about 10^{11} kg.

Whether it precipitates as Na metal or as another compound depends on the composition of the atmosphere that exists. Although not considered in our model, such an atmosphere would contain significant quantities of other moderately volatile elements that could combine with Na to form complex molecules, namely, F, Cl, and S. The species NaCl is inferred to be stable among volcanic gases (e.g., Aiuppa et al. 2003) and has been directly observed in Io's atmosphere (Lellouch et al. 2003; Moullet et al. 2010), and it may therefore be a potential candidate to form surficial deposits. Sodium chloride is also observed as a stable precipitate from experimentally generated volcanic gas analogs (Renggli & Klemme 2020) and is therefore likely to occur as an Na-bearing phase on the Mercurian surface. This is supported by the coinciding distribution pattern of Na and Cl from more recent volcanic deposits found in gamma-ray spectrometer data (Evans et al. 2015).

Here we consider a simplified case, for which the mass of sodium in the atmosphere is uniformly distributed over the surface of Mercury as pure, low-density, Na metal, resulting in a layer less than 1 mm for the CB case. Using a more Na-rich composition like EH4, combined with an increased atmospheric reservoir size of large proto-Mercury, would lead to a factor of four thicker Na layer, but still less than 1 mm. In the volatile cases (i.e., with CO_2 and H_2O), the amount of Na in the atmosphere is identical to the volatile-free cases, as, in our model, the partial pressure of Na is independent of the presence of volatiles. The small dissolved quantities of CO_2 and H_2O in the silicate melt ($\leqslant$1000 ppm) should thereby not influence the activity coefficients of the major rock-forming species. This hypothetical Na metal layer would not outlast meteorite impacts, which are assumed to have removed 50 m to 10 km of early crust (Hyodo et al. 2021). For the enrichment to be preserved, the atmospheric sodium would have to be incorporated into a layer with a thickness exceeding the removed crust. However, for a minimum layer of 50 m we obtain a total Na wt% increase of merely $\sim$1 ppm and $\sim$10 ppb for small and large proto-Mercury cases, respectively. We thus conclude that the collapse of an early Na-rich atmosphere would not contribute to a notable increase of Na in the surface.

4.2. Controls on Mass Loss

The mean column density at the exobase depends on the weighted average of the dominant species' CCSs. Loss rates are directly related to the exobase density. However, using CCSs from Kim & Desclaux (2002) that are about one order of magnitude smaller would reduce the homopause and exobase levels by a few tens of kilometers and decrease the homopause diffusion-limited loss by $\leqslant$2%. The sensitivity of mass loss to the chosen CCSs is therefore weak. In nonvolatile cases, if we consider that all species except Na, K, and Fe condense (FactSage in Section 3), then mean molecular mass and the CCS of the atmosphere decrease, which enhances molecular diffusion

(Equation (4)). This pushes the homopause and therefore the exobase farther from the planet surface, increasing the atmospheric surface area and therefore loss. Furthermore, the absence of SiO leads to a hotter skin temperature as the atmosphere becomes IR transparent, further enhancing loss. The difference of the ionization mass-loss rate at the exobase between an Na, K, and Fe atmosphere and an atmosphere where SiO is a major component at high temperature is thereby about a factor of three larger for all cases.

For rocky exoplanets on short orbits, the atmospheric temperature around our homopause levels (10^{-7} bars) can be as high as 3800 K for a surface temperature of 2400 K (Ito et al. 2015). Mercury possesses different planet parameters (1 $M_{\rm Earth}$ and 0.02 au vs. 0.055 $M_{\rm Earth}$ and 0.3 au for Mercury); however, the more intense early UV flux experienced by Mercury could similarly boost the temperature at the homopause. Calculations with an increased skin temperature of 3800 K at the homopause resulted in about a factor of two higher photoionization loss rates for all cases.

We used photoevaporation as a proxy for thermally driven hydrodynamic escape. Krenn et al. (2021) have shown for a large range of parameters that photoevaporation can underestimate hydrodynamic escape especially at low EUV fluxes. Given our large incident EUV fluxes of about 10^2–10^3 $\mathrm{Js^{-1}\ m^{-2}}$ and our escape parameters (Table 4), we expect to be within one order of magnitude of thermally driven hydrodynamic escape rates (compare EUV fluxes and escape parameters to Figure 4 in Krenn et al. 2021, although our escape parameters for small Mercury lie just below the shown range).

4.3. Atmospheric Evolution and Structure

Figure 8 illustrates the transport of mass away from different levels in the atmosphere. In our model, atmospheric escape can be either energy limited (e.g., $\dot{M}_U$) or diffusion limited (Jeans escape, $\dot{M}_P$, $\dot{M}_{\rm ion}$). Below we describe the role of enhanced atmospheric heating or cooling on diffusion- and energy-limited escape.

Diffusion rates are tied to the homopause density, which determines the homopause altitude. The eddy diffusion coefficient (K_{zz}) needed to determine $n_{\rm hom}$ bears large uncertainties, however. For all cases, a K_{zz} larger than the Earth-derived upper limit of 3.2×10^6 $\mathrm{cm^2\ s^{-1}}$ would most likely be adequate to accommodate proto-Mercury's increased atmospheric temperature, increasing $z_{\rm hom}$ and lowering $n_{\rm hom}$, leading to a slightly larger diffusion and therefore loss rate. Even if we assume a larger K_{zz}, however, homopause diffusion will remain the limiting factor for mass loss. We find for volatile cases that even if K_{zz} is three orders of magnitude larger, the total loss for volatile cases increases by a factor of less than two. The sensitivity of $\dot{M}_{\rm diff}$ and therefore $\dot{M}_{\rm ion}$ to the eddy diffusion coefficient is therefore weak.

Ionization could further increase the exobase temperature, and hence the reported diffusion-limited loss fluxes could be a lower limit. Whether mass loss occurs from the exobase surface, or whether it is the result of an advective outflow, is canonically assessed by the escape parameter (e.g., Genda & Abe 2003). If the escape parameter $\lambda_0 \leqslant 3$, the atmosphere experiences mass outflow owing to its nonzero net velocity, and escape occurs inward of the exobase at the sonic point (where the thermal velocity exceeds the sound speed). If $\lambda_0 \gg 3$, the atmosphere escapes because the mean free path is longer than the scale height, and Jeans escape prevails. Table 4 shows how the exospheric escape parameters are all $4 \leqslant \lambda_0 \leqslant 15$, a near-transitional escape regime between Jeans- and hydrodynamic end-members, which was recently determined to be relevant for the putative magma ocean on the Moon (Tucker et al. 2021). These authors demonstrated via direct simulation Monte Carlo simulations (Bird 1994) that cooling due to escape is important for $\lambda_0 \lesssim 15$. Therefore, in Table 4, based on our escape parameters, it would appear that although ionization may further enhance escape, cooling may temper this loss. In addition, the significant ionization rates of $\dot{M}_{\rm ion} \simeq 10^6$ $\mathrm{kg\ s^{-1}}$ at the semimajor axis of proto-Mercury promote the generation of an ionosphere that is modulated by the planetary magnetic field. Simulations on an early Mars analog have demonstrated that ion escape is efficient at removing material (Egan et al. 2019). Therefore, it is possible that we are underestimating escape by not considering magnetic interactions.

In the concurrent "energy-limited" regime it would appear that if EUV photons are able to absorb onto a sufficiently high flux of molecules (Section 3.2.1), heating would overwhelm cooling. However, based on the escape parameters in Table 4, it appears that cooling associated with escape may be important, arresting loss. At the same time, the study of low-mass, close-in exoplanets orbiting Sun-like stars has posited the idea that low-mass planets are nevertheless born with hydrogen/helium (H/He) envelopes, although these are rapidly lost owing to photoevaporation (Mordasini 2020). For an H/He envelope equivalent to 1% the mass of proto-Mercury, we find that our upper limit on photoevaporation results in the dissipation of an H/He envelope in $10^{4.4}$ yr, which is larger than the lifetime of the molten surface. The possibility of an H/He envelope to persist during the molten surface lifetime is therefore nontrivial and could result in significant heating, which could not only enhance escape but also elongate the melt lifetime past the 10^4 yr we study here.

4.4. Origin and Evolution of Mercury

The elevated core:mantle ratio, coupled with an Na- and S-rich surface, distinguishes Mercury from the other terrestrial planets. Two key hypotheses exist to account for these characteristics: (1) the preferential loss of silicate material, either by evaporation (Fegley & Cameron 1987) or by collisional stripping (Benz et al. 1988), and (2) equilibrium condensation and sorting of metal from silicate in the solar nebula (Lewis 1972; Weidenschilling 1978).

In evaluating hypothesis (1), Fegley & Cameron (1987) concluded that ∼75%–79% of silicate material would need to be lost during a fractional vaporization hypothesis to reproduce the core:mantle ratio of present-day Mercury. In this work, we show that such high fractions of loss of silicate material are untenable, be it from a small or a large proto-Mercury (total mass losses are below 0.3%). The principal reason is that atmospheric cooling timescales are too rapid with respect to evaporation and escape timescales, meaning that integrated loss rates over $\sim 10^4$ yr are small with respect to the mass of proto-Mercury. Moreover, substantial amounts of atmospheric or collisional escape of Mercury's crust are not represented in the high K/U ratio of its surface (McCubbin et al. 2012), as preferential loss of silicate material will predominantly deplete its incompatible lithophile element budget (O'Neill & Palme 2008).

There are several caveats to our conclusions, namely, that our results are valid for dry or C- and H-bearing atmospheres but do not consider the effect of other minor volatiles (Cl, S, F) on the volatility behavior of metals. Metal chlorides and metal sulfides may be important gaseous species under moderate

temperatures (~1000 K; Renggli et al. 2017), increasing their volatility. Second, conditions on the surface of Mercury may have been considerably more reduced than modeled herein (IW-5; Cartier & Wood 2019). Because the partial pressures of most metal-bearing species increase with decreasing fO_2 (Equation (1)), vaporization rates for alkali metals may be an order of magnitude higher (considering that their exponent $n = 1/4$; Sossi et al. 2019).

However, these faster evaporation rates may be offset by the presence of a surficial graphite layer on the magma ocean (Keppler & Golabek 2019). Such a layer is promoted under reducing conditions as the solubility of C in silicate melt decreases from ~360 ppm at the IW buffer to 1 ppm at IW-4 (Duncan et al. 2017; Keppler & Golabek 2019). The extent of a graphite layer therefore depends on the C content of Mercury and its fO_2, both of which are poorly known. A surficial lid would additionally delay cooling of the mantle, unless the lid is regularly broken as possibly occurred for the flotation crust on the Moon (Perera et al. 2018). Nevertheless, the net effect of a graphite lid on Mercury's magma ocean would be to reduce the extent of degassing calculated herein. Therefore, we conclude that the physicochemical characteristics of Mercury cannot have been produced during a magma ocean stage on a near fully grown planet.

These obstacles are ameliorated when considering vapor loss from planetary building blocks. Should Mercury have accreted from smaller, kilometer-size planetesimals, then melting and vaporization on the precursor bodies would have led to more efficient mass loss (e.g., Hin et al. 2017). Thus, vaporization may still be a physically viable mechanism to explain Mercury's composition, provided that it occurred on its precursor bodies. However, another problem arises because moderately volatile elements, such as Na, S, and K, are always more volatile (i.e., their partial pressures are higher for a given activity) than the major mantle components, such as Mg and Si (Sossi et al. 2019). Moreover, as demonstrated herein, Na is more easily lost with respect to Mg and Si owing to its lower molar mass and higher tendency to remain in the gas phase in an adiabatically expanding atmosphere (Section 3.2.1). As such, appealing to evaporative loss of Mg and Si to increase the core:mantle ratio while retaining Na and K is inconsistent with evaporation from a silicate melt on small planetary bodies. Therefore, other hypotheses should be considered.

5. Conclusions

We combined chemical and thermodynamic equilibrium models of the thermal evolution of Mercury's magma ocean and gaseous species derived thereof, to model the thermochemical evolution of an early atmosphere on Mercury. For an initially large Hermean mantle with initial C and H budgets comparable to those of other rocky planets, namely, Earth ("volatile cases"), the lifetime of surficial melt may have reached almost 10^4 yr. Compared to a present-day-sized proto-Mercury without a greenhouse atmosphere, this lifetime is an order of magnitude larger and therefore may enable early atmospheric mass loss to occur over an extended duration. Cases with C and H show that Mercury could have started with a 5–12 bar atmosphere. By contrast, excluding the presence of C and H species results in a thin, short-lived metal- and metal-oxide-bearing atmosphere. The upper atmospheres of volatile cases are dominated by H_2 and CO, whereas nonvolatile cases are mostly Na and SiO.

Photoionization is a minor exospheric loss mechanism, limited by homopause diffusion ($\dot{M}_{\rm diff}$) up to a maximum of a few $\times 10^5$ kg s^{-1}. If C and H volatiles are absent from the atmosphere, the $\dot{M}_{\rm diff}$ limit applies to SiO and Na. Mass-loss rates via photoevaporation, $\dot{M}_U \leqslant 10^{9.5}$ kg s^{-1}, exceed those from all other known mechanisms owing to the high EUV luminosity of the early Sun. This could in the best-case scenario erode an equivalent thickness of up to 1 km of proto-Mercury's crust when assuming high EUV heating efficiencies of 10^{-1}. Atmospheric sputtering $\dot{M}_U \sim 10^{3.4}$ kg s^{-1} (also limited by $\dot{M}_{\rm diff}$) occurs at the exobase, knocking off neutral gas molecules owing to the ram pressure of the solar wind.

By integrating atmospheric loss rates over surficial melt lifetimes, we bracket the expected total mass loss from Mercury's early atmosphere. Based on photoionization, Jeans escape, and plasma heating, the evaporation and loss of the magma ocean of proto-Mercury did not significantly modify its bulk composition. This is because magma ocean cooling times are too short to drive substantial total loss for the determined atmospheric loss fluxes. Photoevaporation can remove an equivalent crustal thickness of up to 2.3 km in about 10,000 yr, which is approximately $\sim 10^{20}$ kg of material. Integrated losses of even the most volatile elements considered here, Na and K, are insignificant with respect to their total budgets when escape is diffusion limited ($\leqslant$0.02% decrease of the initial Na composition, which would be a difference of 3×10^{-4} wt%). Hence, the present Na-rich surface composition may indicate that catastrophic volatile loss during the magma ocean stage did not occur, and that Mercury's peculiar composition is inherited from that of the solar-proximal region of the nebula from which it accreted.

Financial support has been provided by the Swiss National Science Foundation (SNSF) Fund (200021L182771/1). D.J.B. acknowledges SNSF Ambizione grant 173992. P.A.S. was supported by SNSF Ambizione grant 180025, and A.W. by the National Science Foundation EAR 1725025, as well as the Turner Postdoctoral Fellowship. Thanks to S. Suriano, P. Saxena, A. Heays, S.-M. Tsai, and N. Ligterink for discussions relating to this work. Part of this work was conducted at the Jet Propulsion Laboratory, California Institute of Technology, under contract with NASA.

Appendix A
Magma Ocean Model

The evolving surface temperature of the Hermean magma ocean is calculated using the SPIDER code, which is described in detail in Bower et al. (2018, 2019, 2021). Table A1 shows the parameters used to model proto-Mercury. The mass absorption coefficients of H and C volatile species are determined at 1.01 bar, and the coefficients of SiO at 3×10^{-6} bar.

Table A1
Standard Parameters for Magma Ocean Cases

Parameter	Value	Units
Core heat capacity	850	J kg^{-1} K^{-1}
Core density	7200	kg m^{-3}
Core radius	2000	km
Equilibrium temperature, T_∞	440	K
Gravity, g	Table 1	m s^{-2}
Planetary radius, R_P	Table 1	km
Boundary layer scaling, b	10^{-7}	K^{-2}
Al abundance[a]	19500	ppmw
$^{26}Al/Al$ (zero time)	5.25×10^{-5}	…
K abundance[b]	403	ppmw
$^{40}K/K$ (present time)	1.17×10^{-4}	…
Th abundance[b]	49	ppbw
$^{232}Th/Th$ (present time)	1	…
U abundance[b]	28	ppbw
$^{235}U/U$ (present time)	0.007	…
$^{238}U/U$ (present time)	0.993	…
H_2 mass absorption (CIA)	5×10^{-5} [d]	m^2 kg^{-1}
H_2 solubility law		
H_2O mass absorption	10^{-2} [e]	m^2 kg^{-1}
H_2O solubility law		
CO mass absorption	10^{-5} [d]	m^2 kg^{-1}
CO solubility law		
CO_2 mass absorption	10^{-4} [e]	m^2 kg^{-1}
CO_2 solubility law		
SiO mass absorption (large)	10^{-3}	m^2 kg^{-1}
SiO mass absorption (small)	10^{-5}	m^2 kg^{-1}
Initial surface temperature	2400[c]	K

Notes.
[a] Average Al abundance based on the composition of EH4 and NSP source (Table 2).
[b] Average current estimates for bulk heat source from Tosi et al. (2013) and natural abundances from Ruedas (2017).
[c] Similar to maximum temperature estimate of Mercury's surface during accretion and differentiation (Bhatia & Sahijpal 2017).
[d] Lichtenberg et al. (2021).
[e] Bower et al. (2019).

Appendix B
VapoRock Species

The species included in VapoRock are given in Table B1.

Table B1
Species Included in VapoRock (Wolf et al. 2021)

Species					
Al	AlO	AlO_2	Al_2	Al_2O	Al_2O_2
Si	SiO	SiO_2	Si_2	Si_2O_2	Si_3
K	KO	KO_2	K_2	K_2O	
Na	NaO	Na_2	Na_2O		
Mg	MgO	Mg_2			
Ca	CaO	Ca_2			
Fe	FeO				
O	O_2				

Appendix C
Modified Vulcan

We incorporated Na, Si, Mg, K, Fe, and their derivatives into VULCAN by adding 12 reactions (from kinetics.nist.gov) to the preexisting chemistry network based on C, H, and O (Table C1). We initially added more reactions but removed those that had a negligible impact on the resulting atmospheric speciation when omitted.

Table C1
Key Reactions Added to VULCAN

Reaction		
$OH + SiO$	$\rightarrow$	$SiO_2 + H$
$OH + Si$	$\rightarrow$	$SiO + H$
$Si + O_2$	$\rightarrow$	$SiO + O$
$NaO + O$	$\rightarrow$	$Na + O_2$
$Na + H_2O$	$\rightarrow$	$NaOH + H$
$H_2O + NaO$	$\rightarrow$	$NaOH + OH$
$H_2 + NaO$	$\rightarrow$	$NaOH + H$
$HCO + Na$	$\rightarrow$	$CO + NaH$
$Mg + O_2$	$\rightarrow$	$MgO + O$
$H_2O + KO$	$\rightarrow$	$KOH + OH$
$CO_2 + Fe$	$\rightarrow$	$CO + FeO$
Three-body Reactions		
$OH + K + M$	$\rightarrow$	$KOH + M$
$Na + O_2 + M$	$\rightarrow$	$NaO_2 + M$
$NaOH + M$	$\rightarrow$	$OH + Na + M$
$FeO + H_2O + M$	$\rightarrow$	$Fe(OH)_2 + M$

Note. The reactions given affect the speciation of Si, Mg, Fe, Na, K, and Si in the ranges $T = 2000$–873 K and $P = 11.7$–10^{-7} bar.

Appendix D
Collision Cross Sections

The CCSs are shown in Table D1, which were approximated by the circular area of radius equal to the atom or bond length. Furthermore, all bonds were approximated to be covalent.

Table D1
Species Cross Sections (CS) Used

Species	CS (Å^2)	Species	CS (Å^2)
H	0.88	CO_2	10.3
H_2	1.29	KOH	19.6
H_2O	2.84	Na	11.3
O	1.13	K	18.6
O_2	4.08	SiO	8.45
C	1.41	Mg	6.61
CO	4.01	Fe	7.65

Note. CS values are based on sizes of atomic, single-bond, double-bond, and triple-bond data (Clementi et al. 1967; Pyykkö & Atsumi 2009a, 2009b; Pyykkö et al. 2005).

Appendix E
Atmospheric *P–T* Profile

SPIDER determines an atmospheric pressure–temperature profile through an analytical solution to the radiative transfer equations (see Appendix in Abe & Matsui 1985 and Section 3.7.2 in Andrews 2010). The solution gives rise to the skin temperature equation (Equation (7)). Figure E1 shows the volatile (V) and nonvolatile (N3, N5) atmospheric pressure–temperature profiles that are used for FactSage and VULCAN calculations. An unphysical outcome of assuming only radiative equilibrium (no convection) is a temperature discontinuity between the base of the atmosphere and the surface of the magma ocean, which is visually more evident for the nonvolatile cases that have a small optical depth. Nevertheless, for all cases the surface temperature is 2000 K.

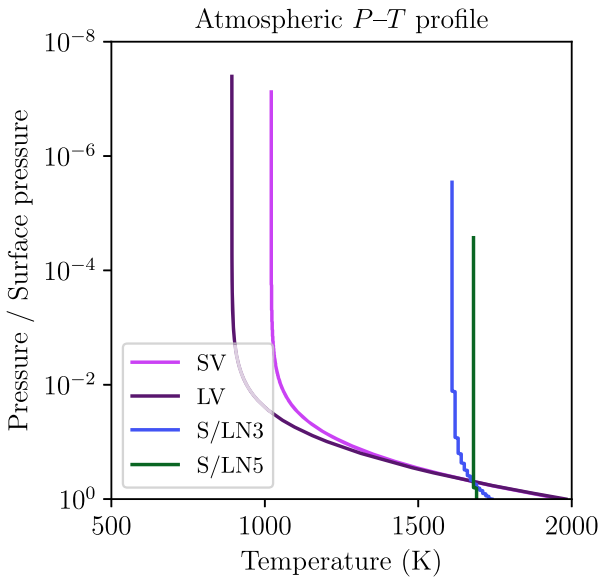

Figure E1. Atmospheric *P–T* profiles of the volatile (V) and nonvolatile (N3, N5) atmospheres surrounding a small (S) and large Mercury. The LN3 and LN5 profiles are omitted, as they are visually indistinguishable from the respective S case profiles.

ORCID iDs

Noah Jäggi https://orcid.org/0000-0002-2740-7965
Diana Gamborino https://orcid.org/0000-0002-7019-6286
Dan J. Bower https://orcid.org/0000-0002-0673-4860
Paolo A. Sossi https://orcid.org/0000-0002-1462-1882
Aaron S. Wolf https://orcid.org/0000-0003-2415-0508
Apurva V. Oza https://orcid.org/0000-0002-1655-0715
Audrey Vorburger https://orcid.org/0000-0002-7400-9142
André Galli https://orcid.org/0000-0003-2425-3793
Peter Wurz https://orcid.org/0000-0002-2603-1169

References

Abe, Y., & Matsui, T. 1985, JGRB, 90, C545
Aiuppa, A., Dongarrà, G., Valenza, M., Federico, C., & Pecoraino, G. 2003, GMS, 139, 41
Andrews, D. G. 2010, An Introduction to Atmospheric Physics (2nd ed.; Cambridge: Cambridge Univ. Press)
Asphaug, E., & Reufer, A. 2014, NatGe, 7, 564
Atreya, S. K., Sandel, B. R., Romani, P. N., et al. 1986, BAAS, 18, 758
Bale, C. W. 2016, Calphad: Computer Coupling of Phase Diagrams and Thermochemistry, 55, 1
Benz, W., Anic, A., Horner, J., & Whitby, J. A. 2008, Mercury, Space Sciences Series of ISSI, Vol. 26 (Berlin: Springer), 7
Benz, W., Slattery, W. L., & Cameron, A. 1988, Icar, 74, 516
Bhatia, G. K., & Sahijpal, S. 2017, M&PS, 52, 295
Bird, G. A. 1994, Molecular Gas Dynamics And The Direct Simulation Of Gas Flows (Berlin: Springer)
Bouvier, L. C., Costa, M. M., Connelly, J. N., et al. 2018, Natur, 558, 586
Bower, D. J., Hakim, K., Sossi, P. A., & Sanan, P. 2021, PSJ, submitted (arXiv:2108.01790)
Bower, D. J., Kitzmann, D., Wolf, A. S., et al. 2019, A&A, 631, A103
Bower, D. J., Sanan, P., & Wolf, A. S. 2018, PEPI, 274, 49
Brown, S. M., & Elkins-Tanton, L. T. 2009, E&PSL, 286, 446
Cartier, C., & Wood, B. J. 2019, Elements, 15, 39
Cassidy, T. A., McClintock, W. E., Killen, R. M., et al. 2016, GeoRL, 43, 11,121
Chao, K.-H., deGraffenried, R., Lach, M., et al. 2021, Geoch, 81, 125735
Chapman, S., & Cowling, T. G. 1970, The Mathematical Theory of Non-uniform Gases: An Account of the Kinetic Theory of Viscosity, Thermal Conduction and Diffusion in Gases (Cambridge: Cambridge Univ. Press)
Charlier, B., Grove, T. L., & Zuber, M. T. 2013, E&PSL, 363, 50
Chau, A., Reinhardt, C., Helled, R., & Stadel, J. 2018, ApJ, 865, 35
Clementi, E., Raimondi, D. L., & Reinhardt, W. P. 1967, JChPh, 47, 1300
Duncan, M. S., Dasgupta, R., & Tsuno, K. 2017, E&PSL, 466, 115
Egan, H., Jarvinen, R., Ma, Y., & Brain, D. 2019, MNRAS, 488, 2108
Elkins-Tanton, L. 2008, E&PSL, 271, 181
Elkins-Tanton, L. T. 2012, AREPS, 40, 113
Evans, L. G., Peplowski, P. N., McCubbin, F. M., et al. 2015, Icar, 257, 417
Fegley, B., & Cameron, A. G. W. 1987, E&PSL, 82, 207
Gamborino, D., Vorburger, A., & Wurz, P. 2019, AnGp, 37, 455
Gebek, A., & Oza, A. V. 2020, MNRAS, 497, 5271
Genda, H., & Abe, Y. 2003, Icar, 164, 149
Ghiorso, M. S., & Sack, R. O. 1995, CoMP, 119, 197
Gronoff, G., Arras, P., Baraka, S., et al. 2020, JGRA, 125, e27639
Grott, M., Breuer, D., & Laneuville, M. 2011, E&PSL, 307, 135
Hin, R. C., Coath, C. D., Carter, P. J., et al. 2017, Natur, 549, 511
Humayun, M., & Cassen, P. 2000, Origin of the Earth and Moon (Tucson, AZ: Univ. Arizona Press), 3
Hyodo, R., Genda, H., & Brasser, R. 2021, Icar, 354, 114064
Ito, Y., & Ikoma, M. 2021, MNRAS, 502, 750
Ito, Y., Ikoma, M., Kawahara, H., et al. 2015, ApJ, 801, 144
Johnson, R. E. 1990, Energetic Charged-Particle Interactions with Atmospheres and Surfaces (Berlin: Springer)
Johnson, R. E. 2004, ApJL, 609, L99
Johnson, R. E., Oza, A., Young, L. A., Volkov, A. N., & Schmidt, C. 2015, ApJ, 809, 43
Johnstone, C. P., Güdel, M., Brott, I., & Lüftinger, T. 2015, A&A, 577, A28
Keppler, H., & Golabek, G. 2019, Geochemical Perspectives Letters, 11, 12
Kim, Y. K., & Desclaux, J. P. 2002, PhRvA, 66, 012708
Korth, H., Anderson, B. J., Johnson, C. L., et al. 2012, JGRA, 117, A00M07
Krenn, A. F., Fossati, L., Kubyshkina, D., & Lammer, H. 2021, A&A, 650, A94
Kruijer, T. S., Touboul, M., Fischer-Gödde, M., et al. 2014, Sci, 344, 1150
Lamoreaux, R. H., & Hildenbrand, D. L. 1984, JPCRD, 13, 151
Lamoreaux, R. H., Hildenbrand, D. L., & Brewer, L. 1987, JPCRD, 16, 419
Lauretta, D. S., Goreva, J. S., Hill, D. H., & Killgore, M. 2007, LPSC, 38, 2236
Lellouch, E., Belton, M., De Pater, I., et al. 1992, Icar, 98, 271
Lellouch, E., Paubert, G., Moses, J. I., Schneider, N. M., & Strobel, D. F. 2003, Natur, 421, 45
Lewis, J. S. 1972, E&PSL, 15, 286
Lichtenberg, T., Bower, D. J., Hammond, M., et al. 2021, JGRE, 126, e06711
McCoy, T. J., Peplowski, P. N., McCubbin, F. M., & Weider, S. Z. 2018, in Mercury: The View after MESSENGER, ed. S. C. Solomon, L. R. Nittler, & B. J. Anderson (Cambridge: Cambridge Univ. Press), 176
McCubbin, F. M., Riner, M. A., Vander Kaaden, K. E., & Burkemper, L. K. 2012, GeoRL, 39, L09202
Mordasini, C. 2020, A&A, 638, A52
Moullet, A., Gurwell, M. A., Lellouch, E., & Moreno, R. 2010, Icar, 208, 353
Murray-Clay, R. A., Chiang, E. I., & Murray, N. 2009, ApJ, 693, 23
Namur, O., Collinet, M., Charlier, B., et al. 2016, E&PSL, 439, 117
Nittler, L. R., Starr, R. D., Weider, S. Z., et al. 2011, Sci, 333, 1847
Nittler, L. R., & Weider, S. Z. 2019, Elements, 15, 33

O'Neill, H. S. C., & Eggins, S. M. 2002, ChGeo, 186, 151
O'Neill, H. S. C., & Palme, H. 2008, RSPTA, 366, 4205
Oza, A. V., Johnson, R. E., Lellouch, E., et al. 2019, ApJ, 885, 168
Peplowski, P. N., Evans, L. G., Stockstill-Cahill, K. R., et al. 2014, Icar, 228, 86
Perera, V., Jackson, A. P., Elkins-Tanton, L. T., & Asphaug, E. 2018, JGRE, 123, 1168
Pyykkö, P., & Atsumi, M. 2009a, CEJ, 15, 186
Pyykkö, P., & Atsumi, M. 2009b, CEJ, 15, 12770
Pyykkö, P., Riedel, S., & Patzschke, M. 2005, CEJ, 11, 3511
Renggli, C. J., King, P. L., Henley, R. W., & Norman, M. D. 2017, GeCoA, 206, 296
Renggli, C. J., & Klemme, S. 2020, JVGR, 400, 106929
Ribas, Á., Merín, B., Bouy, H., & Maud, L. T. 2014, A&A, 561, A54
Ruedas, T. 2017, GGG, 18, 3530
Semenov, D., Henning, T., Helling, C., Ilgner, M., & Sedlmayr, E. 2003, A&A, 410, 611
Siegfried, R. W., & Solomon, S. C. 1974, Icar, 23, 192
Sossi, P. A., & Fegley, B. 2018, RvMG, 84, 393
Sossi, P. A., Klemme, S., O'Neill, H. S., Berndt, J., & Moynier, F. 2019, GeCoA, 260, 204
Spohn, T. 1991, Icar, 90, 222
Stevenson, D. J. 1990, in Origin of the Earth, ed. H. E. Newsom & J. H. Jones (New York: Oxford Univ. Press), 231
Stevenson, D. J., Spohn, T., & Schubert, G. 1983, Icar, 54, 466
Thomas, N., Bagenal, F., Hill, T. W., & Wilson, J. K. 2004, in Jupiter: the planet, satellites and magnetosphere, ed. F. Bagenal, T. E. Dowling, & W. B. McKinnon, Vol. 1 (Cambridge: Cambridge Univ. Press), 561
Tosi, N., Grott, M., Plesa, A.-C., & Breuer, D. 2013, JGRE, 118, 2474
Tsai, S.-M., Lyons, J. R., Grosheintz, L., et al. 2017, ApJS, 228, 20
Tsai, S.-M., Malik, M., Kitzmann, D., et al. 2021, arXiv:2108.01790
Tu, L., Johnstone, C. P., Güdel, M., & Lammer, H. 2015, A&A, 577, L3
Tucker, O. J., Killen, R. M., Johnson, R. E., & Saxena, P. 2021, Icar, 359, 114304
Vander Kaaden, K. E., & McCubbin, F. M. 2016, GeCoA, 173, 246
Visscher, C., & Fegley, B. 2013, ApJL, 767, 12
Vlasov, M. N., & Kelley, M. C. 2015, AnGeo, 33, 857
Volkov, A. N., & Johnson, R. E. 2013, ApJ, 765, 90
Vorburger, A., Wurz, P., Lammer, H., Barabash, S., & Mousis, O. 2015, Icar, 262, 14
Watson, A. J., Donahue, T. M., & Walker, J. C. G. 1981, Icar, 48, 150
Weidenschilling, S. J. 1978, Icar, 35, 99
Weisberg, M. K., Prinz, M., Clayton, R. N., et al. 2000, M&PS, 36, 401
Weisberg, M. K., Prinz, M., & Nehru, C. E. 1990, Metic, 25, 269
Wiik, H. B. 1956, GeCoA, 9, 279
Wolf, A. S., Jäggi, N., Sossi, P. A., Bower, D. J., & Ghiorso, M. S. 2021, VapoRock: Thermodynamics of vaporized silicate rocks & melts for modeling magma ocean atmospheres and stellar nebula, v0.1, Zenodo doi:10.5281/zenodo.4594226
Wurz, P., & Lammer, H. 2003, Icar, 164, 1

Chapter 5

Conclusions

5.1 Advances in sputtering

Sample preparation and laboratory experiments In the context of this thesis I have successfully sourced and transformed minerals that serve as analogues for Mercury and the Moon. This includes the pyroxenes enstatite ($MgSiO_3$) and diopside ($(Ca,Mg)_2Si_2O_6$), as well as the plagioclase labradorite ($Na_{0.4}Ca_{0.6}Al_{1.6}Si_{2.4}O_8$). Furthermore, the lunar regolith sample (68501) was successfully pressed into pellets which have since been irradiated. Direct comparisons to glassy thin-films created through pulsed laser deposition (PLD) from the comparably rough pressed powder pellets has shown that the difference in yield can be explained solely by surface roughness [1]. I can conclude, that the effect of a crystal lattice is not noticeable when comparing mass yields between pellets and thin-films.

Nevertheless, the use of pellets bears several advantages:

- Unlike thin-films or more regolith-like loose powder, pellets approximate the rough surface of a powder with the sturdiness of a thin-film.
- To create a thin-film, large enough compact samples of ideally ≥ 10 mm in diameter are required for ablation. For this purpose, pressed pellets from enstatite powder and Lunar regolith were necessary.
- The irradiation of pellets allowed us to quantify the effect of surface roughness on sputter yield [1].

- The stable nature of a pellet allows for extensive pre- and post-irradiation surface analyses not possible with a powder sample.

Sputter model recreating laboratory data SDTrimSP does a good job recreating sputter data, unlike TRIM, which is part of the widely used SRIM package. The accuracy of recreating experimental results was further enhanced by two models that can increase binding energies and set realistic mineral densities based on tabulated data of mineral components.

The new SDTrimSP models can recreate data exceptionally well. The angular distributions are still underestimated in terms of the degree of forward-sputtering however. I expect that this is mostly tied to the fact that only oxides or atomic species are considered. Larger binding energies might be achieved if the atomic species are allowed to form one of many possible intermediates. The current implementation will always break up the compound and one of the products will continue to travel through the sample. If there are enough free elements available, only the original oxide can form, and therefore the model is limited to

$$SiO_2 \rightleftharpoons Si + O + O \qquad [R1]$$

For the example of silica (SiO_2) a more sophisticated model would need to include the following reactions:

$$SiO_2 \rightleftharpoons Si + O_2 \qquad [R2]$$

$$SiO_2 \rightleftharpoons SiO + O \qquad [R3]$$

$$Si + Si \rightleftharpoons Si_2 \qquad [R4]$$

which increase the number of modeled components from four (unbound Si, unbound O, and bound Si and O in SiO_2) to eight (bound Si and O in SiO, bound O in O_2, and bound Si in Si_2). Each non-atomic species has bond-strengths, which have to be overcome. The effect would thus be somewhere in between the hybrid model (HB), and the hybrid compound model (HB-C) demonstrated in in Chapter 3. To properly evaluate the discrepancy between the newly suggested models and a realistic sputtering behavior, laboratory

experiments investigating the energy distribution of the sputtered neutral particles are necessary.

Importance of sputtering The results in Chapter 3 show a 80% decrease in yield between H^+/He^+ sputtering laboratory results and the still commonly used SRIM package. Although only mentioned in passing, potential sputtering by solar wind He_2^+ is expected to enhance overall sputter yields by 40% [280]. Compared to the 80% decrease in yield between previously used sputter models and laboratory results however, this enhancement would not be enough to prevent ion sputtering to lose in significance when viewed alone. Nevertheless, a better understanding of the sputter process not only allows for better discrimination of space weathering processes, but also opens up modeling process interactions (Sec. 5.3.3).

5.2 Constraints on Mercury's origins

Limitations on evaporative loss Mercury's magma ocean lifetimes are short, even if emissivity is severely reduced by a thick H-C-O atmosphere (500–10000 years). All but one atmospheric loss process was deemed insufficient to cause any substantial loss of Mercury's magma ocean-sourced atmosphere. The exception is upper atmospheric heating. The large uncertainties about the heating efficiency spanning two orders of magnitude can make the process either the main driver of atmospheric loss or negligible. For the species of interest at Mercury, sodium, the conclusion of Chapter 4 is that no amount of atmospheric loss can significantly alter Mercury's initial sodium content. And in general, an early atmosphere around Mercury sourced from either magma ocean evaporation or degassing of volatiles, is not significantly altered by atmospheric loss over the magma ocean lifetime under non-extreme space-weather conditions. This is in line with MESSENGER/GRS detections of uranium and potassium accumulations which is expected to deplete through extensive evaporation. MESSENGER/GRS instead detected 1150 ± 220 ppm K, 220 ± 60 ppm Th, and 90 ± 20 ppm U [309], which implies that the upper mantle did not deplete in volatiles and as a consequence the early crust was

able to accumulate K, Th and U following the partial melting of the upper mantle [310].

5.3 Open questions and future work

The process of kinetic sputtering has so far been well reproducible for flat, glassy thin-films produced from major rock-forming minerals. These first successes are however limited to the total mass yield of the sputter process and a small selection of mineral–thin-film combinations.

5.3.1 Sample properties

Although the amount of laboratory sputter data for minerals relevant for the Moon and Mercury has increased significantly within the scope of this thesis, some major rock-forming minerals are still outstanding. This includes Na-poor to intermediate Na plagioclase (X_{Na} = 0.2-0,5; $Na_{1-x}Ca_xAl_{1+x}Si_{3-x}O_8$), ilmenite ($FeTiO_3$) for the Moon, and sulfides like CaS and MgS for Mercury. These minerals would be paramount to quantify the supply of Na, Ca, Al, Fe, Ti, and S to the respective exospheres. For Ca and Mg-sulfides I would expect a different sputtering behavior because of irradiation induced diffusion, as it occurs in the irradiated Fe-sulfide troilite FeS [311].

Grain size Mineral powder pellets are limited to small grain sizes due to an otherwise insufficient cohesion. The grain size requirement of $\leq 30\,\mu m$ thereby underestimates average lunar regolith [60–80 μm; 9] but might be appropriate for the more intensely weathered regolith of Mercury [possibly $\leq 45\,\mu m$; 116]. Large levels of vitrification could however prevent accumulation of small grain sizes whilst keeping the regolith 'smooth' on the 100 μm level [116].

Surface roughness and porosity The effect of roughness on the sputter yields of mineral pellets has been addressed in the work of Biber *et al.* [1] but is limited to a single pellet–thin-film comparison. The effect that realistic, highly porous and uncompressed regolith would have on sputter yields can be estimated, but remains obscure. Working with uncompressed powder with constrained

intergrain porosity would thereby be ideal but bears challenges due to the suspension-setup of irradiation chambers and for quantifying surface-porosity.

Bulk porosity During this thesis, I obtained bulk porosity measurements of mineral pellets which were ultimately discarded due to the methodology not being applicable to the relevant mineral powder pellets which had to be pressed directly into metal holders. The process would be applicable for uncompressed, porous powders as well but one would have to assume that the porosity between the surface grains coincides with the porosity of the compressed bulk. Also, it is important to note that uncompressed material will express not only intergrain porosity but also an unavoidable surface roughness. Therefore, addressing the effect of roughness first with laboratory experiments is more reasonable because of the expected roughness of a porous sample, and due to the limitations and uncertainties related to creating well-characterized, porous samples.

5.3.2 Analysis methods

Extensive work is still needed to understand sputtering and validate models. This includes obtaining a) the speciation, energy- and angular-distribution of the sputtered material and b) a high-resolution characterization of the irradiated surfaces on a nm-level before and after irradiation, or better, whilst irradiating. An in-situ characterization of the sample would also allow for observing sputter-mediated diffusion. This plays an especially important role in sulfides, as it was shown for troilite FeS by Christoph *et al.* [311].

As an example, total mass yields of Na-bearing plagioclase glass irradiated by solar wind ions was obtained by Hijazi *et al.* [276, 277]. Without obtaining the speciation and the velocity distribution of sputtered material however, it is not possible to argue for or against ion sputtering as a contributing source of sodium. As introduced in Section 1.2, exospheric sodium on Mercury follows the solar wind precipitation pattern, but the velocities of the observed sodium are too low [265, 266]. As an alternative to the irradiation-mediated photon stimulated desorption, the sodium could instead be loosely adsorbed to the surface, which severely reduces binding energies and therefore the mean energy

of the ejecta. This would agree with the observation of latitude-dependent Na in the top layers of Mercury's regolith [41].

5.3.3 Combined processes in laboratory experiments

In the light of the proposed ion sputtering mediated Photon Stimulated Desorption it would be of interest to perform measurements that combine space weathering processes. Accelerating micrometeoroids in the lab might not be reconcilable with a sputter setup, however photons, electrons and heat is. The contribution of ion sputtering alone may be lower than previously anticipated, but this does not make sputtering insignificant as a driver of space weathering!

Recommended literature

Mercury

R. M. Killen, G. Cremonese, H. Lammer, *et al.*, "Processes that promote and deplete the exosphere of mercury," in *Space Science Reviews*, vol. 132, Springer, New York, NY, 2007, pp. 433–509. DOI: 10.1007/s11214-007-9232-0

J. A. Slavin, M. H. Acuña, B. J. Anderson, *et al.*, "MESSENGER observations of magnetic reconnection in Mercury's magnetosphere.," *Science*, vol. 324, no. 5927, pp. 606–610, May 2009. DOI: 10.1126/science.1172011

J. Benkhoff, J. van Casteren, H. Hayakawa, *et al.*, "BepiColombo — Comprehensive exploration of Mercury: Mission overview and science goals," *Planetary and Space Science*, vol. 58, no. 1-2, pp. 2–20, Jan. 2010. DOI: 10.1016/J.PSS.2009.09.020

S. L. Murchie, R. L. Klima, B. W. Denevi, *et al.*, "Orbital multispectral mapping of Mercury with the MESSENGER Mercury Dual Imaging System: Evidence for the origins of plains units and low-reflectance material," *Icarus*, vol. 254, pp. 287–305, Jul. 2015. DOI: 10.1016/J.ICARUS.2015.03.027

D. L. Domingue and C. T. Russell, *The MESSENGER mission to Mercury*. New York: Springer Science & Business Media, 2007. DOI: 10.1007/978-0-387-77214-1

D. L. Domingue, C. R. Chapman, R. M. Killen, *et al.*, "Mercury's weather-beaten surface: Understanding mercury in the context of lunar and asteroidal space

weathering studies," *Space Science Reviews*, vol. 181, no. 1-4, pp. 121–214, Apr. 2014. DOI: 10.1007/S11214-014-0039-5

S. C. Solomon, L. R. Nittler, and B. J. Anderson, *Mercury: The View after MESSENGER*. Cambridge, United Kingdom: Cambridge University Press, Jan. 2018, pp. 1–584. DOI: 10.1017/9781316650684

J. M. Raines, R. M. Dewey, N. M. Staudacher, *et al.*, "Proton precipitation in Mercury's northern magnetospheric cusp," *Journal of Geophysical Research: Space Physics*, e2022JA030397, Oct. 2022. DOI: 10.1029/2022JA030397

The Moon

G. H. Heiken, D. T. Vaniman, and B. M. French, Eds., *Lunar sourcebook-A user's guide to the moon*. Cambridge, United Kingdom: Cambridge University Press, 1991, p. 753

M. A. Wieczorek, B. L. Jolliff, A. Khan, *et al.*, "The Constitution and Structure of the Lunar Interior," *Reviews in Mineralogy and Geochemistry*, vol. 60, no. 1, pp. 221–364, Jan. 2006. DOI: 10.2138/RMG.2006.60.3

Atmo- and exospheres

G. Gronoff, P. Arras, S. Baraka, *et al.*, "Atmospheric Escape Processes and Planetary Atmospheric Evolution," *Journal of Geophysical Research: Space Physics*, vol. 125, no. 8, Aug. 2020. DOI: 10.1029/2019JA027639. arXiv: 2003.03231

C. Grava, R. M. Killen, M. Benna, *et al.*, "Volatiles and Refractories in Surface-Bounded Exospheres in the Inner Solar System," *Space Science Reviews 2021 217:5*, vol. 217, no. 5, pp. 1–47, May 2021. DOI: 10.1007/S11214-021-00833-8

Infrared

W. E. McClintock and M. R. Lankton, "The mercury atmospheric and surface composition spectrometer for the MESSENGER mission," *Space Science Reviews*,

vol. 131, no. 1-4, pp. 481–521, Jul. 2007. DOI: 10.1007/S11214-007-9264-5/METRICS

D. A. Rothery, M. Massironi, G. Alemanno, *et al.*, "Rationale for BepiColombo Studies of Mercury's Surface and Composition," *Space Science Reviews*, vol. 216, no. 4, p. 66, Jun. 2020. DOI: 10.1007/s11214-020-00694-7

Space weathering

P. Wurz, S. Fatemi, A. Galli, *et al.*, "Particles and Photons as Drivers for Particle Release from the Surfaces of the Moon and Mercury," *Space Science Reviews 2022 218:3*, vol. 218, no. 3, pp. 1–83, Mar. 2022. DOI: 10.1007/S11214-022-00875-6

Electron stimulated desorption

J. L. McLain, A. L. Sprague, G. A. Grieves, *et al.*, "Electron-stimulated desorption of silicates: A potential source for ions in Mercury's space environment," *Journal of Geophysical Research: Planets*, vol. 116, no. E3, p. 3007, Mar. 2011. DOI: 10.1029/2010JE003714

Meteroids impact vaporization

D. Janches, A. A. Berezhnoy, A. A. Christou, *et al.*, "Meteoroids as One of the Sources for Exosphere Formation on Airless Bodies in the Inner Solar System," *Space Science Reviews 2021 217:4*, vol. 217, no. 4, pp. 1–41, Apr. 2021. DOI: 10.1007/S11214-021-00827-6

Sputtering

R. Behrisch and W. Eckstein, *Sputtering by particle bombardment : experiments and computer calculations from threshold to MeV energies*. Springer, 2007, p. 507

J. Brötzner, "An Optimised catcher-QCM setup to study the sputtering of Lunar and Hermean surface regolith analogues," PhD thesis, TU Wien, 2022, p. 66. DOI: 10.34726/HSS.2022.91601

Bibliography

[1] H. Biber, J. Brötzner, N. Jäggi, P. S. Szabo, J. Pichler, C. Cupak, *et al.*, "Sputtering Behavior of Rough, Polycrystalline Mercury Analogs," *The Planetary Science Journal*, vol. 3, no. 12, p. 271, Dec. 2022. DOI: 10.3847/PSJ/ACA402.

[2] R. H. Lamoreaux and D. L. Hildenbrand, "High-Temperature Vaporization Behavior of Oxides. I. Alkali Metal Binary Oxides," *Journal of Physical and Chemical Reference Data*, vol. 13, no. 1, pp. 151–173, Jan. 1984. DOI: 10.1063/1.555706.

[3] R. H. Lamoreaux, D. L. Hildenbrand, and L. Brewer, "High-Temperature Vaporization Behavior of Oxides II. Oxides of Be, Mg, Ca, Sr, Ba, B, Al, Ga, In, Tl, Si, Ge, Sn, Pb, Zn, Cd, and Hg," *Journal of Physical and Chemical Reference Data*, vol. 16, no. 3, pp. 419–443, Jul. 1987. DOI: 10.1063/1.555799.

[4] A. S. Wolf, N. Jäggi, P. A. Sossi, and D. J. Bower, "VapoRock: Thermodynamics of Vaporized Silicate Melts for Modeling Volcanic Outgassing and Magma Ocean Atmospheres," *The Astrophysical Journal*, vol. 947, no. 2, p. 64, Apr. 2023. DOI: 10.3847/1538-4357/ACBCC7.

[5] C. Cupak, P. S. Szabo, H. Biber, R. Stadlmayr, C. Grave, M. Fellinger, *et al.*, "Sputter yields of rough surfaces: Importance of the mean surface inclination angle from nano- to microscopic rough regimes," *Applied Surface Science*, vol. 570, p. 151 204, Dec. 2021. DOI: 10.1016/J.APSUSC.2021.151204.

[6] H. Lammer, P. Wurz, M. R. Patel, R. M. Killen, C. Kolb, S. Massetti, S. Orsini, and A. Milillo, "The variability of Mercury's exosphere by particle and radiation induced surface release processes," *Icarus*, vol. 166, no. 2, pp. 238–247, Dec. 2003. DOI: 10.1016/j.icarus.2003.08.012.

[7] P. Wurz, J. A. Whitby, U. Rohner, J. A. Martín-Fernández, H. Lammer, and C. Kolb, "Self-consistent modelling of Mercury's exosphere by sputtering, micro-meteorite impact and photon-stimulated desorption," *Planetary and Space Science*, vol. 58, no. 12, pp. 1599–1616, Oct. 2010. DOI: 10.1016/J.PSS.2010.08.003.

[8] R. M. Killen, L. S. Morrissey, M. H. Burger, R. J. Vervack, O. J. Tucker, and D. W. Savin, "The Influence of Surface Binding Energy on Sputtering in Models of the Sodium Exosphere of Mercury," *The Planetary Science Journal*, vol. 3, no. 6, p. 139, Jun. 2022. DOI: 10.3847/PSJ/AC67DE.

[9] G. H. Heiken, D. T. Vaniman, and B. M. French, Eds., *Lunar sourcebook-A user's guide to the moon*. Cambridge, United Kingdom: Cambridge University Press, 1991, p. 753.

[10] K. E. Vander Kaaden, F. M. McCubbin, P. K. Byrne, N. L. Chabot, C. M. Ernst, C. L. Johnson, and M. S. Thompson, "Revolutionizing Our Understanding of the Solar System via Sample Return from Mercury," *Space Science Reviews*, vol. 215, no. 8, p. 49, Dec. 2019. DOI: 10.1007/s11214-019-0614-x.

[11] J. Benkhoff, J. van Casteren, H. Hayakawa, M. Fujimoto, H. Laakso, M. Novara, P. Ferri, H. R. Middleton, and R. Ziethe, "BepiColombo — Comprehensive exploration of Mercury: Mission overview and science goals," *Planetary and Space Science*, vol. 58, no. 1-2, pp. 2–20, Jan. 2010. DOI: 10.1016/J.PSS.2009.09.020.

[12] J. V. Smith, A. T. Anderson, R. C. Newton, E. J. Olsen, A. V. Crewe, M. S. Isaacson, D. Johnson, and P. J. Wyllie, "Petrologic history of the moon inferred from petrography, mineralogy and petrogenesis of Apollo 11 rocks," *Geochimica et Cosmochimica Acta Supplement, Volume 1. Proceedings of the Apollo 11 Lunar Science Conference held 5-8 January, 1970 in Houston,*

TX. Volume 1: Mineraolgy and Petrology. Edited by A. A. Levinson. New York: Pergammon Press, 1970., p.897, vol. 1, p. 897, 1970.

[13] J. A. Wood, J. Dickey J. S., U. B. Marvin, and B. N. Powell, "Lunar anorthosites and a geophysical model of the moon," *Geochimica et Cosmochimica Acta Supplement, Volume 1. Proceedings of the Apollo 11 Lunar Science Conference held 5-8 January, 1970 in Houston, TX. Volume 1: Mineraolgy and Petrology. Edited by A. A. Levinson. New York: Pergammon Press, 1970., p.965*, vol. 1, p. 965, 1970.

[14] P. H. Warren and J. T. Wasson, "Pristine nonmare rocks and the nature of the lunar crust.," *In: Lunar Science Conference, 8th, Houston, Tex., March 14-18, 1977, Proceedings. Volume 2. (A78-41551 18-91) New York, Pergamon Press, Inc., 1977, p. 2215-2235.*, vol. 2, p. 2215, 1977.

[15] P. H. Warren and J. T. Wasson, "The origin of KREEP," *Rev. Geophys. Space Phys*, vol. 17, pp. 73–88, 1979.

[16] P. H. Warren, "The Magma Ocean Concept and Lunar Evolution," *Annual Review of Earth and Planetary Sciences*, vol. 13, no. 1, pp. 201–240, Nov. 1985. DOI: 10.1146/annurev.ea.13.050185.001221.

[17] M. E. Pritchard and D. J. Stevenson, "Thermal Aspects of a Lunar Origin by Giant Impact," in *Origin of the Earth and Moon*, 2000, pp. 179–196. DOI: 10.2307/j.ctv1v7zdrp.16.

[18] C. K. Shearer and J. J. Papike, "Magmatic evolution of the Moon," *American Mineralogist*, vol. 84, no. 10, pp. 1469–1494, Oct. 1999. DOI: 10.2138/AM-1999-1001.

[19] S. C. Solomon and J. Longhi, "Magma oceanography: 1. Thermal evolution.," *In: Lunar Science Conference, 8th, Houston, Tex., March 14-18, 1977, Proceedings. Volume 1. (A78-41551 18-91) New York, Pergamon Press, Inc., 1977, p. 583-599.*, vol. 1, p. 583, 1977.

[20] M. A. Wieczorek, B. L. Jolliff, A. Khan, M. E. Pritchard, B. P. Weiss, J. G. Williams, *et al.*, "The Constitution and Structure of the Lunar Interior," *Reviews in Mineralogy and Geochemistry*, vol. 60, no. 1, pp. 221–364, Jan. 2006. DOI: 10.2138/RMG.2006.60.3.

[21] J. W. Head, "Lunar volcanism in space and time," *Reviews of Geophysics*, vol. 14, no. 2, pp. 265–300, May 1976. DOI: 10.1029/RG014I002P00265.

[22] I. S. McCallum and J. M. Schwartz, "Lunar Mg suite: Thermobarometry and petrogenesis of parental magmas," *Journal of Geophysical Research: Planets*, vol. 106, no. E11, pp. 27 969–27 983, Nov. 2001. DOI: 10.1029/2000JE001397.

[23] G. Heiken and D. S. McKay, "Petrography of Apollo 17 soils," in *Lunar and Planetary Science Conference Proceedings*, vol. 5, 1974, pp. 843–860.

[24] D. L. Domingue, C. R. Chapman, R. M. Killen, T. H. Zurbuchen, J. A. Gilbert, M. Sarantos, *et al.*, "Mercury's weather-beaten surface: Understanding mercury in the context of lunar and asteroidal space weathering studies," *Space Science Reviews*, vol. 181, no. 1-4, pp. 121–214, Apr. 2014. DOI: 10.1007/S11214-014-0039-5.

[25] D. S. McKay, G. H. Heiken, A. Basu, G. Blanford, S. B. Simon, R. Reedy, B. M. French, and J. Papike, "The Lunar Regolith," in *Lunar sourcebook-A user's guide to the moon*, G. H. Heiken, D. T. Vaniman, and B. M. French, Eds., Cambridge, United Kingdom: Cambridge University Press, 1991, ch. 7, pp. 285–356.

[26] J. M. Raines, R. M. Dewey, N. M. Staudacher, P. J. Tracy, C. M. Bert, M. Sarantos, *et al.*, "Proton precipitation in Mercury's northern magnetospheric cusp," *Journal of Geophysical Research: Space Physics*, e2022JA030397, Oct. 2022. DOI: 10.1029/2022JA030397.

[27] E. D. Gault, F. Horz, E. Brownlee, and B. J. Hartung, "Mixing of the lunar regolith," in *Proceedings of the Fifth Lunar Science Conference*, vol. 3, Houston, Texas: Pergamon Press, Inc., 1974, pp. 2365–2386.

[28] E. S. Costello, R. R. Ghent, and P. G. Lucey, "The mixing of lunar regolith: Vital updates to a canonical model," *Icarus*, vol. 314, pp. 327–344, Nov. 2018. DOI: 10.1016/J.ICARUS.2018.05.023.

[29] C. M. Pieters and S. K. Noble, "Space weathering on airless bodies," *Journal of Geophysical Research: Planets*, vol. 121, no. 10, pp. 1865–1884, Oct. 2016. DOI: 10.1002/2016JE005128@10.1002/(ISSN)2169-9100.JGRE25.

[30] L. A. Taylor, C. M. Pieters, and D. Britt, "Evaluations of lunar regolith simulants," *Planetary and Space Science*, vol. 126, pp. 1–7, Jul. 2016. DOI: 10.1016/J.PSS.2016.04.005.

[31] B. M. Bansal, S. E. Church, P. W. Gast, N. J. Hubbard, J. M. Rhodes, and H. Wiesmann, "The chemical composition of soil from the Apollo 16 and Luna 20 sites," *Earth and Planetary Science Letters*, vol. 17, no. 1, pp. 29–35, Dec. 1972. DOI: 10.1016/0012-821X(72)90256-7.

[32] S. R. Taylor, M. P. Gorton, P. Muir, W. B. Nance, R. Rudowski, and N. Ware, "Composition of the Descartes region, lunar highlands," *Geochimica et Cosmochimica Acta*, vol. 37, no. 12, pp. 2665–2683, Dec. 1973. DOI: 10.1016/0016-7037(73)90271-8.

[33] G. H. Heiken, D. S. McKay, and R. M. Fruland, "Apollo 16 soils: Grain size analyses and petrography," *Proceedings of the Lunar Science Conference, vol. 4, p.251*, vol. 4, p. 251, 1973.

[34] R. L. Korotev, "Compositional Trends in Apollo 16 Soils," *Lunar and Planetary Science Conference XXII*, pp. 565–567, Mar. 1981.

[35] K. J. Houck, "Petrologic variations in Apollo 16 surface soils," *Journal of Geophysical Research: Solid Earth*, vol. 87, no. S01, A197–A209, Nov. 1982. DOI: 10.1029/JB087IS01P0A197.

[36] T. J. McCoy, P. N. Peplowski, F. M. McCubbin, and S. Z. Weider, "The Geochemical and Mineralogical Diversity of Mercury," in *Mercury: The View after MESSENGER*, S. C. Solomon, L. R. Nittler, and B. J. Anderson, Eds., vol. 21, Cambridge, United Kingdom: Cambridge University Press, 2018, ch. 7, pp. 176–190. DOI: 10.1017/9781316650684.008.

[37] S. E. Hawkins, J. D. Boldt, E. H. Darlington, R. Espiritu, R. E. Gold, B. Gotwols, *et al.*, "The mercury dual imaging system on the MESSENGER spacecraft," *Space Science Reviews*, vol. 131, no. 1-4, pp. 247–338, Aug. 2007. DOI: 10.1007/s11214-007-9266-3.

[38] S. A. Hauck, J.-L. Margot, S. C. Solomon, R. J. Phillips, C. L. Johnson, F. G. Lemoine, *et al.*, "The curious case of Mercury's internal structure," *Journal of Geophysical Research: Planets*, vol. 118, no. 6, pp. 1204–1220, Jun. 2013. DOI: 10.1002/jgre.20091.

[39] S. M. Brown and L. T. Elkins-Tanton, "Compositions of Mercury's earliest crust from magma ocean models," *Earth and Planetary Science Letters*, vol. 286, no. 3-4, pp. 446–455, Sep. 2009. DOI: 10.1016/J.EPSL.2009.07.010.

[40] K. E. Vander Kaaden and F. M. McCubbin, "The origin of boninites on Mercury: An experimental study of the northern volcanic plains lavas," *Geochimica et Cosmochimica Acta*, vol. 173, pp. 246–263, Jan. 2016. DOI: 10.1016/j.gca.2015.10.016.

[41] P. N. Peplowski, L. G. Evans, K. R. Stockstill-Cahill, D. J. Lawrence, J. O. Goldsten, T. J. McCoy, *et al.*, "Enhanced sodium abundance in Mercury's north polar region revealed by the MESSENGER Gamma-Ray Spectrometer," *Icarus*, vol. 228, pp. 86–95, Jan. 2014. DOI: 10.1016/J.ICARUS.2013.09.007.

[42] L. R. Nittler and S. Z. Weider, "The surface composition of mercury," *Elements*, vol. 15, no. 1, pp. 33–38, Feb. 2019. DOI: 10.2138/gselements.15.1.33.

[43] D. S. Ebel and C. M. Alexander, "Equilibrium condensation from chondritic porous IDP enriched vapor: Implications for Mercury and enstatite chondrite origins," *Planetary and Space Science*, vol. 59, no. 15, pp. 1888–1894, Dec. 2011. DOI: 10.1016/J.PSS.2011.07.017.

[44] D. S. Ebel and S. T. Stewart, "The Elusive Origin of Mercury," in *Mercury: The View after Messenger*, 2018, ch. 18, pp. 497–515. DOI: 10.1017/9781316650684.019. arXiv: 1712.08234.

[45] W. Benz, W. L. Slattery, and A. Cameron, "Collisional stripping of Mercury's mantle," *Icarus*, vol. 74, no. 3, pp. 516–528, Jun. 1988. DOI: 10.1016/0019-1035(88)90118-2.

[46] A. Chau, C. Reinhardt, R. Helled, and J. Stadel, "Forming Mercury by Giant Impacts," *The Astrophysical Journal*, vol. 865, no. 1, p. 35, Sep. 2018. DOI: 10.3847/1538-4357/aad8b0. arXiv: 1808.02448.

[47] G. Sarid, S. T. Stewart, and Z. M. Leinhardt, "Mercury, the impactor," in *Lunar and Planetary Science Conference*, vol. 45, The Woodlands, TX, 2014, p. 2723.

[48] E. Asphaug and A. Reufer, "Mercury and other iron-rich planetary bodies as relics of inefficient accretion," *Nature Geoscience 2014 7:8*, vol. 7, no. 8, pp. 564–568, Jul. 2014. DOI: 10.1038/ngeo2189.

[49] A. V. Vitiazev, G. V. Pechernikova, V. S. Safronov, A. V. Vitiazev, G. V. Pechernikova, and V. S. Safronov, "Formation of Mercury and removal of its silicate shell.," *merc*, pp. 667–669, 1988.

[50] V. Svetsov, "Cratering erosion of planetary embryos," *Icarus*, vol. 214, no. 1, pp. 316–326, Jul. 2011. DOI: 10.1016/J.ICARUS.2011.04.026.

[51] B. Fegley and A. G. Cameron, "A vaporization model for iron/silicate fractionation in the Mercury protoplanet," *Earth and Planetary Science Letters*, vol. 82, no. 3-4, pp. 207–222, Apr. 1987. DOI: 10.1016/0012-821X(87)90196-8.

[52] G. K. Bhatia and S. Sahijpal, "Did ^{26}Al and impact-induced heating differentiate Mercury?" *Meteoritics and Planetary Science*, vol. 52, no. 2, pp. 295–319, Feb. 2017. DOI: 10.1111/maps.12789.

[53] T. J. McCoy, T. L. Dickinson, and G. E. Lofgren, "Partial melting of the Indarch (EH4) meteorite: A textural, chemical, and phase relations view of melting and melt migration," *Meteoritics and Planetary Science*, vol. 34, no. 5, pp. 735–746, Sep. 1999. DOI: 10.1111/j.1945-5100.1999.tb01386.x.

[54] T. H. Burbine, T. J. McCoy, L. R. Nittler, G. K. Benedix, E. A. Cloutis, and T. L. Dickinson, "Spectra of extremely reduced assemblages: Implications for Mercury," *Meteoritics & Planetary Science*, vol. 37, no. 9, pp. 1233–1244, Sep. 2002. DOI: 10.1111/J.1945-5100.2002.TB00892.X.

[55] S. Berthet, V. Malavergne, and K. Righter, "Melting of the Indarch meteorite (EH4 chondrite) at 1 GPa and variable oxygen fugacity: Implications for early planetary differentiation processes," *Geochimica et Cosmochimica Acta*, vol. 73, no. 20, pp. 6402–6420, Oct. 2009. DOI: 10.1016/J.GCA.2009.07.030.

[56] J. O. Goldsten, E. A. Rhodes, W. V. Boynton, W. C. Feldman, D. J. Lawrence, J. I. Trombka, *et al.*, "The MESSENGER Gamma-Ray and Neutron Spectrometer," *The Messenger Mission to Mercury*, pp. 339–391, Dec. 2007. DOI: 10.1007/978-0-387-77214-1_10.

[57] A. C. Evans, J. Mayers, D. N. Timms, and M. J. Cooper, "Deep Inelastic Neutron Scattering in the Study of Atomic Momentum Distributions," *Zeitschrift fur Naturforschung - Section A Journal of Physical Sciences*, vol. 48, no. 1-2, pp. 425–432, Feb. 1993. DOI: 10.1515/zna-1993-1-271.

[58] J. M. Keller, W. V. Boynton, S. Karunatillake, V. R. Baker, J. M. Dohm, L. G. Evans, *et al.*, "Equatorial and midlatitude distribution of chlorine measured by Mars Odyssey GRS," *Journal of Geophysical Research: Planets*, vol. 111, no. E3, pp. 3–08, Mar. 2006. DOI: 10.1029/2006JE002679.

[59] W. V. Boynton, G. J. Taylor, L. G. Evans, R. C. Reedy, R. Starr, D. M. Janes, *et al.*, "Concentration of H, Si, Cl, K, Fe, and Th in the low- and mid-latitude regions of Mars," *Journal of Geophysical Research: Planets*, vol. 112, no. E12, pp. 12–99, Dec. 2007. DOI: 10.1029/2007JE002887.

[60] C. E. Schlemm, R. D. Starr, G. C. Ho, K. E. Bechtold, S. A. Hamilton, J. D. Boldt, *et al.*, "The X-ray Spectrometer on the MESSENGER Spacecraft," *The Messenger Mission to Mercury*, pp. 393–415, 2007. DOI: 10.1007/978-0-387-77214-1_11.

[61] S. Z. Weider, L. R. Nittler, R. D. Starr, T. J. McCoy, K. R. Stockstill-Cahill, P. K. Byrne, B. W. Denevi, J. W. Head, and S. C. Solomon, "Chemical heterogeneity on Mercury's surface revealed by the MESSENGER X-Ray Spectrometer," *Journal of Geophysical Research E: Planets*, vol. 117, no. 10, pp. 1–15, Dec. 2012. DOI: 10.1029/2012JE004153.

[62] L. R. Nittler, R. D. Starr, S. Z. Weider, T. J. McCoy, W. V. Boynton, D. S. Ebel, *et al.*, "The major-element composition of Mercury's surface from MESSENGER X-ray spectrometry," *Science*, vol. 333, no. 6051, pp. 1847–1850, Sep. 2011. DOI: 10.1126/science.1211567.

[63] L. G. Evans, P. N. Peplowski, E. A. Rhodes, D. J. Lawrence, T. J. McCoy, L. R. Nittler, *et al.*, "Major-element abundances on the surface of mercury: Results from the messenger gamma-ray spectrometer," *Journal of*

Geophysical Research E: Planets, vol. 117, no. 11, pp. 1–14, Dec. 2012. DOI: 10.1029/2012JE004178.

[64] P. N. Peplowski, E. A. Rhodes, D. K. Hamara, D. J. Lawrence, L. G. Evans, L. R. Nittler, and S. C. Solomon, "Aluminum abundance on the surface of Mercury: Application of a new background-reduction technique for the analysis of gamma-ray spectroscopy data," *Journal of Geophysical Research E: Planets*, vol. 117, no. 12, pp. 1–13, Dec. 2012. DOI: 10.1029/2012JE004181.

[65] S. Z. Weider, L. R. Nittler, R. D. Starr, T. J. McCoy, and S. C. Solomon, "Variations in the abundance of iron on Mercury's surface from MESSENGER X-Ray Spectrometer observations," *Icarus*, vol. 235, pp. 170–186, Jun. 2014. DOI: 10.1016/J.ICARUS.2014.03.002.

[66] P. N. Peplowski, D. J. Lawrence, W. C. Feldman, J. O. Goldsten, D. Bazell, L. G. Evans, J. W. Head, L. R. Nittler, S. C. Solomon, and S. Z. Weider, "Geochemical terranes of Mercury's northern hemisphere as revealed by MESSENGER neutron measurements," *Icarus*, vol. 253, pp. 346–363, Jun. 2015. DOI: 10.1016/j.icarus.2015.02.002.

[67] D. J. Lawrence, P. N. Peplowski, A. W. Beck, W. C. Feldman, E. A. Frank, T. J. McCoy, L. R. Nittler, and S. C. Solomon, "Compositional terranes on Mercury: Information from fast neutrons," *Icarus*, vol. 281, pp. 32–45, Jan. 2017. DOI: 10.1016/J.ICARUS.2016.07.018.

[68] K. E. Vander Kaaden, F. M. McCubbin, L. R. Nittler, P. N. Peplowski, S. Z. Weider, E. A. Frank, and T. J. McCoy, "Geochemistry, mineralogy, and petrology of boninitic and komatiitic rocks on the mercurian surface: Insights into the mercurian mantle," *Icarus*, vol. 285, pp. 155–168, Mar. 2017. DOI: 10.1016/j.icarus.2016.11.041.

[69] C. R. Chapman, D. M. Baker, O. S. Barnouin, C. I. Fassett, S. Marchi, W. J. Merline, L. R. Ostrach, L. M. Prockter, and R. G. Strom, "Impact Cratering of Mercury," in *Mercury: The View after Messenger*, S. C. Solomon, L. R. Nittler, and B. J. Anderson, Eds., Cambridge, United Kingdom, 2018, ch. 9, pp. 217–248. DOI: 10.1017/9781316650684.010.

[70] B. W. Denevi, C. M. Ernst, H. M. Meyer, M. S. Robinson, S. L. Murchie, J. L. Whitten, *et al.*, "The distribution and origin of smooth plains on Mercury," *Journal of Geophysical Research: Planets*, vol. 118, no. 5, pp. 891–907, May 2013. DOI: 10.1002/jgre.20075.

[71] S. Z. Weider, L. R. Nittler, R. D. Starr, E. J. Crapster-Pregont, P. N. Peplowski, B. W. Denevi, *et al.*, "Evidence for geochemical terranes on Mercury: Global mapping of major elements with MESSENGER's X-Ray Spectrometer," *Earth and Planetary Science Letters*, vol. 416, pp. 109–120, Apr. 2015. DOI: 10.1016/J.EPSL.2015.01.023.

[72] J. W. Head, C. R. Chapman, R. G. Strom, C. I. Fassett, B. W. Denevi, D. T. Blewett, *et al.*, "Flood volcanism in the northern high latitudes of Mercury revealed by MESSENGER," *Science*, vol. 333, no. 6051, pp. 1853–1856, Sep. 2011. DOI: 10.1126/science.1211997.

[73] L. R. Ostrach, M. S. Robinson, J. L. Whitten, C. I. Fassett, R. G. Strom, J. W. Head, and S. C. Solomon, "Extent, age, and resurfacing history of the northern smooth plains on Mercury from MESSENGER observations," *Icarus*, vol. 250, pp. 602–622, Apr. 2015. DOI: 10.1016/J.ICARUS.2014.11.010.

[74] B. Charlier, T. L. Grove, and M. T. Zuber, "Phase equilibria of ultramafic compositions on Mercury and the origin of the compositional dichotomy," *Earth and Planetary Science Letters*, vol. 363, pp. 50–60, Feb. 2013. DOI: 10.1016/j.epsl.2012.12.021.

[75] O. Namur, M. Collinet, B. Charlier, T. L. Grove, F. Holtz, and C. McCammon, "Melting processes and mantle sources of lavas on Mercury," *Earth and Planetary Science Letters*, vol. 439, pp. 117–128, Apr. 2016. DOI: 10.1016/j.epsl.2016.01.030.

[76] L. G. Evans, P. N. Peplowski, F. M. McCubbin, T. J. McCoy, L. R. Nittler, M. Y. Zolotov, *et al.*, "Chlorine on the surface of Mercury: MESSENGER gamma-ray measurements and implications for the planet's formation and evolution," *Icarus*, vol. 257, pp. 417–427, Sep. 2015. DOI: 10.1016/J.ICARUS.2015.04.039.

[77] S. L. Murchie, T. R. Watters, M. S. Robinson, J. W. Head, R. G. Strom, C. R. Chapman, *et al.*, "Geology of the caloris basin, mercury: A view from MESSENGER," *Science*, vol. 321, no. 5885, pp. 73–76, Jul. 2008. DOI: 10.1126/science.1159261.

[78] C. M. Ernst, B. W. Denevi, O. S. Barnouin, C. Klimczak, N. L. Chabot, J. W. Head, *et al.*, "Stratigraphy of the Caloris basin, Mercury: Implications for volcanic history and basin impact melt," *Icarus*, vol. 250, pp. 413–429, Apr. 2015. DOI: 10.1016/J.ICARUS.2014.11.003.

[79] D. T. Blewett, W. M. Vaughan, Z. Xiao, N. L. Chabot, B. W. Denevi, C. M. Ernst, *et al.*, "Mercury's hollows: Constraints on formation and composition from analysis of geological setting and spectral reflectance," *Journal of Geophysical Research: Planets*, vol. 118, no. 5, pp. 1013–1032, May 2013. DOI: 10.1029/2012JE004174.

[80] W. E. McClintock and M. R. Lankton, "The mercury atmospheric and surface composition spectrometer for the MESSENGER mission," *Space Science Reviews*, vol. 131, no. 1-4, pp. 481–521, Jul. 2007. DOI: 10.1007/S11214-007-9264-5/METRICS.

[81] D. T. Blewett, N. L. Chabot, B. W. Denevi, C. M. Ernst, J. W. Head, N. R. Izenberg, *et al.*, "Hollows on mercury: MESSENGER evidence for geologically recent volatile-related activity," *Science*, vol. 333, no. 6051, pp. 1856–1859, Sep. 2011. DOI: 10.1126/SCIENCE.1211681/SUPPL_FILE/BLEWETT-SOM.PDF.

[82] B. W. Denevi, M. S. Robinson, S. C. Solomon, S. L. Murchie, D. T. Blewett, D. L. Domingue, *et al.*, "The evolution of Mercury's crust: a global perspective from MESSENGER.," *Science*, vol. 324, no. 5927, pp. 613–618, May 2009. DOI: 10.1126/science.1172226.

[83] B. W. Denevi, C. M. Ernst, L. M. Prockter, and M. S. Robinson, "The Geologic History of Mercury," in *Mercury: The View after MESSENGER*, S. C. Solomon, L. R. Nittler, and B. J. Anderson, Eds., vol. 21, Cambridge, United Kingdom: Cambridge University Press, 2018, ch. 6, pp. 144–175. DOI: 10.1017/9781316650684.007.

[84] S. L. Murchie, R. L. Klima, N. R. Izenberg, D. L. Domingue, D. T. Blewett, and J. Helbert, "Spectral Reflectance Constraints on the Composition of Mercury's Surface," in *Mercury: The View after MESSENGER*, S. C. Solomon, L. R. Nittler, and B. J. Anderson, Eds., vol. 21, Cambridge University Press, 2018, ch. 8, pp. 191–216. DOI: 10.1017/9781316650684.009.

[85] R. J. Thomas, D. A. Rothery, S. J. Conway, and M. Anand, "Hollows on Mercury: Materials and mechanisms involved in their formation," *Icarus*, vol. 229, pp. 221–235, Feb. 2014. DOI: 10.1016/J.ICARUS.2013.11.018.

[86] D. T. Blewett, C. M. Ernst, S. L. Murchie, and F. Vilas, "Mercury's hollows," in *Mercury: The view after MESSENGER*, S. C. Solomon, L. R. Nittler, and B. J. Anderson, Eds., vol. 21, Cambridge, United Kingdom: Cambridge University Press, 2018, ch. 12, pp. 324–345. DOI: 10.1017/9781316650684.013.

[87] T. H. Morgan and R. M. Killen, "A non-stoichiometric model of the composition of the atmospheres of Mercury and the Moon," *Planetary and Space Science*, vol. 45, no. 1, pp. 81–94, Jan. 1997. DOI: 10.1016/S0032-0633(96)00099-2.

[88] A. L. Sprague, D. M. Hunten, and K. Lodders, "Sulfur at Mercury, Elemental at the Poles and Sulfides in the Regolith," *Icarus*, vol. 118, no. 1, pp. 211–215, Nov. 1995. DOI: 10.1006/ICAR.1995.1186.

[89] D. T. Blewett, A. C. Stadermann, H. C. Susorney, C. M. Ernst, Z. Xiao, N. L. Chabot, *et al.*, "Analysis of MESSENGER high-resolution images of Mercury's hollows and implications for hollow formation," *Journal of Geophysical Research: Planets*, vol. 121, no. 9, pp. 1798–1813, Sep. 2016. DOI: 10.1002/2016JE005070.

[90] J. Helbert, A. Maturilli, and M. D'Amore, "Visible and near-infrared reflectance spectra of thermally processed synthetic sulfides as a potential analog for the hollow forming materials on Mercury," *Earth and Planetary Science Letters*, vol. 369-370, pp. 233–238, May 2013. DOI: 10.1016/j.epsl.2013.03.045.

[91] P. N. Peplowski, D. J. Lawrence, E. A. Rhodes, A. L. Sprague, T. J. McCoy, B. W. Denevi, *et al.*, "Variations in the abundances of potassium and thorium on the surface of Mercury: Results from the MESSENGER Gamma-Ray Spectrometer," *Journal of Geophysical Research E: Planets*, vol. 117, no. 10, pp. 1–27, 2012. DOI: 10.1029/2012JE004141.

[92] D. J. Lawrence, W. C. Feldman, J. O. Goldsten, S. Maurice, P. N. Peplowski, B. J. Anderson, *et al.*, "Evidence for water ice near mercury's north pole from MESSENGER neutron spectrometer measurements," *Science*, vol. 339, no. 6117, pp. 292–296, Jan. 2013. DOI: 10.1126/science.1229953.

[93] N. L. Chabot, D. J. Lawrence, G. A. Neumann, W. C. Feldman, and D. A. Paige, "Mercury's polar deposits," in *Mercury: The view after MESSENGER*, S. C. Solomon, L. R. Nittler, and B. J. Anderson, Eds., vol. 21, Cambridge, United Kingdom: Cambridge University Press, 2018, ch. 13, pp. 346–370. DOI: 10.1017/9781316650684.014.

[94] C. Cartier and B. J. Wood, "The role of reducing conditions in building mercury," *Elements*, vol. 15, no. 1, pp. 39–45, Feb. 2019. DOI: 10.2138/gselements.15.1.39.

[95] F. Albarède, "Oxygen fugacity," in *Encyclopedia of Astrobiology*, M. Gargaud, R. Amils, J. C. Quintanilla, H. J. (Cleaves, W. M. Irvine, D. L. Pinti, and M. Viso, Eds. Berlin, Heidelberg: Springer Berlin Heidelberg, 2011, pp. 1196–1196. DOI: 10.1007/978-3-642-11274-4_4021.

[96] M. Y. Zolotov, A. L. Sprague, S. A. Hauck, L. R. Nittler, S. C. Solomon, and S. Z. Weider, "The redox state, FeO content, and origin of sulfur-rich magmas on Mercury," *Journal of Geophysical Research: Planets*, vol. 118, no. 1, pp. 138–146, Jan. 2013. DOI: 10.1029/2012JE004274.

[97] R. A. Robie, B. S. Hemingway, and G. S. (U.S.), *Thermodynamic Properties of Minerals and Related Substances at 298.15 K and 1 Bar (105 Pascals) Pressure and at Higher Temperatures*, ser. U.S. Geological Survey bulletin. U.S. Government Printing Office, 1995, p. 461.

[98] O. Namur, B. Charlier, F. Holtz, C. Cartier, and C. McCammon, "Sulfur solubility in reduced mafic silicate melts: Implications for the speciation and distribution of sulfur on Mercury," *Earth and Planetary Science Letters*, vol. 448, pp. 102–114, Aug. 2016. DOI: 10.1016/j.epsl.2016.05.024.

[99] J. M. Karner, S. R. Sutton, J. J. Papike, C. K. Shearer, J. H. Jones, and M. Newville, "Application of a new vanadium valence oxybarometer to basaltic glasses from the Earth, Moon, and Mars," *American Mineralogist*, vol. 91, no. 2-3, pp. 270–277, Feb. 2006. DOI: 10.2138/AM.2006.1830.

[100] M. Wadhwa, "Redox Conditions on Small Bodies, the Moon and Mars," *Reviews in Mineralogy and Geochemistry*, vol. 68, no. 1, pp. 493–510, Jan. 2008. DOI: 10.2138/RMG.2008.68.17.

[101] A. E. Rubin, B. Fegley, and R. Brett, "Oxidation state in chondrites," *Meteorites and the early solar system*, pp. 488–511, 1988.

[102] F. M. McCubbin, M. A. Riner, K. E. Vander Kaaden, and L. K. Burkemper, "Is Mercury a volatile-rich planet?" *Geophysical Research Letters*, vol. 39, no. 9, pp. 1–5, May 2012. DOI: 10.1029/2012GL051711.

[103] J.-L. Margot, S. A. I. Hauck, E. Mazarico, S. Padovan, and S. J. Peale, "Mercury's Internal Structure," in *Mercury: The view after MESSENGER*, A. B. (Solomon SC, Nittler LR, Ed., Cambridge: Cambridge University Press, 2018, ch. 4, pp. 85–113. DOI: 10.1017/9781316650684.005.

[104] S. L. Murchie, R. L. Klima, B. W. Denevi, C. M. Ernst, M. R. Keller, D. L. Domingue, *et al.*, "Orbital multispectral mapping of Mercury with the MESSENGER Mercury Dual Imaging System: Evidence for the origins of plains units and low-reflectance material," *Icarus*, vol. 254, pp. 287–305, Jul. 2015. DOI: 10.1016/J.ICARUS.2015.03.027.

[105] K. E. Vander Kaaden and F. M. McCubbin, "Exotic crust formation on Mercury: Consequences of a shallow, FeO-poor mantle," *Journal of Geophysical Research: Planets*, vol. 120, no. 2, pp. 195–209, Feb. 2015. DOI: 10.1002/2014JE004733.

[106] Y. Li, R. Dasgupta, and K. Tsuno, "Carbon contents in reduced basalts at graphite saturation: Implications for the degassing of Mars, Mercury, and the Moon," *Journal of Geophysical Research: Planets*, vol. 122, no. 6, pp. 1300–1320, Jun. 2017. DOI: 10.1002/2017JE005289.

[107] P. N. Peplowski, D. J. Lawrence, L. G. Evans, R. L. Klima, D. T. Blewett, J. O. Goldsten, *et al.*, "Constraints on the abundance of carbon in near-surface materials on Mercury: Results from the MESSENGER Gamma-Ray Spectrometer," *Planetary and Space Science*, vol. 108, pp. 98–107, Apr. 2015. DOI: 10.1016/J.PSS.2015.01.008.

[108] P. N. Peplowski, R. L. Klima, D. J. Lawrence, C. M. Ernst, B. W. Denevi, E. A. Frank, J. O. Goldsten, S. L. Murchie, L. R. Nittler, and S. C. Solomon, "Remote sensing evidence for an ancient carbon-bearing crust on Mercury," *Nature Geoscience*, vol. 9, no. 4, pp. 273–276, Apr. 2016. DOI: 10.1038/ngeo2669.

[109] M. S. Duncan, R. Dasgupta, and K. Tsuno, "Experimental determination of CO2 content at graphite saturation along a natural basalt-peridotite melt join: Implications for the fate of carbon in terrestrial magma oceans," *Earth and Planetary Science Letters*, vol. 466, pp. 115–128, May 2017. DOI: 10.1016/j.epsl.2017.03.008.

[110] H. Keppler and G. Golabek, "Graphite floatation on a magma ocean and the fate of carbon during core formation," *Geochemical Perspectives Letters*, pp. 12–17, Jul. 2019. DOI: 10.7185/geochemlet.1918.

[111] A. I. Savvatimskiy, "Measurements of the melting point of graphite and the properties of liquid carbon (a review for 1963–2003)," *Carbon*, vol. 43, no. 6, pp. 1115–1142, May 2005. DOI: 10.1016/J.CARBON.2004.12.027.

[112] M. J. Cintala, "Impact-induced thermal effects in the lunar and Mercurian regoliths," *Journal of Geophysical Research*, vol. 97, no. E1, p. 947, Jan. 1992. DOI: 10.1029/91JE02207.

[113] S. E. I. Hawkins, S. L. Murchie, K. J. Becker, C. M. Selby, F. S. Turner, M. W. Noble, *et al.*, "In-flight performance of MESSENGER's Mercury Dual Imaging System," in *Instruments and Methods for Astrobiology and*

Planetary Missions XII, vol. 7441, SPIE, Sep. 2009, 74410Z. DOI: 10.1117/12.826370.

[114] D. L. Domingue, S. L. Murchie, B. W. Denevi, N. L. Chabot, D. T. Blewett, N. R. Laslo, R. M. Vaughan, H. K. Kang, and M. K. Shepard, "Photometric correction of Mercury's global color mosaic," *Planetary and Space Science*, vol. 59, no. 15, pp. 1873–1887, Dec. 2011. DOI: 10.1016/J.PSS.2011.03.014.

[115] D. L. Domingue, S. L. Murchie, B. W. Denevi, C. M. Ernst, and N. L. Chabot, "Mercury's global color mosaic: An update from MESSENGER's orbital observations," *Icarus*, vol. 257, pp. 477–488, Sep. 2015. DOI: 10.1016/J.ICARUS.2014.11.027.

[116] D. L. Domingue, B. W. Denevi, S. L. Murchie, and C. D. Hash, "Application of multiple photometric models to disk-resolved measurements of Mercury's surface: Insights into Mercury's regolith characteristics," *Icarus*, vol. 268, pp. 172–203, Apr. 2016. DOI: 10.1016/J.ICARUS.2015.11.040.

[117] B. Hapke, "Bidirectional reflectance spectroscopy: 1. Theory," *Journal of Geophysical Research: Solid Earth*, vol. 86, no. B4, pp. 3039–3054, Apr. 1981. DOI: 10.1029/JB086IB04P03039.

[118] ——, *Theory of reflectance and emittance spectroscopy*, 2nd ed. Cambridge: Cambridge University Press, 2012, p. 528.

[119] M. Kaasalainen, J. Torppa, and K. Muinonen, "Optimization Methods for Asteroid Lightcurve Inversion: II. The Complete Inverse Problem," *Icarus*, vol. 153, no. 1, pp. 37–51, Sep. 2001. DOI: 10.1006/ICAR.2001.6674.

[120] Y. Shkuratov, V. Kaydash, V. Korokhin, Y. Velikodsky, N. Opanasenko, and G. Videen, "Optical measurements of the Moon as a tool to study its surface," *Planetary and Space Science*, vol. 59, no. 13, pp. 1326–1371, Oct. 2011. DOI: 10.1016/J.PSS.2011.06.011.

[121] C. I. Fassett, M. C. Crowley, C. Leight, M. D. Dyar, D. A. Minton, M. Hirabayashi, B. J. Thomson, and W. A. Watters, "Evidence for rapid topographic evolution and crater degradation on Mercury from sim-

ple crater morphometry," *Geophysical Research Letters*, vol. 44, no. 11, pp. 5326–5335, Jun. 2017. DOI: 10.1002/2017GL073769.

[122] D. A. Rothery, M. Massironi, G. Alemanno, O. Barraud, S. Besse, N. Bott, *et al.*, "Rationale for BepiColombo Studies of Mercury's Surface and Composition," *Space Science Reviews*, vol. 216, no. 4, p. 66, Jun. 2020. DOI: 10.1007/s11214-020-00694-7.

[123] J. W. Salisbury, L. S. Walter, N. Vergo, and D. M. D'Aria, "Mid-infrared (2.1-25 μm) spectra of minerals," Greenbelt, MD, Tech. Rep., 1987.

[124] P. G. Lucey, B. T. Greenhagen, E. Song, J. A. Arnold, M. Lemelin, K. D. Hanna, N. E. Bowles, T. D. Glotch, and D. A. Paige, "Space weathering effects in Diviner Lunar Radiometer multispectral infrared measurements of the lunar Christiansen Feature: Characteristics and mitigation," *Icarus*, vol. 283, pp. 343–351, Feb. 2017. DOI: 10.1016/j.icarus.2016.05.010.

[125] D. T. Britt and C. M. Pieters, "Darkening in black and gas-rich ordinary chondrites: The spectral effects of opaque morphology and distribution," *Geochimica et Cosmochimica Acta*, vol. 58, no. 18, pp. 3905–3919, Sep. 1994. DOI: 10.1016/0016-7037(94)90370-0.

[126] P. G. Lucey and M. A. Riner, "The optical effects of small iron particles that darken but do not redden: Evidence of intense space weathering on Mercury," *Icarus*, vol. 212, no. 2, pp. 451–462, Apr. 2011. DOI: 10.1016/J.ICARUS.2011.01.022.

[127] C. L. Young, M. J. Poston, J. J. Wray, K. P. Hand, and R. W. Carlson, "The mid-IR spectral effects of darkening agents and porosity on the silicate surface features of airless bodies," *Icarus*, vol. 321, pp. 71–81, Mar. 2019. DOI: 10.1016/j.icarus.2018.10.032.

[128] A. E. Wald and J. W. Salisbury, "Thermal infrared directional emissivity of powdered quartz," *Journal of Geophysical Research: Solid Earth*, vol. 100, no. B12, pp. 24 665–24 675, Dec. 1995. DOI: 10.1029/95JB02400.

[129] A. Maturilli, J. Helbert, and L. Moroz, "The Berlin emissivity database (BED)," *Planetary and Space Science*, vol. 56, no. 3-4, pp. 420–425, Mar. 2008. DOI: 10.1016/J.PSS.2007.11.015.

[130] A. Skulteti, A. Kereszturi, M. Szabo, Z. Kereszty, and F. Cipriani, "Mid-infrared spectroscopic investigation of meteorites and perspectives for thermal infrared observations at the binary asteroid Didymos," *Planetary and Space Science*, vol. 184, p. 104 855, May 2020. DOI: 10.1016/j.pss.2020.104855.

[131] A. Maturilli, J. Helbert, J. M. St. John, J. W. Head, W. M. Vaughan, M. D'Amore, M. Gottschalk, and S. Ferrari, "Komatiites as Mercury surface analogues: Spectral measurements at PEL," *Earth and Planetary Science Letters*, vol. 398, pp. 58–65, Jul. 2014. DOI: 10.1016/J.EPSL.2014.04.035.

[132] A. Maturilli, J. Helbert, I. Varatharajan, and H. Hiesinger, "Emissivity Spectra of Analogue Materials at Mercury P-T Conditions," *48th Lunar and Planetary Science Conference, held 20-24 March 2017, at The Woodlands, Texas. LPI Contribution No. 1964, id.1427*, vol. 48, 2017.

[133] I. Varatharajan, A. Maturilli, J. Helbert, G. Alemanno, and H. Hiesinger, "Spectral behavior of sulfides in simulated daytime surface conditions of Mercury: Supporting past (MESSENGER) and future missions (Bepi-Colombo)," *Earth and Planetary Science Letters*, vol. 520, pp. 127–140, Aug. 2019. DOI: 10.1016/j.epsl.2019.05.020.

[134] J. Labed and M. P. Stoll, "Angular variation of land surface spectral emissivity in the thermal infrared: Laboratory investigations on bare soils," *International Journal of Remote Sensing*, vol. 12, no. 11, pp. 2299–2310, 1991. DOI: 10.1080/01431169108955259.

[135] A. Maturilli, J. Helbert, S. Ferrari, and M. D'Amore, "On the effect of emergence angle on emissivity spectra: Application to small bodies Science of solar system materials examined from Hayabusa and future missions (II) 7. Planetary science," *Earth, Planets and Space*, vol. 68, no. 1, p. 84, Dec. 2016. DOI: 10.1186/s40623-016-0464-7.

[136] P. G. Lucey, D. A. Paige, B. T. Greenhagen, J. L. Bandfield, and T. D. Glotch, "Comparison of Diviner Christiansen Feature Position and Visible Albedo: Composition and Space Weathering Implications," *LPI*, no. 1533, p. 1600, 2010. DOI: 10.1029/2005JE002656.

[137] B. T. Greenhagen, P. G. Lucey, M. B. Wyatt, T. D. Glotch, C. C. Allen, J. A. Arnold, *et al.*, "Global silicate mineralogy of the moon from the diviner lunar radiometer," *Science*, vol. 329, no. 5998, pp. 1507–1509, Sep. 2010. DOI: 10.1126/science.1192196.

[138] T. D. Glotch, J. L. Bandfield, P. G. Lucey, P. O. Hayne, B. T. Greenhagen, J. A. Arnold, R. R. Ghent, and D. A. Paige, "Formation of lunar swirls by magnetic field standoff of the solar wind," *Nature Communications 2015 6:1*, vol. 6, no. 1, pp. 1–8, Feb. 2015. DOI: 10.1038/ncomms7189.

[139] I. Weber, A. N. Stojic, A. Morlok, M. P. Reitze, K. Markus, H. Hiesinger, *et al.*, "Space weathering by simulated micrometeorite bombardment on natural olivine and pyroxene: A coordinated IR and TEM study," *Earth and Planetary Science Letters*, vol. 530, p. 115 884, Jan. 2020. DOI: 10.1016/j.epsl.2019.115884.

[140] B. Hapke, "Space weathering from Mercury to the asteroid belt," *Journal of Geophysical Research: Planets*, vol. 106, no. E5, pp. 10 039–10 073, May 2001. DOI: 10.1029/2000JE001338.

[141] M. J. Loeffler, C. A. Dukes, and R. A. Baragiola, "Irradiation of olivine by 4 keV He ¡sup¿+¡/sup¿ : Simulation of space weathering by the solar wind," *Journal of Geophysical Research*, vol. 114, no. E3, E03003, Mar. 2009. DOI: 10.1029/2008JE003249.

[142] E. M. Fischer and C. M. Pieters, "Remote Determination of Exposure Degree and Iron Concentration of Lunar Soils Using VIS-NIR Spectroscopic Methods," *Icarus*, vol. 111, no. 2, pp. 475–488, Oct. 1994. DOI: 10.1006/ICAR.1994.1158.

[143] C. M. Pieters, L. A. Taylor, S. K. Noble, L. P. Keller, B. Hapke, R. V. Morris, C. C. Allen, D. S. McKAY, and S. Wentworth, "Space weathering on airless bodies: Resolving a mystery with lunar samples," *Meteoritics and Planetary Science*, vol. 35, no. 5, pp. 1101–1107, Sep. 2000. DOI: 10.1111/j.1945-5100.2000.tb01496.x.

[144] E. A. Cloutis and M. J. Gaffey, "Lunar Regolith Analogues: Spectral Reflectance Properties of Compositional Variations," *Icarus*, vol. 102, no. 2, pp. 203–224, Apr. 1993. DOI: 10.1006/ICAR.1993.1044.

[145] L. P. Keller and D. S. McKay, "The nature and origin of rims on lunar soil grains," *Geochimica et Cosmochimica Acta*, vol. 61, no. 11, pp. 2331–2341, 1997. DOI: 10.1016/s0016-7037(97)00085-9.

[146] T. Matsumoto, T. Noguchi, Y. Tobimatsu, D. Harries, F. Langenhorst, A. Miyake, and H. Hidaka, "Space weathering of iron sulfides in the lunar surface environment," *Geochimica et Cosmochimica Acta*, vol. 299, pp. 69–84, Apr. 2021. DOI: 10.1016/J.GCA.2021.02.013.

[147] A. Pisello, S. De Angelis, M. Ferrari, M. Porreca, F. P. Vetere, H. Behrens, M. C. De Sanctis, and D. Perugini, "Visible and near-InfraRed (VNIR) reflectance of silicate glasses: Characterization of a featureless spectrum and implications for planetary geology," *Icarus*, vol. 374, p. 114 801, Mar. 2022. DOI: 10.1016/J.ICARUS.2021.114801.

[148] A. Lucchetti, M. Pajola, V. Galluzzi, L. Giacomini, C. Carli, G. Cremonese, G. A. Marzo, S. Ferrari, M. Massironi, and P. Palumbo, "Mercury Hollows as Remnants of Original Bedrock Materials and Devolatilization Processes: A Spectral Clustering and Geomorphological Analysis," *Journal of Geophysical Research: Planets*, vol. 123, no. 9, pp. 2365–2379, Sep. 2018. DOI: 10.1029/2018JE005722.

[149] J. Helbert, E. Jessberger, J. Benkhoff, G. Arnold, M. Banaszkiewicz, A. Bischoff, *et al.*, "MERTIS – A Thermal Infrared Imaging Spectrometer for the Bepi-Colombo Mission," in *Lunar and Planetary Science XXXVI, 1234, CD-ROM-abstract#1753*, Houston, TX, 2005, p. 1753.

[150] H. R. Carlon, "Christiansen effect in IR spectra of soil-derived atmospheric dusts," *Applied Optics*, vol. 18, no. 21, p. 3610, Nov. 1979. DOI: 10.1364/ao.18.003610.

[151] V. C. Farmer, *The Infrared Spectra of Minerals*. Mineralogical Society of Great Britain and Ireland, 1974. DOI: 10.1180/mono-4.

[152] R. D. Aines and G. R. Rossman, "Water in minerals? A peak in the infrared," *Journal of Geophysical Research: Solid Earth*, vol. 89, no. B6, pp. 4059–4071, Jun. 1984. DOI: 10.1029/JB089IB06P04059.

[153] G. R. Hunt and J. W. Salisbury, "Mid-infrared spectral behavior of sedimentary rocks," Optical Physics Laboratory, Hanscom AFB, Massachusetts, Tech. Rep. 356, 1975.

[154] D. B. Nash and J. W. Salisbury, "Infrared reflectance spectra (2.2-15 μm) of plagioclase feldspars," *Geophysical Research Letters*, vol. 18, no. 6, pp. 1151–1154, Jun. 1991. DOI: 10.1029/91GL01008.

[155] J. W. Salisbury, A. Basu, and E. M. Fischer, "Thermal infrared spectra of lunar soils," *Icarus*, vol. 130, no. 1, pp. 125–139, Nov. 1997. DOI: 10.1006/icar.1997.5809.

[156] A. L. Sprague, K. L. Donaldson Hanna, R. W. H. Kozlowski, J. Helbert, A. Maturilli, J. B. Warell, and J. L. Hora, "Spectral emissivity measurements of Mercury's surface indicate Mg- and Ca-rich mineralogy, K-spar, Na-rich plagioclase, rutile, with possible perovskite, and garnet," *Planetary and Space Science*, vol. 57, no. 3, pp. 364–383, Mar. 2009. DOI: 10.1016/J.PSS.2009.01.006.

[157] S. A. Stern, "The lunar atmosphere: History, status, current problems, and context," *Reviews of Geophysics*, vol. 37, no. 4, pp. 453–491, Nov. 1999. DOI: 10.1029/1999RG900005.

[158] P. Wurz, U. Rohner, J. A. Whitby, C. Kolb, H. Lammer, P. Dobnikar, and J. A. Martín-Fernández, "The lunar exosphere: The sputtering contribution," *Icarus*, vol. 191, no. 2, pp. 486–496, Nov. 2007. DOI: 10.1016/J.ICARUS.2007.04.034.

[159] G. Fjeldbo, A. Kliore, D. Sweetnam, P. Esposito, B. Seidel, and T. Howard, "The occultation of Mariner 10 by Mercury," *Icarus*, vol. 29, no. 4, pp. 439–444, Dec. 1976. DOI: 10.1016/0019-1035(76)90063-4.

[160] D. M. Hunten, T. H. Morgan, and D. E. Shemansky, "The mercury atmosphere," in *Mercury*, University of Arizona Press Tucson, 1988, pp. 562–612.

[161] G. Gronoff, P. Arras, S. Baraka, J. M. Bell, G. Cessateur, O. Cohen, *et al.*, "Atmospheric Escape Processes and Planetary Atmospheric Evolution," *Journal of Geophysical Research: Space Physics*, vol. 125, no. 8, Aug. 2020. DOI: 10.1029/2019JA027639. arXiv: 2003.03231.

[162] S. A. Hale and B. Hapke, "A Time-Dependent Model of Radiative and Conductive Thermal Energy Transport in Planetary Regoliths with Applications to the Moon and Mercury," *Icarus*, vol. 156, no. 2, pp. 318–334, Apr. 2002. DOI: 10.1006/ICAR.2001.6768.

[163] A. L. Tyler, R. W. Kozlowski, and D. M. Hunten, "Observations of sodium in the tenuous lunar atmosphere," *Geophysical Research Letters*, vol. 15, no. 10, pp. 1141–1144, Sep. 1988. DOI: 10.1029/GL015I010P01141.

[164] W. E. McClintock, T. A. Cassidy, A. W. Merkel, R. M. Killen, M. H. Burger, and R. J. Vervack, "Observations of Mercury ' s Exosphere : Composition and Structure," in *Mercury: The View after MESSENGER*, S. C. Solomon, L. R. Nittler, and B. J. Anderson, Eds., Cambridge, United Kingdom: Cambridge University Press, 2018, ch. 14, pp. 371–406. DOI: 10.1017/9781316650684.015.

[165] R. M. Killen, G. Cremonese, H. Lammer, S. Orsini, A. E. Potter, A. L. Sprague, *et al.*, "Processes that promote and deplete the exosphere of mercury," in *Space Science Reviews*, vol. 132, Springer, New York, NY, 2007, pp. 433–509. DOI: 10.1007/s11214-007-9232-0.

[166] A. L. Broadfoot, S. Kumar, M. J. Belton, and M. B. McElroy, "Mercury's Atmosphere from Mariner 10: Preliminary Results," *Science*, vol. 185, no. 4146, pp. 166–169, Jul. 1974. DOI: 10.1126/SCIENCE.185.4146.166.

[167] A. L. Broadfoot, D. E. Shemansky, and S. Kumar, "Mariner 10: Mercury atmosphere," *Geophysical Research Letters*, vol. 3, no. 10, pp. 577–580, Oct. 1976. DOI: 10.1029/GL003I010P00577.

[168] J. A. Dunne and E. Burgess, *The Voyage of Mariner 10: Mission to Venus and Mercury*. Washington, D. C.: Scientific and Technical Information Office, NASA, 1978, vol. 424, p. 224.

[169] J. C. Cook, S. A. Stern, P. D. Feldman, G. R. Gladstone, K. D. Retherford, and C. C. Tsang, "New upper limits on numerous atmospheric species in the native lunar atmosphere," *Icarus*, vol. 225, no. 1, pp. 681–687, Jul. 2013. DOI: 10.1016/J.ICARUS.2013.04.010.

[170] G. B. Andrews, T. H. Zurbuchen, B. H. Mauk, H. Malcom, L. A. Fisk, G. Gloeckler, *et al.*, "The energetic particle and plasma spectrometer instrument on the MESSENGER spacecraft," *Space Science Reviews*, vol. 131, no. 1-4, pp. 523–556, Jul. 2007. DOI: 10.1007/S11214-007-9272-5/METRICS.

[171] G. R. Gladstone, S. A. Stern, K. D. Retherford, R. K. Black, D. C. Slater, M. W. Davis, *et al.*, "LAMP: The lyman alpha mapping project on NASA's lunar reconnaissance orbiter mission," *Space Science Reviews*, vol. 150, no. 1-4, pp. 161–181, Jan. 2010. DOI: 10.1007/S11214-009-9578-6/METRICS.

[172] C. Grava, R. M. Killen, M. Benna, A. A. Berezhnoy, J. S. Halekas, F. Leblanc, *et al.*, "Volatiles and Refractories in Surface-Bounded Exospheres in the Inner Solar System," *Space Science Reviews 2021 217:5*, vol. 217, no. 5, pp. 1–47, May 2021. DOI: 10.1007/S11214-021-00833-8.

[173] R. M. Killen and W. H. Ip, "The surface-bounded atmospheres of Mercury and the moon," *Reviews of Geophysics*, vol. 37, no. 3, pp. 361–406, Aug. 1999. DOI: 10.1029/1999RG900001.

[174] A. L. Sprague, R. W. Kozlowski, and D. M. Hunten, "Caloris Basin: An Enhanced Source for Potassium in Mercury's Atmosphere," *Science*, vol. 249, no. 4973, pp. 1140–1143, Sep. 1990. DOI: 10.1126/SCIENCE.249.4973.1140.

[175] H. M. Sullivan and D. M. Hunten, "Lithium, sodium, and potassium in the twilight airglow," *Canadian Journal of Physics*, vol. 42, no. 5, pp. 937–956, May 1964. DOI: 10.1139/p64-087.

[176] D. M. Hunten, F. E. Roach, and J. W. Chamberlain, "A photometric unit for the airglow and aurora," *Journal of Atmospheric and Terrestrial Physics*, vol. 8, no. 6, pp. 345–346, Jun. 1956. DOI: 10.1016/0021-9169(56)90111-8.

[177] R. Killen, D. Shemansky, and N. Mouawad, "Expected emission from mercury's exospheric species, and their ultraviolet-visible signatures," *The Astrophysical Journal Supplement Series*, vol. 181, no. 2, p. 351, Mar. 2009. DOI: 10.1088/0067-0049/181/2/351.

[178] R. Killen, R. Vervack, M. Burger, R. Killen, R. Vervack, and M. Burger, "Variation of g-values of major species with heliocentric velocity," in *EPSC*, 2022, EPSC2022–53. DOI: 10.5194/EPSC2022-53.

[179] A. Vorburger, P. Wurz, S. Barabash, M. Wieser, Y. Futaana, M. Holmström, A. Bhardwaj, and K. Asamura, "First direct observation of sputtered lunar oxygen," *Journal of Geophysical Research: Space Physics*, vol. 119, no. 2, pp. 709–722, Feb. 2014. DOI: 10.1002/2013JA019207.

[180] B. C. Flynn and S. A. Stern, "A Spectroscopic Survey of Metallic Species Abundances in the Lunar Atmosphere," *Icarus*, vol. 124, no. 2, pp. 530–536, Dec. 1996. DOI: 10.1006/ICAR.1996.0228.

[181] M. Sarantos, R. M. Killen, D. A. Glenar, M. Benna, and T. J. Stubbs, "Metallic species, oxygen and silicon in the lunar exosphere: Upper limits and prospects for LADEE measurements," *Journal of Geophysical Research: Space Physics*, vol. 117, no. A3, p. 3103, Mar. 2012. DOI: 10.1029/2011JA017044.

[182] G. R. Gladstone, D. M. Hurley, K. D. Retherford, P. D. Feldman, W. R. Pryor, J. Y. Chaufray, *et al.*, "LRO-LAMP observations of the LCROSS impact plume," *Science*, vol. 330, no. 6003, pp. 472–476, Oct. 2010. DOI: 10.1126/science.1186474.

[183] A. Colaprete, K. Vargo, M. Shirley, D. Landis, D. Wooden, J. Karcz, B. Hermalyn, and A. Cook, "An overview of the ladee ultraviolet-visible spectrometer," *The Lunar Atmosphere and Dust Environment Explorer Mission (LADEE)*, pp. 63–92, Jan. 2015. DOI: 10.1007/978-3-319-18717-4_4.

[184] A. Colaprete, M. Sarantos, D. H. Wooden, T. J. Stubbs, A. M. Cook, and M. Shirley, "Lunar atmosphere: How surface composition and meteoroid impacts mediate sodium and potassium in the lunar exosphere," *Science*, vol. 351, no. 6270, pp. 219–252, Jan. 2016. DOI: 10.1126/SCIENCE.AAD2380.

[185] A. E. Potter and T. H. Morgan, "Discovery of sodium in the atmosphere of Mercury," *Science*, vol. 229, no. 4714, pp. 651–653, Aug. 1985. DOI: 10.1126/science.229.4714.651.

[186] A. E. Potter and T. H. Morgan, "Potassium in the atmosphere of Mercury," *Icarus*, vol. 67, no. 2, pp. 336–340, Aug. 1986. DOI: 10.1016/0019-1035(86)90113-2.

[187] T. H. Zurbuchen, J. M. Raines, G. Gloeckler, S. M. Krimigis, J. A. Slavin, P. L. Koehn, R. M. Killen, A. L. Sprague, R. L. McNutt, and S. C. Solomon, "MESSENGER observations of the composition of Mercury's ionized exosphere and plasma environment.," *Science (New York, N.Y.)*, vol. 321, no. 5885, pp. 90–2, Jul. 2008. DOI: 10.1126/science.1159314.

[188] R. J. Vervack, R. M. Killen, W. E. McClintock, A. W. Merkel, M. H. Burger, T. A. Cassidy, and M. Sarantos, "New discoveries from MESSENGER and insights into Mercury's exosphere," *Geophysical Research Letters*, vol. 43, no. 22, pp. 11, 545–11, 551, Nov. 2016. DOI: 10.1002/2016GL071284.

[189] A. Doressoundiram, F. Leblanc, C. Foellmi, and S. Erard, "Metallic species in Mercury's exosphere: EMMI/new technology telescope observations," *Astronomical Journal*, vol. 137, no. 4, pp. 3859–3863, Apr. 2009. DOI: 10.1088/0004-6256/137/4/3859.

[190] V. Mangano, S. Massetti, A. Milillo, C. Plainaki, S. Orsini, R. Rispoli, and F. Leblanc, "THEMIS Na exosphere observations of Mercury and their correlation with in-situ magnetic field measurements by MESSENGER," *Planetary and Space Science*, vol. 115, pp. 102–109, Sep. 2015. DOI: 10.1016/J.PSS.2015.04.001.

[191] W. E. McClintock, R. J. Vervack, E. T. Bradley, R. M. Killen, N. Mouawad, A. L. Sprague, M. H. Burger, S. C. Solomon, and N. R. Izenberg, "MESSENGER observations of mercury's exosphere: Detection of magnesium and distribution of constituents," *Science*, vol. 324, no. 5927, pp. 610–613, May 2009. DOI: 10.1126/SCIENCE.1172525.

[192] R. J. Vervack, W. E. McClintock, R. M. Killen, A. L. Sprague, B. J. Anderson, M. H. Burger, E. T. Bradley, N. Mouawad, S. C. Solomon, and N. R. Izenberg, "Mercury's complex exosphere: results from MESSENGER's third flyby.," *Science (New York, N.Y.)*, vol. 329, no. 5992, pp. 672–5, Aug. 2010. DOI: 10.1126/science.1188572.

[193] M. H. Burger, R. M. Killen, W. E. McClintock, A. W. Merkel, R. J. Vervack, T. A. Cassidy, and M. Sarantos, "Seasonal variations in Mercury's dayside calcium exosphere," *Icarus*, vol. 238, pp. 51–58, Aug. 2014. DOI: 10.1016/J.ICARUS.2014.04.049.

[194] R. M. Killen and J. M. Hahn, "Impact vaporization as a possible source of Mercury's calcium exosphere," *Icarus*, vol. 250, pp. 230–237, Apr. 2015. DOI: 10.1016/J.ICARUS.2014.11.035.

[195] M. Sarantos, R. M. Killen, W. E. McClintock, E. Todd Bradley, R. J. Vervack, M. Benna, and J. A. Slavin, "Limits to Mercury's magnesium exosphere from MESSENGER second flyby observations," *Planetary and Space Science*, vol. 59, no. 15, pp. 1992–2003, Dec. 2011. DOI: 10.1016/J.PSS.2011.05.002.

[196] A. W. Merkel, T. A. Cassidy, R. J. Vervack, W. E. McClintock, M. Sarantos, M. H. Burger, and R. M. Killen, "Seasonal variations of Mercury's magnesium dayside exosphere from MESSENGER observations," *Icarus*, vol. 281, pp. 46–54, Jan. 2017. DOI: 10.1016/j.icarus.2016.08.032.

[197] T. A. Bida and R. M. Killen, "Observations of Al, Fe, and Ca+ in Mercury's exosphere," in *EPSC-DPS Joint Meeting 2011*, vol. 2011, 2011, p. 1621.

[198] ——, "Observations of the minor species Al and Fe in Mercury's exosphere," *Icarus*, vol. 289, pp. 227–238, Jun. 2017. DOI: 10.1016/j.icarus.2016.10.019.

[199] D. Gamborino Uzcanga, A. H. Vorburger, and P. Wurz, "Mercury's Sodium Exosphere: An ab initio Calculation to Interpret MASCS/UVVS Observations from MESSENGER," in *Annales geophysicae discussions*, Copernicus Publications, 2018, pp. 1–24.

[200] R. M. Killen, M. H. Burger, R. J. J. Vervack, and T. A. Cassidy, "Understanding Mercury's exosphere: models derived from MESSENGER observations," in *Mercury: The view after MESSENGER*, S. C. Solomon, L. R. Nittler, and B. J. Anderson, Eds., Cambridge, United Kingdom: Cambridge University Press, 2018, ch. 21, p. 15. DOI: 10.1017/9781316650684.016.

[201] B. Teolis, M. Sarantos, ·. N. Schorghofer, B. Jones, C. Grava, A. Mura, *et al.*, "Surface Exospheric Interactions," *Space Science Reviews 2023 219:1*, vol. 219, no. 1, pp. 1–33, Jan. 2023. DOI: 10.1007/S11214-023-00951-5.

[202] P. Wurz, S. Fatemi, A. Galli, J. Halekas, Y. Harada, N. Jäggi, *et al.*, "Particles and Photons as Drivers for Particle Release from the Surfaces of the Moon and Mercury," *Space Science Reviews 2022 218:3*, vol. 218, no. 3, pp. 1–83, Mar. 2022. DOI: 10.1007/S11214-022-00875-6.

[203] S. Glasstone, *Sourcebook on the space sciences.* Van Nostrand, Princeton, 1965, p. 937.

[204] C. Montgomery, "Directional characteristics of lunar thermal emission," in *2nd Thermophysics Specialist Conference*, American Institute of Aeronautics and Astronautics (AIAA), Apr. 1966. DOI: 10.2514/6.1967-291.

[205] V. G. Kunde, R. A. Hanel, and L. W. Herath, "High spectral resolution ground-based observations of Venus in the 450- to 1250-cm-1 region," *Icarus*, vol. 32, no. 2, pp. 210–224, Oct. 1977. DOI: 10.1016/0019-1035(77)90060-4.

[206] D. A. Paige, M. A. Siegler, J. K. Harmon, G. A. Neumann, E. M. Mazarico, D. E. Smith, M. T. Zuber, E. Harju, M. L. Delitsky, and S. C. Solomon, "Thermal stability of volatiles in the north polar region of mercury," *Science*, vol. 339, no. 6117, pp. 300–303, Jan. 2013. DOI: 10.1126/SCIENCE.1231106.

[207] R. M. Killen, "Source and maintenance of the argon atmospheres of Mercury and the Moon," *Meteoritics & Planetary Science*, vol. 37, no. 9, pp. 1223–1231, Sep. 2002. DOI: 10.1111/J.1945-5100.2002.TB00891.X.

[208] T. E. Madey, B. V. Yakshinskiy, V. N. Ageev, and R. E. Johnson, "Desorption of alkali atoms and ions from oxide surfaces: Relevance to origins of Na and K in atmospheres of Mercury and the Moon," *Journal of Geophysical Research: Planets*, vol. 103, no. E3, pp. 5873–5887, Mar. 1998. DOI: 10.1029/98JE00230.

[209] M. J. Schaible, M. Sarantos, B. A. Anzures, S. W. Parman, and T. M. Orlando, "Photon-Stimulated Desorption of MgS as a Potential Source of Sulfur in Mercury's Exosphere," *Journal of Geophysical Research: Planets*, vol. 125, no. 8, e2020JE006479, Aug. 2020. DOI: 10.1029/2020JE006479.

[210] T. A. Cassidy, A. W. Merkel, M. H. Burger, M. Sarantos, R. M. Killen, W. E. McClintock, and R. J. Vervack, "Mercury's seasonal sodium exosphere: MESSENGER orbital observations," *Icarus*, vol. 248, pp. 547–559, Mar. 2015. DOI: 10.1016/j.icarus.2014.10.037.

[211] B. Yakshinskiy and T. Madey, "Desorption induced by electronic transitions of Na from SiO2: relevance to tenuous planetary atmospheres," *Surface Science*, vol. 451, no. 1-3, pp. 160–165, Apr. 2000. DOI: 10.1016/S0039-6028(00)00022-4.

[212] White and O. R., "The solar output and its variation," in *Proceedings of a Workshop, held in Boulder, Colorado, April 26-28*, Boulder: Colorado Associated University Press, 1977.

[213] C. J. Bennett, J. L. McLain, M. Sarantos, R. D. Gann, A. Desimone, and T. M. Orlando, "Investigating potential sources of Mercury's exospheric Calcium: Photon-stimulated desorption of Calcium Sulfide," *Journal of Geophysical Research: Planets*, vol. 121, no. 2, pp. 137–146, Feb. 2016. DOI: 10.1002/2015JE004966.

[214] S. Soter and J. Ulrichs, "Rotation and Heating of the Planet Mercury," *Nature*, vol. 214, no. 5095, pp. 1315–1316, Jun. 1967. DOI: 10.1038/2141315a0.

[215] T. M. Orlando, A. L. Sprague, G. A. Grieves, D. Schriver, P. M. Trávníček, J. L. Mclain, and R. D. Starr, "Electron Stimulated Desorption as a Source Mechanism for Ions in Mercury's Space Environment," *LPI*, no. 1533, p. 2246, 2010. DOI: 10.1029/2006GL028518.

[216] J. L. McLain, A. L. Sprague, G. A. Grieves, D. Schriver, P. Travinicek, and T. M. Orlando, "Electron-stimulated desorption of silicates: A potential source for ions in Mercury's space environment," *Journal of Geophysical Research: Planets*, vol. 116, no. E3, p. 3007, Mar. 2011. DOI: 10.1029/2010JE003714.

[217] B. V. Yakshinskiy and T. E. Madey, "Photon-stimulated desorption of Na from a lunar sample: temperature-dependent effects," *Icarus*, vol. 168, no. 1, pp. 53–59, Mar. 2004. DOI: 10.1016/J.ICARUS.2003.12.007.

[218] L. S. Morrissey, O. J. Tucker, R. M. Killen, S. Nakhla, and D. W. Savin, "Solar Wind Ion Sputtering of Sodium from Silicates Using Molecular Dynamics Calculations of Surface Binding Energies," *The Astrophysical Journal Letters*, vol. 925, no. 1, p. L6, Jan. 2022. DOI: 10.3847/2041-8213/AC42D8.

[219] M. G. Kivelson and M. G. Kivelson, *Introduction to space physics*. Cambridge University Press, 1995.

[220] D. Schriver, P. Trávníček, M. Ashour-Abdalla, R. L. Richard, P. Hellinger, J. A. Slavin, *et al.*, "Electron transport and precipitation at Mercury during the MESSENGER flybys: Implications for electron-stimulated desorption," *Planetary and Space Science*, vol. 59, no. 15, pp. 2026–2036, Dec. 2011. DOI: 10.1016/J.PSS.2011.03.008.

[221] D. Janches, A. A. Berezhnoy, A. A. Christou, G. Cremonese, T. Hirai, M. Horányi, J. M. Jasinski, and M. Sarantos, "Meteoroids as One of the Sources for Exosphere Formation on Airless Bodies in the Inner Solar System," *Space Science Reviews 2021 217:4*, vol. 217, no. 4, pp. 1–41, Apr. 2021. DOI: 10.1007/S11214-021-00827-6.

[222] J. D. Carrillo-Sánchez, J. M. Plane, W. Feng, D. Nesvorný, and D. Janches, "On the size and velocity distribution of cosmic dust particles entering the atmosphere," *Geophysical Research Letters*, vol. 42, no. 15, pp. 6518–6525, Aug. 2015. DOI: 10.1002/2015GL065149.

[223] P. Borin, G. Cremonese, F. Marzari, and A. Lucchetti, "Asteroidal and cometary dust flux in the inner solar system," *Astronomy & Astrophysics*, vol. 605, A94, Sep. 2017. DOI: 10.1051/0004-6361/201730617.

[224] P. Pokorný, M. Sarantos, and D. Janches, "A Comprehensive Model of the Meteoroid Environment around Mercury," *The Astrophysical Journal*, vol. 863, no. 1, p. 31, Aug. 2018. DOI: 10.3847/1538-4357/AAD051. arXiv: 1807.02749.

[225] P. Borin, G. Cremonese, F. Marzari, M. Bruno, and S. Marchi, "Statistical analysis of micrometeoroids flux on Mercury," *Astronomy & Astrophysics*, vol. 503, no. 1, pp. 259–264, Aug. 2009. DOI: 10.1051/0004-6361/200912080.

[226] P. Borin, M. Bruno, G. Cremonese, and F. Marzari, "Estimate of the neutral atoms' contribution to the Mercury exosphere caused by a new flux of micrometeoroids," *Astronomy & Astrophysics*, vol. 517, no. 14, A89, Jul. 2010. DOI: 10.1051/0004-6361/201014312.

[227] E. Grün, M. Horanyi, and Z. Sternovsky, "The lunar dust environment," *Planetary and Space Science*, vol. 59, no. 14, pp. 1672–1680, Nov. 2011. DOI: 10.1016/J.PSS.2011.04.005.

[228] P. Pokorný, D. Janches, M. Sarantos, J. R. Szalay, M. Horányi, D. Nesvorný, and M. J. Kuchner, "Meteoroids at the Moon: Orbital Properties, Surface Vaporization, and Impact Ejecta Production," *Journal of Geophysical Research: Planets*, vol. 124, no. 3, pp. 752–778, Mar. 2019. DOI: 10.1029/2018JE005912.

[229] Y. Langevin, "The regolith of Mercury: present knowledge and implications for the Mercury Orbiter mission," *Planetary and Space Science*, vol. 45, no. 1, pp. 31–37, Jan. 1997. DOI: 10.1016/S0032-0633(96)00098-0.

[230] A. A. Berezhnoy, "Chemistry of impact events on Mercury," *Icarus*, vol. 300, pp. 210–222, Jan. 2018. DOI: 10.1016/J.ICARUS.2017.08.034.

[231] A. A. Berezhnoy and B. A. Klumov, "Impacts as sources of the exosphere on Mercury," *Icarus*, vol. 195, no. 2, pp. 511–522, Jun. 2008. DOI: 10.1016/J.ICARUS.2008.01.005.

[232] P. Wurz and H. Lammer, "Monte-Carlo simulation of Mercury's exosphere," *Icarus*, vol. 164, no. 1, pp. 1–13, Jul. 2003. DOI: 10.1016/S0019-1035(03)00123-4.

[233] F. Leblanc and R. E. Johnson, "Mercury's sodium exosphere," *Icarus*, vol. 164, no. 2, pp. 261–281, Aug. 2003. DOI: 10.1016/S0019-1035(03)00147-7.

[234] V. Mangano, A. Milillo, A. Mura, S. Orsini, E. De Angelis, A. M. Di Lellis, and P. Wurz, "The contribution of impulsive meteoritic impact vapourization to the Hermean exosphere," *Planetary and Space Science*, vol. 55, no. 11, pp. 1541–1556, Sep. 2007. DOI: 10.1016/J.PSS.2006.10.008.

[235] D. Gamborino, A. Vorburger, and P. Wurz, "Mercury's subsolar sodium exosphere: An ab initio calculation to interpret MASCS/UVVS observations from MESSENGER," *Annales Geophysicae*, vol. 37, no. 4, pp. 455–470, Jul. 2019. DOI: 10.5194/ANGEO-37-455-2019.

[236] A. A. Berezhnoy, "Chemistry of impact events on the Moon," *Icarus*, vol. 226, no. 1, pp. 205–211, Sep. 2013. DOI: 10.1016/J.ICARUS.2013.05.030.

[237] R. R. Valiev, A. A. Berezhnoy, B. F. Minaev, V. E. Chernov, and V. N. Cherepanov, "Ab Initio Study of Electronic States of Astrophysically Important Molecules," *Russian Physics Journal*, vol. 59, no. 4, pp. 536–543, Aug. 2016. DOI: 10.1007/S11182-016-0803-Y.

[238] M. H. Burger, R. M. Killen, W. E. McClintock, R. J. Vervack, A. W. Merkel, A. L. Sprague, and M. Sarantos, "Modeling MESSENGER observations of calcium in Mercury's exosphere," *Journal of Geophysical Research: Planets*, vol. 117, E00L11, Dec. 2012. DOI: 10.1029/2012JE004158.

[239] S. Kameda, I. Yoshikawa, M. Kagitani, and S. Okano, "Interplanetary dust distribution and temporal variability of Mercury's atmospheric Na," *Geophysical Research Letters*, vol. 36, no. 15, p. 15 201, Aug. 2009. DOI: 10.1029/2009GL039036.

[240] A. Mutzke, R. Schneider, W. Eckstein, R. Dohmen, K. Schmid, U. von Toussaint, and G. Badelow, *SDTrimSP Version 6.00*, 2019.

[241] R. Behrisch, H. H. Andersen, H. Bay, M. T. Robinson, H. Sigmund, and R. R, *Sputtering by particle bombardment*. Springer-Verlag New York, 1981, vol. 1.

[242] J. Geiss, F. Buehler, H. Cerutti, and P. Eberhardta, "15. Solar-Wind Composition Experiment," *Apollo 15: Preliminary Science Report*, vol. 1, 1972.

[243] R. O. Pepin, "Rare gases in the past and present solar wind," in *Ancient sun: fossil record in the earth, moon and meteorites.*, Boulder, CO, 1980.

[244] J. T. Gosling, "The Solar Wind," *Encyclopedia of the Solar System*, pp. 99–116, Jan. 2007. DOI: 10.1016/B978-012088589-3/50009-8.

[245] R. M. Walker, "Nature of the fossil evidence - Moon and meteorites," in *The Ancient Sun: Fossil Record in the Earth, Moon and Meteorites*, Boulder, CO, 1980, p. 11.

[246] E. Kallio, S. Dyadechkin, P. Wurz, and M. Khodachenko, "Space weathering on the Moon: Farside-nearside solar wind precipitation asymmetry," *Planetary and Space Science*, vol. 166, pp. 9–22, Feb. 2019. DOI: 10.1016/J.PSS.2018.07.013.

[247] S. Fatemi, A. R. Poppe, and S. Barabash, "Hybrid Simulations of Solar Wind Proton Precipitation to the Surface of Mercury," *Journal of Geophysical Research: Space Physics*, vol. 125, no. 4, e2019JA027706, Apr. 2020. DOI: 10.1029/2019JA027706.

[248] J. A. Slavin, M. H. Acuña, B. J. Anderson, D. N. Baker, M. Benna, S. A. Boardsen, *et al.*, "MESSENGER observations of magnetic reconnection in Mercury's magnetosphere.," *Science*, vol. 324, no. 5927, pp. 606–610, May 2009. DOI: 10.1126/science.1172011.

[249] G. A. DiBraccio, J. A. Slavin, S. A. Boardsen, B. J. Anderson, H. Korth, T. H. Zurbuchen, J. M. Raines, D. N. Baker, R. L. McNutt, and S. C. Solomon, "MESSENGER observations of magnetopause structure and dynamics at Mercury," *Journal of Geophysical Research: Space Physics*, vol. 118, no. 3, pp. 997–1008, Mar. 2013. DOI: 10.1002/jgra.50123.

[250] D. J. Gershman, J. A. Slavin, J. M. Raines, T. H. Zurbuchen, B. J. Anderson, H. Korth, D. N. Baker, and S. C. Solomon, "Magnetic flux pileup and plasma depletion in Mercury's subsolar magnetosheath," *Journal of Geophysical Research: Space Physics*, vol. 118, no. 11, pp. 7181–7199, Nov. 2013. DOI: 10.1002/2013JA019244.

[251] S. M. Imber, J. A. Slavin, S. A. Boardsen, B. J. Anderson, H. Korth, R. L. McNutt, and S. C. Solomon, "MESSENGER observations of large dayside flux transfer events: Do they drive Mercury's substorm cycle?" *Journal of Geophysical Research: Space Physics*, vol. 119, no. 7, pp. 5613–5623, Jul. 2014. DOI: 10.1002/2014JA019884.

[252] D. C. Delcourt, S. Grimald, F. Leblanc, J.-J. Berthelier, A. Millilo, A. Mura, S. Orsini, and T. E. Moore, "A quantitative model of the planetary $NaNa^+$ contribution to Mercury's magnetosphere," *Annales Geophysicae*, vol. 21, no. 8, pp. 1723–1736, Aug. 2003. DOI: 10.5194/angeo-21-1723-2003.

[253] E. Kallio and P. Janhunen, "Solar wind and magnetospheric ion impact on Mercury's surface," *Geophysical Research Letters*, vol. 30, no. 17, pp. 1–4, Sep. 2003. DOI: 10.1029/2003GL017842.

[254] S. Massetti, S. Orsini, A. Milillo, A. Mura, E. De Angelis, H. Lammer, and P. Wurz, "Mapping of the cusp plasma precipitation on the surface of Mercury," *Icarus*, vol. 166, no. 2, pp. 229–237, Dec. 2003. DOI: 10.1016/J.ICARUS.2003.08.005.

[255] M. Pfleger, H. Lichtenegger, P. Wurz, H. Lammer, E. Kallio, M. Alho, A. Mura, S. McKenna-Lawlor, and J. Martín-Fernández, "3D-modeling of Mercury's solar wind sputtered surface-exosphere environment," *Planetary and Space Science*, vol. 115, pp. 90–101, Sep. 2015. DOI: 10.1016/J.PSS.2015.04.016.

[256] R. M. Winslow, N. Lugaz, L. Philpott, C. J. Farrugia, C. L. Johnson, B. J. Anderson, C. S. Paty, N. A. Schwadron, and M. A. Asad, "Observations of Extreme ICME Ram Pressure Compressing Mercury's Dayside Magnetosphere to the Surface," *The Astrophysical Journal*, vol. 889, no. 2, p. 184, Feb. 2020. DOI: 10.3847/1538-4357/AB6170. arXiv: 1903.00577.

[257] M. Benna, B. J. Anderson, D. N. Baker, S. A. Boardsen, G. Gloeckler, R. E. Gold, *et al.*, "Modeling of the magnetosphere of Mercury at the time of the first MESSENGER flyby," *Icarus*, vol. 209, no. 1, pp. 3–10, Sep. 2010. DOI: 10.1016/J.ICARUS.2009.11.036.

[258] S. Fatemi, N. Poirier, M. Holmström, J. Lindkvist, M. Wieser, and S. Barabash, "A modelling approach to infer the solar wind dynamic pressure from magnetic field observations inside Mercury's magnetosphere," *Astronomy & Astrophysics*, vol. 614, A132, Jun. 2018. DOI: 10.1051/0004-6361/201832764.

[259] R. M. Winslow, C. L. Johnson, B. J. Anderson, D. J. Gershman, J. M. Raines, R. J. Lillis, *et al.*, "Mercury's surface magnetic field determined from proton-reflection magnetometry," *Geophysical Research Letters*, vol. 41, no. 13, pp. 4463–4470, Jul. 2014. DOI: 10.1002/2014GL060258.

[260] T. A. Bida, R. M. Killen, and T. H. Morgan, "Discovery of calcium in Mercury's atmosphere," *Nature*, vol. 404, no. 6774, pp. 159–161, Mar. 2000. DOI: 10.1038/35004521.

[261] R. M. Killen, T. A. Bida, and T. H. Morgan, "The calcium exosphere of Mercury," *Icarus*, vol. 173, no. 2, pp. 300–311, Feb. 2005. DOI: 10.1016/j.icarus.2004.08.022.

[262] W. E. McClintock, E. T. Bradley, R. J. Vervack, R. M. Killen, A. L. Sprague, N. R. Izenberg, and S. C. Solomon, "Mercury's exosphere: Observations during MESSENGER's first mercury flyby," *Science*, vol. 321, no. 5885, pp. 92–94, Jul. 2008. DOI: 10.1126/SCIENCE.1159467.

[263] M. Horányi, J. R. Szalay, S. Kempf, J. Schmidt, E. Grün, R. Srama, and Z. Sternovsky, "A permanent, asymmetric dust cloud around the Moon," *Nature 2015 522:7556*, vol. 522, no. 7556, pp. 324–326, Jun. 2015. DOI: 10.1038/nature14479.

[264] A. W. Merkel, R. J. Vervack, R. M. Killen, T. A. Cassidy, W. E. McClintock, L. R. Nittler, and M. H. Burger, "Evidence Connecting Mercury's Magnesium Exosphere to Its Magnesium-Rich Surface Terrane," *Geophysical Research Letters*, vol. 45, no. 14, pp. 6790–6797, Jul. 2018. DOI: 10.1029/2018GL078407.

[265] M. Sarantos, R. M. Killen, A. S. Sharma, and J. A. Slavin, "Influence of plasma ions on source rates for the lunar exosphere during passage through the Earth's magnetosphere," *Geophysical Research Letters*, vol. 35, no. 4, p. L04105, Feb. 2008. DOI: 10.1029/2007GL032310.

[266] M. Sarantos, R. M. Killen, A. Surjalal Sharma, and J. A. Slavin, "Sources of sodium in the lunar exosphere: Modeling using ground-based observations of sodium emission and spacecraft data of the plasma," *Icarus*, vol. 205, no. 2, pp. 364–374, Feb. 2010. DOI: 10.1016/J.ICARUS.2009.07.039.

[267] E. S. Mashkova and V. A. Molchanov, "Medium-energy ion scattering by solid surfaces. Part I," *Radiation Effects*, vol. 16, no. 3-4, pp. 143–187, Oct. 1972. DOI: 10.1080/00337577208231218.

[268] ——, "Medium energy ion scattering by solid surfaces. Part II," *Radiation Effects*, vol. 23, no. 4, pp. 215–270, 1974. DOI: 10.1080/00337577408244188.

[269] G. M. McCracken, "The behaviour of surfaces under ion bombardment," *Reports on Progress in Physics*, vol. 38, no. 2, p. 241, Feb. 1975. DOI: 10.1088/0034-4885/38/2/002.

[270] R. Behrisch, G. Betz, G. Carter, B. Navinsek, J. Whitton, J. Roth, B. Scherzer, P. Townsend, and G. K. Wehner, *Sputtering by particle bombardment II*. Springer Berlin, 1983, vol. 52, p. 11.

[271] P. Sigmund, "Theory of sputtering. I. Sputtering yield of amorphous and polycrystalline targets," *Physical Review*, vol. 184, no. 2, pp. 383–416, Aug. 1969. DOI: 10.1103/PhysRev.184.383. arXiv: PhysRev.184.383.

[272] F. Aumayr and H. Winter, "Potential sputtering," *Philosophical Transactions of the Royal Society of London. Series A: Mathematical, Physical and Engineering Sciences*, vol. 362, no. 1814, M. W. Thompson, J. S. Colligon, and R. Smith, Eds., pp. 77–102, Jan. 2004. DOI: 10.1098/rsta.2003.1300.

[273] A. F. Barghouty, F. W. Meyer, P. R. Harris, and J. H. Adams, "Solar-wind protons and heavy ions sputtering of lunar surface materials," *Nuclear Instruments and Methods in Physics Research Section B: Beam Interactions with Materials and Atoms*, vol. 269, no. 11, pp. 1310–1315, Jun. 2011. DOI: 10.1016/J.NIMB.2010.12.033.

[274] F. W. Meyer, P. R. Harris, C. N. Taylor, H. M. Meyer, A. F. Barghouty, and J. H. Adams, "Sputtering of lunar regolith simulant by protons and singly and multicharged Ar ions at solar wind energies," *Nuclear Instruments and Methods in Physics Research, Section B: Beam Interactions*

with Materials and Atoms, vol. 269, no. 11, pp. 1316–1320, Jun. 2011. DOI: 10.1016/j.nimb.2010.11.091.

[275] S. T. Alnussirat, A. F. Barghouty, J. E. Edmunson, M. S. Sabra, and D. L. Rickman, "Contributions of solar-wind induced potential sputtering to the lunar surface erosion rate and it's exosphere," *Nuclear Instruments and Methods in Physics Research, Section B: Beam Interactions with Materials and Atoms*, vol. 420, pp. 33–39, Apr. 2018. DOI: 10.1016/j.nimb.2018.01.020.

[276] H. Hijazi, M. E. Bannister, H. M. Meyer, C. M. Rouleau, A. F. Barghouty, D. L. Rickman, and F. W. Meyer, "Anorthite sputtering by H+ and Ar q+ (q=1-9) at solar wind velocities," *Journal of Geophysical Research: Space Physics*, vol. 119, no. 10, pp. 8006–8016, Oct. 2014. DOI: 10.1002/2014JA020140.

[277] H. Hijazi, M. E. Bannister, H. M. Meyer, C. M. Rouleau, and F. W. Meyer, "Kinetic and potential sputtering of an anorthite-like glassy thin film," *Journal of Geophysical Research: Planets*, vol. 122, no. 7, pp. 1597–1609, Jul. 2017. DOI: 10.1002/2017JE005300.

[278] P. S. Szabo, R. Chiba, H. Biber, R. Stadlmayr, B. M. Berger, D. Mayer, *et al.*, "Solar wind sputtering of wollastonite as a lunar analogue material – Comparisons between experiments and simulations," *Icarus*, vol. 314, pp. 98–105, Nov. 2018. DOI: 10.1016/J.ICARUS.2018.05.028.

[279] P. Szabo, D. Weichselbaum, H. Biber, C. Cupak, A. Mutzke, R. Wilhelm, and F. Aumayr, "Graphical user interface for SDTrimSP to simulate sputtering, ion implantation and the dynamic effects of ion irradiation," *Nuclear Instruments and Methods in Physics Research Section B: Beam Interactions with Materials and Atoms*, vol. 522, pp. 47–53, Jul. 2022. DOI: 10.1016/J.NIMB.2022.04.008.

[280] P. S. Szabo, H. Biber, N. Jäggi, M. Brenner, D. Weichselbaum, A. Niggas, *et al.*, "Dynamic Potential Sputtering of Lunar Analog Material by Solar Wind Ions," *The Astrophysical Journal*, vol. 891, no. 1, p. 100, Mar. 2020. DOI: 10.3847/1538-4357/ab7008.

[281] G. Sauerbrey, "Verwendung von Schwingquarzen zur Wägung dünner Schichten und zur Mikrowägung," *Zeitschrift für Physik*, vol. 155, no. 2, pp. 206–222, 1959. DOI: 10.1007/BF01337937.

[282] G. Hayderer, M. Schmid, P. Varga, H. P. Winter, and F. Aumayr, "A highly sensitive quartz-crystal microbalance for sputtering investigations in slow ion-surface collisions," *Review of Scientific Instruments*, vol. 70, no. 9, pp. 3696–3700, Sep. 1999. DOI: 10.1063/1.1149979.

[283] A. Golczewski, K. Dobes, G. Wachter, M. Schmid, and F. Aumayr, "A quartz-crystal-microbalance technique to investigate ion-induced erosion of fusion relevant surfaces," *Nuclear Instruments and Methods in Physics Research Section B: Beam Interactions with Materials and Atoms*, vol. 267, no. 4, pp. 695–699, Feb. 2009. DOI: 10.1016/J.NIMB.2008.10.088.

[284] J. Brötzner, "An Optimised catcher-QCM setup to study the sputtering of Lunar and Hermean surface regolith analogues," PhD thesis, TU Wien, 2022, p. 66. DOI: 10.34726/HSS.2022.91601.

[285] P. S. Szabo, "Experimental and simulated sputtering of Gold, Iron and Wollastonite with a Catcher-QCM setup," PhD thesis, Technische Universität Wien, 2017.

[286] D. H. Lowndes, D. B. Geohegan, A. A. Puretzky, D. P. Norton, and C. M. Rouleau, "Synthesis of Novel Thin-Film Materials by Pulsed Laser Deposition," *Science*, vol. 273, no. 5277, pp. 898–903, Aug. 1996. DOI: 10.1126/SCIENCE.273.5277.898.

[287] M. Küstner, W. Eckstein, E. Hechtl, and J. Roth, "Angular dependence of the sputtering yield of rough beryllium surfaces," *Journal of Nuclear Materials*, vol. 265, no. 1-2, pp. 22–27, Feb. 1999. DOI: 10.1016/S0022-3115(98)00648-5.

[288] B. M. Berger, P. S. Szabo, R. Stadlmayr, and F. Aumayr, "Sputtering measurements using a quartz crystal microbalance as a catcher," *Nuclear Instruments and Methods in Physics Research Section B: Beam Interactions with Materials and Atoms*, vol. 406, pp. 533–537, Sep. 2017. DOI: 10.1016/J.NIMB.2016.11.039.

[289] R. Behrisch and W. Eckstein, *Sputtering by particle bombardment : experiments and computer calculations from threshold to MeV energies*. Springer, 2007, p. 507.

[290] J. F. Ziegler, J. P. Biersack, and M. D. Ziegler, *SRIM, the stopping and range of ions in matter*. SRIM Co, 2008.

[291] J. P. Biersack and W. Eckstein, "Sputtering studies with the Monte Carlo Program TRIM.SP," *Applied Physics A 1984 34:2*, vol. 34, no. 2, pp. 73–94, Jun. 1984. DOI: 10.1007/BF00614759.

[292] I. Bizyukov, A. Mutzke, R. Schneider, and J. Davis, "Evolution of the 2D surface structure of a silicon pitch grating under argon ion bombardment: Experiment and modeling," *Nuclear Instruments and Methods in Physics Research Section B: Beam Interactions with Materials and Atoms*, vol. 268, no. 17-18, pp. 2631–2638, Sep. 2010. DOI: 10.1016/J.NIMB.2010.06.035.

[293] U. von Toussaint, A. Mutzke, and A. Manhard, "Sputtering of rough surfaces: a 3D simulation study," *Physica Scripta*, vol. T170, no. T170, p. 014 056, Dec. 2017. DOI: 10.1088/1402-4896/aa90be.

[294] W. Möller and W. Eckstein, "Tridyn — A TRIM simulation code including dynamic composition changes," *Nuclear Instruments and Methods in Physics Research Section B: Beam Interactions with Materials and Atoms*, vol. 2, no. 1-3, pp. 814–818, Mar. 1984. DOI: 10.1016/0168-583X(84)90321-5.

[295] W. Möller, W. Eckstein, and J. P. Biersack, "Tridyn-binary collision simulation of atomic collisions and dynamic composition changes in solids," *Computer Physics Communications*, vol. 51, no. 3, pp. 355–368, Nov. 1988. DOI: 10.1016/0010-4655(88)90148-8.

[296] M. T. Robinson and I. M. Torrens, "Computer simulation of atomic-displacement cascades in solids in the binary-collision approximation," *Physical Review B*, vol. 9, no. 12, p. 5008, Jun. 1974. DOI: 10.1103/PhysRevB.9.5008.

[297] W. D. Wilson, L. G. Haggmark, and J. P. Biersack, "Calculations of nuclear stopping, ranges, and straggling in the low-energy region," *Physical Review B*, vol. 15, no. 5, p. 2458, Mar. 1977. DOI: 10.1103/PhysRevB.15.2458.

[298] E. Fermi and E. Teller, "The Capture of Negative Mesotrons in Matter," *Physical Review*, vol. 72, no. 5, p. 399, Sep. 1947. DOI: 10.1103/PhysRev.72.399.

[299] J. Lindhard and M. Scharff, "Energy Dissipation by Ions in the kev Region," *Physical Review*, vol. 124, no. 1, p. 128, Oct. 1961. DOI: 10.1103/PhysRev.124.128.

[300] O. B. Firsov, "A qualitative interpretation of the mean electron excitation energy in atomic collisions," *Zhur. Eksptl'. i Teoret. Fiz.*, vol. 36, 1959.

[301] O. S. Oen and M. T. Robinson, "Computer studies of the reflection of light ions from solids," *Nuclear Instruments and Methods*, vol. 132, no. C, pp. 647–653, Jan. 1976. DOI: 10.1016/0029-554X(76)90806-5.

[302] H. Bethe, "Bremsformel für elektronen relativistischer geschwindigkeit," *Zeitschrift für Physik*, vol. 76, no. 5-6, pp. 293–299, 1932.

[303] F. Bloch, "Bremsvermögen von Atomen mit mehreren Elektronen," *Zeitschrift für Physik*, vol. 81, no. 5-6, pp. 363–376, May 1933. DOI: 10.1007/BF01344553/METRICS.

[304] J. F. Ziegler and J. P. Biersack, "The Stopping and Range of Ions in Matter," *Treatise on Heavy-Ion Science*, pp. 93–129, 1985. DOI: 10.1007/978-1-4615-8103-1_3.

[305] H. M. Urbassek, "Molecular-dynamics simulation of sputtering," *Nuclear Instruments and Methods in Physics Research Section B: Beam Interactions with Materials and Atoms*, vol. 122, no. 3, pp. 427–441, Feb. 1997. DOI: 10.1016/S0168-583X(96)00681-7.

[306] D. Frenkel, B. Smit, J. Tobochnik, S. R. McKay, and W. Christian, "Understanding Molecular Simulation," *Computers in Physics*, vol. 11, no. 4, p. 351, Jun. 1997. DOI: 10.1063/1.4822570.

[307] J. R. Beeler, *Radiation effects computer experiments*. Amstercam, New York, Oxford: North-Holland Publishing Company, 2012, p. 881.

[308] M. Finnis, *Interatomic forces in condensed matter*. Oxford University Press, 2003, vol. 1, p. 285.

[309] P. N. Peplowski, L. G. Evans, S. A. Hauck, T. J. McCoy, W. V. Boynton, J. J. Gillis-Davis, *et al.*, "Radioactive elements on Mercury's surface from MESSENGER: implications for the planet's formation and evolution.," *Science (New York, N.Y.)*, vol. 333, no. 6051, pp. 1850–2, Sep. 2011. DOI: 10.1126/science.1211576.

[310] N. C. Michel, S. A. Hauck, S. C. Solomon, R. J. Phillips, J. H. Roberts, and M. T. Zuber, "Thermal evolution of Mercury as constrained by MESSENGER observations," *Journal of Geophysical Research: Planets*, vol. 118, no. 5, pp. 1033–1044, May 2013. DOI: 10.1002/jgre.20049.

[311] J. M. Christoph, G. M. Minesinger, C. Bu, C. A. Dukes, and L. T. Elkins-Tanton, "Space Weathering Effects in Troilite by Simulated Solar-Wind Hydrogen and Helium Ion Irradiation," *Journal of Geophysical Research. Planets*, vol. 127, no. 5, May 2022. DOI: 10.1029/2021JE006916.

[312] D. L. Domingue and C. T. Russell, *The MESSENGER mission to Mercury*. New York: Springer Science & Business Media, 2007. DOI: 10.1007/978-0-387-77214-1.

[313] S. C. Solomon, L. R. Nittler, and B. J. Anderson, *Mercury: The View after MESSENGER*. Cambridge, United Kingdom: Cambridge University Press, Jan. 2018, pp. 1–584. DOI: 10.1017/9781316650684.

Declaration of Originality

Name, Vorname:	Jäggi, Noah
Matrikelnummer:	13-931-589
Studiengang:	Physik
Leiter der Arbeit:	PD Dr. Galli, André
Titel der Dissertation:	The surfaces of the Moon and Mercury: an experimental and numerical approach to ion sputtering

Ich erkläre hiermit, dass ich diese Arbeit selbständig verfasst und keine anderen als die angegebenen Quellen benutzt habe. Alle Stellen, die wörtlich oder sinngemäss aus Quellen entnommen wurden, habe ich als solche gekennzeichnet. Mir ist bekannt, dass andernfalls der Senat gemäss Artikel 36 Absatz 1 Buchstabe r des Gesetzes über die Universität vom 5. September 1996 und Artikel 69 des Universitätsstatuts vom 7. Juni 2011 zum Entzug des Doktortitels berechtigt ist. Für die Zwecke der Begutachtung und der Überprüfung der Einhaltung der Selbständigkeitserklärung bzw. der Reglemente betreffend Plagiate erteile ich der Universität Bern das Recht, die dazu erforderlichen Personendaten zu bearbeiten und Nutzungshandlungen vorzunehmen, insbesondere die Doktorarbeit zu vervielfältigen und dauerhaft in einer Datenbank zu speichern sowie diese zur Überprüfung von Arbeiten Dritter zu verwenden oder hierzu zur Verfügung zu stellen.

Bern, May 15, 2023

Noah Jäggi